ELECTROLESS Ni-P-Ti BASED NANOCOMPOSITE COATINGS

by

Zhi Li

Submitted in partial fulfilment of the requirements

for the degree of Doctor of Philosophy

at

Dalhousie University

Halifax, Nova Scotia

April 2021

I dedicate this thesis to my wife and my son

And to my parents who always support me and tell me never ever give up

Table of Contents

List of Tables

List of Figures

Abstract

Infrastructures in various industries, such as oil and gas, chemical, automotive etc., are subjected to aggressive erosive and corrosive environments. A potential candidate for the protection of such infrastructures is electroless Ni-P coating owing to its high hardness and good corrosion resistance. Nevertheless, Ni-P has low toughness, which tends to readily crack and fracture under load. To toughen Ni-P coating, superelastic NiTi particles are an attractive addition. The high price of the NiTi particles, however, restricts their application. Ti particles have much lower price (5-10 times lower) than NiTi particles, which can be employed as an alternative to the NiTi particles. Therefore, to reduce cost, Ti particles were utilized as an addition in the present study. Ni-P-NiTi composite coatings with different Ti concentrations were successfully prepared on low carbon steel substrates by co-plating Ni-P and Ti nanoparticles followed by annealing of Ni-P-Ti coatings. To systematically investigate the effects of the formation of superelastic NiTi phase after annealing on the mechanical, wear, and corrosion properties of the composite coatings, a series of tests were conducted such as scratch, bend, tensile, nanoindentation, single particle erosion, corrosion, and erosion-corrosion tests. The formation of NiTi phase after annealing was substantiated by slow scan XRD, point and line scan EDS. The superelastic effect of NiTi particles was also verified by nanoindentation tests. Compared to Ni-P-Ti coatings annealed at 700°C and 800°C for 5 hours, Ni-P-Ti coatings annealed at 650°C for 2 hours exhibited higher Vickers hardness, scratch toughness, scratch resistance due to the formation of high amount of superelastic NiTi phase. Different toughening mechanisms such as crack deflection, crack bridging, transformation toughening induced by superelastic NiTi particles were observed and identified in the aforementioned tests. In conclusion, the formation of superelastic NiTi phase not only improved the toughness, scratch, indentation, erosion resistance but also considerably enhanced the corrosion and erosion-corrosion resistance of Ni-P coating. As a result, the annealed Ni-P-Ti coatings (i.e., Ni-P-NiTi coatings) may be employed to protect low carbon steel components or in applications where the high cracking resistance, high wear, or impact resistance, and/or high corrosion resistance are required.

List of Abbreviations Used

AE	Acoustic Emission
CR	Corrosion Rate
COF	Coefficient of Friction
CBN	Cubic Boron Nitride
DMAB	Dimethylamine Borane
EN	Electroless Nickel
EIS	Electrochemical Impedance Spectroscopy
EDS	Energy Dispersive Spectroscopy
FCC	Face Centered Cubic
HV	Vickers Hardness
NOL	Naval Ordnance Laboratory
OM	Optical Microscopy
PP	Potentiodynamic Polarization
PD	Porosity Density
PM	Powder Metallurgy
SE	Superelastic Effect
SME	Shape Memory Effect
SCE	Saturated Calomel Electrode
SEM	Scanning Electron Microscopy
SPE	Single Particle Erosion

SPEC	Slurry Pot Erosion-Corrosion
TEM	Transmission Electron Microscopy
VIM	Vacuum Induction Melting
XRD	X-ray Diffraction
XPS	X-ray Photoelectron Spectroscopy

Acknowledgements

First and foremost, I would like to thank my supervisor Professor Zoheir Farhat. I am really grateful for the precious opportunity that he gave me to study in Canada. I am lucky to have him not just as my supervisor, but as my mentor and philosopher. I still remember the day that I went to the corrosion lab and he told me that researchers need patience, passion, and persistence. This is also true for life outside of research. He is such a great man who always inspires, supports, and helps me to be the best of myself. From him, I learned how to design experiments, how to write an academic journal paper, and how to reply reviewers' comments. Because of him, my writing has significantly improved. I really appreciate his guidance, advice, financial support, and especially for his kindness and patience during my entire PhD study period. I could not imagine that I would ever finish my PhD study without his guidance and support.

I would like to express my sincerest appreciation to Dr. George Jarjoura. I am truly thankful for his support and guidance on corrosion. Owing to him, I learned about corrosion and how to perform potentiodynamic polarization and electrochemical impedance spectroscopy tests and how to analyze the testing results. Without his guidance and help, I could not finish the corrosion part of my program. I am very grateful to Dr. Su-Ling Brooks for her guidance on experimental design and as my committee member. I also want to thank Dr. Md. Aminul Islam for his support and help on erosion-corrosion tests.

I appreciate the help, assistance, and support that I received from my colleagues and friends Ahmad Raza Khand Rana, Brandon Gorman, Chuhong Wang, Nikki Cameron, Marissa Maclean, Marciel Gaier, and Mark Yao Amegadzie. I also would like to thank Patricia Scallion for her help and support on SEM tests.

I do not know what to say to thank my parents, who have encouraged and supported me since I was a child and always tell me never ever give up. I also have no words to express my love and gratitude to my wife Wumei who have suffered and sacrificed since the beginning of my PhD study period. I would like to say thank you to my lovely son Yanbing

who always understands and supports me and has been a source of happiness and inspiration to me.

Zhi Li

Halifax, April 2021

Chapter 1 Introduction

Low carbon steel has been extensively utilized in automotive, oil and gas, and construction industries owing to their low cost and wide availability [1]. For example, in the oil and gas industry, pipelines, made of low carbon steel, are considered to be one of the most economical methods to transport petroleum products [2]. However, the wear and corrosion resistance of steel pipelines is inadequate to withstand aggressive environments [3]. The material degradation of pipelines prompted by wear and corrosion is a serious problem in the petroleum industry due to the presence of particulates (*i.e.* sands or other solid particles) and corrosive species (Cl^-, O_2, H_2S and CO_2) [4]. To protect the pipelines from wear and corrosion, various preventative measures have been employed including different pipeline materials or protective coatings [5-7]. Nevertheless, using durable materials may not always be the most cost-effective solution [5]. Additionally, whilst the application of epoxy or polymer-based coatings have exhibited some improvement, each of these coatings have their limitations. Epoxy-based coatings are incapable of providing sufficient protection against certain chemicals in crude oil [6] and polymer-based coatings may suffer thermal damage during the assembly process [7], in addition to their low hardness. Furthermore, with the ever-increasing demand for energy, today's pipelines operate at higher temperatures and pressure. This new reality has necessitated the search for superior coatings.

Electroless Ni-P coatings have been widely employed in many industries as protective coatings due to their high hardness, superior adhesion strength, and exceptional corrosion resistance [8-10]. Electroless Ni-P coatings are built upon the initial electroless nickel plating research first introduced in 1946 by Brenner and Riddell [11]. In comparison with electroplating, electroless Ni-P plating is an autocatalytic chemical reduction process which does not require the application of external electric current [12]; also, electroless Ni-P plating can be applied to irregular or complex shape components due to its autocatalytic nature [13]. Furthermore, electroless plating can produce uniform coating with superior adhesion, less coating internal stress, and wider range of coating thickness compared to electroplating [14]. As such, electroless Ni-P coatings have the potential to be a protective

material for steel pipelines. Recently, Ni-P based composite coatings have been developed to further improve the properties of the Ni-P coatings. For example, Ni-P-SiO_2 composite coatings have been reported to improve the hardness and corrosion resistance of the binary Ni-P coatings [15]. Tungsten addition provides lower coefficient of friction and improves the wear resistance [16, 17]. Better cavitation erosion resistance has been achieved from Ni-P-SiC coating [18]. Although these composite coatings show improvements in hardness and corrosion resistance, they have little effect on toughness. Ni-P coatings have been shown to exhibit low toughness and tend to crack readily under load or during impact [4, 14, 19], which restricts their applications.

NiTi alloy is known for its shape memory and superelastic effects. For the superelastic effect, the NiTi austenite phase transforms to a detwinned martensite phase under loading with large recoverable strain due to a stress-induced phase transformation [25]. During unloading, the detwinned martensite phase converts back to the austenite phase with large strain recovery. Compared to conventional metals or alloys, superelastic NiTi alloy exhibits much higher recoverable strain. Due to its superelastic effect, NiTi alloy has high toughness and wear resistance.

Owing to the phenomenal properties of NiTi alloy, one way to toughen Ni-P coating is to add superelastic NiTi particles into brittle Ni-P matrix. However, directly adding superelastic NiTi particles into Ni-P matrix to prepare Ni-P-NiTi coatings is not cost-effective. The high price of superelastic NiTi powder limits the applications in Ni-P-NiTi composite coatings [20, 21]. Because the price of Ti powder is 5-10 times lower than that of the NiTi powder, due to the difficulty of preparing superelastic NiTi powder [22], Ti powder is chosen as the alternative to the NiTi powder. Hence, in the present study, to reduce cost, instead of directly adding NiTi particles into the electroless plating solution, Ti particles were added into the solution followed by annealing of Ni-P-Ti coatings to prepare Ni-P-NiTi composite coatings. In addition, the cohesion strength between NiTi particles and Ni matrix after annealing is expected to be higher due to the interdiffusion compared to the as-deposited Ni-P-NiTi coatings prepared by electroless co-depositing Ni-P and pre-alloyed NiTi particles.

First and foremost, the synthesis of Ni-P-NiTi coatings through electroless co-depositing Ni-P and Ti particles followed by annealing of Ni-P-Ti coatings is a predominant objective. Second, the mechanical properties of prepared Ni-P-NiTi coatings such as toughness, hardness, and Young's modulus are critical because the properties are directly related to their resistance to a degradative environment. Third, in order to obtain a comprehensive and systematic investigation of Ni-P-Ti based composite coatings, the composite coatings will be tested under different degradative conditions including scratch, bend, indentation, erosion, corrosion, and erosion-corrosion.

The specific objectives of this research are as follows:

1. Successfully prepare Ni-P-NiTi composite coatings on low carbon steel substrates by electroless co-plating Ti nanoparticles and Ni-P followed by annealing of as-deposited Ni-P-Ti coatings at optimal annealing conditions.
2. Characterize the Ni-P-Ti based composite coatings including composition, microstructure, deposition rate, surface morphology etc.
3. Investigate the formation of the superelastic NiTi particles and assess their effect on the performance of the composite coatings under various degradative conditions: scratch, bend, indentation, erosion, corrosion, and erosion-corrosion.
4. Compare the performance of the composite coatings with that of the Ni-P coating.
5. Identify different toughening, corrosion, and wear mechanisms under various degradative conditions.

Chapter 2 Literature Review

2.1 NiTi Alloy

NiTi alloy is known for its shape memory and superelastic effects. Due to these effects, NiTi alloy exhibits unique properties.

2.1.1 Shape Memory Effect (SME)

Buehler and his coworkers first discovered the shape memory effect in an equal-atomic NiTi alloy in the Naval Ordnance laboratory (NOL) [23]. Therefore, the shape memory alloy is named “NiTiNOL”. Shape memory effect relates to a phenomenon that NiTi alloy is able to recover its original shape upon heating after an initial deformation. Figure 2-1 shows the phenomenon of the shape recovery behavior of NiTi alloy. A straight NiTi rod is placed on two supports (Figure 2-1 (a)). When applying a load at the middle of the rod, the rod is deformed (Figure 2-1 (b). The deformation remains on the rod after unloading (Figure 2-1 (c)), demonstrating that the deformation is non-elastic. However, it reverts to its original shape instantaneously when the bent rod is heated up to above a critical temperature (Figure 2-1 (d)). This behavior is known as the shape memory effect. In other words, shape memory effect means that upon heating above a critical temperature, the residual deformation on a deformed specimen can be completely recovered, and the specimen restores its original shape.

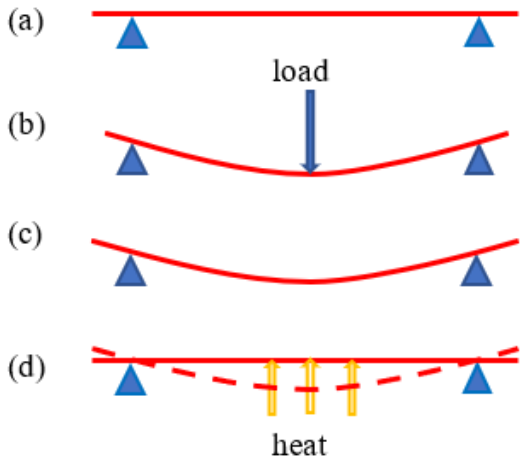

Figure 2-1 Shape memory effect of NiTi alloy.

2.1.2 Superelastic Effect (SE)

Superelastic behavior refers to a large reversible elastic response to all applied loads. That is, when superelastic NiTi alloy is subjected to a load it deforms and upon unloading it restores its original shape with a large deformation recovery. The deformation of the NiTi alloy can completely recover after unloading, thus "elastic", however, the deformation process does not obey the classic Hooke's law of elasticity and involves large recovery, thus superelastic. Superelasticity is due to stress-induced phase transformation in the NiTi alloy upon loading and the reverse phase transformation upon unloading. For traditional metals and alloys, the recoverable elastic strain is only up to 2-3 %, whereas superelastic strain can reach up to 10-12 % [24, 25].

2.1.3 Phases and Precipitates in the Ni-Ti System

The shape memory and superelastic effects are associated with phase transformations in equiatomic NiTi alloy. Generally, three phases are observed during the phase transformation in equiatomic NiTi alloy, austenitic phase, martensitic phase, and R phase.

Austenite phase (B_2 parent phase) of NiTi alloy is a high temperature phase which is related

to the superelastic and shape memory effects owing to its important role in the martensitic transformation. The austenite phase has a CsCl crystal structure at room temperature [26], as shown in Figure 2-2.

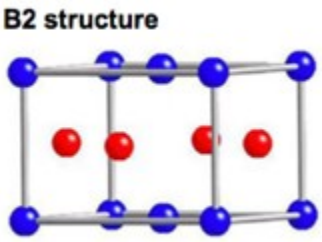

Figure 2-2 Crystal structure (CsCl) of austenite phase, blue spheres: Ti, red spheres: Ni [26].

When austenite phase in NiTi alloy is cooled from high temperature to below a certain critical temperature, martensite phase (B19') forms. B19' martensite phase has a monoclinic crystal structure and is more stable than an intermediate martensite phase B19 which has orthorhombic crystal structure. Figure 2-3 shows the crystal structures of B19' and B19 [26].

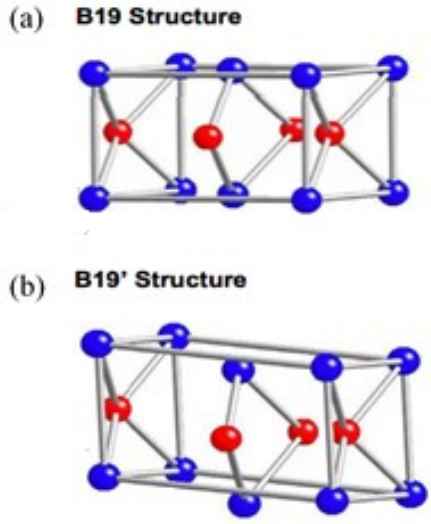

Figure 2-3 (a) Crystal structure (orthorhombic) of intermediate martensite phase B19, (b) crystal structure (monoclinic) of martensite phase B19', blue spheres: Ti, red spheres: Ni [26].

The R-phase has a trigonal crystal structure and is an intermediate phase that forms before the formation of martensitic phase B19' during the martensitic phase transformation. The R-phase transformation is associated with an increase in the electrical resistance of NiTi alloy [26]. Generally, the austenite phase directly transforms to the martensitic phase, which is called one step martensitic phase transformation. In some cases, martensitic phase transformation is found to occur in two stages, first from B_2 to a trigonal R-phase and then from R phase to B19' martensitic phase [27]. This two-step transformation is associated with the presence of Ni_4Ti_3 particles precipitate [26].

Under different temperatures and composition, various other precipitates such as $NiTi_2$, Ni_3Ti, Ni_3Ti_2 and Ni_4Ti_3 can form according to the Ni-Ti phase diagram [27]. Figure 2-4 shows the phase diagram of NiTi alloy.

Ti_2Ni has cubic crystal structure with a lattice constant of 1.132 nm, and has 96 atoms in its unit cell [28]. Ti_2Ni precipitates in the Ti-rich NiTi-based alloy during aging. The crystal structure of Ni_3Ti is hexagonal with lattice parameters of a = 0.51010 nm and c = 0.83068 nm [28]. During heat treatment, Ni_3Ti precipitates in the Ni-rich NiTi-based alloy. Ti_2Ni_3 has two different structures: tetragonal (at 373 K with a = 0.3095 nm and c = 1.3585 nm) and orthorhombic (at 298 K with a=0.3095 nm, b=0.4398 nm, c=1.3544 nm) [28]. Ti_3Ni_4 has rhombohedral crystal structure and is associated with the two-step martensitic phase transformation [28].

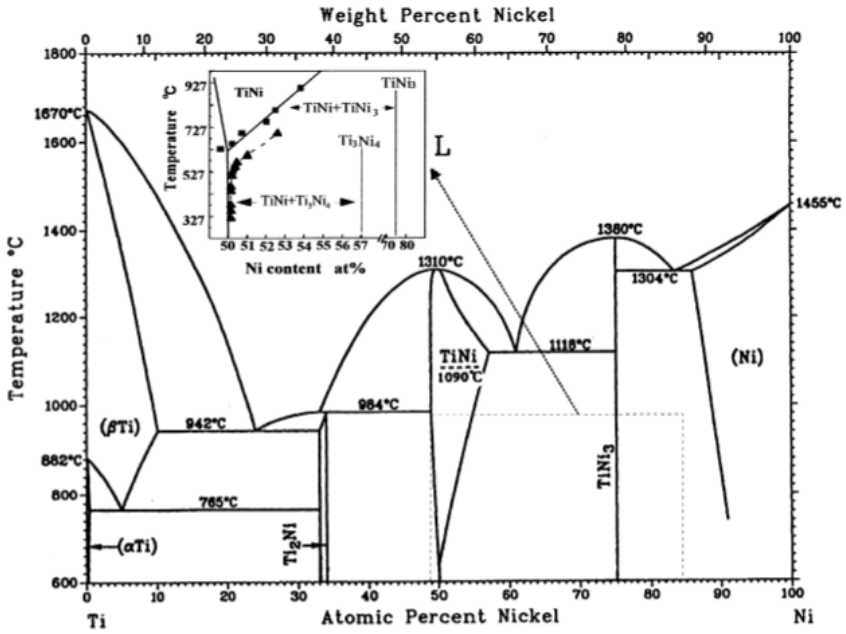

Figure 2-4 NiTi alloy phase diagram [27]

2.1.4 Phase Transformation

Phase transformation of NiTi alloy is characterized by four critical temperatures, M_s (martensitic phase transformation start temperature), M_f (martensitic phase transformation finish temperature), A_s (austenitic phase transformation start temperature), A_f (austenitic phase finish temperature), as shown in Figure 2-5 [29] .When NiTi is cooled from the austenite phase (parent phase) to a temperature below M_f without mechanical load, twinned martensite phase forms. The martensite phase forms in different variants, however, austenite has only one variant [30]. Upon forming martensite, these variants accommodate themselves (by self-accommodation) to form twinned martensite [30]. The martensite phase can convert back to austenite phase when heated to a temperature above A_f.

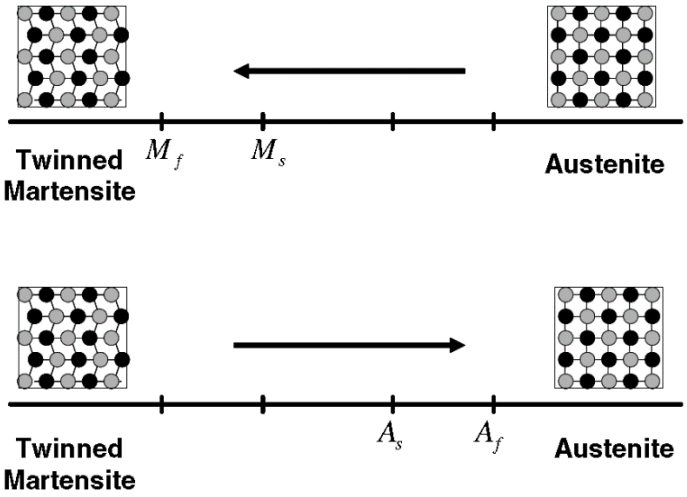

Figure 2-5 Thermally induced phase transformation of NiTi without mechanical load [29].

Figure 2-6 shows the detwinning process of NiTi with an applied stress (a) and the reverse transformation upon heating (b) [29]. The twinned martensite phase transforms to detwinned martensite when an external load is applied due to reorientation of variants. The macroscopic shape changes and the deformation remains after unloading because of the detwinning process (Figure 2-7). When heating to a temperature above A_f, the detwinned martensite transforms back to austenite with complete shape recovery (Figure 2-7 (b)).

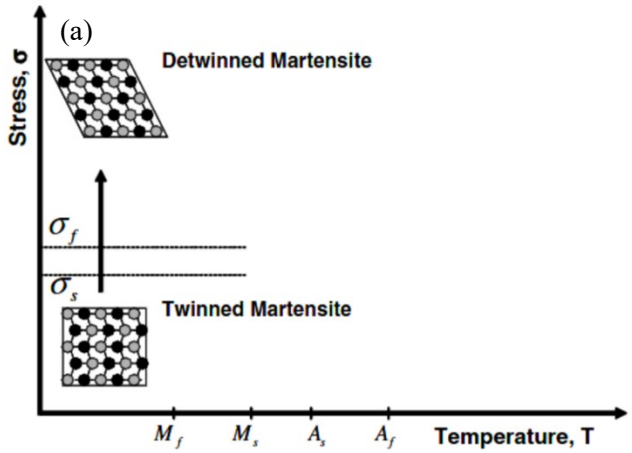

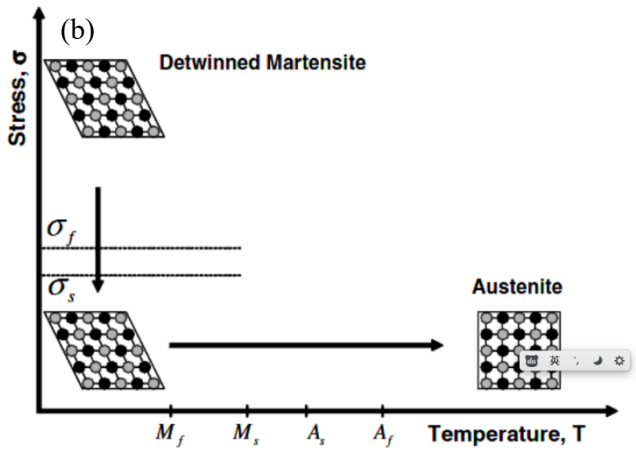

Figure 2-6 (a) Detwinning process of NiTi with an applied stress; (b) reverse transformation upon heating [29].

The martensite phase can also form by subjecting the austenite phase to a critical stress above the M_s temperature, which is known as austenite to martensite transformation stress. This phenomenon is known as stress induced martensitic transformation (SIMT). The transformation is accompanied by a large macroscopic strain. During unloading, the reverse transformation occurs, and the generated strain fully recovers. This is the superelastic effect.

As shown in Figure 2-7 [29], the martensitic transformation start and finish stresses are defined as σ^{Ms} and σ^{Mf}, respectively. Similarly, the reverse transformation start and finish stresses are named σ^{As} and σ^{Af}, respectively. Furthermore, if the temperature is above A_f, the full strain recovery occurs, while if the temperature is between M_s and A_f, only partial strain recovery takes place.

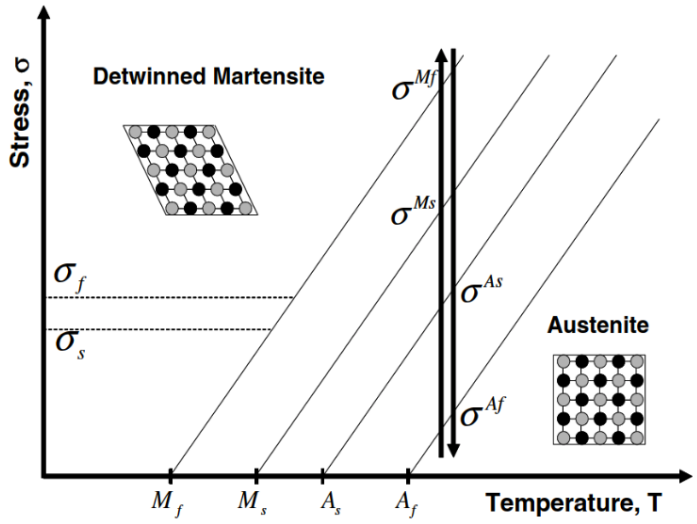

Figure 2-7 Various stresses in superelastic effect [23]

2.1.5 The Formation of NiTi by Solid State Diffusion

The formation of NiTi using solid state diffusion process opened new possibilities for the production of NiTi-based composites that were not feasible using traditional measures (i.e., vacuum induction melting). Hu et al. [31] attempted to produce NiTi by annealing Ni-Ti diffusion couple. They found that $NiTi_2$, NiTi, and Ni_3Ti have formed at the Ni-Ti interface when annealed at 650°C. Ni_3Ti first nucleated on the Ni side, subsequently $NiTi_2$ formed on the Ti side, and NiTi finally developed at the $NiTi_2$ and Ni_3Ti interface. Figure 2-8 shows the diffusion process between Ti and Ni [31].

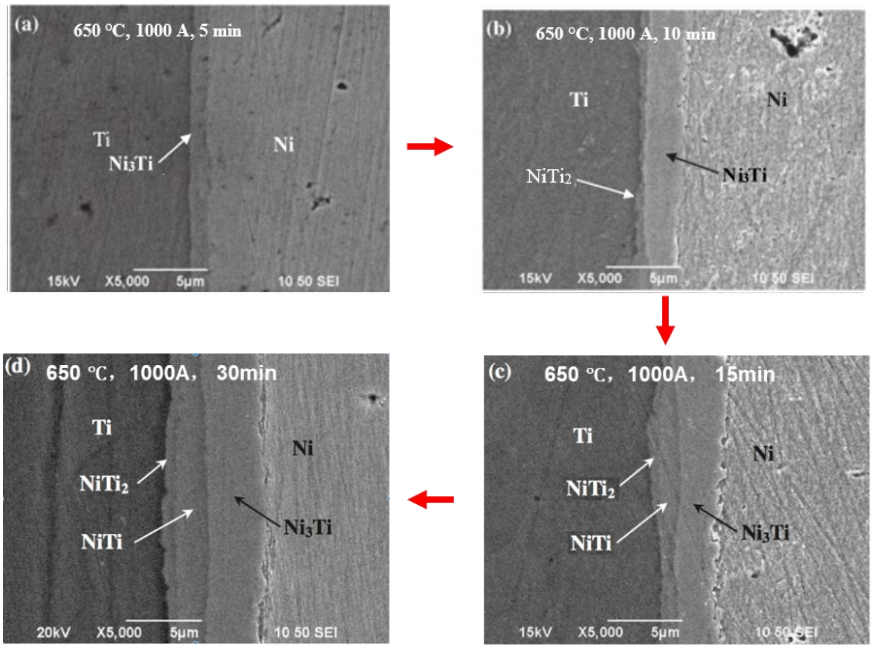

Figure 2-8 Solid state diffusion process in Ni-Ti diffusion couple [31]

Whitney [32] adopted powder metallurgy technique to prepare NiTi alloy and investigated the diffusion process during sintering. Figure 2-9 shows the diffusion process between the Ti and Ni particles. He has shown that the diffusion occurs between Ni and Ti particles as sintering time increases.

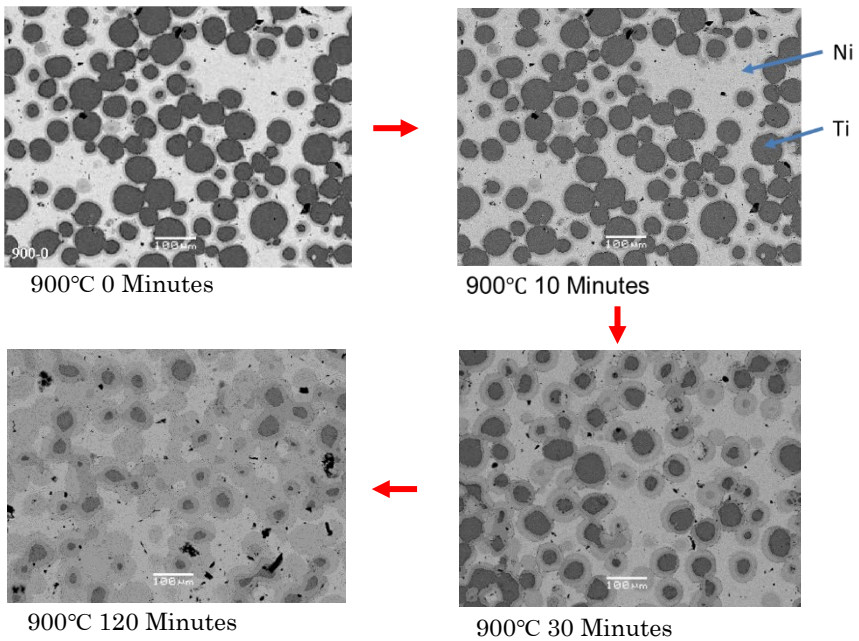

Figure 2-9 Diffusion process between Ti and Ni powder [32].

Feng et al. [33] employed HSC Chemistry software to calculate the Gibbs free energies of different reactions during Ti and Ni diffusion process. They found that Gibbs energies for different formation reactions decreased in the following order: NiTi, $NiTi_2$, and Ni_3Ti. According to thermodynamics, the first formed phase is Ni_3Ti because its formation Gibbs free energy is the lowest. $NiTi_2$ and NiTi are subsequently formed due to their relatively higher formation Gibbs free energies compared to Ni_3Ti. Figure 2-10 shows the temperature (T_0) dependence of standard Gibbs energies (ΔG) for different reactions in Ti-Ni system [33]. Their work predicted that the Ni_3Ti formation reaction has the lowest Gibbs free energy over a wide temperature range.

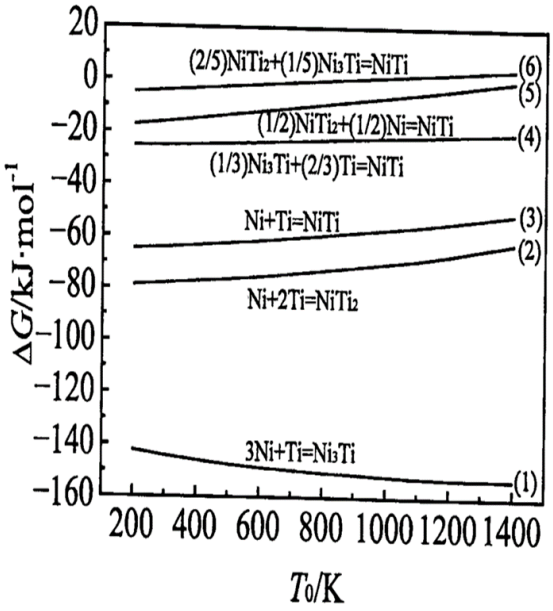

Figure 2-10 Standard Gibbs energies of different reactions in the Ni-Ti system [33]

In addition, Laeng et al. [34] investigated the phase formation process of Ni-Ti via solid state reaction, and they also found that thermodynamics favors the formation of Ni_3Ti,

$NiTi_2$ and NiTi in this order. This implies that the direct formation of NiTi from elemental Ni and Ti in solid state is not thermodynamically favored. The order of the reactions during the diffusion process of Ni-Ti at 1223K is given as follows [34]:

$$3Ni + Ti \rightarrow Ni_3Ti,\ \Delta G_{1223K} = -112.9\ kJmol^{-1},$$

$$Ni + 2Ti \rightarrow NiTi_2,\ \Delta G_{1223K} = -67.0\ kJmol^{-1},$$

$$Ni + Ti \rightarrow NiTi,\ \Delta G_{1223K} = -55.9\ kJmol^{-1},$$

$$1/2NiTi_2 + 1/2Ni \rightarrow NiTi,\ \Delta G_{1223K} = -22.4\ kJmol^{-1},$$

$$1/3Ni_3Ti + 2/3Ti \rightarrow NiTi,\ \Delta G_{1223K} = -18.2\ kJmol^{-1},$$

$$2/5NiTi_2 + 1/5Ni_3Ti \rightarrow NiTi,\ \Delta G_{1223K} = -6.5\ kJmol^{-1},$$

In the copper and brass diffusion couple experiment, Smigelkas and Kirkendall [35] found that zinc diffuses faster than copper and the original interface shifts to compensate for this diffusion rate difference, this phenomenon is known as “Kirkendall effect”. The Kirkendall effect is also observed during annealing process of Ni-Ti couple. Bastin and Rieck [36] studied the solid interdiffusion process in the Ni-Ti system using tungsten wire as inert makers at the interface before annealing and they noticed that the tungsten wire shifted to another position after annealing. Figure 2-11 shows the back-scattered electron image of a Ti-Ni diffusion couple [36].

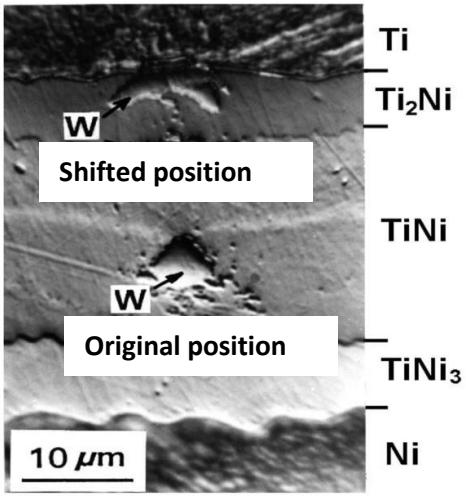

Figure 2-11 Back-scattered image of Kirkendall effect in Ni and Ti diffusion couple (800 °C, 72 h) [36].

Another effect derived from Kirkendall's work is the Kirkendall pores which form during the diffusion process. The formation of pores occurs due to the difference in diffusion rates of the two elements. Pores are observed on the side where the element has higher diffusion rate in a diffusion couple. Hasannaeimi et al. [37] investigated the annealing process of Ni-Ti coatings and noticed micro-pores in the coatings when annealed at 1000 °C for 10 h. They concluded that these pores are the result of Kirkendall effect due to the difference in the diffusivity of Ni and Ti atoms. Figure 2-12 shows the Kirkendall pores in Ni-49 at% Ti composite coating prepared by electro-codeposition of Ni and Ti microparticles followed by annealing [37].

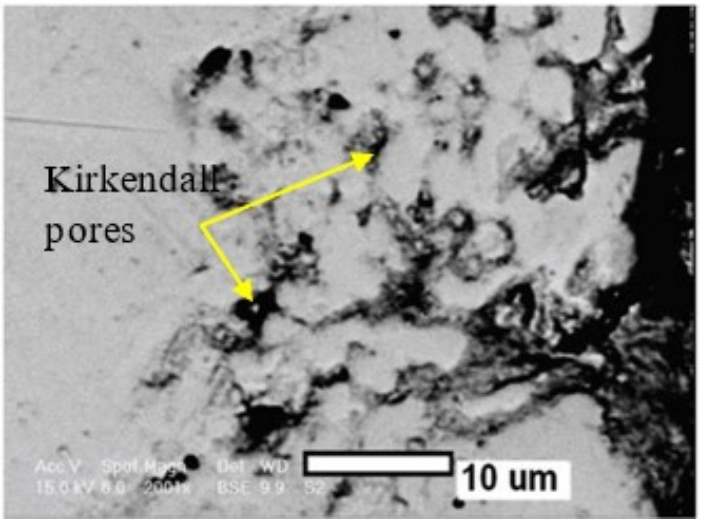

Figure 2-12 Kirkendall pores in Ni-49 at% Ti coating [37]

There are some disagreements between the diffusion rates of Ni and Ti. Some studies asserted that Ni has higher diffusion rate than Ti, while other studies disagreed. The diffusion rate plays an important role in the heat treatment process. Therefore, to draw a conclusion, different studies regarding the diffusion rates of Ni and Ti are summarized in

Table 2-1. From Table 2-1, only one paper [38] mentioned that the bulk diffusion rates of Ti at 750 °C and 950 °C are 7.0×10^{-12} cm^2/s and 2.0×10^{-10} cm^2/s, respectively, which are higher than those of Ni at the same temperatures (5.5×10^{-15} cm^2/s at 750 °C and 1.5×10^{-12} cm^2/s at 950 °C). However, the authors in this paper neither measured nor calculated the diffusion rates of Ni and Ti [3]. They even did not provide the references for these diffusion rates data [3]. On the other hand, the Kirkendall voids or pores are observed on the Ni side by many researchers [5-13] during annealing or sintering process of Ni and Ti inasmuch as Ni has a higher diffusivity in Ti or NiTi than Ti does in Ni or NiTi, which resulted in voids or pores on the Ni side. Furthermore, the authors of two other studies [14, 15] measured the diffusion rates of Ni and Ti in NiTi phase. Divinski et al. [14] measured the diffusion rates of Ni and Ti in a Ni-49.4 at% Ti alloy by employing the radiotracer technique with Ti^{44} and Ni^{63}[14]. They found that Ni showed a higher diffusivity than Ti by one to two orders of magnitude in a temperature range of 950 to 1280 K. Liu et al. [15] also utilized radiotracer technique to measure the diffusion coefficients of Ni and Ti in a Ni-50.07 at% Ti alloy using trace elements of Ti^{44} and Ni^{63}. They found that Ni diffuses faster in Ni-50.07 at% Ti alloy than Ti does in a temperature range between 673 K and 923 K [15]. Therefore, based on the studies concerning the diffusion rates of Ni and Ti tabulated in Table 2-1, it can be concluded that Ni diffuses faster in Ti or NiTi phase than Ti does in Ni or NiTi phase.

Table 2-1 Diffusion rate of Ni in Ti or in NiTi as well as diffusion rate of Ti in Ni or in NiTi

	Diffusion rate (cm^2/s)		
Temperature(°C)	Ni in Ti	Ti in Ni	References
37 (310 K)	3.45×10^{-12}	1.44×10^{-12}	[39]
227 (500 K)	2.53×10^{-8}	1.66×10^{-8}	
327 (600 K)	4.07×10^{-8}	3.57×10^{-8}	
427 (700 K)	2.00×10^{-7}	1.85×10^{-7}	

Temperature (°C)	Bulk diffusion rate of Ni (cm^2/s)	Bulk diffusion rate of Ti (cm^2/s)	References
750 (1023 K)	5.5×10^{-15}	7.0×10^{-12}	[38]
950 (1223 K)	1.5×10^{-12}	2.0×10^{-10}	
650-940 (925-1213 K)	It is found that Ni is by far the fastest moving component in Ti, Ti_2Ni and NiTi		[40]
900 (1173 K)	Pores are observed on Ni side because Ni diffuses faster to the Ti side than Ti does to the Ni side (Ni-Ti diffusion couple)		[41]
1000 (1273 K)	Porous structures are found in Ni-49 at% Ti coatings after annealing inasmuch as the diffusivity of Ni is higher than that of Ti		[37]
925 (1198 K)	The central Kirkendall pores are observed in annealed Ti coated Ni wires since Ni diffuses radially out faster from the core than Ti replaces it		[42]
1000 (1273 K)	Ni has lower evaporation energy in comparison with Ti, so Ni atoms diffuse into Ti ones much faster than Ti atoms towards Ti which contributed to the creation of new pores in the locations where occupied by Ni atoms primarily		[43]
800 (1073 K)	Kirkendall voids are observed on the Ni side in an annealed Ni coated Ti-6Al-4V due to higher diffusivity of Ni than that of Ti		[44]
self-propagating high-temperature synthesis NiTi porous alloy	Ti has a slower diffusion rate than Ni. Kirkendall pores will form at the sites where Ni left.		[45]

Temperature(°C)	Diffusion rate (cm^2/s)		References
894 (1167 K)	Kirkendall pore formation results from the shrinkage of an Ni-rich area due to the much faster diffusion rate of nickel compared to titanium		[46]
600-1000 (873-1273 K)	Most of pores are found in the region with rich Ni element, this can be explained by the Kirkendall diffusion theory, in which nickel has a thermal diffusion coefficient and moves faster than titanium.		[47]
850-1000 (1123-1273K)	The diffusion of nickel into titanium is faster than that of titanium atoms into nickel, and this unbalance of mass transfer results in pore formation in the nickel rich region.		[48]
Temperature(°C)	Ni in Ni-49.4at%Ti	Ti in Ni-49.4at%Ti	References
677 (950 K)	1.0×10^{-12}	1.0×10^{-14}	[49]
807 (1080 K)	3.0×10^{-12}	3.0×10^{-13}	
1007 (1280 K)	8.0×10^{-11}	1.0×10^{-11}	
Temperature(°C)	Ni in Ni-50.2at%Ti	Ti in Ni-50.2at%Ti	References
400 (673 K)	2.52×10^{-16}	6.23×10^{-17}	[50]
650 (923 K)	5.73×10^{-13}	2.37×10^{-13}	
925 (1198 K)	The pore near the center of the Ti coated Ni wires is generated via the kirkendall effect, driven by Ni having a higher intrinsic diffusivity than Ti in the NiTi phase.		[51]

2.2 Electroless Ni-P coatings

The electroless Ni-P-based composite coatings can be prepared by electroless co-depositing Ni-P and enforcing particles from a Ni-P ion bath suspended with enforcing particles. Therefore, the electroless Ni-P plating reactions and process should be introduced.

2.2.1 Synthesis Mechanisms

Four reducing agents, sodium hypophosphite, sodium borohydride, dimethylamine borane (DMAB) and hydrazine are used as chemical reduction of nickel in the electroless nickel plating. The sodium hypophosphite ($NaH_2PO_2 \cdot H_2O$) is widely adopted in the electroless Ni-P (EN) plating solution in which $NiSO_4$ is used as Ni source. Several mechanisms were proposed to illustrate the reactions during the deposition process.

1) The first electroless nickel plating mechanism was proposed by Brenner and Riddell [52]. They considered that the actual nickel reductant is atomic hydrogen which is produced by the reaction of water with hypophosphite:

   $H_2PO_2^- + H_2O = H_2PO_3^{2-} + H^+ + 2H_{ads}$

   $Ni^{2+} + 2H_{ads} = Ni^0 + 2H^+$

   $H_{ads} + H_{ads} \rightarrow H_2$

   $H_2PO_2^- + H_{ads} \rightarrow H_2O + P + OH^-$

2) The hydride theory was first introduced by Hersch [53]. Hydride ions play a vital role in the nickel ion reducing action which is released by the reaction of hypophosphite with water according to the hydride mechanism:

   Acid: $H_2PO_2^- + H_2O = HPO_3^{2-} + 2H^+ + H^-$

   Alkaline: $H_2PO_2^{2-} + 2OH^- = HPO_3^{2-} + H_2O + H^-$

   $Ni^{2+} + 2H^- = Ni^0 + 2H \rightarrow Ni^0 + H_2$

   $H^+ + H^- \rightarrow H_2$

3) In the electrochemical mechanism [52], the electrons are produced by catalytic oxidation of the hypophosphite at the catalytic surface which in turn reduce nickel and hydrogen ions:

$$H_2PO_2^- + H_2O = H_2PO_3^- + 2H^+ + 2e^-$$

$$Ni^{2+} + 2e^- = Ni$$

$$2H^+ + 2e^- = H_2$$

$$H_2PO_2^- + 2H^+ + e^- = P + 2H_2O$$

2.2.2 Preparation Processes

To acquire a superior adhesion between a steel substrate and a coating, the substrate needs to be pre-treated. Metal substrates such as steel, aluminum or magnesium first need to be ground using grit abrasive papers and fine polished using diamond solutions. Following polishing, the substrates are degreased usually using acetone. Before the plating, the substrates must also be treated using alkaline cleaning and acid etch solutions. Alkaline cleaning is performed in a solution containing sodium hydroxide or sodium carbonate etc. The acid etch, on the other hand, is performed using H_2SO_4 or HCl solution [14]. The specific pre-treatment process depends on the substrate, different substrates may require different pre-treatment processes.

The chemical and physical properties of an electroless nickel coating are determined by its composition, which, in turn, is decided by the formulation and operating conditions of the plating bath. Typically, the composition of an electroless plating solution is a source of nickel ions, a reducing agent, suitable complexing agents, and stabilizers/inhibitors. The widely used nickel source is nickel sulfate. Other nickel salts, like nickel chloride and nickel acetate, are used for limited applications. Among different reducing agents, hypophosphite is preferred due to its low cost, easy process control, and super corrosion resistance of the deposit [12].

Organic acids or their salts are usually adopted as complexing agents. Complexing agents

have three principal functions in the electroless plating bath [12]. First, they prevent the pH of the solution from decreasing too fast. Second, they inhibit the precipitation of nickel salts. Third, they decrease the concentration of free nickel ions. In addition, stabilizers are used to inhibit the homogeneous reaction, which prevents the subsequent random decomposition of the entire plating bath.

During electroless nickel plating, the concentration of the main salt and reducing agent, bath temperature, and pH all affect the deposition process. The deposition rate and the amount of the reduced metal increase with the increase in concentration of the metal source or the reducing agent. However, there is an optimal concentration for each component. When the concentration of the main salt or reducing agent exceeds its optimal concentration, the stability of the bath decreases and even the bath decomposes. This, in turn, decreases the reduced Ni and slows down the deposition rate [12].

Bath temperature plays a key role in the deposition rate of an electroless bath. The solution is steady at the low temperatures while that leads to low deposition rates. On the other hand, very high temperatures can possibly make the bath excessively active, which increases the possibility of decomposition of the bath and finally decreases the deposition rate [54]. All practical Ni-P baths operate at temperatures of 60 °C and over. Nevertheless, when the temperature exceeds about 90 °C, the bath may decompose [55]. Figure 2-13 shows the effect of bath temperature on the plating rate of electroless nickel deposits [54].

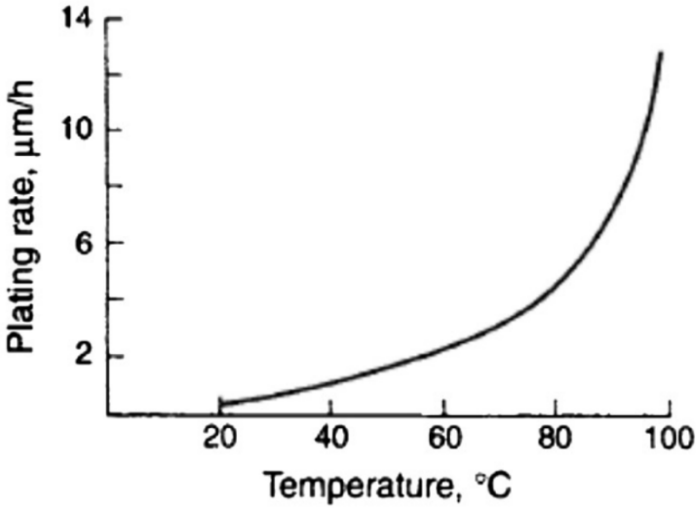

Figure 2-13 The effect of bath temperature on plating rate [54]

Operating pH value has significant influence on the phosphorus concentration in the deposit. Generally, higher pH values lead to lower phosphorus concentrations in the deposits, while lower pH values yield high phosphorus deposits. Molla et al. [56] reported that phosphorus concentration decreased as the pH values shifted from 3 to 7 and they also found that the deposition rate reached its maximum at pH value of 5. In addition, Chen et al. [57] observed that acidic baths lead to increased phosphorous content within the coatings. They also found that the deposits obtained from acidic baths developed internal tensile stresses, whereas deposits obtained from alkaline baths developed internal compressive stresses. Furthermore, coatings synthesized from acidic bath exhibit excellent adhesion to steel substrate, which is a reason why the acidic baths are widely adopted in industry. Figure 2-14 shows the effect of solution pH on plating rate [56] and Figure 2-15 shows the effect of solution pH on phosphorus content of the coating [56]

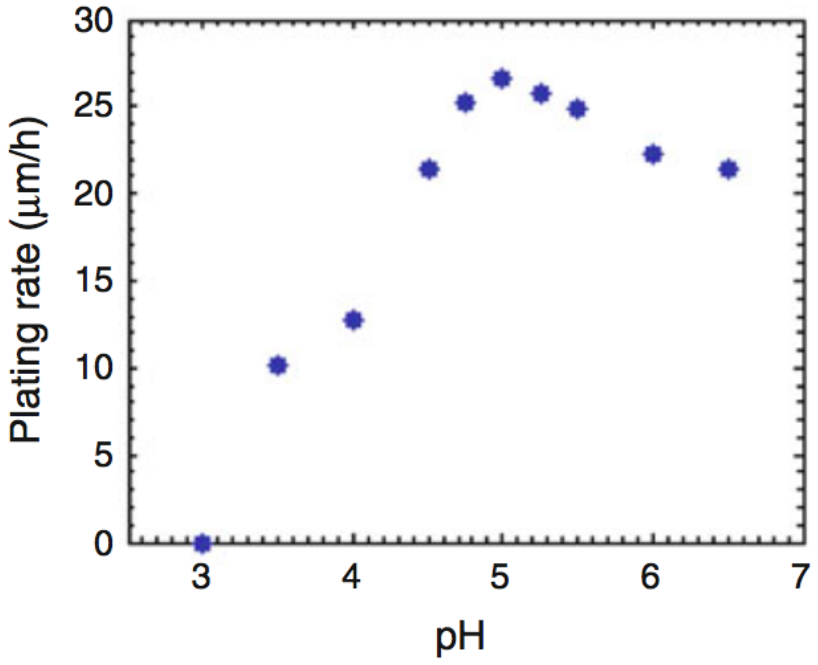

Figure 2-14 Effect of solution pH on deposition rate [56]

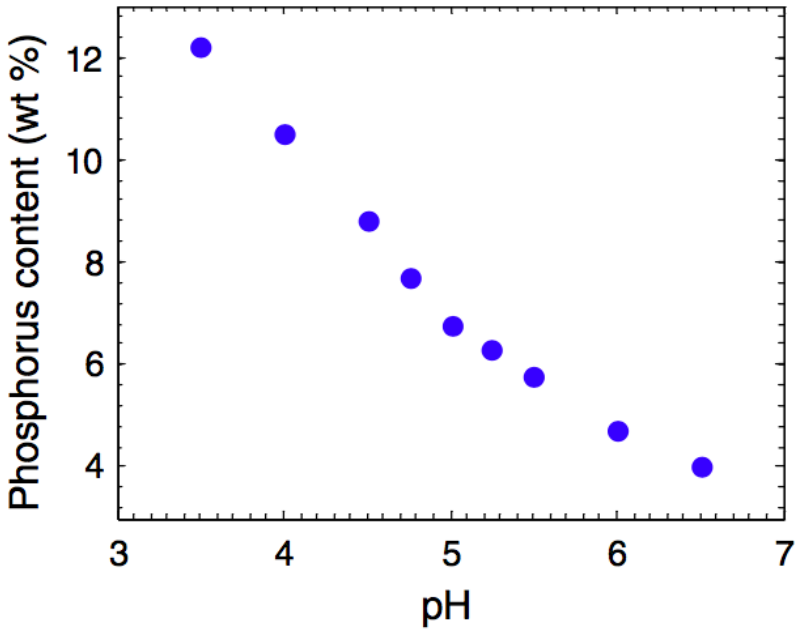

Figure 2-15 Effect of solution pH on phosphorus content of deposit [56]

2.2.3 Properties of Ni-P coatings

Electroless Ni-P coatings have low toughness and limited ductility, high hardness. The ductility of electroless nickel coatings depends on the composition. As-deposited Ni-P coatings with relatively high phosphorus content exhibit a ductility of 1-1.5% (as elongation) [54]. On the other hand, the ductility of the as-deposited Ni-P coatings with low phosphorus content is significantly decreased and even reduced to zero [54].

The micro-hardness of as-deposited Ni-P coatings is about 500 to 600 HV_{100} (HV_{100} is the Vickers Hardness at 100 g load) [58]. The micro-hardness of as-deposited Ni-P coating is dependent on its phosphorus content. Generally, the as-deposited Ni-P coating with low phosphorus content has high micro-hardness, while the coating with high phosphorus content exhibits low micro-hardness but high corrosion-resistance [58]. The hardness can be improved by heat treatment to as high as 1100 HV_{100}, nearly equal to most commercial hard chromium coatings [12]. However, high temperature heat treatment cannot be adopted because parts of the coatings may warp, or the strength of substrate may drop. In order to

mitigate the negative effect of high temperature annealing, longer annealing times and lower annealing temperatures are employed.

The Young's modulus of bulk Ni is approximately 205 GPa [59]. On the other hand, the reported Young's modulus of Ni-P coating falls within a wide range of 40 to 200 GPa [59-61]. The reason for this variation is that Young's modulus is very sensitive to deposition parameters and coating composition [59-61]. Luo et al. reported that the Young's modulus of Ni-P coating decreases from 200 GPa to 85 GPa as the plating temperature increases from 40 °C to 80 °C [59]. Coating composition, especially the phosphorus content also affects Young's modulus. It is found that the Young's modulus of Ni-P coating first increases with an increase in phosphorus content then decreases as the phosphorus content continues to increase, the highest Young's modulus value is achieved at the intermediate phosphorus content [12]. Karthikeyan et al. found that the Young's modulus of electroless Ni-P based composite coating increases as annealing temperature increases [61].

Wear is a damage to a solid surface due to relative motion between two or three contacting surfaces [58]. Generally, wear is a progressive process that causes the loss of material. Ni-P coatings have good wear resistance due to their relatively high hardness and lubricity. For example, Leon-Patino et al. [62] investigated the tribological behavior of as-deposited and annealed Ni-P coatings using reciprocating sliding tests and found that the annealed Ni-P coatings have higher wear resistance than as-deposited coatings, and the highest wear resistance is achieved on the coatings annealed at 400 °C. In addition, Hadipour et al. [63] designed a multilayer Ni-P coating with different P content in each layer and reported that the Ni-P multilayer coating with the phosphorus content sequence of Ni-low P/Ni-medium P/Ni-high P from the surface to the substrate showed much higher wear resistance than monolithic Ni-P coating.

Frictional properties of as-deposited Ni-P coatings are excellent and are similar to those of chromium coatings because the phosphorus content provides a natural lubricity, which can be very useful for applications such as plastic molding [64]. The coefficient of friction for electroless Ni-P versus steel is 0.12–0.13 for lubricated conditions and 0.43–0.44 for un-lubricated conditions [58]. The frictional properties of these coatings slightly vary with

phosphorus content and heat treatment [65].

Electroless Ni-P coatings have good corrosion resistance because of their amorphous nature and phosphorus content. The corrosion resistance of amorphous alloys is better than equivalent polycrystalline materials because amorphous alloys have no grain or phase boundaries [66]. Coating composition, heat treatment and coating porosity can affect the corrosion resistance of the electroless Ni-P coatings. In acidic environment, high phosphorus content (12%) coatings have high corrosion resistance while these coatings have poor corrosion resistance in hot sodium hydroxide [67]. During annealing of Ni-P, the formation of nickel phosphide precipitates consumes the phosphorus in the coatings, thus decreasing the corrosion resistance of the coatings [68]. It is well known that increasing the porosity reduces the corrosion resistance of the nickel phosphorus coatings since the pores are vulnerable sites for localized corrosion [69].

Erosion is a progressive wear process, gradually removes material due to mechanical interaction between the abrasive particles and the material's surface. For ductile materials, the material loss is normally a result of repeated deformation and cutting actions caused by solid particle impingement [70]. For brittle materials, the material loss is generally caused by cracking and fracture of the materials followed by removing fracture debris through impacts [70]. Figure 2-16 shows the relationship between impact angle and wear rate for ductile and brittle materials [71]. For ductile materials, the highest wear rate occurs at low impact angle, whereas the highest wear rate is reached at high impact angle for brittle materials.

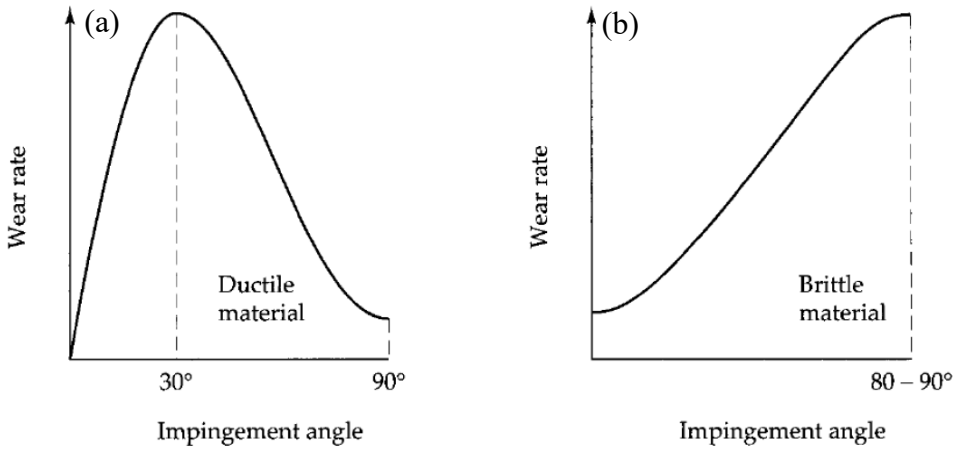

Figure 2-16 Relationship between impact angle and wear rate for (a) ductile and (b) brittle materials [71].

To the best of author's knowledge, the erosion behavior of electroless Ni-P coatings has not been comprehensively and systematically investigated. Wang et al. [14] found that the erosion resistance of electroless Ni-P coatings is inferior to that of the API X100 steel substrate because the Ni-P coatings is brittle. Jiang et al. [68] reported that the Ni-P coating heat treated at 500°C for 1 hour exhibited the best erosion resistance. Lin et al. [72] investigated the cavitation erosion behavior of electroless Ni-P and Ni-P-SiC coatings and found that the Ni-P-SiC coatings exhibited superior cavitation erosion resistance.

2.3 Electroless Ni-P Based Composite Coatings

2.3.1 Incorporation of Second Phase Particles

In order to improve the mechanical or electrochemical properties of electroless Ni-P coatings, Ni-P based composite coatings have been developed. Various reinforcements like metals, oxides, and other additions such as carbides, nitrides etc. have been reported to be added to the electroless nickel plating solution to form the Ni-P based composite coatings.

Incorporation of metal element into Ni-P matrix by adding metallic salt into electroless plating solution has been investigated recently. For example, Chen and Lin [73] studied the deposition and crystallization processes of Ni-Cu-P deposits and found that the concentration of copper salt ($CuSO_4$) in the electroless bath greatly influenced the Cu content in Ni-Cu-P deposit; the amorphous Ni-21.66Cu-11.60P deposit crystallized at annealing temperatures between 366.5 and 461.4 °C. Palaniappa et al. [16] also found that crystalline deposits were formed with the incorporation of tungsten and the phosphide precipitation was inhibited by the addition of tungsten during annealing.

On the other hand, the fabrication of Ni-P-Ti coatings from an electrodeposition solution

containing nickel and titanium salts has been reported with little success due to the high reactivity of the Ti ions which results in TiN and TiO_2 [74]. The preparation of Ni-P-Ti coatings by electroless plating has the same problem. However, to the best of the author's knowledge, the electroless co-deposition of Ni-P-Ti coatings from a Ni-ion bath and Ti suspension has not been reported. Hu et al. [75], however, reported Ni-Ti (particles)-Re (rare earth) was co-deposited on the surface of diamond particles using electroless plating by adding 2 ~ 3 μm Ti particles and trace rare earth salt to the electroless bath.

Several factors such as particle properties and plating parameters affect the incorporation of particles into the Ni-P matrix.

Particle size is important for preparing Ni-P composite coatings. Particles should be large enough to settle down along with the nickel and phosphorus elements during the electroless plating process, but not too large to significantly increase the surface roughness of the composite coatings [64]. The optimal particle size is dependent on the desired coating thickness. Balaraju suggested that the suitable particle size is in a range of 4-7 μm, whereas other researchers indicated smaller particle size (sub-micro) [64] . Besides particle size, particle shape also affects the deposition of the composite coatings. Low surface roughness can be achieved by incorporating small spherical particles, and high surface roughness is reported from incorporation of large, angular particles [64]. Balaraju et al. found that alumina particle size could affect the composition, microstructure and hardness of electroless Ni-P-Al_2O_3 composite coatings [76].

To prevent agglomeration of particles and keep the particles uniformly dispersing in the plating solution, appropriate agitation is necessary during the plating process. A low stirring speed results in a laminar flow that is unable to obtain uniform particle dispersion; on the other hand, a high stirring speed results in a purely turbulent flow that lowers the particle content within the coating due to inadequate time for the particles to settle down on the substrate surface [64]. Therefore, the optimal stirring speed is to create a flow that is between the laminar flow and turbulent flow.

Sample orientation in the electroless plating solution is also a critical factor since the particles are deposited within the Ni-P matrix by gravity. It is reported that the particle content within the composite coating is doubled by changing the sample orientation from vertical to horizontal [64].

Undeniably, particle concentration in the plating solution is the most critical factor that affects the final particle content within the composite coating. Generally, the particle content within the composite coating increases as the particle concentration in the plating solution rises. However, there is a saturation point or optimal concentration for the particles to maintain uniform dispersion in the plating solution [64]. When the particle concentration is higher than the point, agglomeration of the particles is expected to occur. Sadreddini and Afshar [77] found that the SiO_2 nanoparticle content in the Ni-P-SiO_2 composite coating increases as the particle concentration in the electroless plating solution rises to 12.5 g/L, while the particle content in the coating decreases when the particle concentration in the plating solution is higher than 12.5 g/L due to the agglomeration of the nanoparticles. They also reported that the particle concentration in the plating solution affects deposition rate, the highest deposition rate is achieved at the particle concentration of 12.5 g/L.

2.3.2 Effects of Additions on Coatings' Properties

The addition of a second phase into Ni-P matrix has been reported to improve the existing properties of electroless Ni-P coating. For example, in comparison to Ni-P coatings, Ni-Cu-P coatings have superior corrosion resistance in 20% NaCl solution and in 1.0 N HCl [78]. Sadreddini and Afshar [77] stated that the improved corrosion resistance should be ascribed to the lower porosity of Ni-P-SiO_2 than that of Ni-P coatings. On the other hand, Rabizadeh et al. [79] indicated that the Ni-P-SiO_2 possesses the superior corrosion resistance over the Ni-P coating because the SiO_2 nano-particles in the Ni-P coating reduce the effective metallic area that is available for corrosion. However, Si_3N_4 particle incorporation in Ni–P matrix indicated a marginal decrement in corrosion current density compared to the Ni–P coatings [80]. Araghi et al. [81] also found that although the Ni-P-B_4C composite coating exhibited good corrosion resistance in a polarization test in protecting the AZ91D magnesium alloy substrate, it was not superior to Ni-P coating.

The hardness and the wear resistance of deposits could be improved through adding tungsten to the binary Ni–P alloy, either in an amorphous or crystalline state, which is found by Tsai et al. [82] and Palaniappa et al. [16], respectively. The improved hardness and wear resistance of Ni-P-TiO_2 coatings over Ni-P coatings have also been reported [83, 84]. Compared to Ni-P coating, the wear resistance and hardness have been improved by incorporation of submicron Si_3N_4 particles in the deposit, and the maximum hardness and wear resistance were achieved on composite coatings heat-treated at 400℃ [85]. Similarly, Araghi et al. [81] reported that ternary Ni–P–B_4C composite coating showed a higher hardness and superior wear resistance compared to Ni-P coating. It is found that through both the incorporation of nano-SiC particles and the application of a post-heat treatment, the optimal cavitation erosion resistance is reached in distilled water and in a NaCl solution [72]. Vojtech [86] investigated the abrasion resistance of the different electroless Ni-P based composite coatings and found that the Ni-P-SiC exhibited the best abrasion resistance among Ni-P, Ni-P-Al_2O_3 and Ni-P-SiC coatings.

Erosion-corrosion resistance is critical for protective coatings applied on oil and gas pipelines. The material loss rate due to erosion-corrosion is much higher than that due to the individual erosion or corrosion. The material loss caused by erosion-corrosion includes pure erosion contribution, pure corrosion contribution, and the synergism contribution. Therefore, erosion-corrosion process is more complex than the pure erosion or pure corrosion. The synergism contribution consists of erosion enhanced corrosion and corrosion enhanced erosion. The erosion-corrosion resistance of Ni-P or Ni-P based composite coatings has been of considerable interest over the last two decades. For example, Ni-P-B_4C composite exhibits superior erosion-corrosion resistance in acidic chloride solutions at a normal abrasive impact compared to Ni-P coating [87]. Calderon et al. [88] investigated the erosion-corrosion resistance of Ni-P-SiC composite coatings and suggested that grain refining and microstructure changes caused by SiC particles contributed to the improved erosion-corrosion resistance. More recently, Tamilarasan et al. [3] studied the influence of reduced graphene oxide (rGO) on the erosion-corrosion behavior of Ni-P-rGO coatings and found that incorporation of rGO particles significantly improve the erosion-corrosion resistance and the best result is obtained at a concentration of 50 mg/L of rGO in the plating solution.

Among all aforementioned studies, the effects of second phase additions on hardness, corrosion and wear resistance have been studied. However, the effects of NiTi addition on the mechanical (especially toughness), erosion, corrosion, and erosion-corrosion behavior of Ni-P-Ti and Ni-P-NiTi composite coatings have not been comprehensively and systematically investigated.

2.4 Cracking and Toughening Mechanisms

2.4.1 Crack Types

Five major cracks may be observed on the surface of brittle materials subjected to indentation contact, which are shown in Figure 2-17 [89]. First, cone cracks, typically generate by elastic loading of spherical or flat-punch indenters, which spread away from the surface at a certain angle to the load axis. Second, in elastic-plastic contacts, radical cracks may be generated parallel to the load axis. Third, median cracks are generated beneath the plastic deformation zone and propagate parallel to the axis of loading. Fourth, half-penny crack results from the joining of radial cracks beneath the surface [89]. Fifth, lateral crack is formed beneath the deformation zone and propagates parallel to the surface.

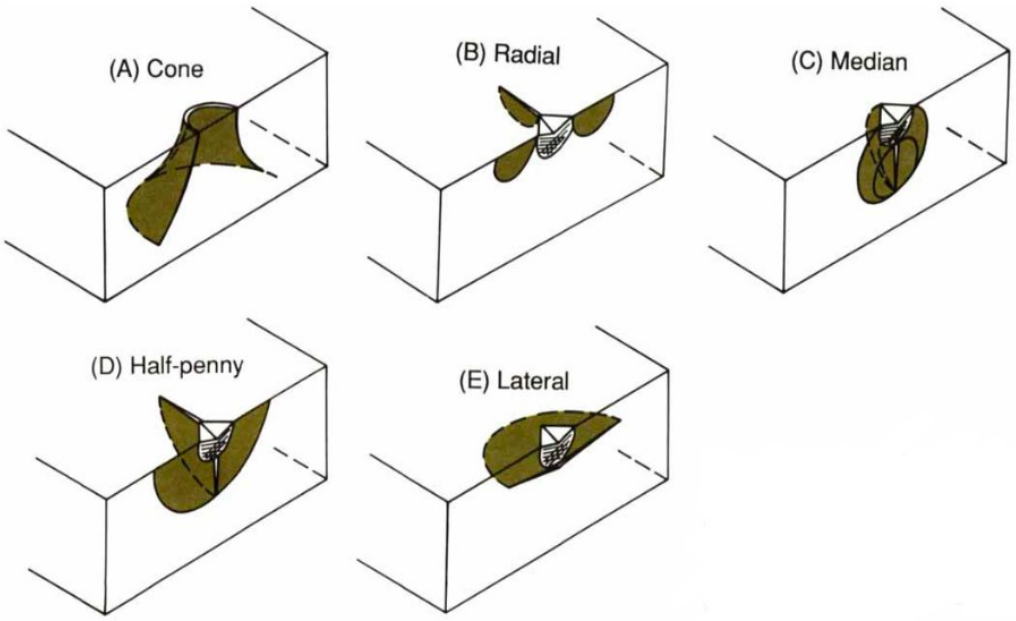

Figure 2-17 Five major crack types [89]

2.4.2 Hertzian Contact

Hertzian contacts are encountered in numerous practical applications, such as, in bearings, gears, etc. Hertzian contact tests using a spherical indenter penetrating into a material have been employed in materials testing. In order to assess bulk material or coating ability to support a static load and even shed light on material behavior under a dynamic load (i.e., wear), Hertzian indentation tests have also been adopted to study cracking and fracture of brittle materials. Consider two elastic bodies in contact, Hertz assumed that the surfaces are non-conforming, frictionless, and strains are elastic [90]. Figure 2-18 shows the Hertzian indentation process [91].

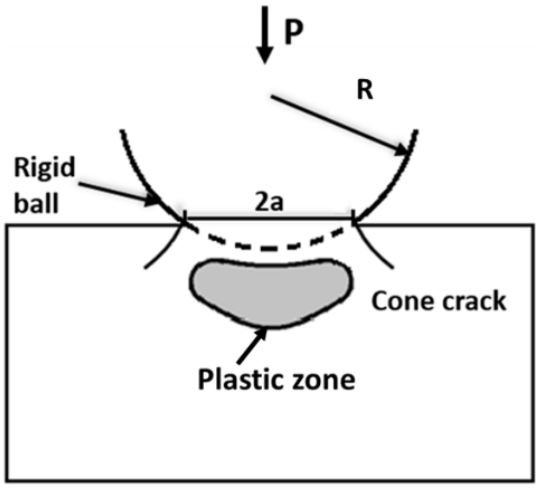

Figure 2-18 Hertzian indentation process on brittle material [91]

The analysis of the Hertzian stress distribution plays a pivotal role in predicting and investigating cracking types and damage modes. Although Hertzian contact is developed for elastic contact, it is often used as an approximation to predict material's behavior under elastic-plastic contact. Hertzian indentation analysis is often employed to evaluate damage modes during the contact process on brittle materials. The initiating position and driving

stresses of cracks can be predicted and identified using Hertzian stress distribution analysis [92]. The propagation angle of cone cracks can also be determined using Hertzian stress distribution analysis [93]. Generally, the initiation of cracks is related to the principal stresses. The schematic diagrams of principal stress trajectories and contours are shown in Figure 2-19. The diameter of contact area is marked as a-a. Ring cracks are associated with the maximum tensile stress σ_1 initiating at the surface around the contact edge (Figures 2-19 (a) and (b)), Ring cracks then advance along σ_3 trajectory resulting in a cone shape crack (Figures 2-19 (c) and (d)) [94]. The formation of the radial cracks is attributed to the maximum tensile hoop stress σ_2 under elastic-plastic contact (Figures 2-19 (a) and (e)) [94]. The delamination of brittle materials or coatings (lateral cracks) is ascribed to the maximum shear stress τ_{13}, which is below the contact surface (Figure 2-19 (f)) [95].

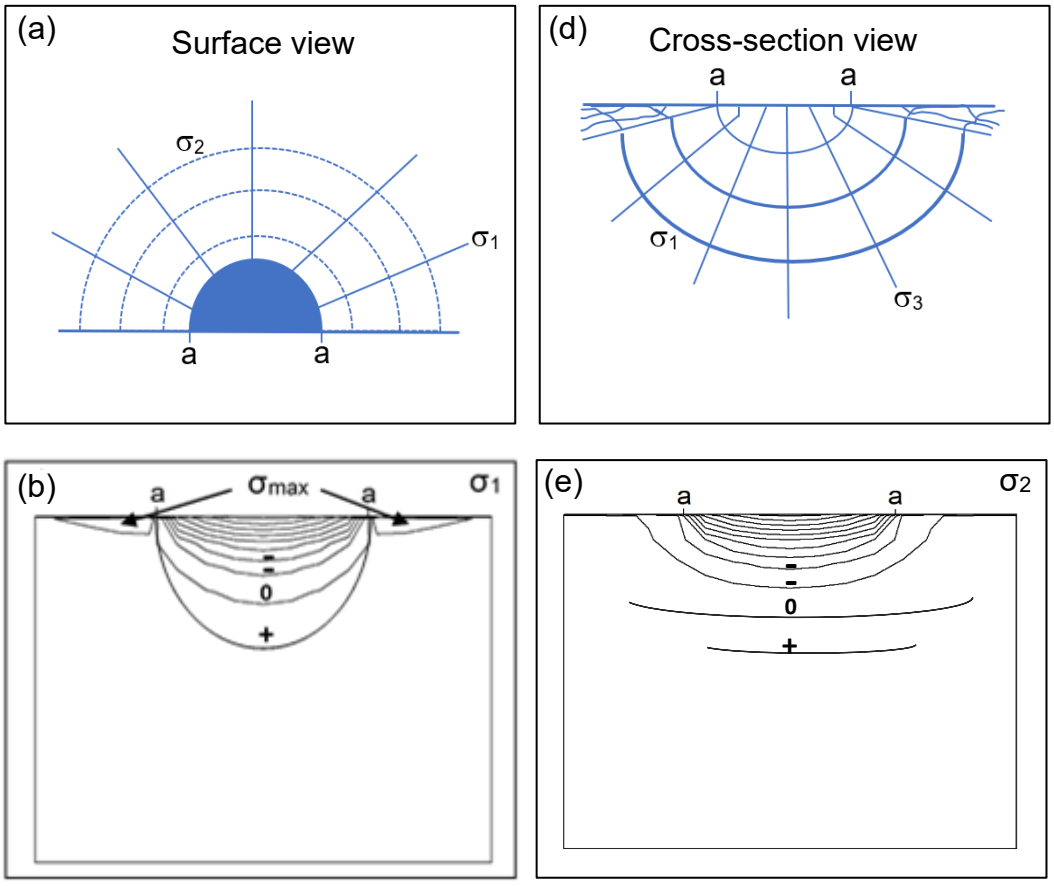

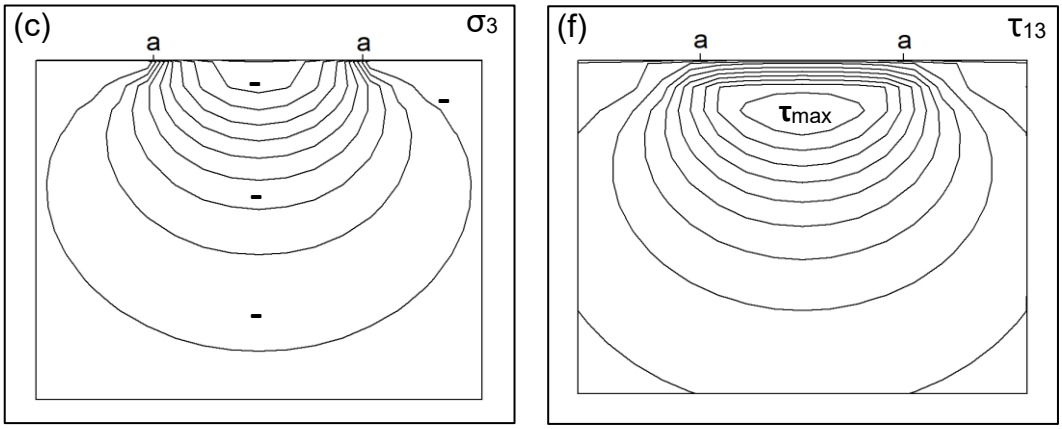

Figure 2-19 Schematic diagrams of principal stress trajectories and contours: (a) surface view and (c) cross-section view of principal stress trajectories; (b)(d)(e)(f) principal stress contours

2.4.3 Toughening Mechanisms

The toughness of brittle materials can be improved by the addition of ductile particles. The interactions between cracks and ductile particles can prevent the initiation and propagation of cracks, which improve the toughness of brittle materials. Different toughening mechanisms include crack bridging, crack deflection, micro-cracking, and transformation toughening.

The schematic diagram of crack bridging process is shown in Figure 2-20 [96]. When a crack propagates through ductile particles, the stress field at the crack tip could be relieved through the plastic deformation of the ductile particle, which results in blunting of the crack tip in the ductile particle (Figure 2-20 (a)). The crack wake is bridged by a particle when the crack tip passes through the particle (Figure 2-20 (b)). Due to the severe plastic deformation of the ductile particles, the ductile particles are either pulled out from the matrix (Figure 2-20 (c)) or pulled in tension to failure (Figure 2-20 (d)), depending on the adhesive strength between the ductile particles and brittle matrix. Crack bridging consumes the driven energy for crack propagation, which results in improved toughness.

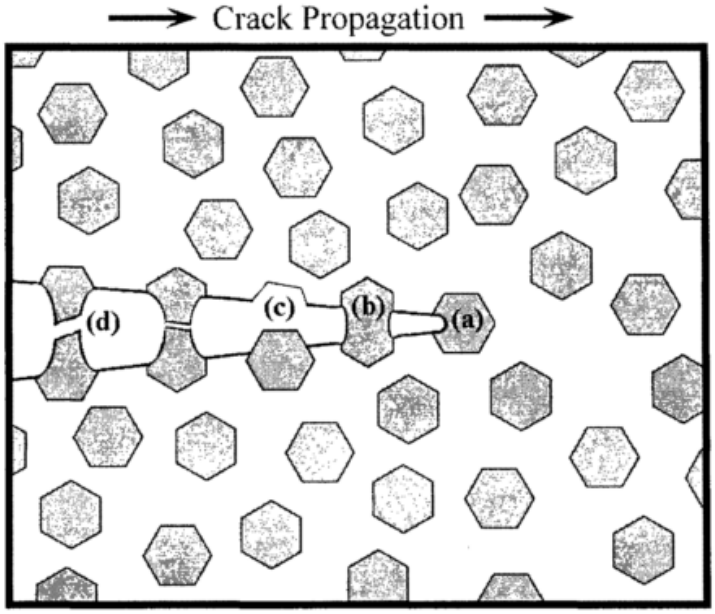

Figure 2-20 Schematic diagram of crack bridging, (a) crack tip blunting (b) particle bridging the crack wake (c) particle debonding (d) particle plastically deforming to failure [96].

Crack deflection induced by ductile particles plays an important role in improving toughness of brittle materials. Crack deflection could reduce the driving energy for crack propagation by deviation of the crack path. The reduction in crack driving energy could considerably increase the toughness and decrease the growth rates of the cracks [97]. The schematic diagram of crack deflection is shown in Figure 2-21 [98]. Crack deflection can occur in two different manners. One is crack deflection without contact between the ductile particle and the crack, the other is crack deflection with contact between the ductile particle and the crack. For the first case, the crack tip approaches a particle. The stress field at the crack tip causes the elastic deformation of the particle. The elastic deformation absorbs the driving energy of the crack and deflects away the crack tip (Figure 2-21 (a)). For the second case, a crack propagates around the ductile particle and results in plastic deformation of the particle (Figure 2-21 (b)). However, the driving force of the crack is not high enough to cause the debonding or failure of the particles. The interaction between the crack and the particle changes the path of the crack propagation. The change in crack path could lower the driving force for crack propagation, thus improves the toughness.

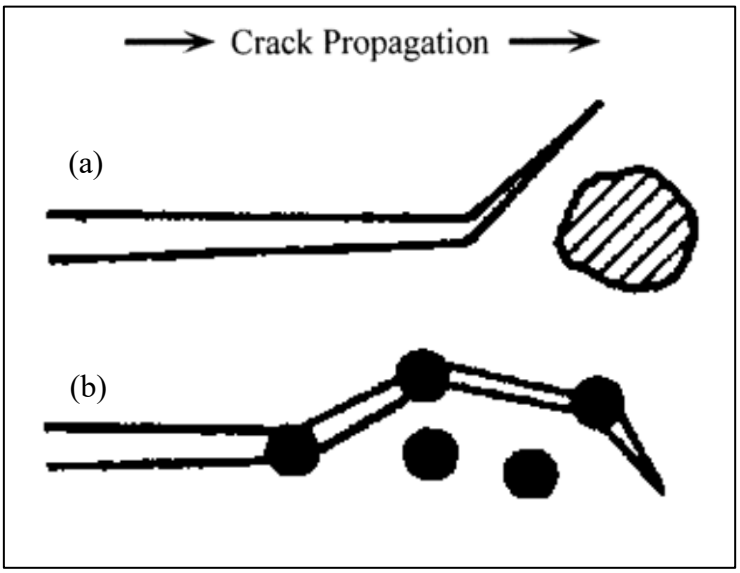

Figure 2-21 Schematic diagram of crack deflection, (a) crack deflection without contact between ductile particle and crack, (b) crack deflection with contact between ductile particles and crack [98]

Microcracking is another important toughening mechanism in improvement of brittle materials' toughness. Stress-induced microcracking is an irreversible process that results in crack driving energy dissipation and contributes to an increase in toughness [96]. A large crack branches into many microcracks, which consumes the driving energy for crack propagation, thus improves toughness. Microcracking is induced due to the presence of second phase ductile particles since the mechanical properties of the ductile particles are different from those of the brittle matrix [96]. The formation of microcracks close to a large crack reduces the stress field at the large crack tip. The schematic diagram of microcracking toughening is shown in Figure 2-22 [96]. Due to the interaction between the stress field at the crack tip and the ductile particles, a zone of microcracking is formed at the crack tip (Figure 2-22 (a)). In the crack wake, a region of residual microcracks is also observed (Figure 2-22 (b)). Besides the mechanical properties of the particles and matrix, the extent of microcracking is also dependent on the grain size of the matrix and the particle size of the ductile particles. Microcracking has been proved to be an effective mechanism to increase the toughness of brittle materials [4, 96].

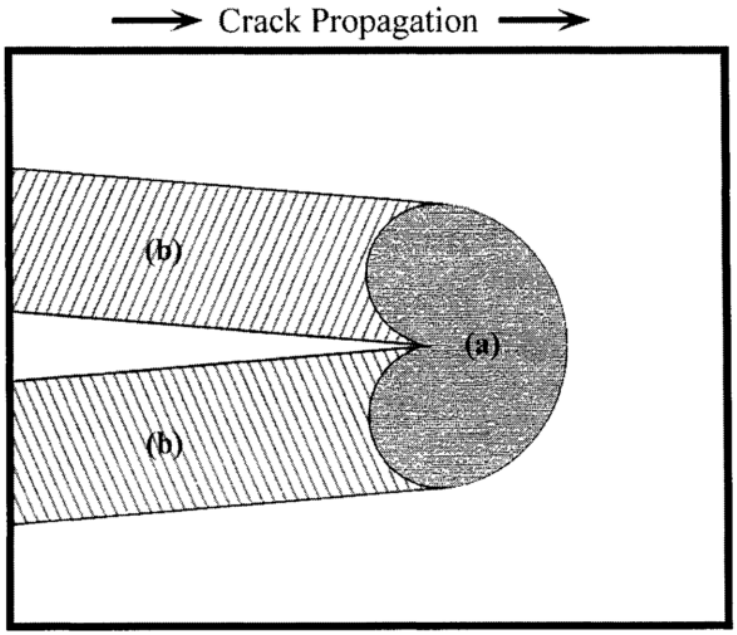

Figure 2-22 Schematic diagram of microcracking toughening, region (a) process zone around the crack tip where microcracking occurs and region (b) the microcracked zone left in the crack wake [96].

Transformation toughening was first observed in ceramics containing zirconia as a second phase particle. Under applied stress, zirconia transforms from a tetragonal to a monoclinic phase accompanied by energy absorption and volume increase. This phenomenal is called "stress-induced phase transformation". The energy absorption consumes the driving energy for crack propagation and the volume increase results in a compressive stress field around the particle. The compressive stress field further reduces the driving force and shields or blunts the crack tip. Figure 2-23 shows a schematic diagram of transformation toughening [96]. The stress field at the crack tip induces the phase transformation in the region around the crack tip, which locally relieves the stress field and absorbs fracture energy (Figure 2-23 (a)). The resultant region of transformed particles left in the crack wake is observed in Figure 2-23 (b). Due to energy absorption and volume increase during the phase transformation process, transformation toughening is an effective manner to significantly

improve the toughness of brittle materials. NiTi alloy is also known for its stress-induced phase transformation (superplastic effect). Under applied stress, NiTi alloy also undergoes phase transformation, austenite phase transforms to a detwinned martensite phase with an absorption of strain energy and an increase in volume. Therefore, superelastic NiTi is expected to improve the toughness of brittle materials or coatings.

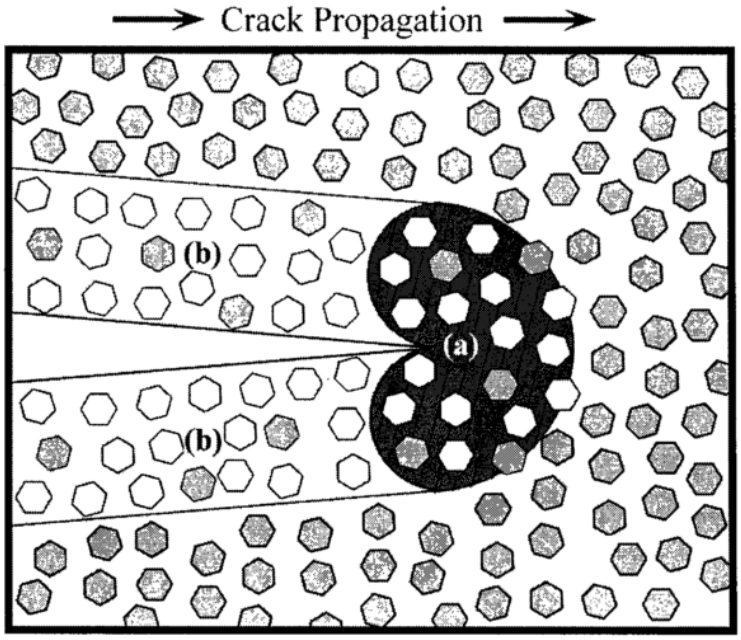

Figure 2-23 Schematic diagram of transformation toughening, (a) process zone around the crack tip where particles undergo phase transformation and (b) the resultant zone of transformed particles left in the crack wake [96].

2.5 Sliding Wear Behavior

Sliding wear is a relative motion between two moving bodies in contact under load. The most basic mechanisms of sliding wear include abrasion, adhesion, and delamination. More details on these mechanisms are discussed as below.

2.5.1 Abrasive Wear

Abrasion can be described as damage to a surface by a hard material, which is the most common mechanism [99]. Depending on the degree of severity, sometimes, abrasion is also referred to as scratching, scoring, and gouging. There are two forms of abrasion [99]. The first one is known as "two-body-abrasion", which is a harder material sliding against a softer one. In the second case, loose hard particles sliding between rubbing surfaces cause the abrasion. In both situations, wear occurs through removing the material from the softer surface by a harder surface or particle.

Micro-ploughing, micro-cutting and micro-cracking are combined effects in the abrasive wear. In an ideal case, micro-ploughing doesn't result in any detachment of material from a surface being worn due to a single pass of one hard asperity [99]. In the micro-ploughing, the material is usually displaced sideways forming a ridge near to the groove. Micro-cutting and micro-ploughing are commonly observed in ductile materials. By cutting of a material ahead of the asperities, pure micro-cutting occurs, which results in a formation of a chip equal in volume to the wear groove produced. The proportion of micro-cutting to micro-ploughing is determined by the hardness and the attack angle of the asperity [99]. When the attack angle is high and the hardness of the harder material is much higher than the soft material, micro-cutting will dominate resulting in higher wear rates than micro-ploughing. On the other hand, for low impact angle, micro-ploughing is more dominant compared to micro-cutting.

For ductile materials, micro-cracking of ridges as a result of repeated passing of the slider on the same wear track can cause material loss. For brittle materials, fracture and delamination occur when microcracks above or below connect to each other. Fracture and delamination of brittle materials result in high material loss rate.

2.5.2 Adhesive Wear

Adhesive wear originates from adhesion between two surfaces that are placed in contact. When two surfaces are brought into contact, asperities of the two surfaces make physical contact. When the asperities come into contact, they strongly adhere to each other and form asperity junctions [99]. Continued sliding causes the junctions to be sheared and finally separated from the surfaces. This process leads to fragments of the softer material adhering

to the harder one.

2.5.3 Delamination

When two sliding surfaces come into contact, delamination may occur, normal and tangential loads are transmitted via the contact regions. Subsequently, with repeated sliding, plastic shear deformation accumulates below the surface due to surface traction exerted by the harder asperities on the softer surface. As the cyclic loading continues, crack initiation and propagation occur parallel to the surface and finally extending to the surface and forming thin sheet-like wear debris. Delamination can also transpire on brittle materials. Cracks initiate under the surface by shear stress at a certain depth, then propagate along a direction parallel to the surface, which often extends to the surface and cause delamination.

Chapter 3 Methodology

3.1 Substrate and Ti Powder Characterization

3.1.1 Low Carbon Steel Substrate

Two kinds of low carbon steels (API X100 and AISI 1018) were utilized as substrates. Cylindrical API X100 steel discs (8 mm in radius, 6 mm in thickness) were employed as substrates for scratch, Hertzian indentation, nanoindentation, and single particle erosion tests. Cylindrical AISI 1018 steel discs (8 mm in radius, 6 mm in thickness) were used as substrates for corrosion and scratch-corrosion tests. AISI 1018 Steel coupons (18 mm × 10 mm × 6 mm) were utilized as substrates for corrosion, erosion, and erosion-corrosion tests in a slurry pot erosion-corrosion tester. The elemental compositions of API X100 and AISI 1018 steel substrates are given in Table 3-1. The API X100 and AISI 1018 steel substrates both consist of α-ferrite and bainite in their microstructure [100]. The properties of API X100 and AISI 1018 steels are given in Table 3-2 [5].

Table 3-1 Composition of API X100 and AISI 1018 steel substrates [101]

Wt (%)	API X100	AISI 1018
C	0.103	0.182
Mn	1.221	0.754
Cu	0.009	0.186
Cr	0.070	0.181
Ti	0.018	0.008
Si	0.121	0.095
V	0.036	0.001
P	0.010	0.040
S	0.001	0.021
Fe	Balance	Balance

Table 3-2 Properties of API X100 and AISI 1018 steel substrates [5]

Properties	API X100	AISI 1018
Density (g/cm^3)	7.87	7.87
Average grain size (μm)	5±2	7±3
Young's modulus (GPa)	210	205
Vickers hardness (GPa)	2.50	1.7
Yield strength (MPa)	690	370
Tensile strength (MPa)	820	440

3.1.2 Ti Nanoparticles

Commercial Ti particles with a nominal mean size of 70 nm purchased from US Research Nanomaterials Inc. were employed as a second phase addition. Hitachi S-4700 Scanning Electron Microscope was used to observe the as-received Ti powder. The size distribution of as-received Ti powder was measured using laser diffraction particle size analyzers (Malvern 3000). SEM micrograph of as-received Ti powder is shown in Figure 3-1 (a). It is seen that the Ti particles are spherical, and the particle size is in a range of 40-400 nm (Figure 3-1 (a)). Figure 3-1 (b) shows the particle size distribution of Ti powder. A bimodal particle size distribution is observed. One major particle size is approximately 40 nm, while the other is approximately 4 μm. The values of D_{10}, D_{50}, and D_{90} were found to be 0.019 μm, 0.064 μm, and 5.010 μm, respectively.

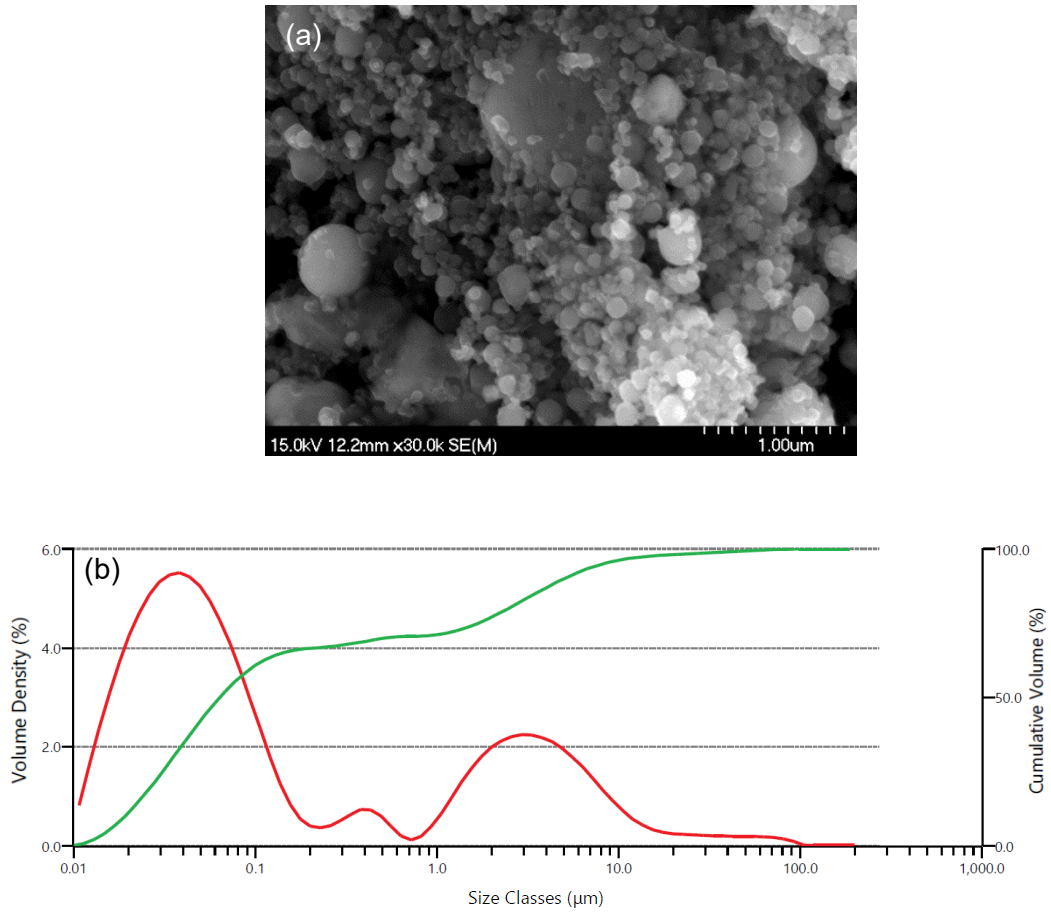

Figure 3-1 (a) SEM micrograph and (b) particle size distribution of Ti powder

3.2 Coating Preparation

3.2.1 Electroless Ni-P-Ti Coating

Before electroless plating, the API X100 and AISI 1018 steel substrates were pretreated. The pretreatment steps of the substrates included grinding, polishing, alkali clean, and acid clean in sequence, which are summarized in Table 3-3. Between each step, the substrates were thoroughly rinsed using distilled water.

Table 3-3 Pretreatment steps of steel substrates

Pretreatment steps	Conditions
1. Grinding	Using 240, 320, 400 and 600 SiC papers
2. Polishing	Using 9 μm, 3 μm, and 1 μm diamond solutions
3. Alkali clean	submerged in heated alkali solution (85°C) for 5 mins Composition of alkali solution: 30 g/L Na_3PO4, 50 g/L Na_2CO_3 and 30 g/L NaOH.
4. Acid clean	Immersed in 20 vol% H_2SO_4 solution for 15 seconds.

Industrial solutions containing $NaPO_2H_2$ as reductant and $NiSO_4$ as nickel source were utilized as electroless Ni-P and Ni-P-Ti plating solutions. Different amount of spherical Ti particles were separately added into the electroless plating solutions (1 liter). To prevent the oxidation of Ti particles, weighing and handling of Ti powder were completed in a glovebox filled up with argon gas (purity: 99.999%). The oxygen concentration in the glovebox was maintained at 0.1%. In order to enhance the adhesive strength of Ni-P-Ti coatings, before electroless Ni-P-Ti plating, a thin layer of Ni-P (approximately 8 μm in thickness) was deposited. Table 3-4 shows the electroless Ni-P-Ti plating parameters. Ni-P coatings were also prepared under the same parameters for comparison. During plating, 25 vol% NaOH solution was periodically dripped into the plating solution to adjust the pH. A pH meter and a thermometer were utilized to monitor the pH and temperature during plating, respectively. The thickness of coatings is approximately 50 μm.

Table 3-4 Electroless Ni-P-Ti plating parameters

Parameters	Values
Temperature	88 ± 2 °C
pH	4.7 ± 0.1
Magnetic stirring speed	300 rpm
Plating time	4 hours

3.2.2 Annealing of Ni-P-Ti Coatings

In order to determine the annealing conditions for Ni-P-Ti coating to form the NiTi phase, the annealing time was estimated under different annealing temperatures using Fick's second law [102]:

$$\frac{\partial C}{\partial t} = D\frac{\partial^2 C}{\partial x^2} \quad 3.1$$

Where, C is the concentration; t is the time; x is the diffusion distance; D is the diffusion coefficient. To solve the equation, some assumptions were made as follows [102]:

1. Prior to diffusion, the diffusion solute atoms are homogeneously dispersed with concentration of C_0.
2. The x value is zero at the surface and increases as the distance increases into the solid.
3. Just before the diffusion process begins, the time is assumed to be zero.

The boundary conditions are assumed as:

For $t = 0$, $C = C_0$ at $0 \leq x \leq \infty$

For $t > 0$, $C=C_s$ (the constant surface concentration) at $x = 0$; $C=C_0$ at $x = \infty$

After applying the boundary conditions to equation 3.1, the solution is as following [102]:

$$\frac{C_X - C_0}{C_S - C_0} = 1 - erf\left(\frac{x}{2\sqrt{Dt}}\right) \quad 3.2$$

Here, C_x is the concentration at depth x after diffusion time t. The expression $erf(x/2\sqrt{Dt})$ is the Gaussian error function, which is defined by [102]:

$$erf(z) = \frac{2}{\sqrt{\pi}}\int_0^z e^{-y^2}dy \quad 3.3$$

Partial Gaussian error function values are given in Table 3-5 [102].

Table 3-5 Partial Gaussian error function values [102]

z	erf(z)	z	erf(z)
0	0	0.55	0.5633
0.025	0.0282	0.60	0.6039
0.05	0.0564	0.65	0.6420
0.10	0.1125	0.70	0.6778
0.15	0.1680	0.75	0.7112
0.20	0.2227	0.80	0.7421
0.25	0.2763	0.85	0.7707
0.30	0.3286	0.90	0.7970
0.35	0.3794	0.95	0.8209
0.40	0.4284	1.0	0.8427
0.45	0.4755	1.1	0.8802
0.50	0.5205	1.2	0.9103

The diffusion coefficient in equation 3.2 can be expressed as [102]:

$$D = D_0 \ exp(-\frac{Q_d}{RT}) \tag{3.4}$$

Where, D_0 is a temperature-independent preexponential (m^2/s); Q_d is the activation energy for diffusion (J/mol); R is the gas constant (8.31J/mol*K); T is the absolute temperature (K).

When taking natural logarithms on both sides of equation 3.4, it yields the following equation: [102]

$$lnD = lnD_0 \ -\frac{Q_d}{R}(\frac{1}{T}) \tag{3.5}$$

Maaza [103] determined the diffusion coefficient (D) of Ni into Ti at different temperatures using grazing-angle neutron reflectometry:

$$lnD = 8.172 - 1740(\frac{1}{T}) \quad 3.6$$

Assuming the final concentration of Ni in NiTi alloy is 50% and the diffusion starts with pure Ni and Ti. Therefore, C_x = 50%, C_0 = 0%, C_s = 100%, substituting these values into equation 3.2, and referring to Table 3-5, the relationship between D and t becomes:

$$t = \frac{x^2}{0.88\,D} \quad 3.7$$

The mean particle size (D_{50}) of spherical Ti nanoparticles determined from particle size distribution is 0.064 μm. Assuming x is equal to the mean radius of Ti particles (0.032 μm), Then combining equations 3.6 and 3.7, the relationship between t and T can be expressed as follows:

$$t = 1.16 \times 10^{-15} exp(1740(\frac{1}{T}) - 8.172) \quad 3.8$$

The diffusion time at different annealing temperatures calculated by equation 3.8 is given in Table 3-6. It is found that the annealing time decreases as the annealing temperature increases. At low temperature (500-600 °C), the annealing time is too long. However, at high temperature (900-1000 °C), the microstructure and properties of steel substrate can be affected. Therefore, medium annealing temperatures (700 and 800°C for 5 hours) were chosen as annealing conditions for annealing the Ni-P-Ti coatings.

Table 3-6 Relationship between annealing time and annealing temperature for Ni diffusion into Ti

Annealing temperature (°C)	Annealing temperature (K)	t (h)
500	773	8.64
550	823	7.53
600	873	6.67
650	923	5.99
700	973	5.44
750	1023	4.98
800	1073	4.60
850	1123	4.28
900	1173	4.01
1000	1273	3.57
1100	1373	3.23
1150	1423	3.09

After analyzing the coatings annealed at 700 and 800 °C for 5 hours, it was found that the annealing temperature was too high and annealing time was too long for annealing Ni-P-Ti coatings due to the formation of high amount of Ni_3Ti phase since the aforementioned calculation did not consider the diffusion of Ti into Ni and the size effect of Ti nanoparticles (nanoparticles have high surface energy). The relationship between diffusion coefficient (D) of Ti into Ni at different temperatures was determined by Sohrabi [104]:

$$lnD = 7.440 - 1241(\frac{1}{T}) \tag{3.9}$$

Considering the interdiffusion of Ni into Ti and Ti into Ni, the relationship between t (annealing time) and T (annealing temperature) can be expressed as follows:

$$t = 1.16 \times 10^{-15} \frac{exp(2981(\frac{1}{T}) - 15.612)}{exp(1740(\frac{1}{T}) - 8.172) + exp(1241(\frac{1}{T}) - 7.440)} \tag{3.10}$$

The diffusion time at different annealing temperatures calculated by the equation 3.10 is given in Table 3-7. It was found that the annealing time decreased when considering the interdiffusion between Ni and Ti compared to only considering diffusion of Ni into Ti.

Table 3-7 Relationship between annealing time and annealing temperature for interdiffusion between Ni and Ti

Annealing temperature (°C)	Temperature (K)	t(h)
500	773	4.50
550	823	4.00
600	873	3.60
650	923	3.28
700	973	3.01
750	1023	2.79
800	1073	2.61
850	1123	2.45
900	1173	2.31
1000	1273	2.08
1100	1373	1.91
1150	1423	1.83

From Table 3-7, 2 hours annealing at 650 °C is also a suitable and reasonable time. Further, annealing at 650 °C does not change the mechanical properties of low carbon steel substrates based on Fe-C phase diagram [1]. In addition, Hu et al. [31] found that the superelastic NiTi phase was formed between $NiTi_2$ and Ni_3Ti phases at the Ni-Ti interface annealed at 650°C for 2 hours, which is similar to our calculations. Therefore, based on the results in Table 3-7 and reported literature [31], 650 °C for 2 hours was chosen as the annealing condition for the following study. Therefore, three annealing profiles (700°C for 5 hours, 800°C for 5 hours, 650°C for 2 hours) were performed on Ni-P-Ti coatings in a vacuum furnace under a pressure of 1×10^{-5} Torr. The heating and cooling rates were both set to 20 °C/min. Ni-P coatings were also annealed under the same three annealing conditions for comparison.

3.3 Coating Characterization

Surface topography and surface roughness were evaluated using 3D optical profilometer. The coated samples were cross sectioned using Buehler isomet 1000 saw with cubic boron nitride (CBN) blade at 100 rpm and a load of 200 g. Surfaces and cross-sections of coatings were examined using scanning electron microscope (SEM), energy dispersive spectroscopy (EDS), and optical microscope (OM). The operating voltage and current for SEM and EDS were 15 kV and 15 μA, respectively. All the SEM images were acquired using secondary electron mode. Different phases within the coatings were identified using a Bruker D8 Advance X-ray diffractometer (XRD). In order to ensure that all the peaks are included, the coatings were scanned from 20° to 120° (2 theta). Vickers hardness was measured on the cross-sections of coatings using a micro-indentation hardness tester. A diamond pyramid indenter was employed under a load of 100 g for 10 s. Hardness tests were performed on three samples and in three separate locations for each sample. The test results were averaged, and the standard deviations were used as error bars in the plotted figures. The Vickers hardness can be derived from the following equation [105]:

$$HV = \frac{1.8554P}{d^2} \quad 3.11$$

Where, P (kgf) is the applied load and d is the diagonal length of the indent on the cross-section of the coating (mm).

3.4 Scratch Test

Scratch tests were conducted on steel substrates, as-deposited and annealed Ni-P and Ni-P-Ti coatings (thickness: approximately 50 μm) using a Universal Micro-Tribometer according to ASTM standard (C1624–05) [106]. To avoid the effect surface roughness on scratch test, the coatings surfaces were polished using abrasive paper and diamond solutions (3 μm and 1 μm). A conical diamond indenter (radius: 200 μm) coupled with acoustic emission (AE) sensor was employed. An increasing load (0 N- 44.1 N) scratch test was conducted with a sliding distance of 10 mm. The acoustic emission (AE) sensor is capable of detecting acoustic signals (due to cracking) during scratch. The scratch tracks under increasing load were examined using laser confocal optical microscope (OM) to determine the location of the initial cracks and the load required to initiate cracks (initial or first crack load). Based on AE signals and OM observations, the initial crack load can

be determined confidently. Initial or first crack load (L_{C1}) can be determined using the below equation [106]:

$$L_{C1} = \frac{S}{L} \times P_{max} \quad 3.12$$

Where, S is the distance from starting point to initial crack location (μm); L is the total scratch length (10,000 μm) and P_{max} is the maximum load (44.1N).

Scratch resistance can be determined using multiple passes scratch tests under a constant load. Multiple passes (5, 10, 20 and 40 passes) scratch tests were performed under a constant load of 9.8 N for a length of 5 mm (one pass). Confocal optical microscope was employed to measure the width of scratch tracks (tested under constant load) for subsequent calculation of wear volume loss and wear rates. The volume loss after the multiple passes scratch tests can be calculated using the following equation [107]:

$$Volume\ loss = \frac{D^2 t}{8}\left[2sin^{-1}\frac{b}{D} - sin\left(2sin^{-1}\frac{b}{D}\right)\right] \quad 3.13$$

Here, D is the diameter of scratch indenter tip (0.4 mm); t is the scratch length (5 mm) and b is the width of scratch scar measured by optical microscope. The wear rate is the slope of the curve of volume loss against number of passes (or scratch distance) [108].

Fracture toughness can also be measured by scratch tests. When the applied load is higher than the first crack load, cracking and fracture transpire. Akono and Ulm [109] correlated cracking and fracture during scratch to fracture toughness using dimensional analysis and the energetic contour-independent J-integral for a conical scratch indenter. Figure 3-2 shows a schematic diagram of a conical indenter used for scratch tests. The relationship between fracture toughness and scratch testing parameters are as follows [109]:

$$K_C = \frac{F_{eq}}{\sqrt{2pA}} \quad 3.14$$

$$F_{eq} = \begin{cases} \sqrt{F_T^2 + \frac{3}{5}F_V^2} & if\ \theta > 0 \\ F_T & if\ \theta = 0 \end{cases} \quad 3.15$$

$$2pA = 4(tan\emptyset/cos\emptyset)d^3 \quad 3.16$$

Where, K_c is the fracture toughness; F_{eq} is the equivalent force; F_T is the horizontal force and F_v is the vertical force; $2pA$ is the scratch indenter shape function; θ is the inclined angle of the indenter; Φ is half-apex angle of the indenter; d is the scratch depth under constant load.

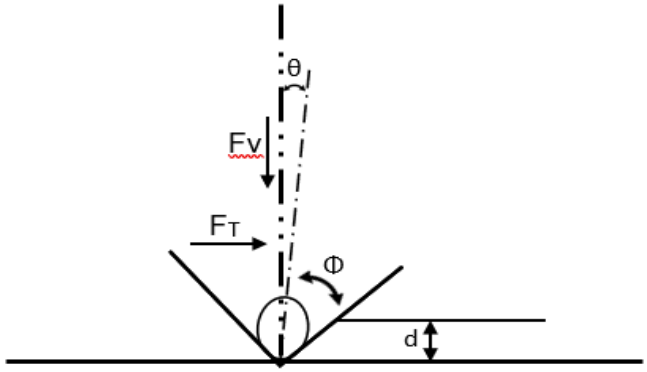

Figure 3-2 Schematic diagram of a conical indenter used for scratch tests.

Each scratch test was conducted on three samples and on three different locations for each sample to confirm repeatability and reproducibility. The test results were averaged, and the standard deviations were used as error bars in plotted graphs.

3.5 Nanoindentation Test

Nanoindentation tests were performed on annealed Ti particles in the annealed Ni-P-Ti coatings to confirm the superelastic effect. A three-cycle test with applied load of 5 mN, 10 mN, and 15 mN was adopted. During the test, a 5 mN load was applied and maintained for 10 seconds, followed by unloading to 3 mN, and then a higher load was applied, the

next cycle began until the load reached the maximum load (15 mN). The loading and unloading rates are both 0.83 mNs^{-1}. The nanoindentation tests were conducted on 3 to 5 particles at different locations to confirm repeatability and reproducibility. The test results were averaged, and the standard deviations were utilized as error bars.

A typical nanoindentation load-depth curve is shown in Figure 3-3. The hardness (H) and Young's modulus (E) can be determined from the load-depth curve by utilizing Oliver and Pharr method [110]. In Figure 3-3, F_t is the maximum load applied on sample; h_t is the total depth; *dF/dh* is the slope of the unloading curve at maximum load.

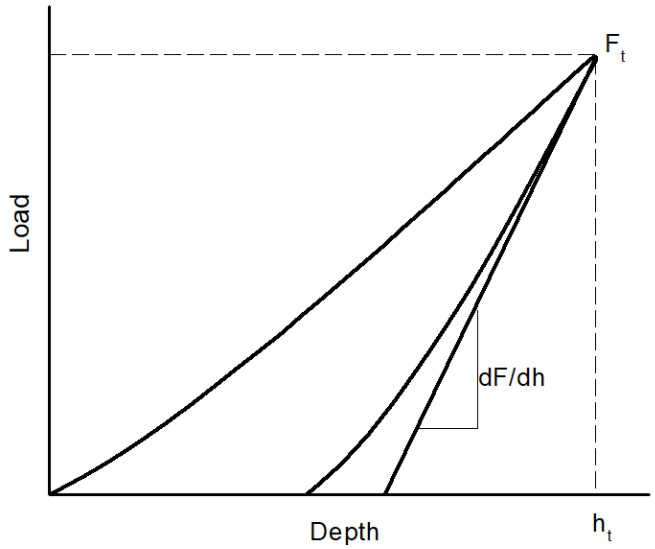

Figure 3-3 Typical nanoindentation load-depth curve

The hardness (*H*) can be calculated using the following equations [110]:

$$H = \frac{F_t}{A} \tag{3.17}$$

$$A = kh_c^2 \tag{3.18}$$

$$h_c = h_t - [\frac{2(\pi - 2)}{\pi}][\frac{F_t}{dF/dh}] \tag{3.19}$$

Here, A is the contact area; k is a constant, which is equal to 24.5 for an ideal geometry Berkovich indenter; h_c is the nanoindentation contact depth.

Young's modulus can be determined by the following equations [110]:

$$\frac{1}{E^*} = \frac{1-v^2}{E} + \frac{1-v_i^2}{E_i} \tag{3.20}$$

$$E^* = \frac{dF}{dh}\frac{1}{2}\frac{\sqrt{\pi}}{\sqrt{A}} \tag{3.21}$$

Where, E^* is the effective modulus; E and E_i are the Young's moduli of tested material and indenter, respectively; v and v_i are the Poisson's ratios of tested material and indenter, respectively. The Poisson's ratio for the tested material has been assumed as 0.3.

3.6 Bend Test

A PASCO ME-8237 bend testing device was employed to perform three-point bend tests on the bilayer specimens. The loading rate was approximately 1 N/s. A schematic of the three-point bend test is shown in Figure 3-4. It is shown that the applied load (P) is the force loaded on the sample at the center directly contacting the sample and l is the length between the two bottom supports. The dimensions of the coated sample are also shown in Figure 3-4 using w as the width of the sample, t as the thickness of the composite coating, and T as the thickness of the substrate. During bend tests, the force and associated displacement were recorded automatically via the PASCO software. An acoustic emission sensor (1283 USB AE Mode) was employed to detect the released fracture energy caused by cracking and record the acoustic emission waves during the formation of cracks. The sensor has the capacity to collect amplitude, counts and energy of cracking, which was attached to the surface of the specimen. Figure 3-5 shows the setup of bend testing. For each Ti content, three specimens were tested. The test results were averaged, and the standard deviations were used as error bars in plotted graphs.

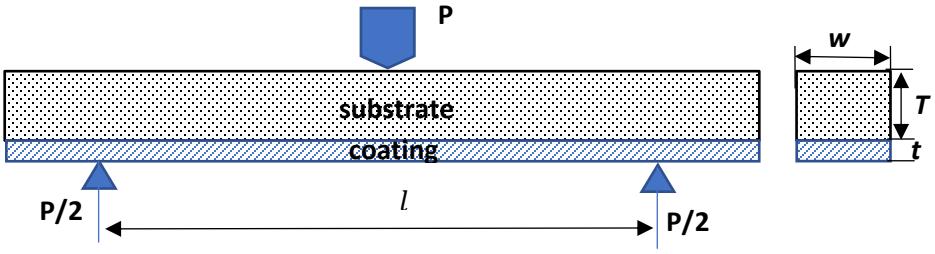

Figure 3-4 Schematic of three-point bend test

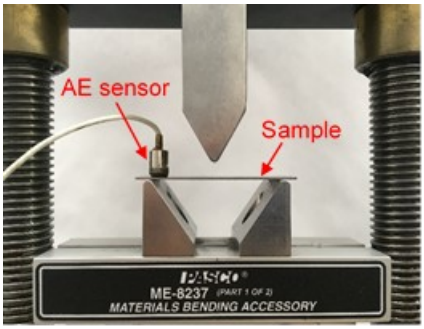

Figure 3-5 Setup of bend testing

Using the parameters defined in Figure 3-4, the elastic moduli of the API X100 steel substrate (E_s) as well as the coating-substrate bilayer (E_b) can be obtained using equations 3.22 [111] and 3.23 [112] respectively as follows:

$$E_s = \frac{al^3}{4wT^3} \tag{3.22}$$

$$E_b = \frac{al^3}{4w(t+T)^3} \tag{3.23}$$

where a is the slope of the initial linear part of the load-displacement curve. As the property of interest solely lies in the coating, a method introduced by Rouzaud [111] to determine the coating's elastic modulus (E_c) using equation 3.24 is as follows:

$$\frac{E_c}{E_s} = \frac{T}{3t}\frac{P_2 - P_1}{P_1} \tag{3.24}$$

where P_2 is the load needed to initiate the first crack in the coating and P_1 is the load acting on the substrate for the same displacement as on the coating-substrate bilayer.

Furthermore, the fracture strength (σ_c) of the composite coatings can be acquired by following equations:

$$I = \frac{w(T+t)^3}{12} \tag{3.25}$$

$$\sigma_c = \frac{E_c}{E_s}\frac{Plt}{8I} \tag{3.26}$$

where, I is the moment of inertia of the coating-substrate bilayer; and P is the force required to initiate the first crack in the composite coating.

3.7 Tensile Test

Standalone Ni-P-Ti composite coatings were prepared for tensile test using AISI 1018 steel bow-tie tensile coupons as the substrates. The dimensions of the steel tensile coupons are shown in Figure 3-6. In order to facilitate preparing standalone coatings, the substrates (without pretreatment) were directly immersed in the Ni-P-Ti plating solution for 12 hours using the plating parameters given in Table 3-4. After removing from the plating solution, the specimens were air dried, then the composite coatings were manually and carefully peeled off from the steel coupon substrates. The surface roughness and the oxide layer on the surface of the steel coupons have resulted in a weak bond between the coupon and the coating which allowed for the easy removal of the standalone coating. The thickness of the standalone coatings is approximately 100 μm. The quality of as-deposited Ni-P and Ni-P-Ti standalone coatings were examined using optical microscope under 1000 times magnification. The coatings without cracks were then annealed at 650°C for 2 hours.

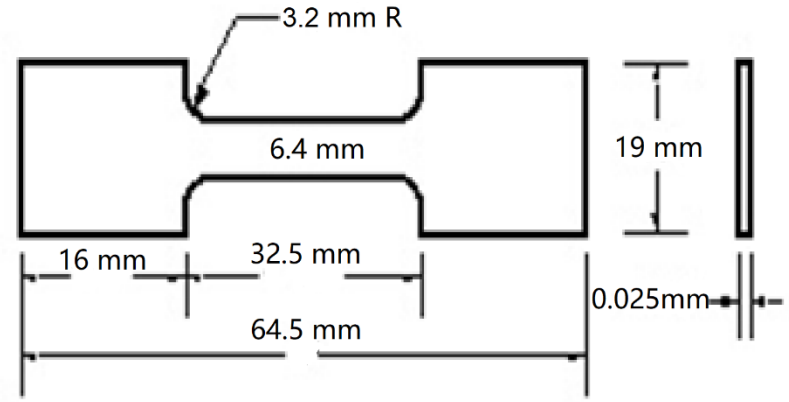

Figure 3- 6 Dimensions of AISI 1080 steel coupon substrate.

Before tensile tests, all the coatings were examined using optical microscope under 1000 times magnification. The coatings without cracks were utilized for tensile test. Tensile testing was conducted on as-deposited and annealed standalone coatings. A PASCO ME-8238 device equipped with a 7100 N load cell (precision: 0.1 N) was employed for tensile tests. The tests were carried out at a strain rate of 1×10^{-5} s^{-1}. The load-displacement data was automatically recorded by the software (PASCO Capstone) during the tensile testing process. Samples were tested until fracture. The Young's modulus and toughness are calculated directly from the resultant stress-strain curve. The experimental set-up for a tensile test conducted on a standalone composite coating is shown in Figure 3-7. For each Ti content, three samples were tested to confirm the repeatability. The results were averaged, and the standard deviations were used as error bars in plotted graphs.

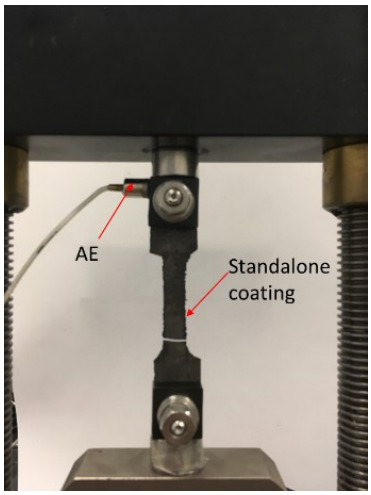

Figure 3-7 Tensile testing on a standalone coating

3.8 Hertzian Indentation Test

A PASCO ME-8236 testing device was employed to perform the indentation testing on the specimens. A WC-6Co spherical indenter having a radius of 0.795 mm was used to conduct indentation tests on the coatings. The thickness and surface roughness of coatings are approximately 50 μm and 2 μm, respectively. The indentation rate was 0.1 mm/min and the maximum load was set to 2000 N. The indentation rate was so low that the applied load could be considered as quasi-static. The load-displacement data were automatically recorded by the software (PASCO Capstone) during the indentation testing process. In order to collect crack acoustic signals and determine the first crack load, an acoustic emission (AE) sensor was attached to the specimens. After the indentation tests, the specimens were examined under optical microscopy. The stress distribution was also calculated using the following equations [113]:

$\frac{\sigma_r}{\sigma_0}=-\frac{L^3R^2Z}{(L^4+Z^2)(1+L^2)^2}-(1-2\nu)[\frac{Z}{L(1+L^2)}-\frac{1}{3R^2}(1-\frac{Z^3}{L^3})]+\frac{Z}{L}[L(1+\nu)arctan(\frac{1}{L})-(1-\nu)\frac{L^2}{1+L^2}-2\nu]$	3.27
$\frac{\sigma_\theta}{\sigma_0}=-\frac{1-2\nu}{3R^2}(1-\frac{Z^3}{L^3})+\frac{Z}{L}[L(1+\nu)\arctan(\frac{1}{L})-(1-\nu)\frac{L^2}{1+L^2}-2\nu]$	3.28

$\frac{\sigma_z}{\sigma_0} = -\frac{Z^3}{L(L^4+Z^2)}$	3.29
$\frac{\tau_{zr}}{\sigma_0} = -\frac{LRZ^2}{(1+L^2)(L^4+Z^2)}$	3.30
$\sigma_1 = \frac{1}{2}(\sigma_r+\sigma_z) + \sqrt{[\frac{1}{2}(\sigma_r - \sigma_z)]^2 + \tau_{zr}^2}$	3.31
$\sigma_2 = \sigma_\theta$	3.32
$\sigma_3 = \frac{1}{2}(\sigma_r+\sigma_z) - \sqrt{[\frac{1}{2}(\sigma_r - \sigma_z)]^2 + \tau_{zr}^2}$	3.33
$\tau_{13} = \frac{1}{2}(\sigma_1 - \sigma_3)$	3.34
$R^2 = (1+L^2)(1-\frac{Z^2}{L^2})$ $R = r/a$ $Z = z/a$	3.35
$L = [\frac{1}{2}(R^2+Z^2-1+\sqrt{(R^2+Z^2-1)^2+4Z^2}]^{\frac{1}{2}}$	3.36

Where, the *r* and z are cylindrical coordinates and R and Z are the reduced coordinates; L is a quantity defined by relationship in the equation 3.36; σ_r, σ_θ, σ_z and τ_{zr} (shear stress) are the general stresses in cylindrical coordinates (r, θ, z); σ_0 is the maximum contact pressure; σ_1, σ_2, σ_3 and τ_{13} (shear stress) are the principal stresses; ν is the Poisson's ratio of the tested material; a is the contact radius and can be calculated by the following equation [90]:

$$a = (\frac{3}{4}\frac{PD}{E^*})^{1/3} \quad 3.37$$

Where, P is the applied load; D is the radius of the indenter; and E^* is the effective modulus given by [114]:

$$E^* = (\frac{1-\nu_1^2}{E_1} + \frac{1-\nu_2^2}{E_2})^{-1} \quad 3.38$$

Where, ν_1 and E_1 are the Poisson's ratio and Young's modulus of the indenter, respectively; ν_2 and E_2 are the Poisson's ratio and Young's modulus of the tested material, respectively.

The mean contact pressure (p_0) can be derived by [114]:

$$p_0 = \frac{P}{\pi a^2} \quad 3.39$$

The maximum contact pressure can be denoted as σ_0, and given by the following equation [114]:

$$\sigma_0 = \frac{3}{2}p_0 \quad 3.40$$

More details regarding the calculation of Hertzian stress distribution can be found in Appendix A.

3.9 Single Particle Erosion (SPE) Test

For single particle erosion tests, WC-Co spherical particles (radius: 500 μm) were employed as an erodent. The hardness of the WC-Co particles is approximately 75 HRC. The Poisson's ratio and elastic modulus of WC-Co particles are approximately 0.26 and 650 GPa, respectively [115]. SEM micrograph of WC-Co erodent particle is shown in Figure 3-8. In order to study the effect of impact angle on erosion mechanisms, samples were tested at four different angles of 30°, 45°, 60° and 90°. A schematic of the single particle erosion tester is shown in Figure 3-9. The tester consists of a compressed air supply and regulator, a solenoid valve, a polycarbonate barrel, and an adjustable sample holder vice. The pressure can be adjusted to change the velocity of the particle. The solenoid valve allows compressed air to flow through the system and drives the particle to pass through

the polycarbonate barrel, which finally impacts the sample. The adjustable sample holder vice is capable of varying the impact angle. The testing pressure used in this study is 60 psi, which corresponds to average particle velocity of 52 ± 4 m/s [100]. For each Ti concentration (1 g/L, 2 g/L, 3 g/L), single particle erosion tests were conducted on three samples to ensure repeatability.

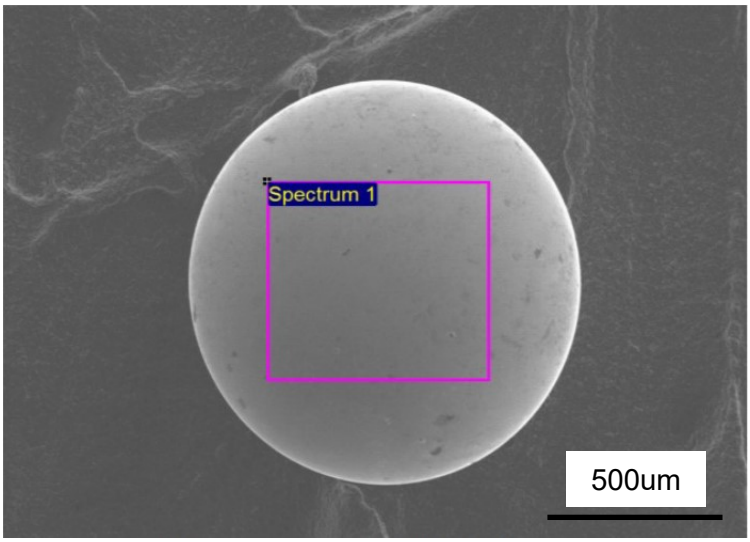

Figure 3-8 SEM micrograph of WC-Co erodent particle

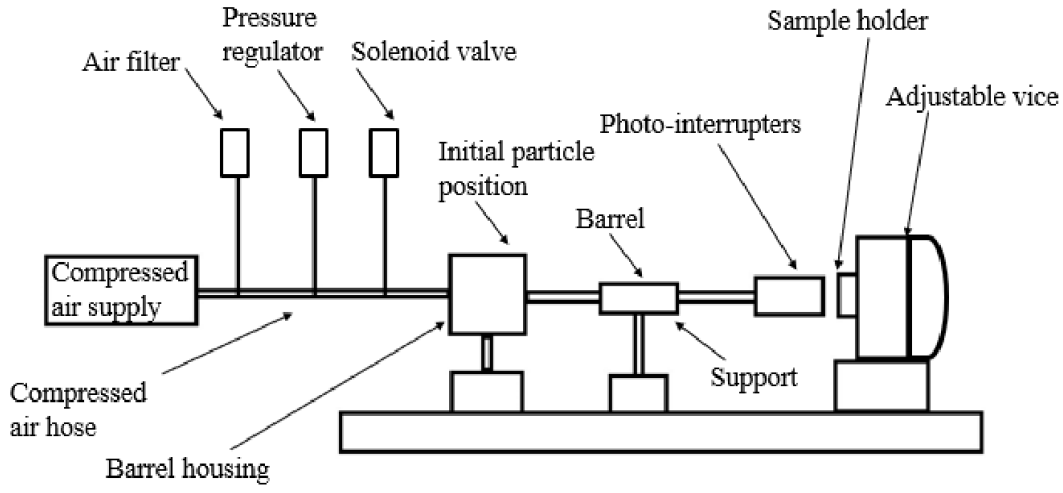

Figure 3-9 Schematic of apparatus utilized for single particle erosion testing.

3.10 Static Corrosion Test

Potentiodynamic polarization (PP) and electrochemical impedance spectroscopy (EIS) tests were performed to evaluate the corrosion resistance of different coatings in a 3.5 wt% sodium chloride solution at room temperature. The tests were conducted using a PAR 273A potentiostat controlled by a Scribner software, CorrWare. A three-electrode cell was utilized consisting of a coated sample as a working electrode, a saturated calomel electrode (SCE) as a reference electrode, and platinum as a counter electrode. 1 cm^2 of the coated surface was exposed to the electrolyte. Prior to each PP test and EIS test, the samples were maintained in an open circuit state for 2 hours to obtain a steady state. In the case of PP tests, a potential range from -0.25 V to + 0.25 V vs. the open circuit potential was employed with a scan rate of 0.167 mV/s. In a typical EIS test, an AC amplitude of 10 mV was applied to each sample over a range of frequencies from 1 mHz to 1 kHz. During the testing process, the cell was placed in a faraday cage to shield external electrical noise. For each Ti concentration (1 g/L, 2 g/L, 3 g/L), PP and EIS tests were performed on three samples to confirm the repeatability and reproducibility of the testing results. The testing results were averaged.

3.11 Slurry Pot Erosion-Corrosion (SPEC) Test

Pure corrosion, pure erosion and erosion-corrosion tests were conducted on AISI 1018 steel, Ni-P and Ni-P-Ti coatings in a slurry pot erosion-corrosion (SPEC) tester. The schematic of the SPEC tester is shown in Figure 3-10. The slurry was held in a glass container (4 L). An impeller driven by a motor was employed to impel the slurry. Before the SPEC test, the specimen is cathodically protected during the test to provide material loss caused by pure erosion. Then except for the testing surface, other faces of the specimen were covered with epoxy. A test area of 1.8 cm^2 was exposed to the abrasive slurry. The abrasive slurry is composed of 35 wt% AFS 50-70 silica sand and 3.5 wt % sodium chloride solution. The SEM micrograph of AFS 50-70 angular silica sand particles is shown in Figure 3-11. The average size of the abrasive particles ranges 200-300 μm. The impact velocity at an

impeller speed of 900 rpm during erosion-corrosion testing process is measured to be in a range of 0.26 – 2.21 m/s [116]. The slurry temperature is approximately 45 °C and the testing time is 6 hours. Pure erosion tests were conducted on samples without corrosion via cathodic protection. Pure corrosion tests (in the absence of abrasive particles) and erosion enhanced corrosion tests (in the presence of abrasive particles) under flowing conditions (900 rpm) were conducted in a 3.5 wt% NaCl solution using the polarization resistance technique [117]. A three-electrode cell and a Gamry potentiostat were utilized for electrochemical tests and cathodic protection [116]. A sample, a saturated calomel electrode (SCE), and platinum electrode were used as a working electrode, a reference electrode, and a counter electrode in the three-electrode cell, respectively. A potential range from -0.25 V to + 0.25 V vs. the open circuit potential was employed with a scan rate of 0.167 mV/s. Each test was repeated twice to confirm the repeatability and the test results were averaged; the standard deviations were used as error bars.

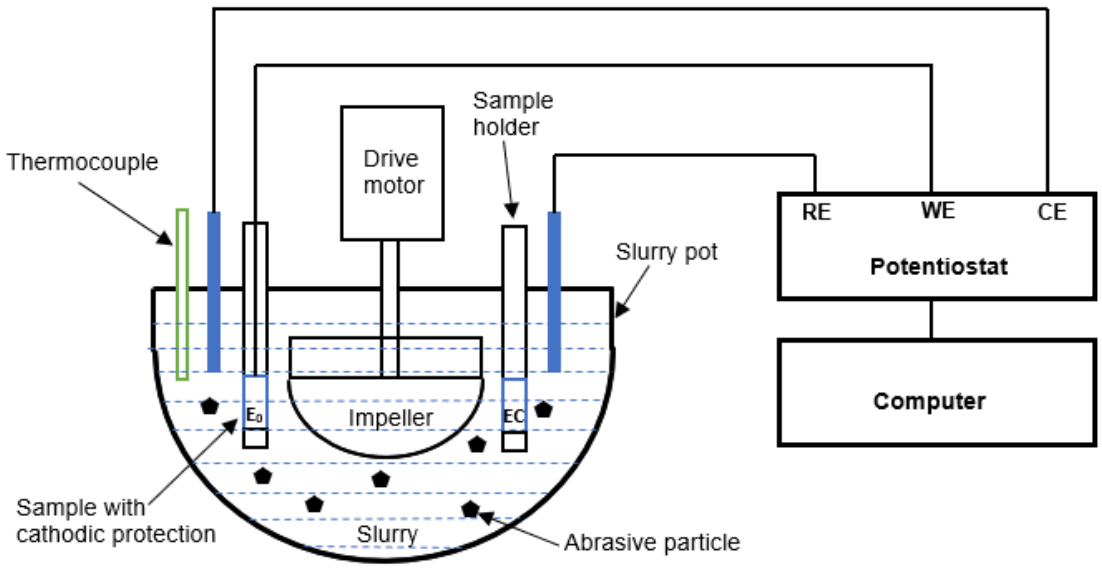

Figure 3-10 Schematic of slurry pot erosion-corrosion tester

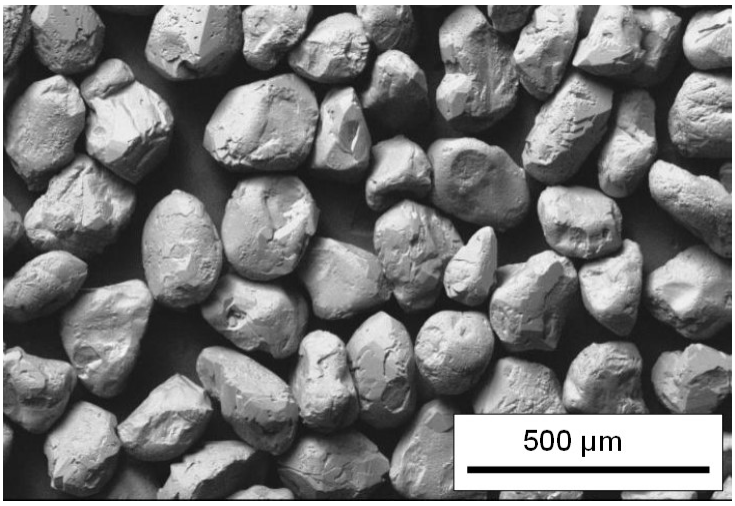

Figure 3-11 SEM micrograph of AFS 50-70 abrasive sand particles

A micro-balance having a reading accuracy of 0.01 mg was utilized to measure the mass loss after SPEC test. Material loss rate is reported as $cm^3 \cdot h^{-1} \cdot cm^{-2}$. According to the ASTM G119-09, the total erosion-corrosion material loss rate (K_{ec}) can be expressed as follows [118]:

$$K_{ec} = K_{eo} + K_{co} + K_S \quad 3.41$$

Where, K_{eo} is the material loss rate caused by pure erosion; K_{co} is the material loss rate caused by pure corrosion and K_s is the material loss rate caused by synergy between erosion and corrosion. The total material loss rate, according to the ASTM G119-09, can also be expressed by the following relationship [118]:

$$K_{ec} = K_e + K_c = K_{eo} + K_{co} + \Delta K_e + \Delta K_c \quad 3.42$$

Where, K_e is the total erosion rate; K_c is the total corrosion rate; ΔK_e is the corrosion-enhanced erosion rate and ΔK_c is the erosion-enhanced corrosion rate. Combining equations 3.41 and 3.42, the synergy material loss rate (K_s) and its components can be expressed as follows [118]:

$$K_s = \Delta K_e + \Delta K_c = K_{ec} - (K_{eo} + K_{co}) \quad 3.43$$

$$\Delta K_c = K_c - K_{co} \quad 3.44$$

$$\Delta K_e = K_s - \Delta K_c \quad 3.45$$

Chapter 4 Results and Discussion

4.1 Coating Characterization

4.1.1 As-deposited Coatings

The average deposition rate was calculated by dividing the coating thickness over the deposition time. Deposition rates at various Ti content in the plating bath can be seen in Figure 4-1. It can be observed that the deposition rates decreased with the increase of Ti content. Similar decreasing trend was also observed by other researchers via adding other types of particles into Ni-P plating solutions [119-121]. It is known that at the beginning of electroless plating, for steel substrate, nickel atoms will be displaced from the bath by iron, then the displaced nickel deposits act as a catalyst to accelerate the plating process [12]. However, increasing Ti content in the bath resulted in an increase in the number of Ti particles that are deposited onto the substrate surface by gravity. This led to a decrease in available active sites (or catalytic surface area) of the substrate, the whole deposition rate would decease subsequently [119, 122].

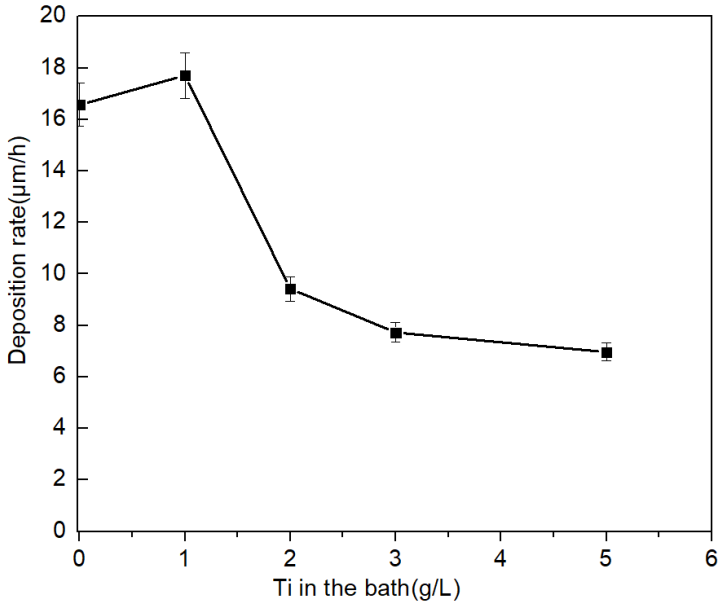

Figure 4-1 Deposition rates at various Ti content in the bath.

The 3D surface morphologies and surface roughness of as-deposited Ni-P and Ni-P-Ti coatings are shown in Figures 4-2 and 4-3, respectively. The 3D surface profilometer scanning area is 4 mm×4 mm. The as-deposited Ni-P coating has a smooth surface having the lowest surface roughness (0.39 μm). As Ti content in the plating solution increased, the surfaces of Ni-P-Ti coatings became rough, and nodular structures were observed on the surface. From Figure 4-3, it is clearly seen that the surface roughness of Ni-P-Ti coatings increased rapidly with the increase of Ti content in the plating solution. The highest surface roughness was reached at 5 g/L Ti content (3.3 μm), as seen in Figure 4-3.

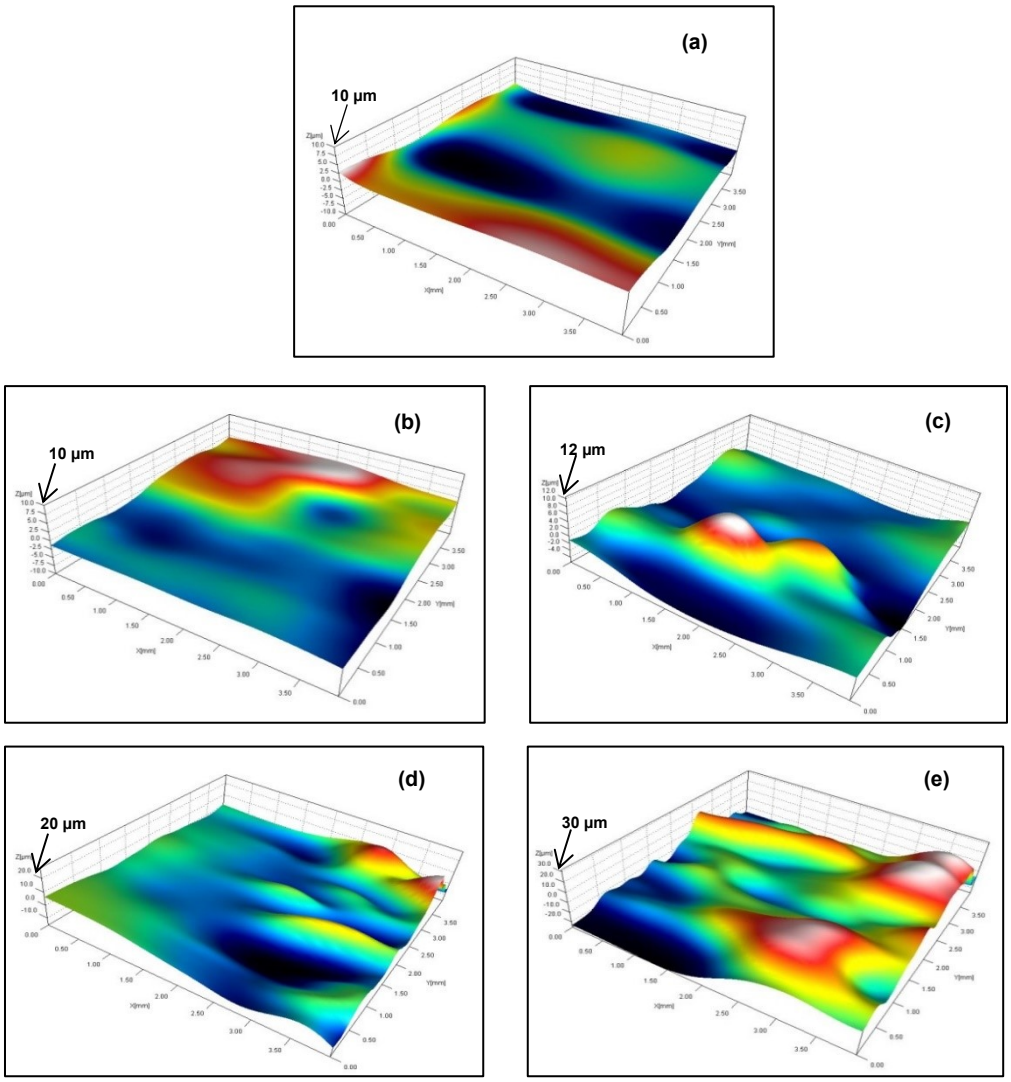

Figure 4-2 3D surface morphologies of as-deposited Ni-P and Ni-P-Ti coatings at different Ti content: (a) Ni-P coating (b) 1g/L; (c) 2g/L; (d) 3g/L; (e) 5g/L.

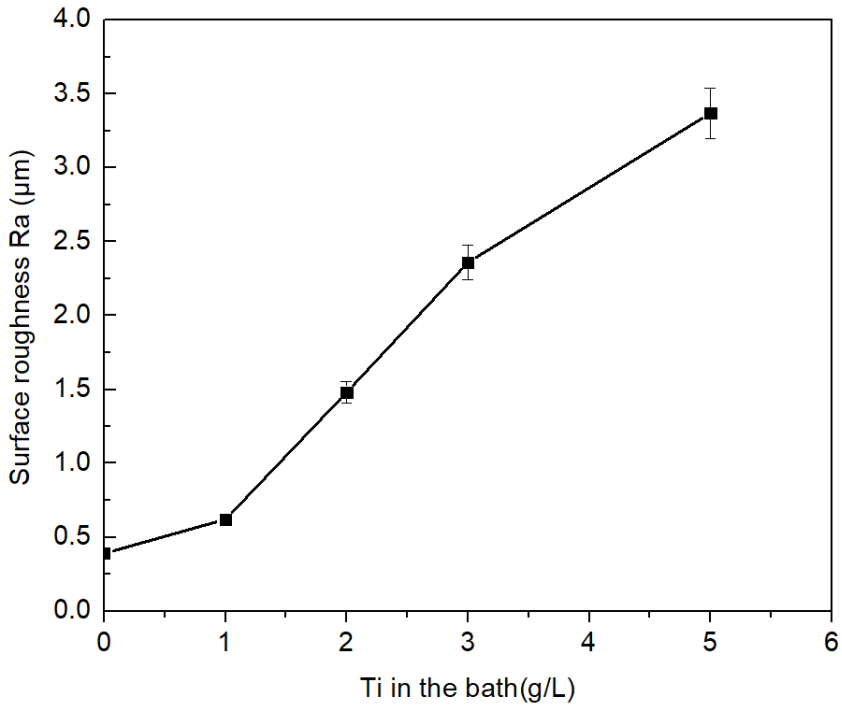

Figure 4-3 Surface roughness of as-deposited Ni-P and Ni-P-Ti coatings

SEM cross-section micrographs and the associated Ti EDS maps of as-deposited Ni-P-Ti coatings are shown in Figure 4-4. Figures 4-4 ((a), (c), (e), (g)) are the cross-section micrographs of Ni-P-Ti coatings. As can be seen from Figures 4-4 ((a), (c), (e), (g)), spherical Ti particles are distributed in the coatings and the Ti particles are well bonded with the Ni-P matrix. Figures 4-4 ((b) (d) (f) (h)) are the associated Ti EDS maps of the cross-section micrographs, respectively. It can be observed that the Ti particles were uniformly dispersed in the Ni-P matrix except in the 5g/L Ni-P-Ti coating. Ti particles exhibited agglomeration in the 5g/L Ti content coating due to the high Ti concentration in the plating solution. Nano-particles tend to agglomerate in coatings at high concentration, as also observed by other researchers [123, 124].

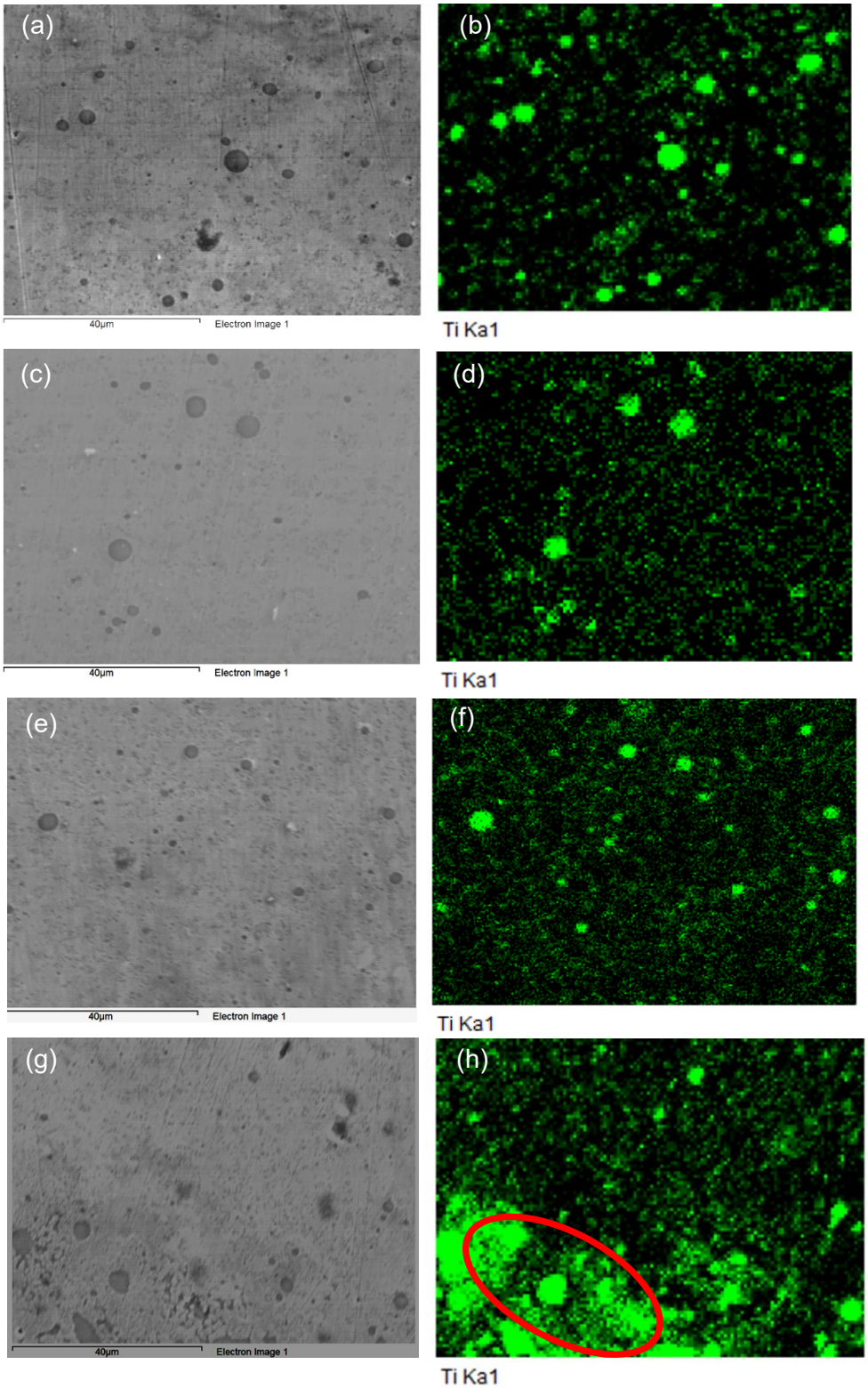
(a)
40µm
Electron Image 1
(b)
Ti Ka1
(c)
40µm
Electron Image 1
(d)
Ti Ka1
(e)
40µm
Electron Image 1
(f)
Ti Ka1
(g)
40µm
Electron Image 1
(h)
Ti Ka1

Figure 4-4 SEM cross-section micrographs and corresponding Ti EDS maps of as-deposited Ni-P-Ti coatings at different Ti content: (a) (b) 1g/L, (c) (d) 2g/L, (e) (f) 3g/L, (g) (h) 5g/L, red circle in (h) is particle agglomeration.

Another observation that can be made is by analyzing the amount of Ti within the composite coatings compared to the concentration of Ti in the initial plating solution. This was determined via EDS and the comparison is shown in Figure 4-5. It is observed that the weight percent (wt%) of Ti in the coatings increased as the concentration of Ti in the initial plating solution increased. The rate of this increase is also found to increase sharply between 0 g/L and 2 g/L. However, once 2 g/L is exceeded, the rate begins to gradually decrease. This is due to the increasing possibility of agglomeration which decreases particles incorporation into the Ni-P matrix [119-121]. The Ti content in the coatings achieved its maximum value of 21.8 wt% at 5 g/L of Ti content in the plating solution. However, at this Ti concentration, the Ti particles in the coating agglomerate extensively, as observed in Figure 4-4 (h). The compositions of Ni-P and Ni-P-Ti coatings are given in Table 4-1. It is observed that the Ni and P content decreases as the Ti content increases within the coatings.

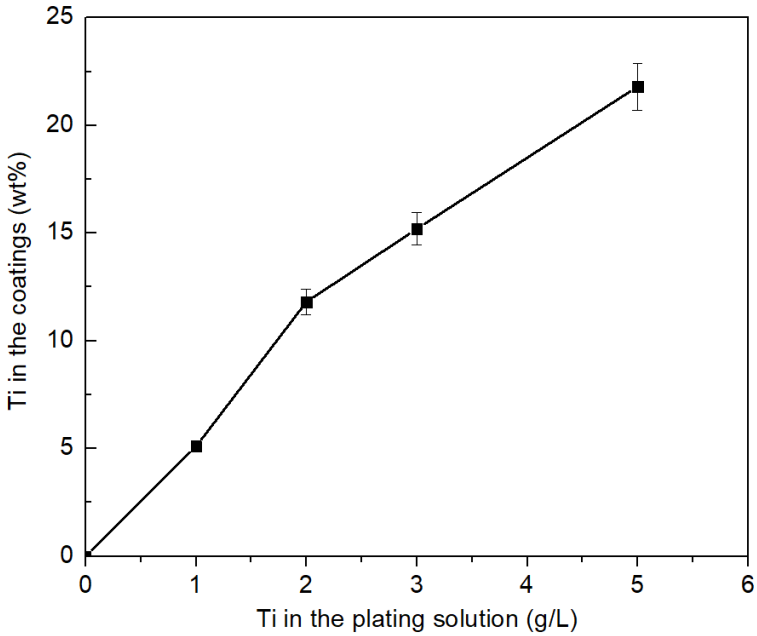

Figure 4-5 Weight percent (wt%) of Ti in the coatings at various Ti content in the bath

Table 4-1 Compositions of Ni-P and Ni-P-Ti coatings

Coatings	Ni (wt%)	P (wt%)	Ti (wt%)
Ni-P	89.9	10.1	0.0
Ni-P-1gTi	86.0	8.9	5.1
Ni-P-2gTi	79.3	8.9	11.8
Ni-P-3gTi	78.1	6.7	15.2
Ni-P-5gTi	72.0	6.2	21.8

Figure 4-6 shows the XRD patterns of Ti nanopowder, as-deposited Ni-P and Ni-P-Ti coatings. The as-deposited Ni-P and Ni-P-Ti coatings have a broad amorphous peak at the 2-theta position of 45°. Ti peak with low intensity and broad width was detected in the XRD pattern for each as-deposited Ni-P-Ti coating containing different Ti content, respectively. This low intensity and broad width associated with Ti may be attributed to the low Ti content and the fine nano-size of the Ti particles, respectively. Nano-particles tended to present broad XRD peaks, as confirmed by the XRD pattern of Ti nano-powder in Figure 4-6. In addition, the main peak of Ti was at the 2theta position of 40°, which overlapped with the peak of amorphous Ni-P coating [2]. As a result, it lowered the intensity of the Ti peak. It is also observed that TiO peak is present in the XRD patterns of Ti nano-powder, which was probably due to the oxidation of Ti nano-powder.

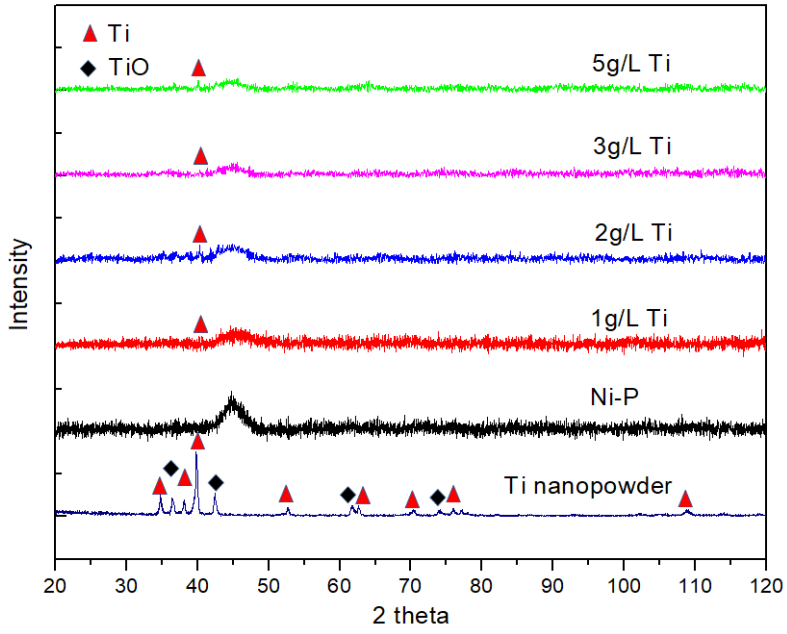

Figure 4-6 XRD patterns of Ti nano-powder, as-deposited Ni-P and Ni-P-Ti coatings

4.1.2 Coatings Annealed at 700 °C and 800 °C for 5 Hours

XRD patterns of annealed Ni-P coatings are presented in Figure 4-7. The Ni-P coatings were completely crystallized at annealing temperatures of 700 ℃ and 800 ℃. It is known that the amorphous Ni-P coatings start to become crystalline nickel phosphide and face centered cubic (FCC) nickel at temperatures above 300 ℃ [125, 126]. In addition, as the annealing temperature increased from 700 ℃ to 800 ℃, the intensity of Ni peak increased. Here, it is important to note that the Ni-P coatings both presented highly preferred orientation at the two annealing temperatures. The dominant peak was at the 2-theta position of 51.9°, which was associated with the (200) crystal plane of Ni. This preferred orientation was also found in pure Ni coating [123].

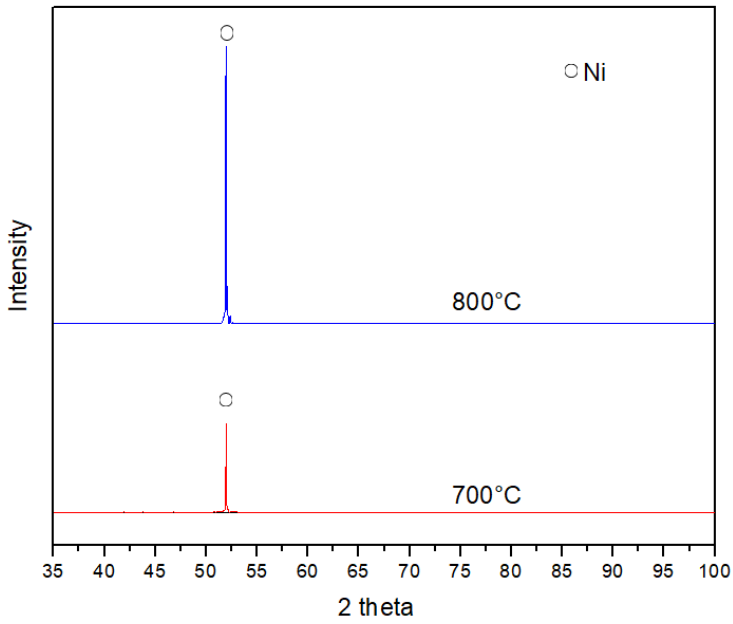

Figure 4-7 XRD pattern of annealed Ni-P coatings.

XRD patterns of Ni-P and Ni-P-Ti coatings annealed at 700 ℃ and at 800 ℃ are shown in Figures 4-8 and 4-9, respectively. In order to investigate the details of the XRD patterns of the annealed Ni-P coatings, the XRD patterns of Ni-P coatings annealed at 700 ℃ and 800 ℃ in Figure 4-7 were zoomed-in, which are also shown in Figures 4-8 and 4-9, respectively. Compared to the XRD patterns of the annealed Ni-P coatings, the preferred orientation was inhibited by the presence of Ti particles during the annealing process of the Ti containing coatings. Four different peaks associated with Ni are observed in the XRD patterns, (111) peak at the 2 theta position of 44.507°, (200) peak at the 2 theta position of 51.845°, (220) peak at the 2 theta position of 76.369°, and (311) peak at the 2 theta position of 92.943° as given by Ni powder diffraction file (PDF ID: 00-004-0850 [127]) . This suggested that adding Ti particles changed the percentage of crystalline nickel phase in the coating and inhibited the preferred orientation of (200) nickel in the Ni-P-Ti coatings after annealing. This result was also confirmed by previous researchers [123, 128], and could be attributed to two reasons. First, the Ti particles in composite coatings reacted with Ni to form NiTi intermetallic during the annealing process, which reduced the amount of preferred growth

of (200) Ni grains. Second, the preferred growth of nickel phase was shielded by the distributed Ti nanoparticles, which acted as nucleation sites during the annealing process [123]. Moreover, it is worth noting that the crystallization of Ni_3P was detected and the presence of $TiNi_3$ and NiTi were also identified after annealing at different temperatures, which is consistent with published results [2]. In order to separate the XRD peaks of NiTi from the other XRD peaks of Ni_3P and Ni, an XRD slow scan with a step size of 0.01°/s was employed. The XRD slow scan patterns of 3 g/L Ti coating annealed at 700 °C are shown in Figures 4-8 (b) and (c). The XRD slow scan patterns of 3 g/L Ti coating annealed at 800 °C are shown in Figures 4-9 (b) and (c). According to NiTi (austenite: cubic) powder diffraction file (PDF ID: 04-008-5982 [129]), the strongest peak of NiTi is located at an angle of $2\theta = 41.609°$ from the (110) plane; the second strongest peak of NiTi is located at an angle of $2\theta = 75.931°$ from the (211) plane. These two strongest peaks with low intensity were observed in Figures 4-8 (b) and (c) as well as in Figures 4-9 (b) and (c), respectively. This low intensity of NiTi peaks shown in the slow scan XRD patterns is due to the low quantity, nano-size, and highly dispersive distribution of the NiTi particles [130-132]. Other nanoparticles such as nano-SiC, nano-SiO_2, and nano-TiO_2 show very weak or even no diffraction peaks in the XRD patterns of Ni-P based composite coatings, confirmed by other researchers [130-132].

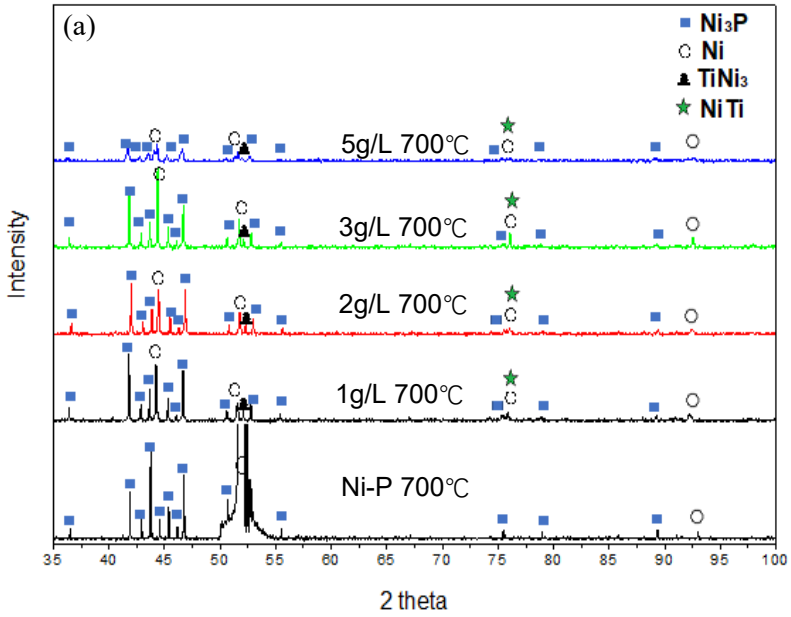

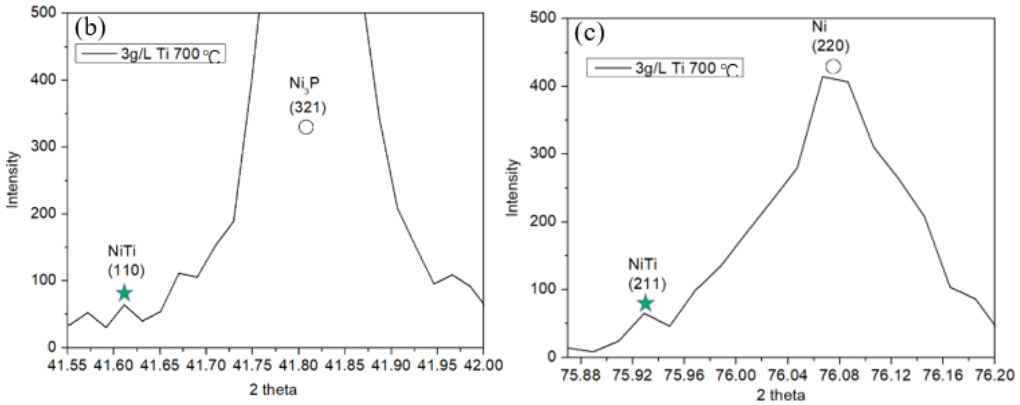

Figure 4-8 XRD patterns of Ni-P and Ni-P-Ti coatings annealed at 700℃, (a) normal scan (0.2°/s), (b) and (c) slow scan (0.01°/s)

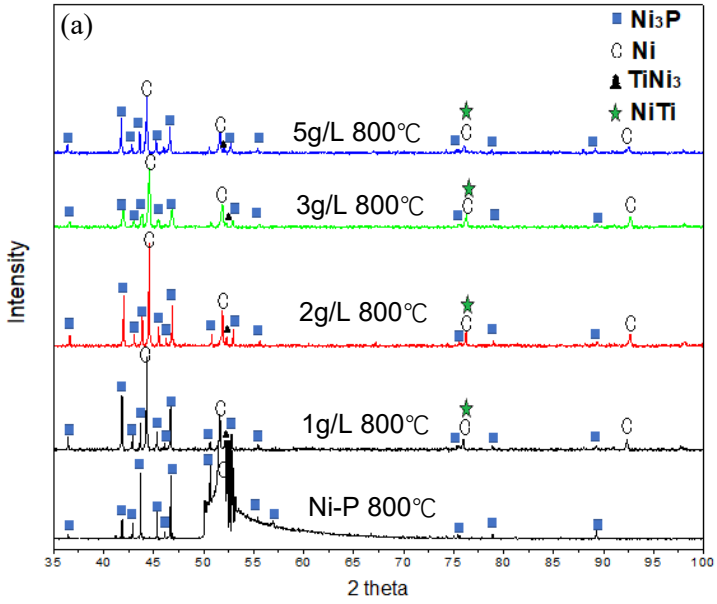

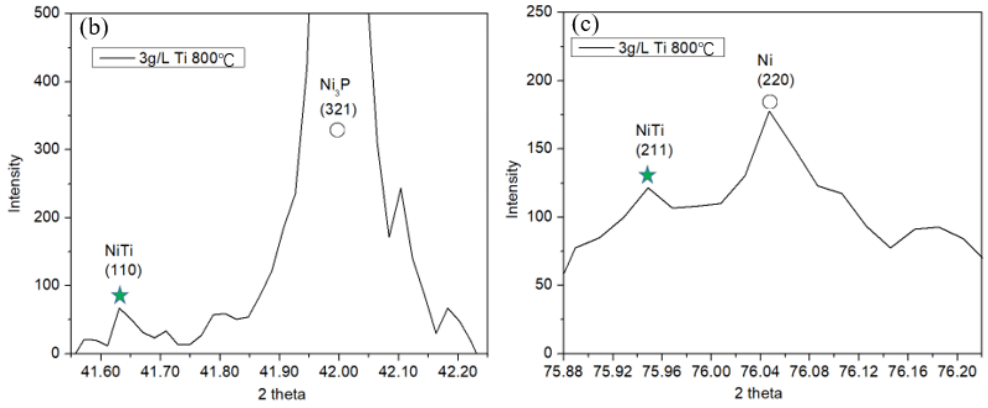

Figure 4-9 XRD patterns of Ni-P and Ni-P-Ti coatings annealed at 800°C, (a) normal scan(0.2°/s), (b) and (c) slow scan (0.01°/s)

4.1.3 Coatings Annealed at 650 °C for 2 Hours

Because 5g/L Ni-P-Ti coating shows agglomeration of Ti particles, 5g/L Ni-P-Ti coating was not investigated in the following studies. The corresponding Ti concentrations in the coatings for 1g/L, 2 g/L, and 3 g/L Ti in the plating solutions are 5.1 wt%, 11.8 wt%, and 15.2 wt%, respectively. Therefore, in the rest of the manuscript, 1 g/L, 2 g/L, 3 g/L Ti coatings are referred to as 5.1 wt%, 11.8 wt%, 15.2 wt% Ti coatings.

Figure 4-10 (a) shows the XRD patterns of annealed Ni-P coatings. After annealing at 650°C for 2 hours, the Ni-P coating is completely crystallized (Figure 4-10 (a)). The annealed Ni-P coating exhibits highly preferred orientation and the dominant peak is associated with the Ni (200) crystal plane at a 2 theta position of 51.845° [127]. This preferred orientation is formed due to the preferred growth of the Ni (200) plane which has a low plane energy, confirmed as well by other researchers [123].

Figure 4-10 (b) shows the XRD patterns of the annealed Ni-P-Ti composite coatings as well as the annealed Ni-P coating at 650 °C for 2 hours. During the annealing process of the Ni-P-Ti composite coatings, Ti particles prevent the preferred orientation of Ni (200), observed in Figure 4-10 (b), similar to the Ni-P-Ti coatings annealed at 700°C and 800°C

for 5 hours. It is important to note that Ni_3P, NiTi (B_2, austenite phase) and Ni_3Ti peaks are also observed in the XRD patterns of the composite coatings after annealing.

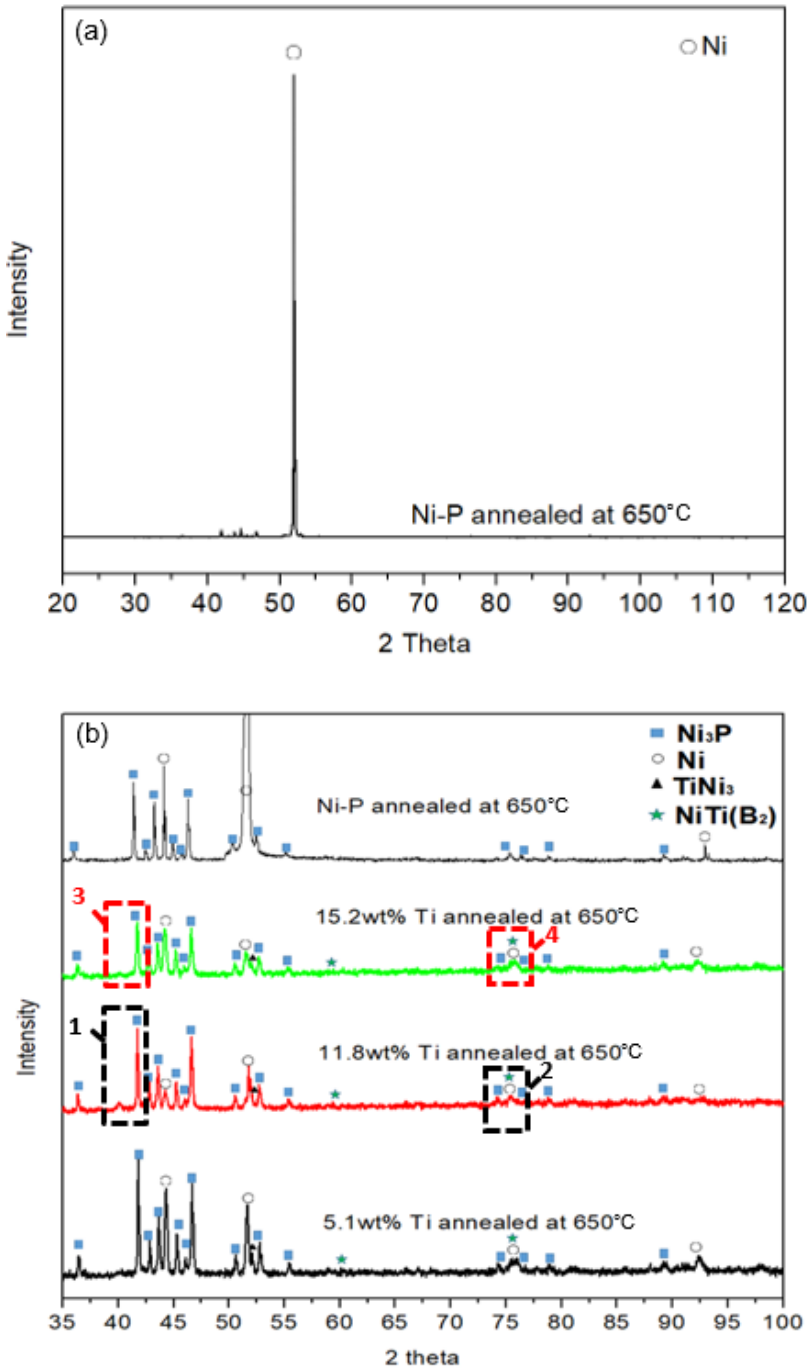

Figure 4-10 (a) annealed Ni-P coatings, (b) annealed Ni-P-Ti composite coatings.

It has been observed that the NiTi XRD peaks are overlapped with the Ni or Ni_3P peaks. To separate these peaks, XRD slow scans (step size: 0.01°/s) were conducted. The XRD slow scan patterns of annealed 11.8 wt% Ti coating and annealed 15.2 wt% Ti coating are shown in Figures 4-11 and 4-12, respectively. Figures 4-11 and 4-12 also show standard XRD patterns of NiTi [129], Ni [127], and Ni_3P [133] , respectively. The slow scan patterns show that the NiTi (100) and (211) peaks both have low intensity (Figures 4-11 and 4-12). This is mainly because of the low amount of the NiTi within the composite coatings. These slow scan XRD patterns confirm the formation of NiTi in the composite coatings during annealing. This conclusion is in accordance with the inference obtained from the previous study [108].

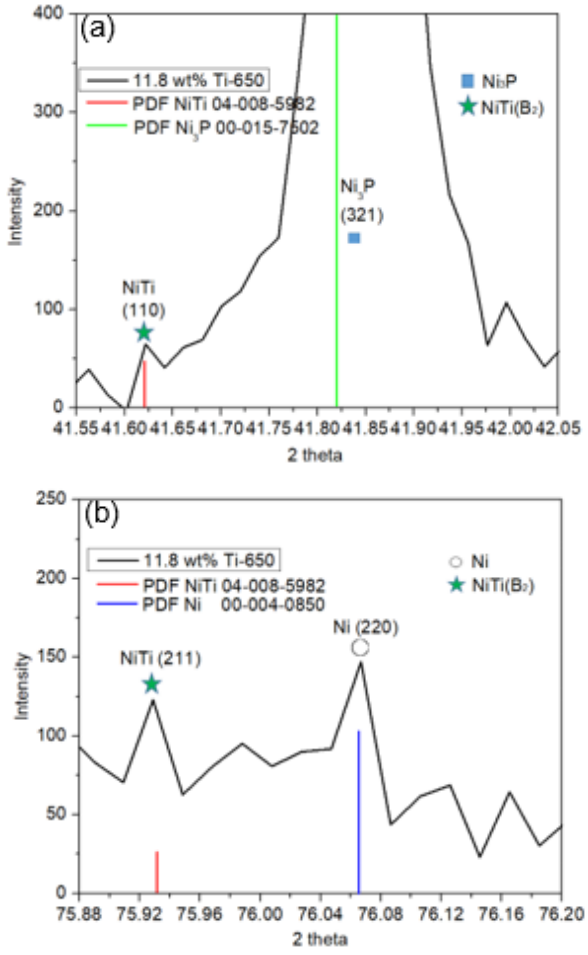

Figure 4-11 Slow scan XRD patterns of 11.8 wt% Ti coating annealed at 650°C. (a) slow scan (0.01°/s) of square area 1 in Figure 4-10 (b), (b) slow scan (0.01°/s) of square area 2 in Figure 4-10 (b)

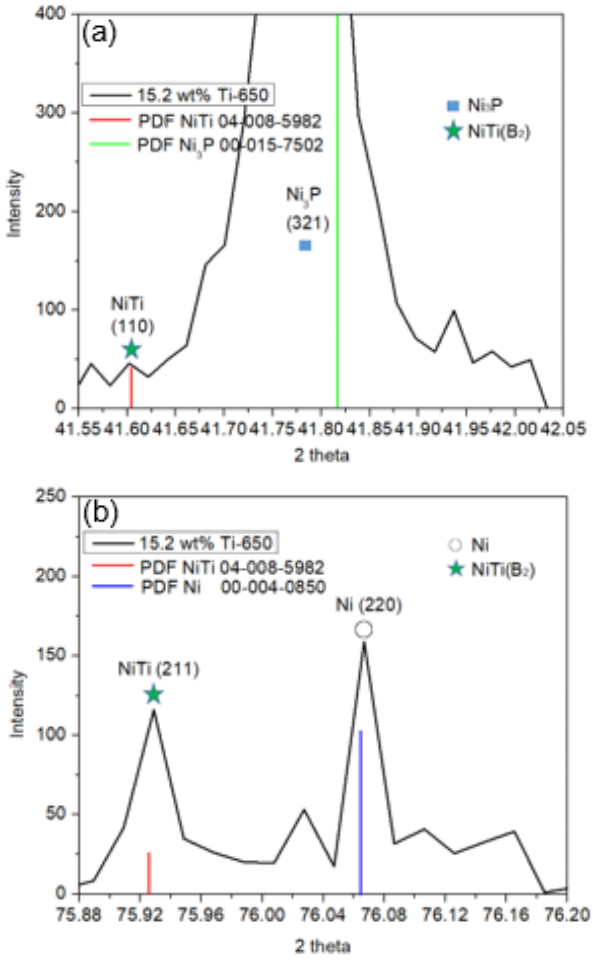

Figure 4-12 Slow scan XRD patterns of 15.2 wt% Ti coating annealed at 650°C. (a) slow scan (0.01°/s) of square area 3 in Figure 4-10 (b), (b) slow scan (0.01°/s) of square area 4 in Figure 4-10 (b)

Surface SEM micrographs of as-deposited and annealed Ni-P and Ni-P-Ti coatings are shown in Figure 4-13. A nodular structure is observed on as-deposited Ni-P coating (Figure 4-13 (a)). Some pore morphologies are also observed on the surface of as-deposited Ni-P coating due to the evolution of hydrogen during the oxidation of $NaPO_2H_2$ in the electroless plating process [134]. After annealing, the surface morphology of Ni-P coating does not change significantly because of the relatively low annealing temperature (650°C), as shown in Figure 4-13 (b). On the other hand, compared to as-deposited Ni-P coating, a refined nodular and denser morphology is observed on the surface of as-deposited Ni-P-Ti coatings (Figures 4-13 (c), (e)) due to the presence of Ti particles. Ti nano-particles fill the pores in the Ni-P matrix and prevent the growth of Ni-P nodules, which results in dense and fine surface morphology [69]. A similar structure is also observed on the annealed Ni-P-Ti coatings (Figures 4-13 (d), (f)).

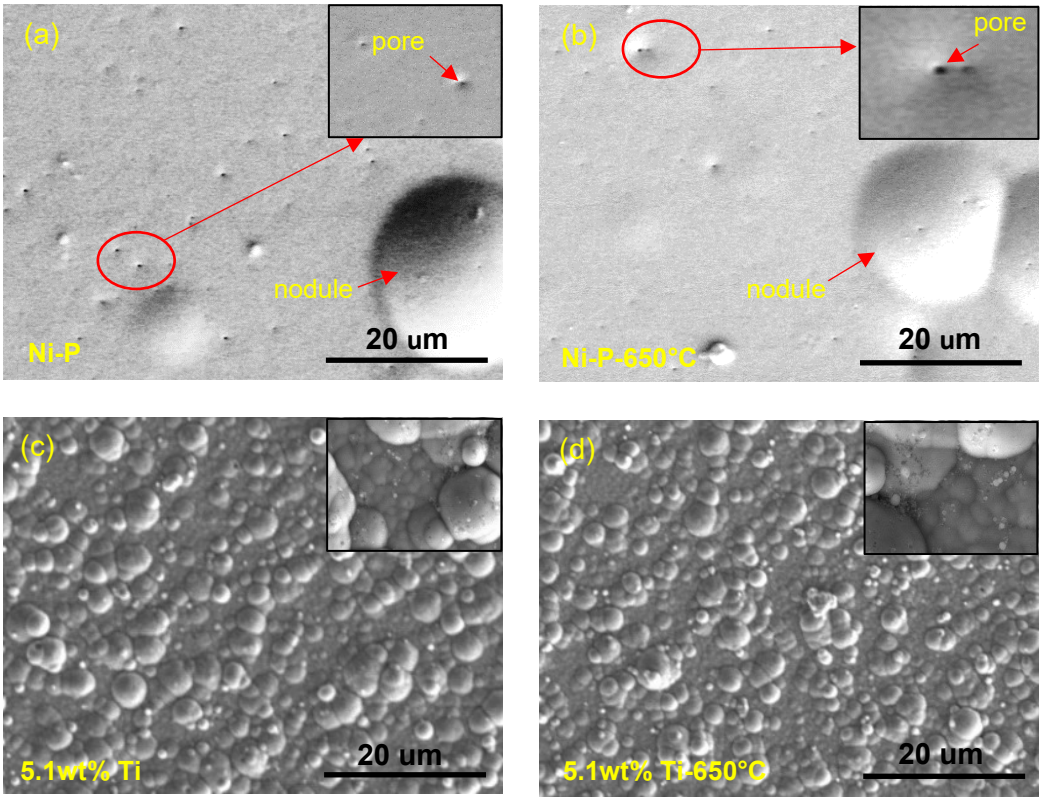

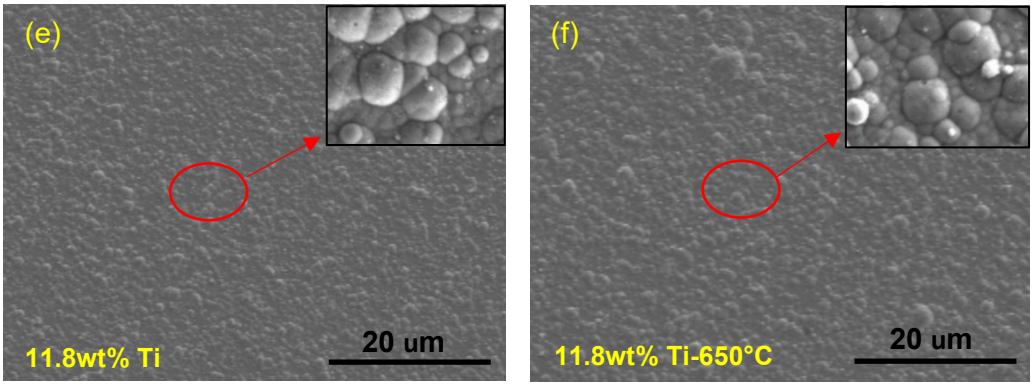

Figure 4-13 Representative surface SEM micrographs of as-deposited and annealed Ni-P and Ni-P-Ti coatings

The cross-sectional SEM micrographs of as-deposited and annealed 11.8 wt% Ti coatings are shown in Figure 4-14. Figure 4-14 (a) shows the cross-sectional SEM micrograph of as-deposited 11.8 wt% Ti coating. It is noted that the thickness of the coating is uniform, and the coating is dense without porous or other defects. In addition, the spherical Ti particles are uniformly distributed within the coating. Furthermore, the coating is bonded well with the steel substrate, and the interface between the coating and the steel substrate can be clearly seen. After annealing, there are no obvious changes within the cross-section of the coating (Figure 4-14 (b)).

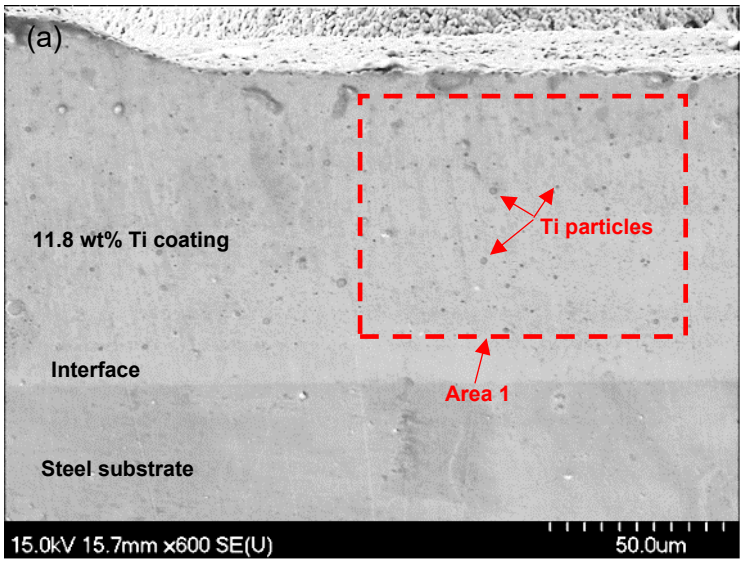

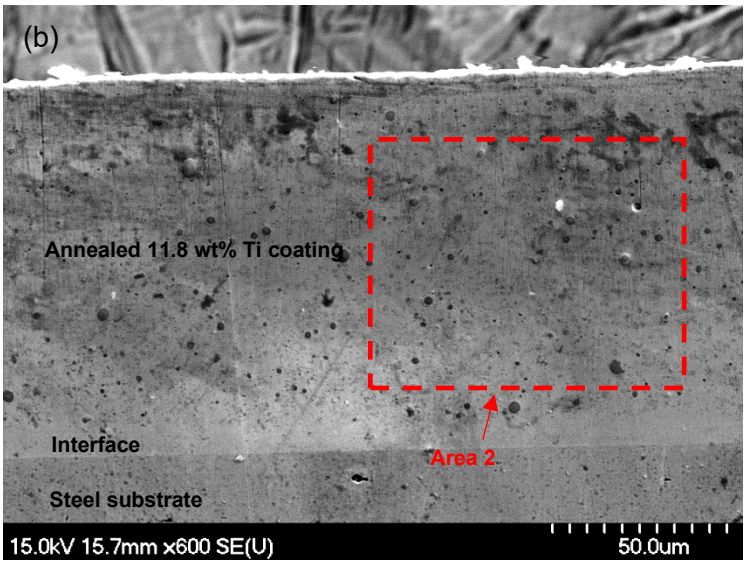

Figure 4-14 Cross-sectional SEM micrographs of (a) as-deposited 11.8 wt % Ti coating and (b) annealed 11.8 wt% Ti coating

In order to investigate the particles distribution within the coatings before and after annealing, elemental EDS map was employed. The EDS maps of different elements of as-deposited 11.8 wt% Ti coating in Figure 4-14 (a) area 1 are shown in Figure 4-15. It is noted that the spherical Ti particles are distributed uniformly within the area 1. No particles agglomeration is observed in Figures 4-15 (a) and (b).

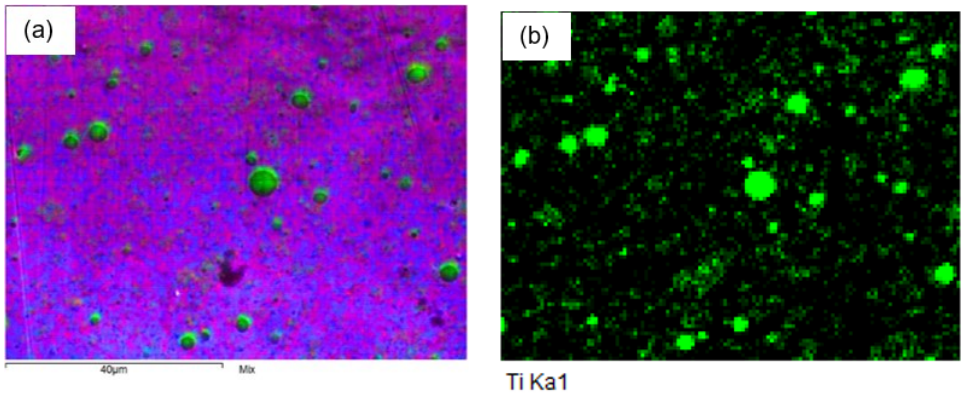

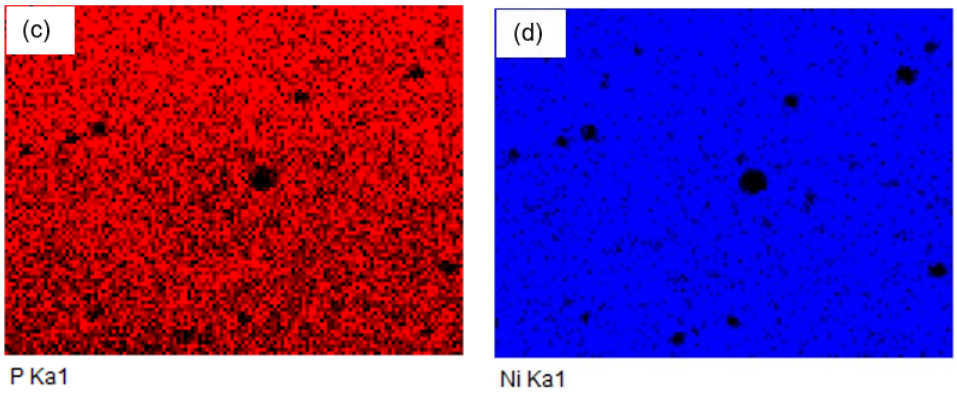

Figure 4-15 Elemental EDS maps of the area 1 in Figure 4-14 (a) (as-deposited 11.8 wt% Ti coating), (a) mix elemental EDS map, (b) Ti EDS map, (c) P EDS map and (d) Ni EDS map

The EDS maps of different elements of annealed 11.8 wt% Ti coating in Figure 4-14 (b) area 2 are shown in Figure 4-16. After annealing, there is no obvious change for the particles distribution compared to the as-deposited coating. However, it is worth noting that the Ni atoms diffused into the Ti particles to form the NiTi intermetallic phase (Figure 4-16 (a)).

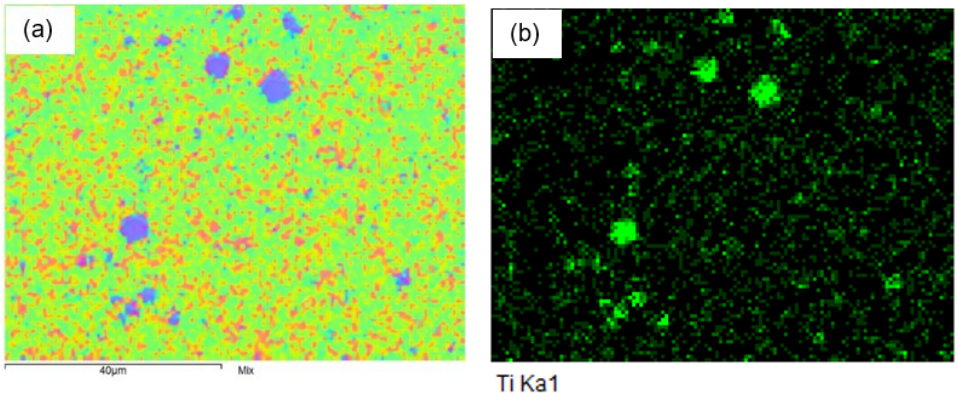

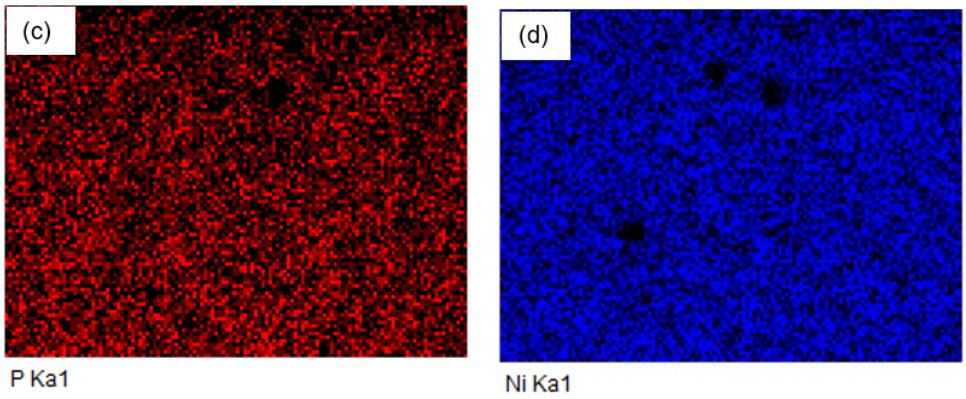

Figure 4-16 Elemental EDS maps of the area 2 in Figure 4-14 (b) (annealed 11.8 wt% Ti coating), (a) mix elemental EDS map, (b) Ti EDS map, (c) P EDS map and (d) Ni EDS map

To further investigate the annealed Ti particles and confirm the formation of NiTi phase, SEM and EDS examinations were conducted on annealed Ni-P-Ti coatings. The SEM micrographs and the point EDS spectra of annealed particles in the 15.2 wt% Ti coatings are shown in Figure 4-17. The EDS results of the particles shown in Figure 4-17 (a) and (b) are listed in Table 4-2. From Figure 4-17, it is observed that the NiTi intermetallic particles are metallurgically bonded well to the Ni-P matrix. This is due to the diffusion layer between the particles and matrix which improved the interface strength. From Table 4-2, it is important to note that NiTi and Ni_3Ti phases were formed in the annealed particles. This means that, after annealing, the amorphous coatings transformed to the crystalline matrix with superelastic NiTi and Ni_3Ti phases.

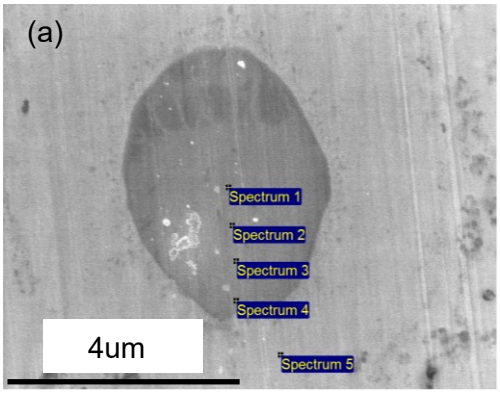
(a)
Spectrum 1
Spectrum 2
Spectrum 3
Spectrum 4
Spectrum 5
4um

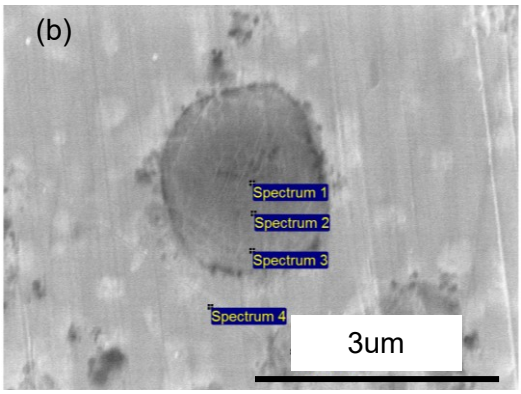
(b)
Spectrum 1
Spectrum 2
Spectrum 3
Spectrum 4
3um

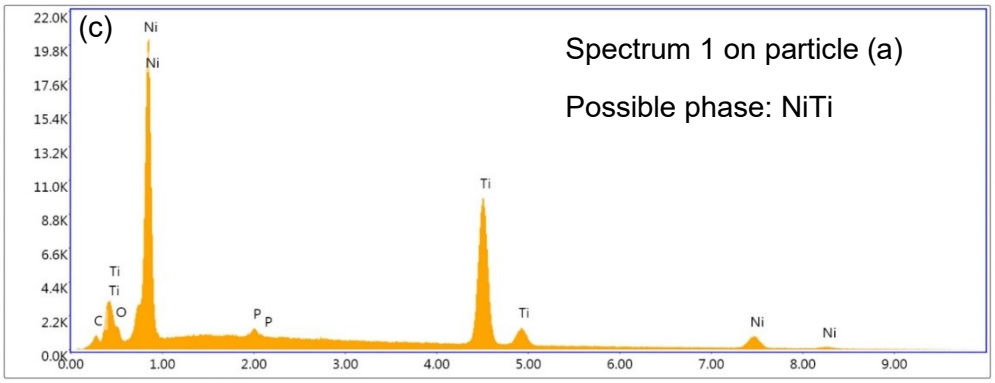
(c)
Spectrum 1 on particle (a)
Possible phase: NiTi
Ni
Ni
Ti
Ti
Ti
C
O
P
P
Ti
Ni
Ni
22.0K
19.8K
17.6K
15.4K
13.2K
11.0K
8.8K
6.6K
4.4K
2.2K
0.0K
0.00
1.00
2.00
3.00
4.00
5.00
6.00
7.00
8.00
9.00

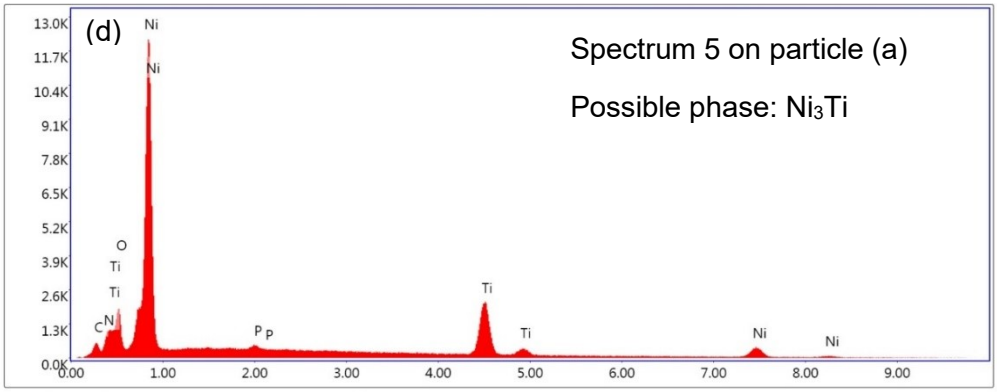
(d)
Spectrum 5 on particle (a)
Possible phase: Ni3Ti
Ni
Ni
O
Ti
Ti
C
N
P
P
Ti
Ti
Ni
Ni
13.0K
11.7K
10.4K
9.1K
7.8K
6.5K
5.2K
3.9K
2.6K
1.3K
0.0K
0.00
1.00
2.00
3.00
4.00
5.00
6.00
7.00
8.00
9.00

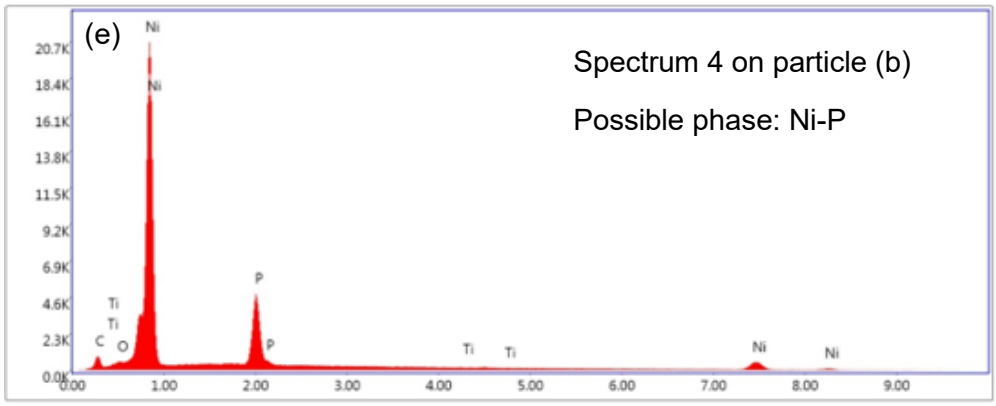

Figure 4-17 Representative SEM micrographs and EDS spectra of particle (a) and particle (b) annealed at 650°C; (c) EDS spectrum 1 in micrograph (a); (d) EDS spectrum 5 in micrograph (a); (e) EDS spectrum 4 in micrograph (b)

Table 4-2 EDS results of particles (a) and (b) in Figure 4-17

Particle (a)				Particle (b)			
EDS	Ni at%	Ti at%	Possible phase	EDS	Ni at%	Ti at%	Possible Phase
1	51.72	48.28	NiTi	1	48.74	51.26	NiTi
2	51.48	48.52	NiTi	2	53.56	46.44	NiTi
3	52.41	47.59	NiTi	3	74.59	25.41	Ni_3Ti
4	54.85	45.15	NiTi	4	97.33	2.67	Ni
5	75.64	24.34	Ni_3Ti				

To further confirm the formation of superelastic NiTi phase within the annealed Ni-P-Ti coatings. EDS line scan was performed on annealed particles in 5.1 wt% Ti coating. The EDS line scan (AB) as well as atomic percent distribution of Ni and Ti along the line AB for annealed 5.1 wt% Ti coating are shown in Figures 4-18 (a) and (b), respectively. It is observed that the NiTi and Ni_3Ti phases were formed within the annealed particles. NiTi phase was surrounded by a thin layer of Ni_3Ti phase. The line scan results are well consistent with the point EDS results.

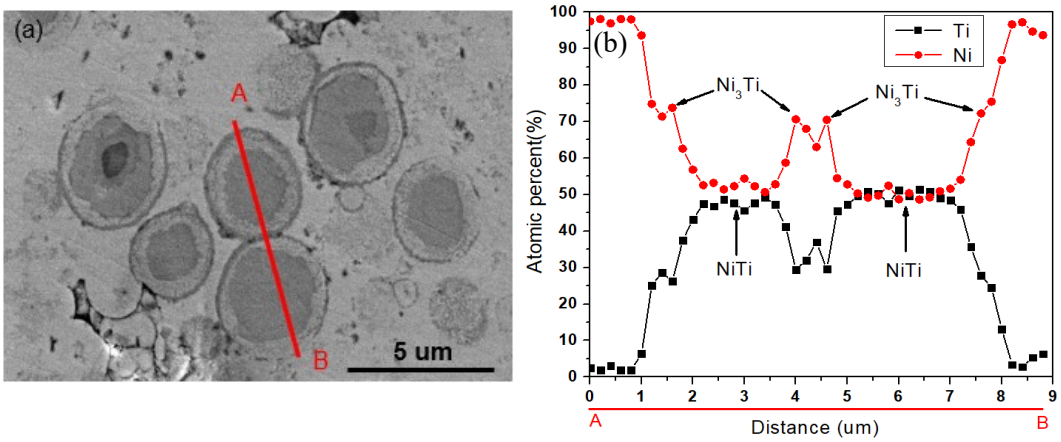

Figure 4-18 (a) EDS line scan location (AB) across two particles in annealed 5.1 wt% Ti coating, (b) corresponding EDS line scan results

In order to investigate the microstructural development mechanisms of Ni-P-Ti coating during annealing, the Gibbs free energies (ΔG) of various reactions were calculated using HSC chemistry software (Outokumpu technology: version 6). The results are summarized in Table 4-3. These Gibbs free energy results are comparable to other studies [31, 34]. Equation 4.2 for the formation of Ni_3Ti phase has the lowest Gibbs free energy, and equation 4.1 for the formation of $NiTi_2$ phase shows the second lowest Gibbs free energy. Therefore, Ni_3Ti and $NiTi_2$ phases are expected to form at the start of annealing.

Table 4-3 Gibbs free energy of various possible reactions during annealing of Ni-P-Ti coating

Reactions	Gibbs free energy	
$Ni + 2Ti \rightarrow NiTi_2$	$\Delta G_{650°C} = -71.3\ kJ/mol$	4.1
$3Ni + Ti \rightarrow Ni_3Ti$	$\Delta G_{650°C} = -151.2\ kJ/mol$	4.2
$Ni + Ti \rightarrow NiTi$	$\Delta G_{650°C} = -57.9\ kJ/mol$	4.3
$\frac{1}{2}NiTi_2 + \frac{1}{2}Ni \rightarrow NiTi$	$\Delta G_{650°C} = -22.5\ kJ/mol$	4.4
$\frac{1}{3}Ni_3Ti + \frac{2}{3}Ti \rightarrow NiTi$	$\Delta G_{650°C} = -7.6\ kJ/mol$	4.5
$\frac{2}{5}NiTi_2 + \frac{1}{5}Ni_3Ti \rightarrow NiTi$	$\Delta G_{650°C} = -6.2\ kJ/mol$	4.6

Based on the Gibbs free energy and EDS results, the microstructural development process of Ni-P-Ti coating during annealing is illustrated in Figure 4-19. Because Ni atoms have much higher diffusion rate than Ti, the diffusion of Ni atoms into Ti particles is dominant [51]. Due to the lowest Gibbs free energy, at the beginning of annealing, Ni_3Ti phase is first formed in a Ti particle on the side close to the Ni matrix, while the $NiTi_2$ phase is formed near the center of the Ti particle (Figure 4-19 (b)). Then, NiTi phase is formed between the Ni_3Ti and $NiTi_2$ phase (Figure 4-19 (c)) because of the reaction equations 4.4 and 4.5. As annealing continues, more Ti phase reacts with Ni to form $NiTi_2$ phase, and the NiTi phase continues to grow (Figure 4-19 (d)). Eventually, $NiTi_2$ phase completely transforms to NiTi phase that is surrounded by a thin layer of Ni_3Ti phase (Figure 4-19 (e)). This microstructure development process is also confirmed by other researchers [31, 51]. Hu et al. also calculated the formation Gibbs free energies for different intermetallic NiTi phases at different diffusion temperatures (300-1000°C) and confirmed that the Ni_3Ti and $NiTi_2$ phases have lower formation Gibbs free energies than NiTi phase [31]. They observed that Ni_3Ti and $NiTi_2$ phases formed before NiTi phase at the Ni-Ti interface, then NiTi phase formed between these two phases in Ni-Ti diffusion couples annealed at 650 °C. Puente et al. also confirmed that the NiTi phase was formed between $NiTi_2$ and Ni_3Ti phases when annealing Ti-coated Ni micro-wires [51]. In their study, SEM results revealed a similar microstructural development process, which is consistent with the present study [51]. On the other hand, compared to annealing at 650 °C for 2 hours, when annealing at higher temperature or longer hours (over annealing), NiTi phase reacts with Ni to form Ni_3Ti phase due to high Ni concentration. Then the amount of NiTi phase decreases, and the amount of Ni_3Ti phase increases (Figure 4-19 (f)).

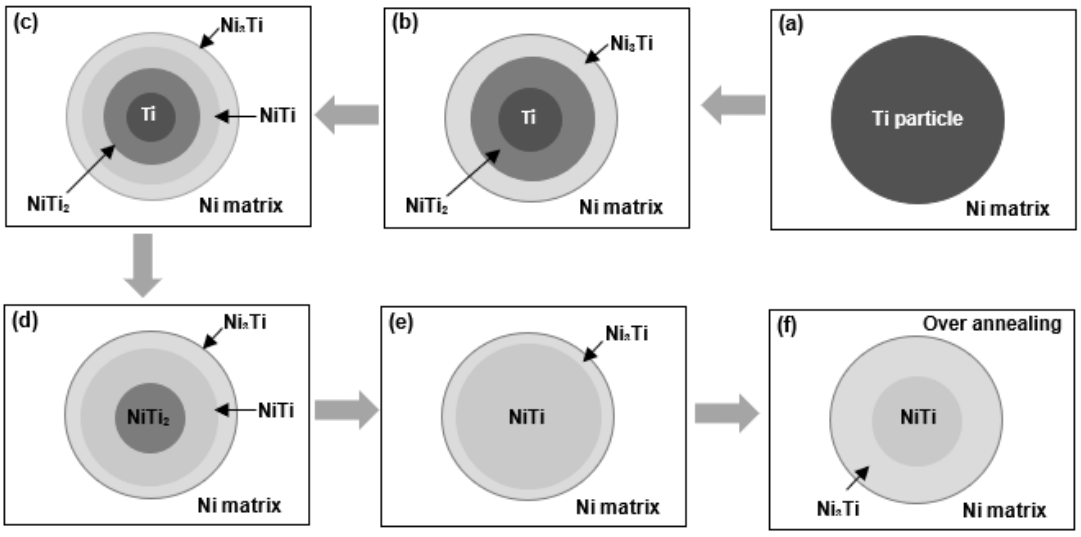

Figure 4-19 A schematic of microstructure development of Ni-P-Ti coating during annealing.

The comparison of slow scan XRD patterns of Ni-P-Ti coatings annealed at different conditions is shown in Figure 4-20. By superimposing the standard XRD patterns of NiTi, the superelastic NiTi phase is identified within the coatings annealed at various conditions. In addition, it is observed that as annealing temperature decreases, the intensity of NiTi XRD peaks increases for both annealed 11.8 wt% Ti and 15.2 wt% Ti coatings. This indicates that the amount of superelastic NiTi phase increases with a decrease in annealing temperature since the concentration of NiTi within the coatings is proportional to the intensity of its XRD peaks [135]. This is mainly because the NiTi phase converts to Ni_3Ti phase when annealing at high temperature (700 and 800 °C) and long time (5 hours), as illustrated in Figure 4-19 (f).

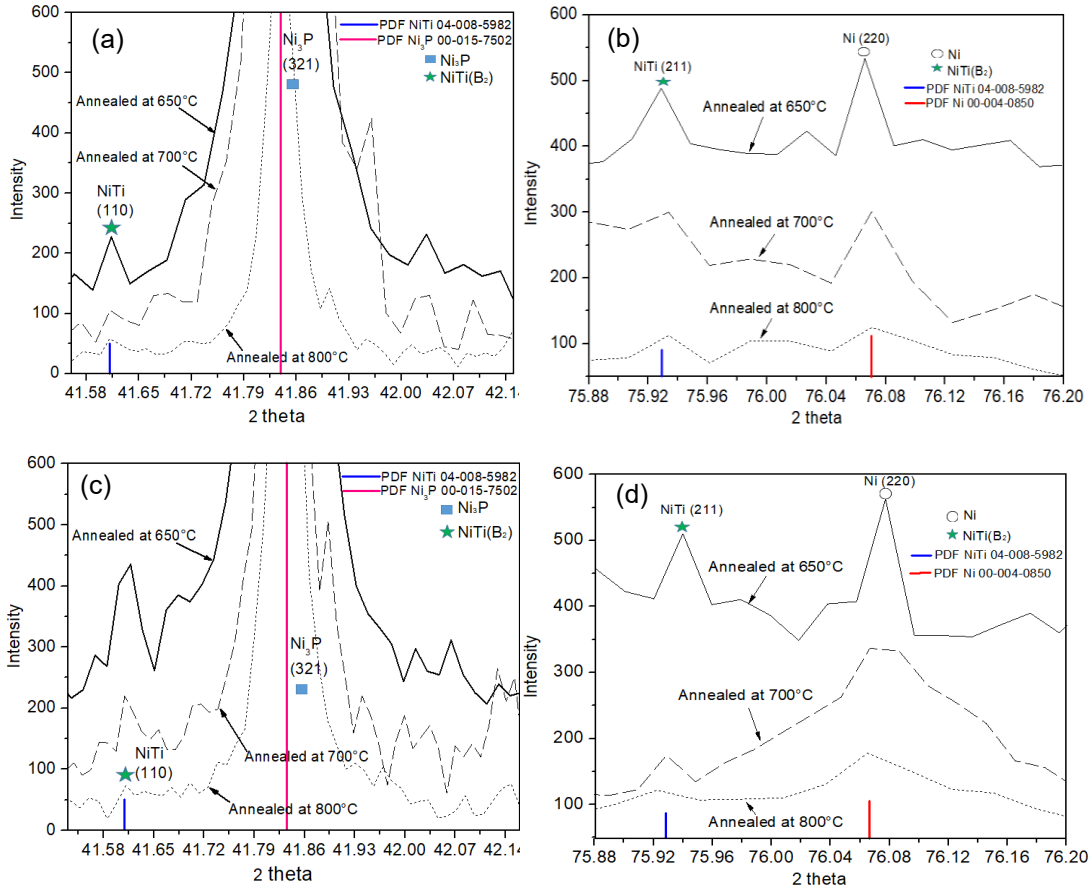

Figure 4-20 Slow scan (0.01°/s) XRD patterns of (a) (b) 11.8 wt% Ti coatings and (c) (d) 15.2 wt% Ti coatings annealed at different conditions

The grain size of annealed coatings was calculated using Scherrer equation [136]:

$$D = \frac{K\lambda}{\beta cos\theta} \qquad 4.7$$

Where, D is the grain size (nm); K is Scherrer constant (=0.9); λ is the wavelength of the Cu x-ray (0.15406 nm); β is the full width at half maximum (radians) of XRD peaks and θ is the position (radians) of XRD peaks.

The three strongest XRD peaks of Ni and Ni_3P in Figures 4-8, 4-9, and 4-10 were used to calculate the crystallite sizes of Ni and Ni_3P, respectively. The results were averaged, and the standard deviations were employed as error bars in plotted graphs. The crystallite sizes of Ni and Ni_3P calculated using equation 4.7 are shown in Figure 4-21. For a given annealing temperature, the crystallite sizes of Ni and Ni_3P decrease as Ti content increases. This is mainly because the nano Ti particles function as barriers to prevent the growth of Ni and Ni_3P grains during annealing [123]. As the Ti content increases, larger amount of Ti particles distribute within the coatings, which decreases the distance between Ti particles. This reduction in particle space makes the inhibition of Ni and Ni_3P growth by Ti particles more effective. On the other hand, for a given Ti content, as the annealing temperature rises, the crystallite sizes of Ni and Ni_3P increase. The crystallite sizes are expected to be larger when annealing at higher temperature due to the higher diffusion rates of elements and reorientation of crystallites [137].

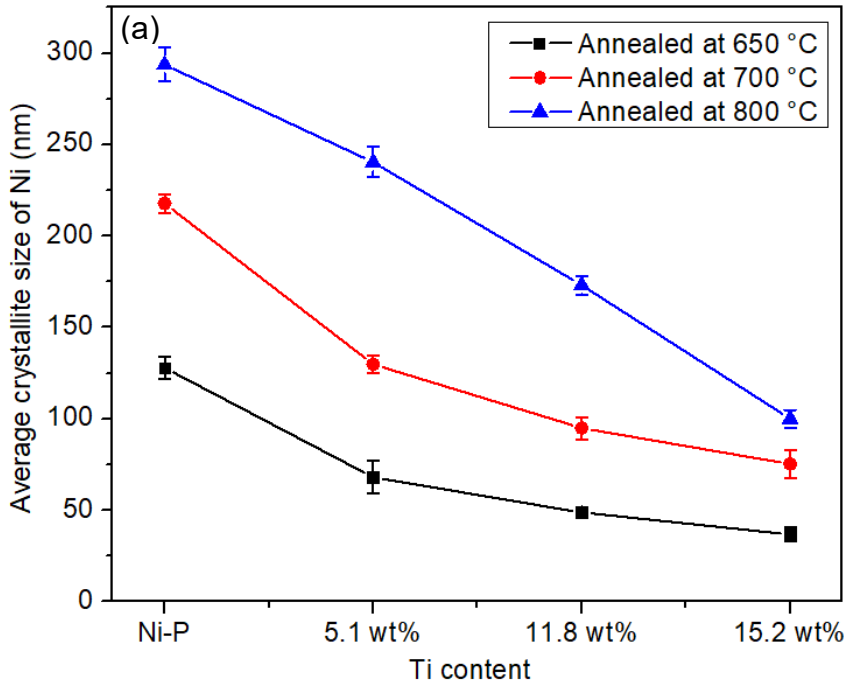

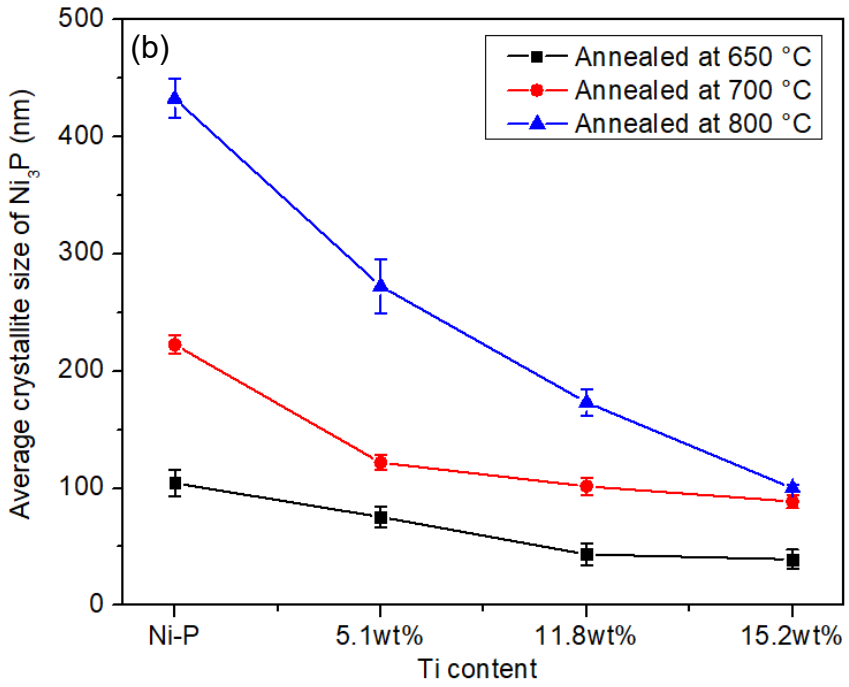

Figure 4-21 Crystallite sizes of (a) Ni and (b) Ni_3P annealed at various temperatures

Vickers hardness of as-deposited and annealed coatings is shown in Figure 4-22. For as-deposited coatings, as Ti content increases, the Vickers hardness decreases. This is mainly because the addition of relatively softer Ti particles into hard Ni-P matrix lowers the hardness of as-deposited composite coatings [64]. On the other hand, for a given annealing temperature, the Vickers hardness values of annealed coatings rise with the increase in Ti content due to the precipitation of Ni_3P second phase and dispersion strengthening mechanisms of the nanoparticles. In addition, for a given Ti content, as the annealing temperature decreases, the Vickers hardness increases. This is probably because of Hall-Petch strengthening. As the annealing temperature drops, the grain size decreases, according to Hall-Petch relationship between grain size and strength, the Vickers hardness (or strength) of annealed coatings increases [102].

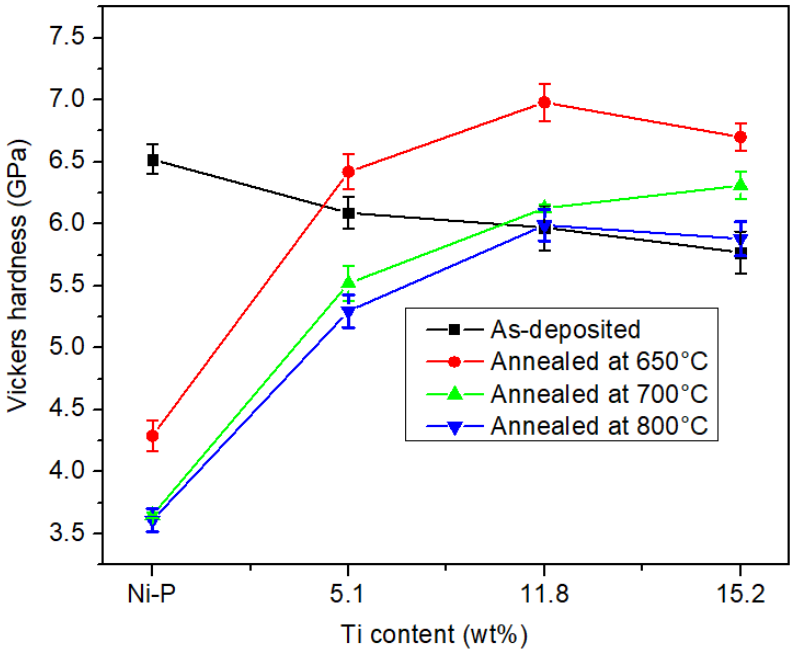

Figure 4-22 Vickers hardness of as-deposited and annealed coatings (at different annealing temperatures)

4.2 Scratch Behavior

4.2.1 As-deposited and Annealed Coatings (700°C and 800°C for 5 Hours)

Typical optical micrographs of scratch tracks and initial cracks of as-deposited coatings containing different content of Ti particles are shown in Figure 4-23. It is observed that the first crack distance of the as-deposited Ni-P coating is 1.3 mm. Compared to the as-deposited Ni-P coating, the first crack distance of 15.2 wt% Ti content Ni-P-Ti coating increased to 2.9 mm due to Ti particles toughening. However, the first crack distance of

21.8 wt% Ni-P-Ti coating is 1.4 mm which is only slightly higher than that of the as-deposited Ni-P coating due to the agglomeration of the Ti particles.

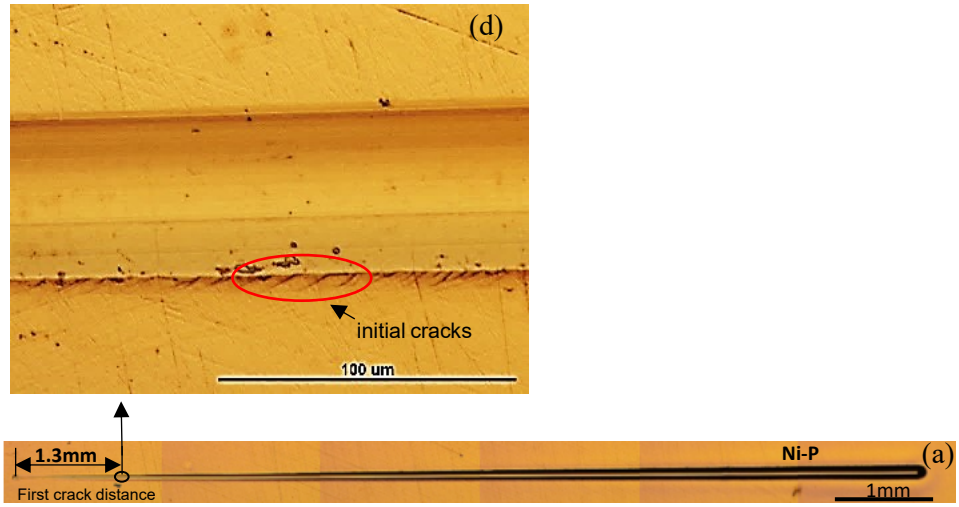

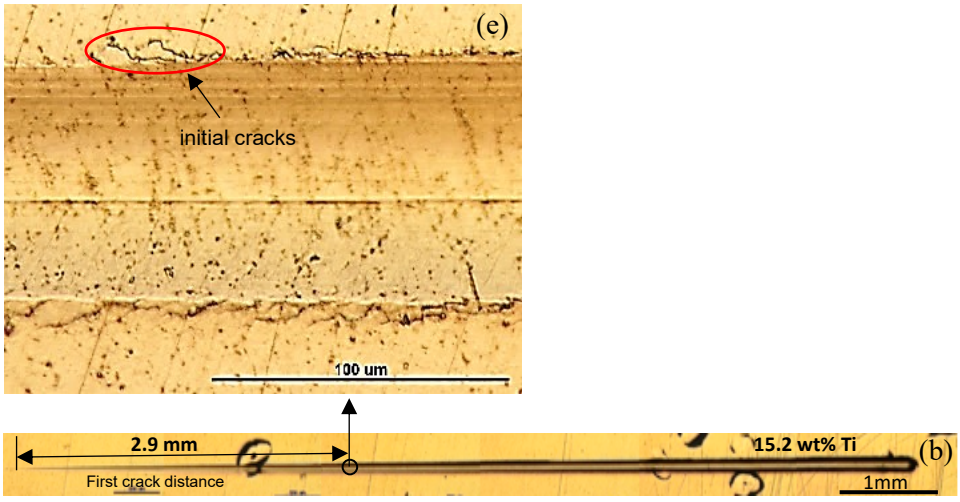

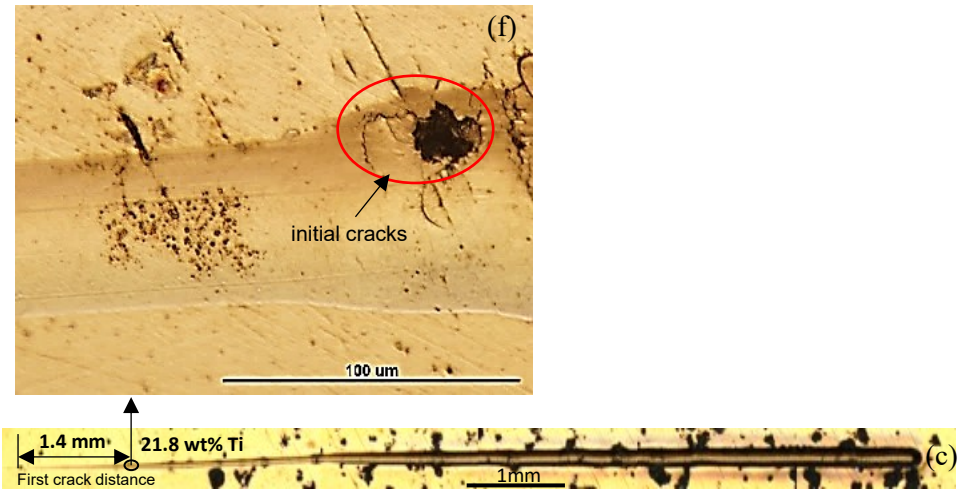

Figure 4- 23 Typical optical micrographs of scratch tracks and initial cracks of as-deposited coatings containing different content of Ti particles: (a) Ni-P, (b) 15.2 wt% Ti, (c) 21.8 wt% Ti, (d) (e) (f) corresponding high magnification of optical micrographs of initial cracks

Typical optical micrographs of scratch tracks and initial cracks of annealed (at 700°C) coatings containing different content of Ti particles are shown in Figure 4-24. It is seen that initial cracks for the annealed Ni-P coatings are observed on the side of the scratch track and the corresponding first crack distance is 1.5 mm. However, initial cracks for the annealed 15.8 wt% Ni-P-Ti coating and 21.8 wt% Ni-P-Ti coatings are both observed inside the scratch tracks, and the first crack distances for these two coatings were found to be 6.8 mm and 1.5 mm, respectively.

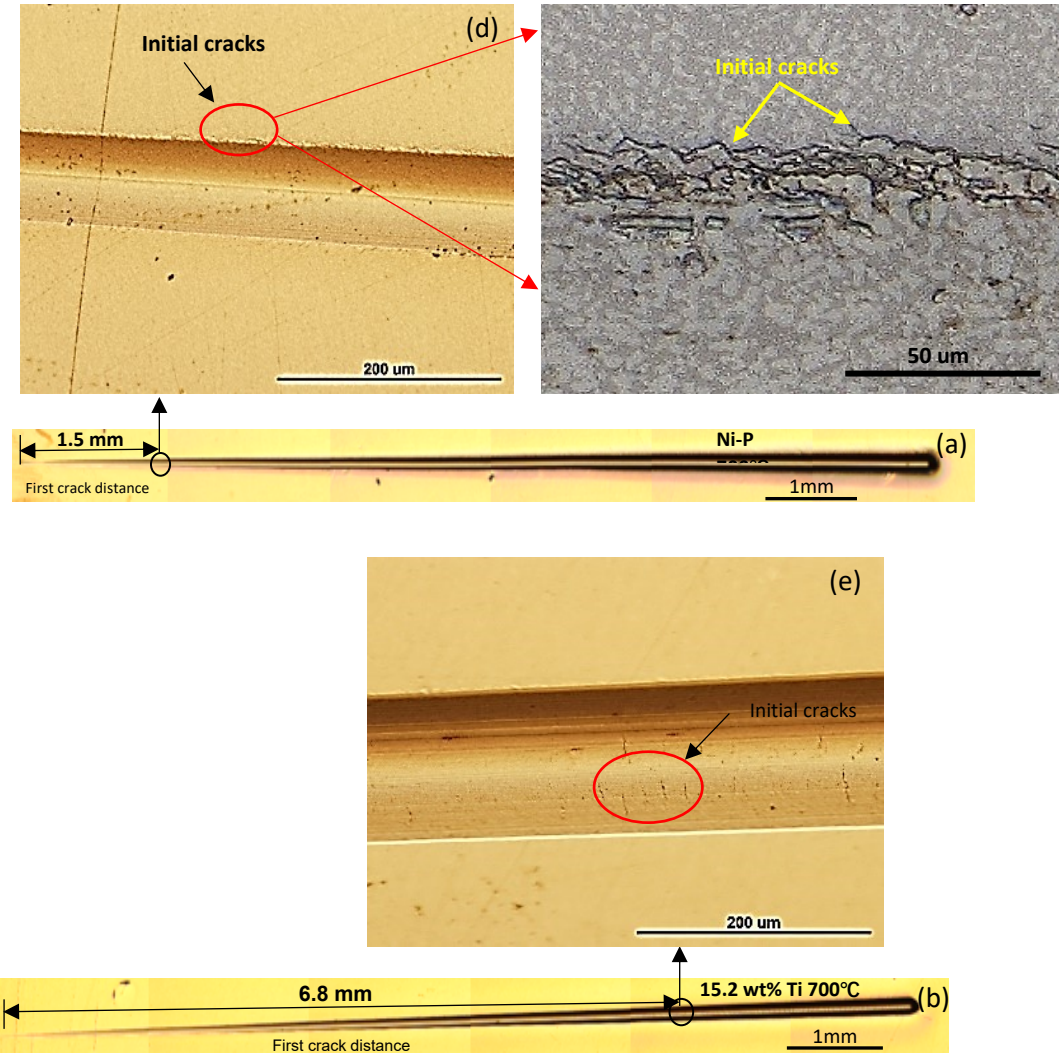
Initial cracks
(d)
200 um
Initial cracks
50 um
1.5 mm
First crack distance
Ni-P
(a)
1mm
(e)
Initial cracks
200 um
6.8 mm
First crack distance
15.2 wt% Ti 700°C
(b)
1mm

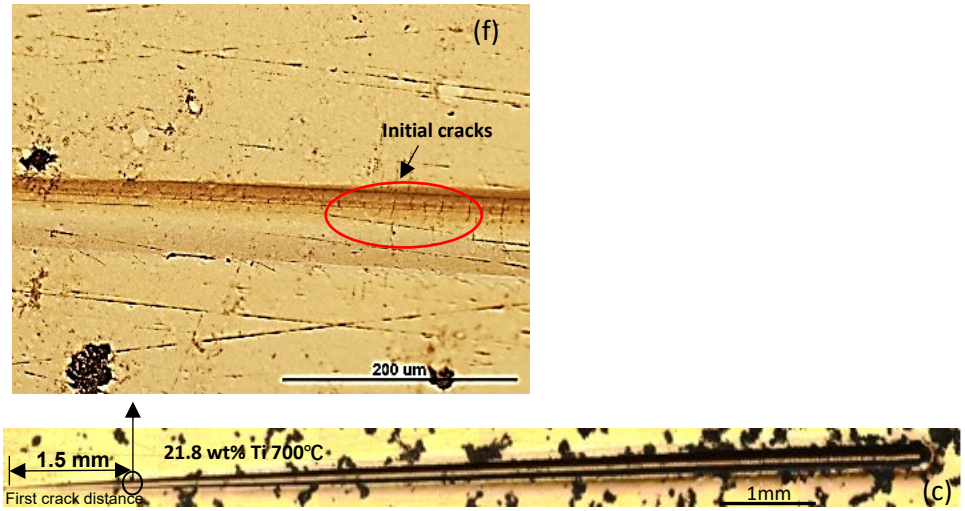

Figure 4-24 Typical optical micrographs of scratch tracks and initial cracks of annealed coatings (700°C) containing different content of Ti particles: (a) Ni-P; (b) 15.2 wt% Ti; (c) 21.8 wt% Ti; (d) (e) (f) corresponding high magnification of optical micrographs of initial cracks

Typical optical micrographs of scratch tracks and initial cracks of annealed (at 800°C) coatings containing different content of Ti particles are shown in Figure 4-25. It is observed that initial cracks for the annealed Ni-P coatings are seen on the side of the scratch track and the first crack is observed at the distance of 1.4 mm from the start point of the scratch track. On the other hand, the initial cracks for the annealed 15.2 wt% Ni-P-Ti and the annealed 21.8 wt% Ni-P-Ti coatings are both observed inside the scratch tracks; the first crack distance for these two coatings was found to be 4.4 mm and 1.4 mm, respectively.

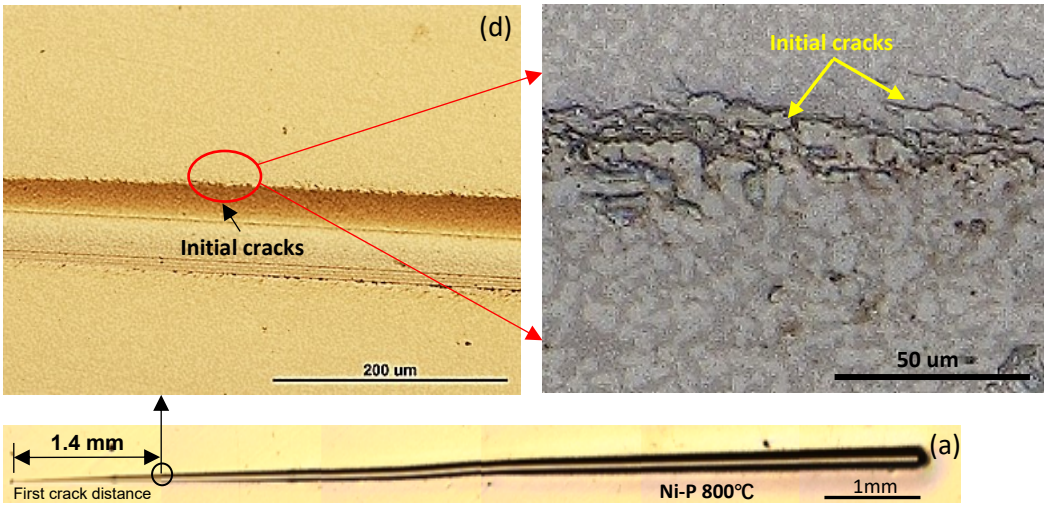
(d)
Initial cracks
200 um
Initial cracks
50 um
1.4 mm
First crack distance
(a)
Ni-P 800℃
1mm

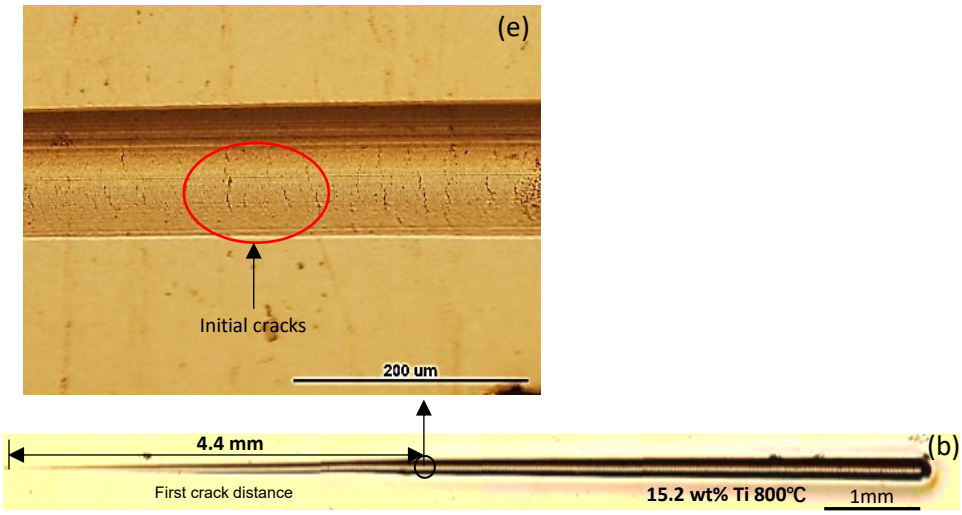
(e)
Initial cracks
200 um
4.4 mm
First crack distance
(b)
15.2 wt% Ti 800℃
1mm

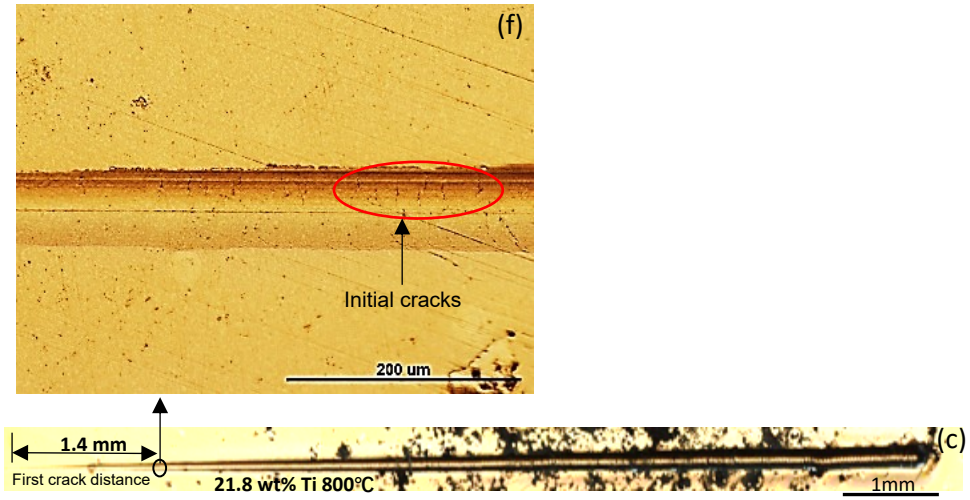

Figure 4-25 Typical optical micrographs of scratch tracks and initial cracks of annealed (at 800°C) coatings containing different content of Ti particles: (a) Ni-P, (b) 15.2 wt% Ti, (c) 21.8 wt% Ti, (d) (e) (f) corresponding high magnification optical micrographs of initial cracks

The L_{C1} values of as-deposited and annealed Ni-P and Ni-P-Ti coatings are shown in Figure 4-26. It is observed that the L_{C1} values of the as-deposited coatings increased as the Ti concentration in the coatings increased as well except for the as-deposited 21.8 wt% Ti coating. The same trend can be also seen in the annealed coatings. This behavior could be attributed to the different toughening mechanisms (crack deflection, crack bridging and crack shielding) by ductile particles (Ti particles or NiTi intermetallic particles). Higher content of particles resulted in higher toughness of bulk composite materials, a finding which has been confirmed by other studies [138, 139]. However, for any given condition (as-deposited or annealed), the 21.8 wt% Ti content coating had the lowest L_{C1} value because of the agglomeration of Ti or NiTi intermetallic particles. It is found that Ni-P coating with significant particles agglomerations was easier to crack compared to the Ni-P coating without any particles during scratch testing process [124].

From Figure 4-26, it is observed that the L_{C1} values of the annealed coatings improved in comparison with the as-deposited counterparts. This is mainly because after annealing, the amorphous structure of the coatings transformed to a tougher crystalline coatings with Ni, Ni_3P and intermetallic NiTi phases. It is also observed that for a given Ti content, the L_{C1} value of the coating annealed at 700 ℃ was higher than that of the coating annealed at 800 ℃. The reason is that the strength of coating annealed at 800 ℃ decreased in comparison with the coating annealed at 700 ℃ due to grain coarsening at the higher temperature. Furthermore, the highest L_{C1} value was reached on the 15.2 wt% Ti content Ni-P-Ti coating annealed at 700 ℃, which is 5 times higher than that of as-deposited Ni-P. This can be attributed to the fact that this coating had the highest content of NiTi intermetallic particles without agglomeration. Another reason is that the 15.2 wt% Ti content Ni-P-Ti coating annealed at 700℃ had higher metallurgical bond strength between the particles and the Ni-P matrix after annealing in comparison with the as-deposited coating, due to the diffusion or reaction between the Ti particles and the Ni-P matrix. In addition, after annealing, the Ti particles transformed to the superelastic NiTi, which improved the toughness of the coating as a result of transformation toughening mechanism.

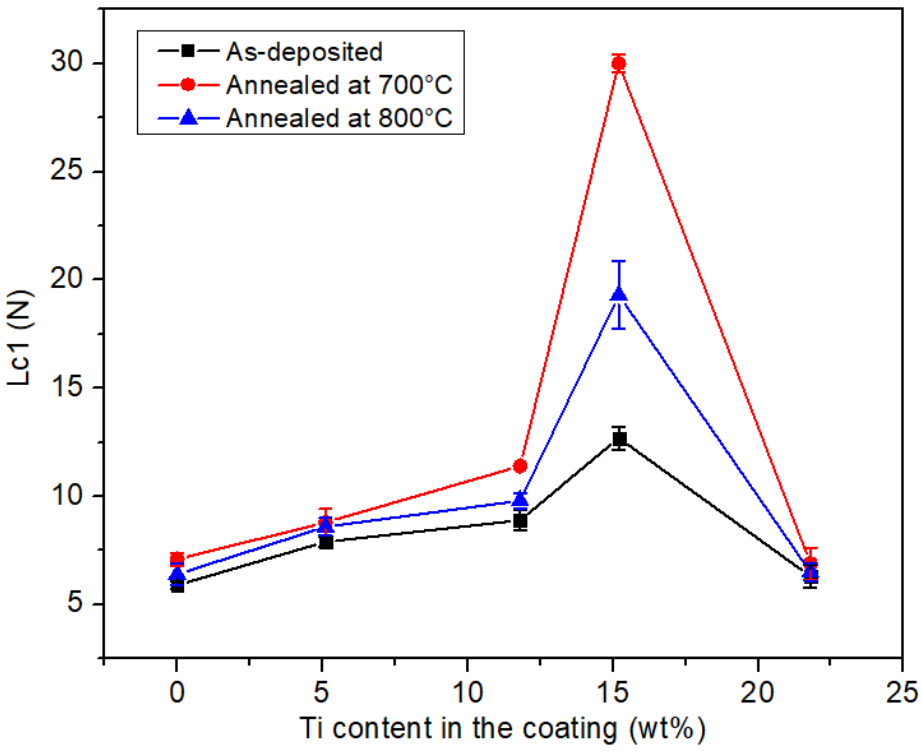

Figure 4-26 The L_{C1} values of as-deposited and annealed Ni-P and Ni-P-Ti coatings

In order to investigate the toughening mechanisms of annealed 15.2 wt% Ti content Ni-P-Ti coating during scratch tests, SEM and EDS investigations were carried out. Crack deflection, crack bridging, and crack shielding induced by NiTi intermetallic particles are observed on the scratch track. In addition, to confirm the probability for the transformation toughening to occur, the mean contact pressure during the scratch testing process was computed using Hertzian contact theory for the elastic contact between a spherical indenter and an elastic half-space, determined by equations 3.27-3.40 (Chapter 3). The radius of the indenter tip is 200 µm. Assuming v_1=0.25, E_1=55 GPa for the coating [60], and v_2=0.20, E_2=1050 GPa for the diamond spherical indenter [140]. The mean contact pressure for the scratch tests was found to be 5.85 GPa for the maximum applied scratch load (44.1 N). It is reported that the stress required to induce the martensitic phase transformation of NiTi alloy is in the range of 100-400 MPa at 25 °C [24, 141, 142], depending on the composition and heat treatment history of the NiTi alloy. Hence, the mean contact pressure for the

scratch tests is higher than the stress required for phase transformation of NiTi alloy. Therefore, transformation toughening from the NiTi particles can be expected to occur.

SEM micrograph of crack deflection induced by a particle and EDS point spectra locations on the particle are shown in Figure 4-27. As can be seen, cracks struck a particle, then changed their propagating paths, which moved along the interface between the NiTi intermetallic particle and the Ni-P matrix. EDS results of the particle in Figure 4-27 (b) are presented in Table 4-4. Based on Figure 4-27 and Table 4-4, the schematic of crack deflection induced by a NiTi intermetallic particle can be seen in Figure 4-28, the arrow is the crack propagation direction. After annealing, the Ti particle transformed to multiple phases, the order of different phases from the inner layer to the outer layer of the particle is Ti, Ti_2Ni, NiTi and $TiNi_3$ in sequence, as also confirmed by other researchers [31, 143]. Crack deflection is one of the critical toughening mechanisms. It is well established that the crack deflection could locally lower the crack driving force by the deviation of the crack path. This decrease in crack driving force could significantly improve the toughness and reduce the growth rates of the subcritical crack [144]. The fracture toughness may increase by up to a factor of 3 due to crack deflection by the incorporation of ductile particles, as has been reported for ceramic composite materials [145].

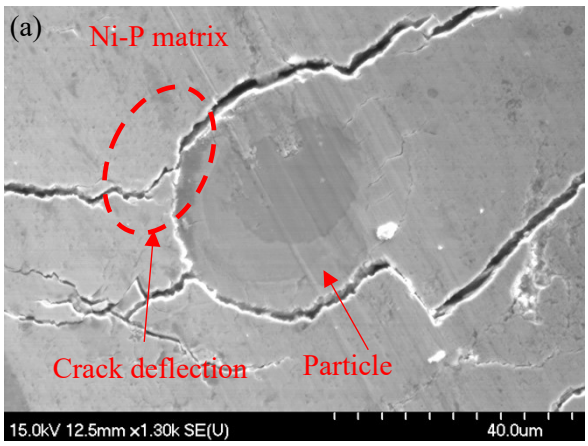

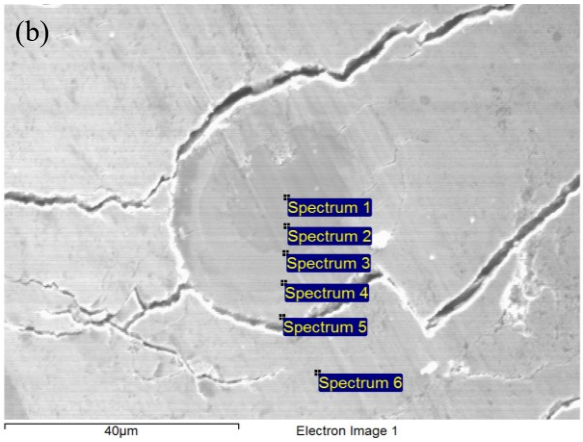

Figure 4-27 (a) SEM micrograph of crack deflection induced by a particle and (b) EDS point spectra locations on the particle

Table 4-4 EDS results of the particle in Figure 4-27 (b).

EDS	Ni at%	Ti at%	Possible phase
1	1.27	98.73	Ti
2	3.94	96.06	Ti
3	34.87	65.13	$NiTi_2$
4	44.33	55.67	NiTi
5	76.89	23.11	Ni_3Ti
6	98.67	1.33	Ni

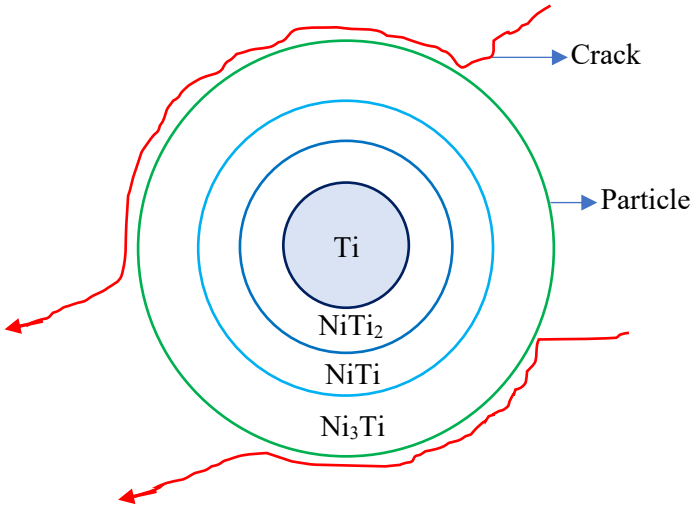

Figure 4-28 Schematic of crack deflection induced by a NiTi intermetallic particle

Figure 4-29 shows SEM micrograph of crack bridging induced by a particle and the EDS point spectra locations on the particle. The EDS results of the particle in Figure 4-29 (b) are summarized in Table 4-5. From Figure 4-29 and Table 4-5, it is observed that a crack encountered an intermetallic NiTi particle, subsequently the crack tip propagated past the particle while the crack wake was bridged. Following that, the particle was pulled out from the Ni-P matrix, as schematically presented in Figure 4-30 based on Figure 4-29 and Table 4-5. The arrow in Figure 4-30 indicates the crack propagation direction. Crack bridging is one of the most important toughening mechanisms in ceramic matrix composite. Bartolome et al. [146] found that the increase in toughness value of mullite-molybdenum composite in comparison with mullite could be attributed to the crack bridging induced by the molybdenum particles. Because most of the far-field stress was transferred to develop the bridging, in order to advance the crack tip, higher applied stress intensities were required, which improved the toughness of the coating. This toughness improvement and similar toughening mechanism were also confirmed by several other studies [138, 147, 148].

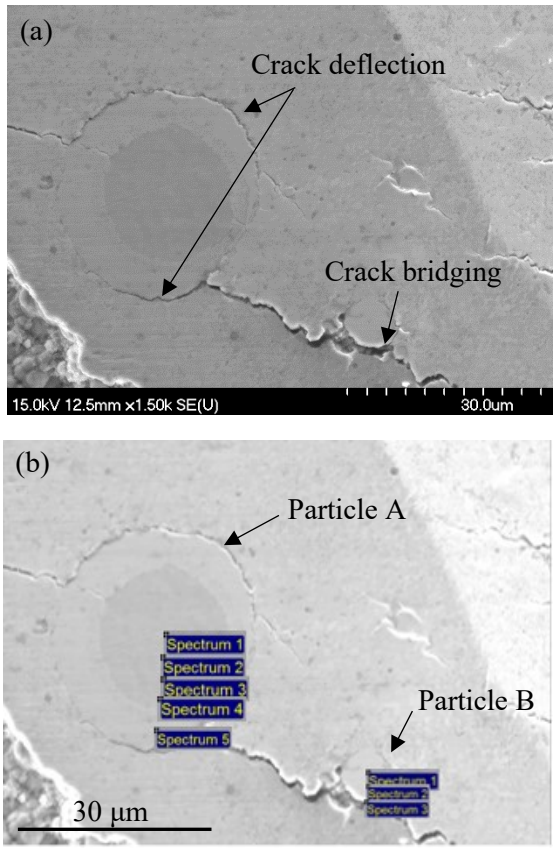

Figure 4-29 (a) SEM micrograph of crack bridging induced by a particle and (b) EDS point spectra locations on the particle

Table 4-5 EDS results of the particles A and B in Figure 4-29 (b)

Particle A				Particle B			
EDS	Ni at%	Ti at%	Possible Phase	EDS	Ni at%	Ti at%	Possible Phase
1	2.72	97.28	Ti	1	48.74	51.26	NiTi
2	32.48	67.52	$NiTi_2$	2	53.56	46.44	NiTi
3	52.41	47.59	NiTi	3	74.59	25.41	Ni_3Ti
4	54.85	45.15	NiTi				
5	75.64	24.34	Ni_3Ti				

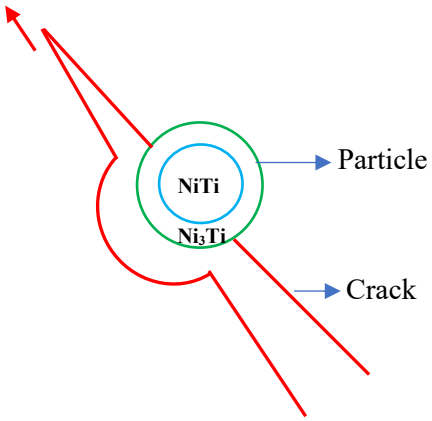

Figure 4-30 Schematic of crack bridging induced by an intermetallic NiTi particle

SEM micrograph of crack shielding induced by a particle and the EDS point spectra locations on the particle are shown in Figure 4-31. EDS results of the particle in Figure 4-31 (b) are listed in Table 4-6. Based on Figure 4-31 and Table 4-6, crack shielding by the particle is sketched in Figure 4-32, where the arrow indicates the crack propagation direction. As the crack encountered the particle, the driving energy of the crack propagation was absorbed by the particle and the crack stopped propagating due to the transformation toughening of the superelastic NiTi phase. The stress field in front of the propagating crack induced the NiTi phase in the particle to undergo martensitic phase transformation. The austenite phase in the particle transformed to the martensite phase. Accompanying with this phase transformation was the energy absorption near the crack tip, which lowered the driving force of the crack. In addition, the volume of the particle increased after the phase transformation [4]. This increased volume resulted in compressive stresses around the crack tip, which further reduced the driving force for crack propagation and subsequently decreased the stress intensity at the crack tip. Eventually, the crack lost the driving force and was shielded or arrested by the particle. The transformation toughening mechanism from the superelastic NiTi alloy has been proven to effectively improve the toughness of brittle materials [4, 149]. Furthermore, crack branching can also be observed in Figure 4-

32, where a microcrack branched out from a major crack, this microcrack was then deflected by the intermetallic NiTi particle and ultimately stopped propagating. Faber et al. [150] suggested that the stress around a crack tip can be relieved through microcracking which lowers the whole driving force of the crack. They also pointed out that the energy of a large crack can be consumed by branching fine cracks, consequently lowering the driving energy for the large crack propagation.

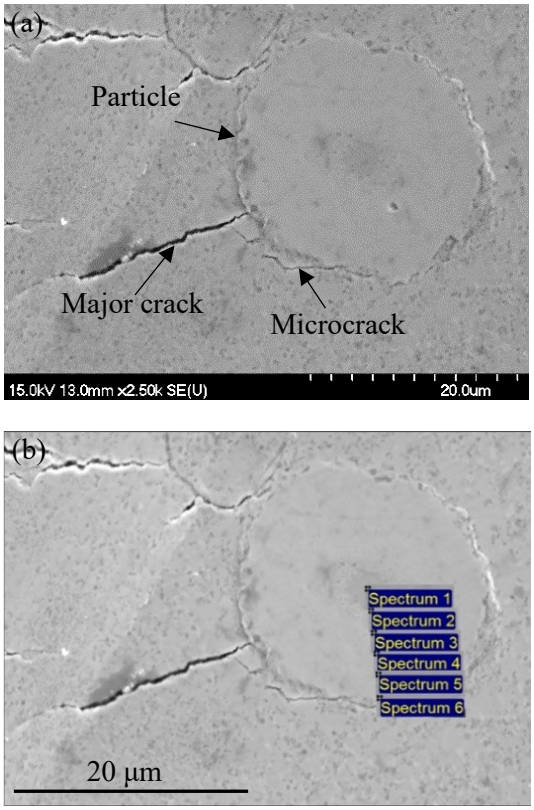

Figure 4-31 (a) SEM micrograph of crack shielding by a particle and (b) EDS point spectra locations on the particle

Table 4-6 EDS results of the particle in Figure 4-31 (b)

EDS	Ni at%	Ti at%	Possible Phase
1	4.36	95.64	Ti
2	33.75	66.25	$NiTi_2$
3	43.87	56.13	NiTi
4	45.36	54.64	NiTi
5	52.85	47.15	NiTi
6	74.66	25.34	Ni_3Ti

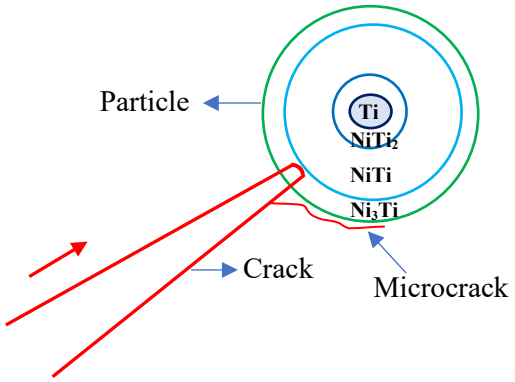

Figure 4-32 Schematic of crack shielding induced by a NiTi particle

Volume loss of constant load scratch testing on as-deposited and annealed coatings can be seen in Figure 4-33. The slope of volume loss against scratch passes curve represents the wear rate. The wear rates of constant load scratch testing on as-deposited and annealed Ni-P and Ni-P-Ti coatings are shown in Figure 4-34. The coefficient of friction (COF) of constant load scratch testing on as-deposited and annealed Ni-P and Ni-P-Ti coatings is shown in Figure 4-35. For each specimen, the COF of the coating was obtained by averaging the COF values of the 5 passes,10 passes, 20 passes and 40 passes of the scratch tests. From Figure 4-35, it is observed that the COF values of the coatings are found to be within a range of 0.10-0.25. The COF of the as-deposited coatings slightly increased with the increase of the Ti content in the coatings. However, the COF of the annealed coatings

decreased with the increase of the Ti content except for the 21.8 wt% Ti coating. Further, after annealing, for a given Ti content, the COF values of the annealed coatings are higher than that of the as-deposited coating.

From Figures 4-33 and 4-34, it can be observed that for the as-deposited coatings, the general trend is that the scratch resistance decreased with the increase of the Ti content. However, for the annealed coatings, except for the 21.8 wt% Ti content coating, the scratch resistance increased as the Ti content in the coatings increased as well. It is well known that hardness, elastic modulus and toughness are the main factors that affect the scratch resistance of materials [124]. The relationship between coating hardness and volume loss was proposed by Archard [151]. Archard gave the relationship between the volume loss V, applied load L, sliding distance S, wear coefficient K and hardness H of materials. The relationship expressed by the Archard is given by V= KLS/H. Therefore, high hardness improves scratch resistance of coatings [152]. For the as-deposited coatings, with the increase of the Ti content, the hardness of the coatings decreased, which resulted in the decrease of the scratch resistance of the coatings. However, for a given annealing temperature, except for the 21.8 wt% Ti content coating, the hardness of annealed coatings increased with the increase of Ti content. As a result, the scratch resistance of the annealed coatings improved as the Ti content increased. In addition, for a given condition, the 21.8 wt% Ti content coatings had higher wear rates in comparison with other Ti content coatings because of the agglomeration of particles in the coatings. It has been reported that the wear resistance of composite coatings deteriorated by the agglomerated particles during wear testing process because of the loss of the dispersion strengthening effect [124, 152, 153].

As can be seen in Figures 4-33 and 4-34, the scratch resistance of the annealed Ni-P coatings decreased dramatically because the hardness of the annealed Ni-P coatings decreased compared to the as-deposited Ni-P coating. Furthermore, the as-deposited Ni-P coating had the highest scratch resistance compared to the other as-deposited coatings. However, for the annealed coatings, the highest scratch resistance was obtained on the 15.2 wt% Ti content coating annealed at 700°C because it had highest hardness compared to the

other Ti content annealed coatings. The lowest wear rate (2.31 $\times 10^{-5}$ mm^3/pass) was reached on the 15.2 wt% Ti content coating annealed at 700 ℃, which was lower than the wear rate (2.81×10^{-5} mm^3/pass) of the as-deposited Ni-P coating.

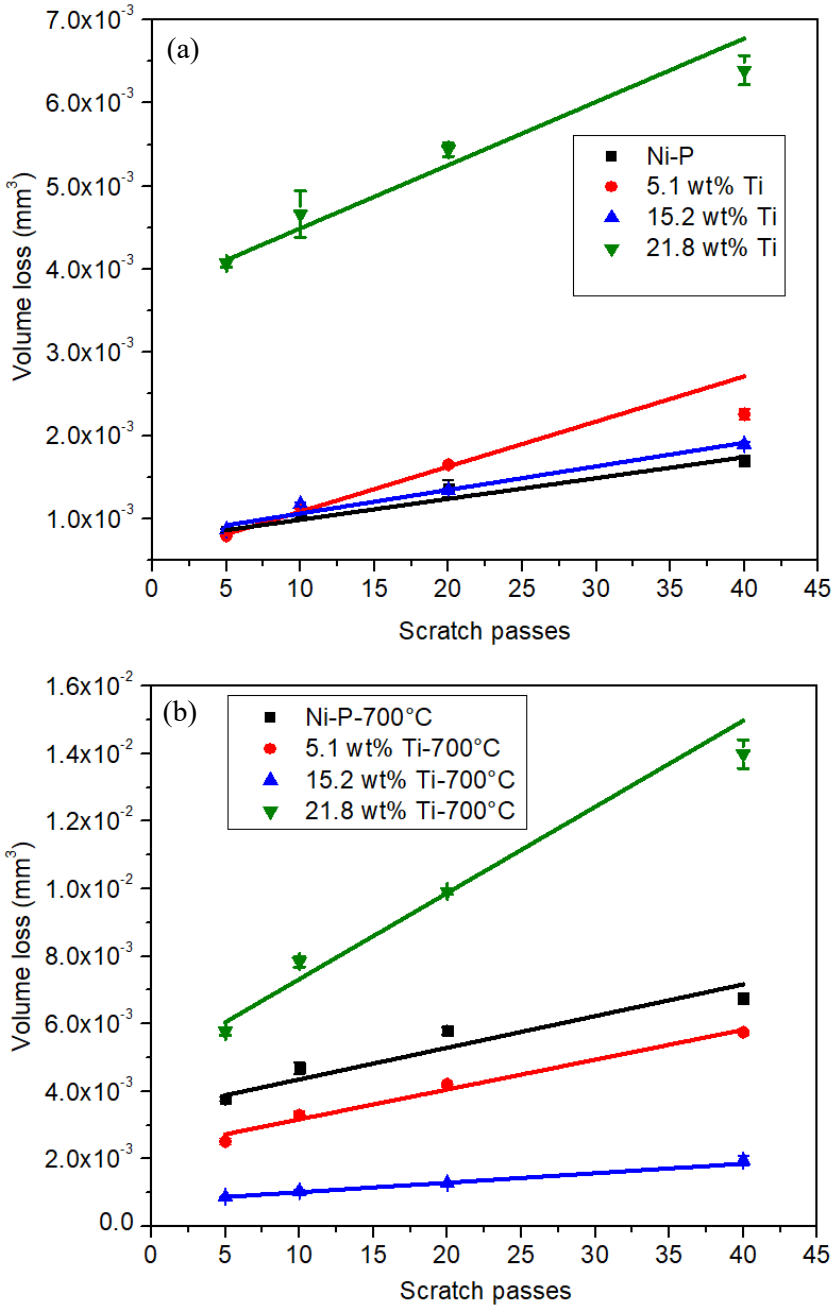

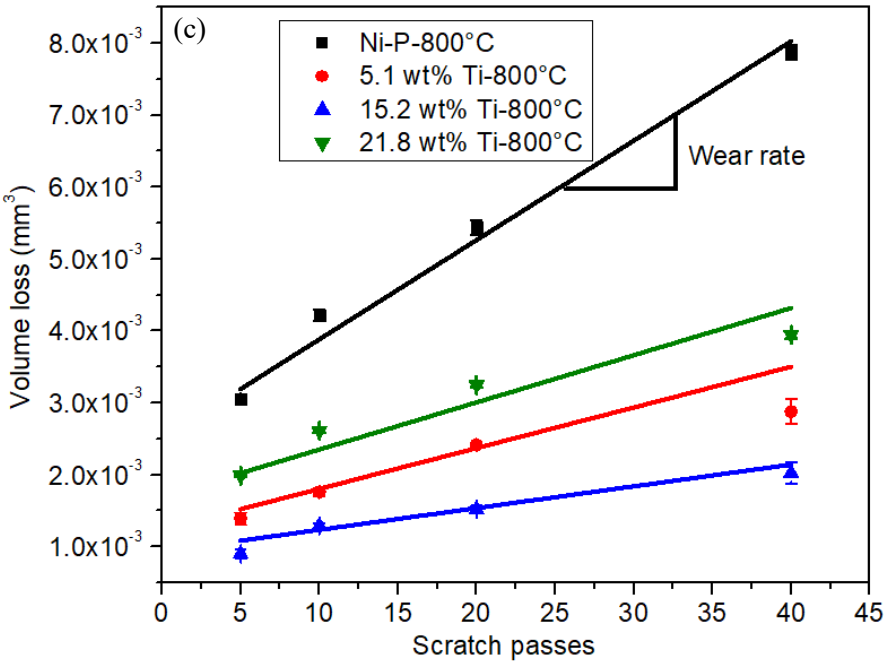

Figure 4-33 Volume loss of constant load scratch testing on as-deposited coatings as well as on coatings annealed at different temperatures: (a) as-deposited, (b) annealed at 700℃, (c) annealed at 800℃

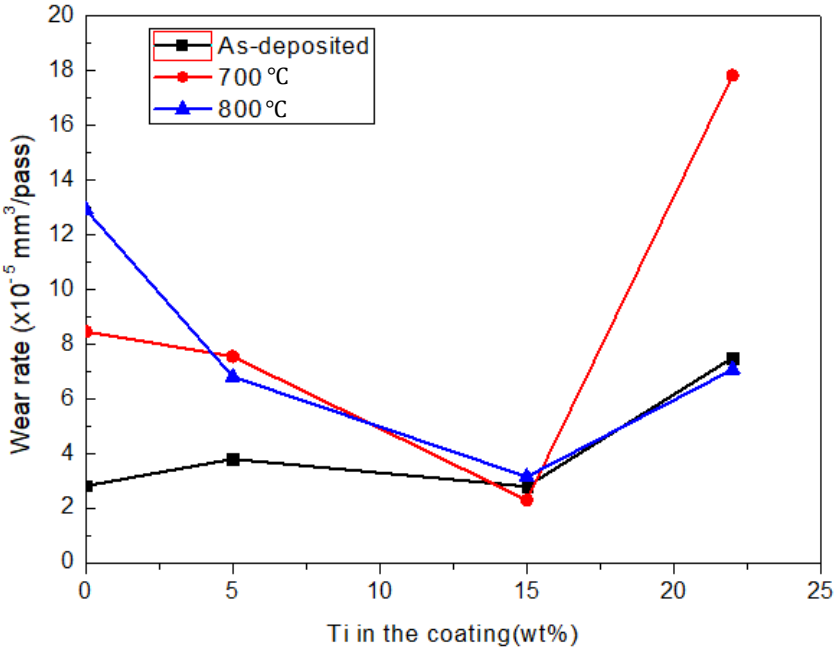

Figure 4-34 Wear rates of constant load scratch testing on as-deposited and annealed Ni-P and Ni-P-Ti coatings

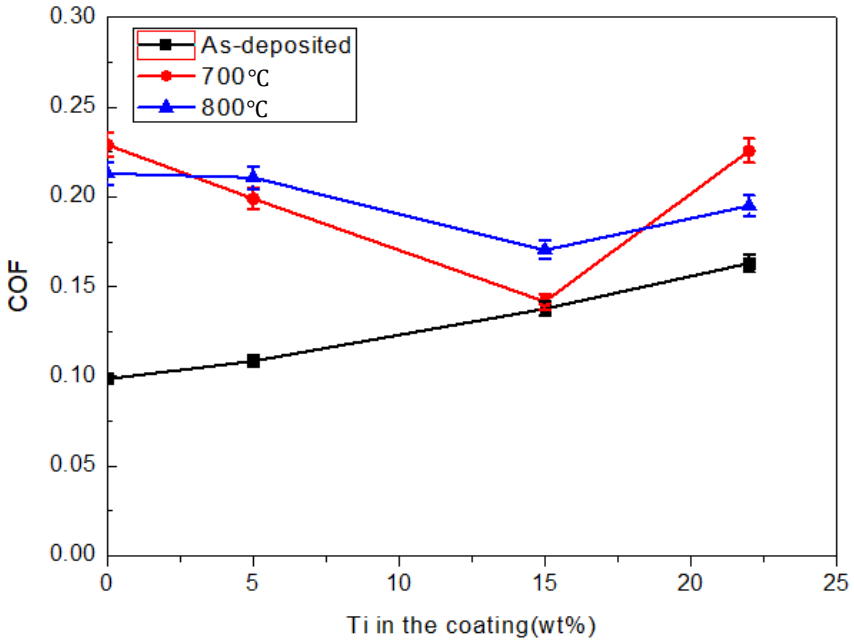

Figure 4-35 COF of constant load scratch testing on as-deposited and annealed Ni-P and Ni-P-Ti coatings

4.2.2 Coatings Annealed at 650 °C for 2 hours and Comparison

Representative optical micrographs of scratch tracks and initial cracks as well as corresponding AE signals for coatings annealed at 650 °C for 2 hours are shown in Figure 4-36. It is observed that initial crack size decreases as the Ti content increases. For annealed Ni-P coating, the initial crack crosses the scratch track, whereas only very fine initial crack is observed inside the scratch track for annealed 15.2 wt% Ti coating. These results are aligned with AE signals. As the Ti content increases, the intensity of AE signals decreases, which indicates that the energy released by cracking diminishes and cracking becomes less severe. In addition, under the maximum load (44.1 N), at the end of the scratch track (scratch direction: from left to right), cracks propagate outside of the scratch track for annealed Ni-P coating, whereas the cracks are restricted to inside the scratch track for annealed 5.1 wt% Ti coating. Furthermore, no obvious cracks are observed inside or

outside of the scratch track for annealed 15.2 wt% Ti coating under maximum load (44.1 N).

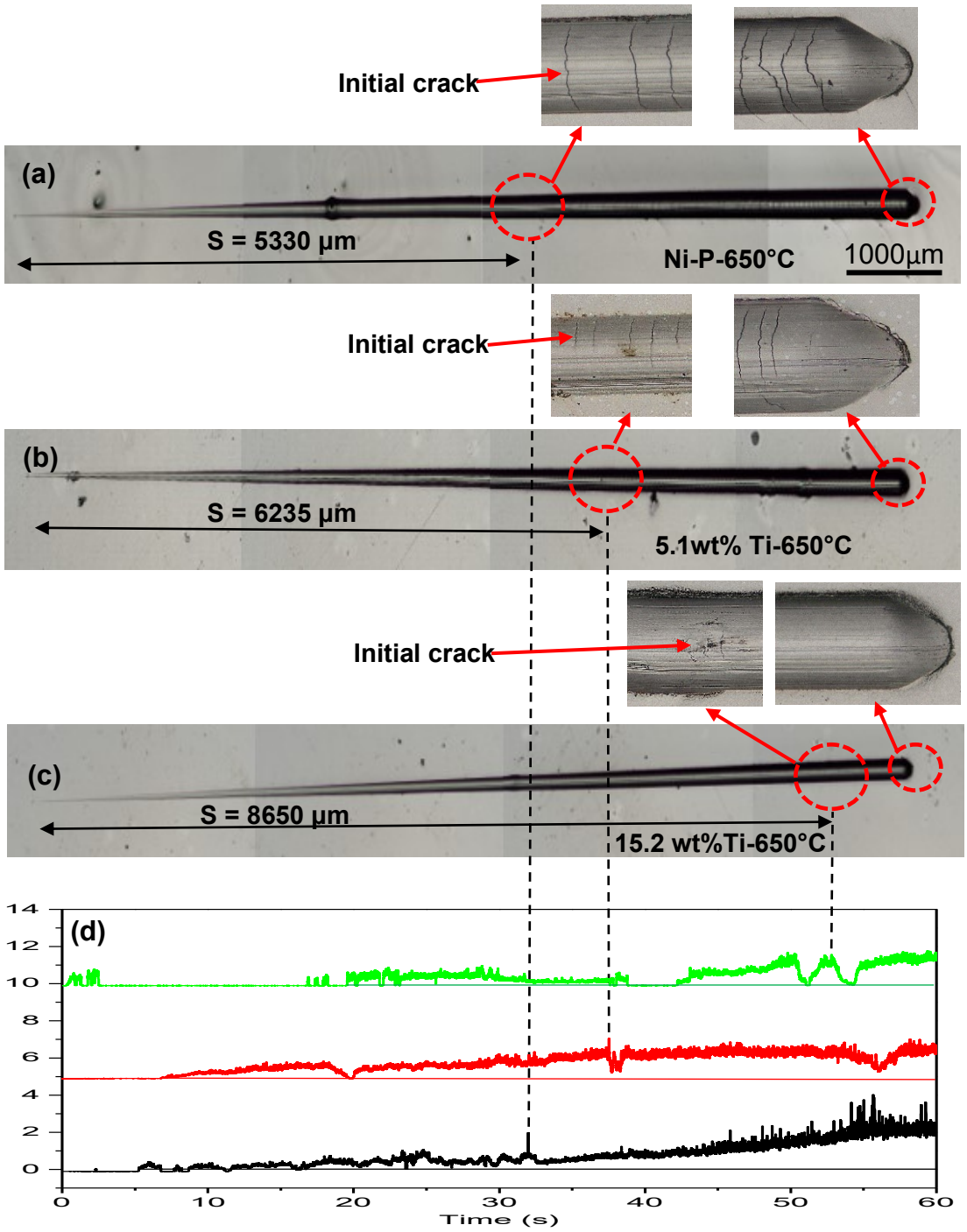

Figure 4-36 Representative optical micrographs of scratch tracks under increasing load (4.9 N-44.1N) for annealed coatings (650°C for 2 hours), (a) Ni-P-650°C, (b) 5.1 wt% Ti-650°C, (c) 15.2 wt% Ti-650°C and (d) corresponding AE signals (volts) for cracking

Scratch hardness is a measure of a material's resistance to dynamic surface deformation [154]. Scratch tests were conducted on API X100 steel substrate, as-deposited and annealed coatings according to the ASTM G171-03 [155] to evaluate the scratch hardness. The scratch hardness is given by [155]:

$$HS_P = \frac{8P}{\pi w^2} \qquad 4.8$$

Where, HS_P is the scratch hardness (GPa); P is the normal force (N) and w is the width of scratch scar (m).

The scratch hardness values of API X100 steel substrate, as-deposited and annealed coatings are shown in Figure 4-37. The error bars in Figure 4-37 are standard deviations. It is observed that API X100 steel has the lowest scratch hardness (3.08 GPa), whereas 11.8 wt% Ti coating annealed at 650 °C for 2 hours exhibits the highest scratch hardness (9.71 GPa). For as-deposited coatings, as Ti content increases, the scratch hardness decreases. This is mainly because the addition of relatively softer Ti particles into hard Ni-P matrix lowers the hardness of as-deposited composite coatings [64]. On the other hand, for a given annealing temperature, the scratch hardness values of annealed coatings rise with the increase in Ti content due to the precipitation and dispersion strengthening mechanisms. In addition, as the annealing temperature decreases, the scratch hardness increases. This is possibly because of Hall-Petch strengthening. As the annealing temperature drops, the grain size decreases, according to Hall-Petch relationship between grain size and strength, the scratch hardness (or strength) of annealed coatings increases [102].

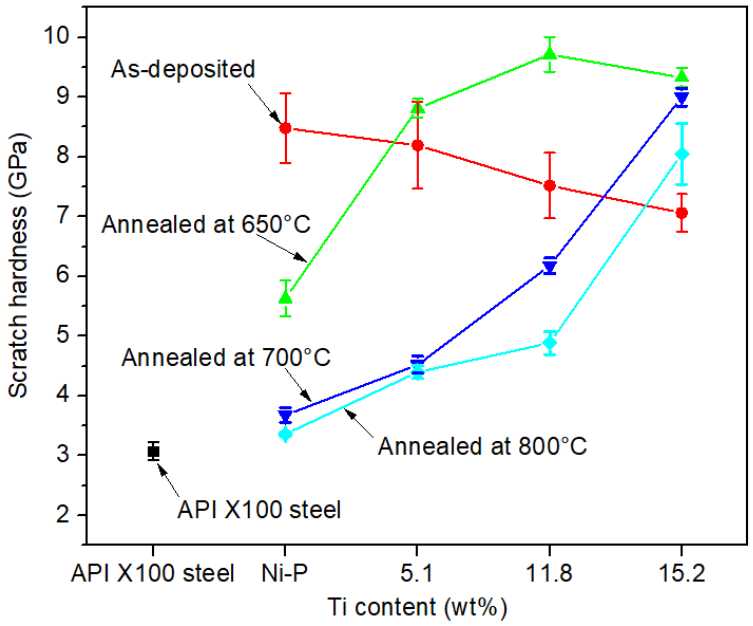

Figure 4-37 Scratch hardness of API X100 steel, as-deposited and annealed coatings

Initial crack load (L_{CI}) is the load required to initiate cracks during increasing load scratch test [106]. Initial crack load was determined using the equation 3.12 (Chapter 3). Initial crack loads of as-deposited coatings and coatings annealed at different temperatures are shown in Figure 4-38. As-deposited Ni-P coating has the lowest initial crack load (6.1 N), whereas 15.2 wt% Ti coating annealed at 650 °C for 2 hours possesses the highest initial crack load (38.6 N). The comparison of initial crack loads between as-deposited coatings and coatings annealed at 700 °C and 800 °C for 5 hours has been discussed in the previous section 4.2.1. Compared to coatings annealed at 700 °C and 800 °C for 5 hours, coatings annealed at 650 °C for 2 hours have much higher initial crack load. This is mainly because of the decrease in grain size and increase in amount of superelastic NiTi phases at lower annealing temperature and shorter annealing time.

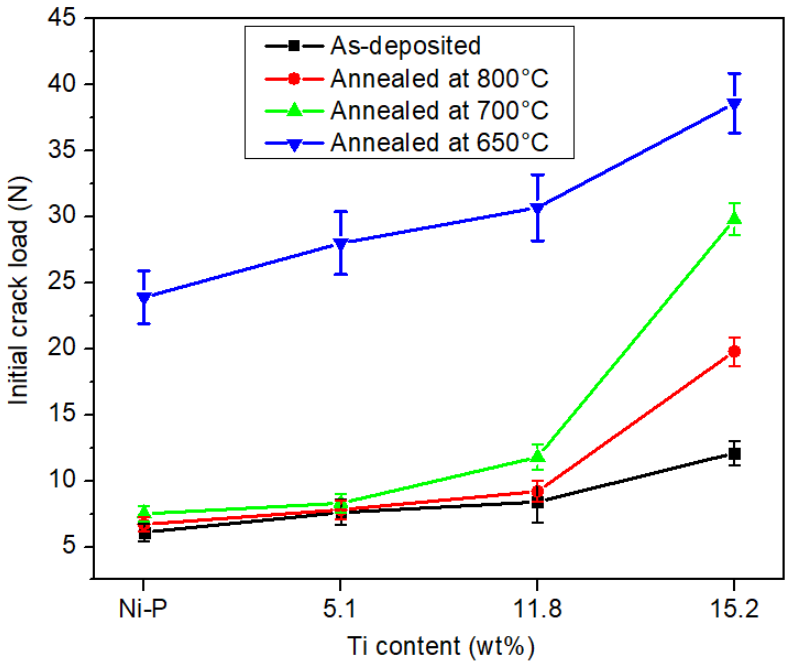

Figure 4-38 Initial crack loads of as-deposited coatings as well as coatings annealed at different temperatures

Since all the initial crack loads of as-deposited and annealed coatings are lower than 40 N, the load (40 N) was employed to perform the constant load scratch test. Under this load (40 N), all the as-deposited and annealed coatings has cracked, the fracture toughness can be determined by equations 3.14-3.16 (Chapter 3). The fracture toughness of as-deposited and annealed coatings are shown in Figure 4-39. As-deposited Ni-P coating has the lowest average fracture toughness value (7.7 MPa*$m^{1/2}$). This value is in agreement with the fracture toughness result acquired via single-edge notch tensile test (7.1 ± 0.6 MPa*$m^{1/2}$) [156]. The highest average fracture toughness (37.6 MPa*$m^{1/2}$) is achieved on the 15.2 wt% Ti coating annealed at 650 °C for 2 hours. This value is close to the fracture toughness of electrodeposited Ni-43wt% Co coating (38 MPa*$m^{1/2}$) [157] but lower than that of the pure Ni coating (53.93 MPa*$m^{1/2}$) [158] electrodeposited from a sulfamate bath. For as-deposited and annealed coatings, as Ti content increases, the fracture toughness rises owing to the ductile particles toughening. Compared to as-deposited coatings, the annealed coatings exhibit higher fracture toughness due to the crystallization and the formation of superelastic NiTi after annealing. In addition, as the annealing temperature increases, the

fracture toughness decreases due to the increase in grain size, which lowers the toughness of the annealed coatings. These results are well consistent with the results of initial crack load.

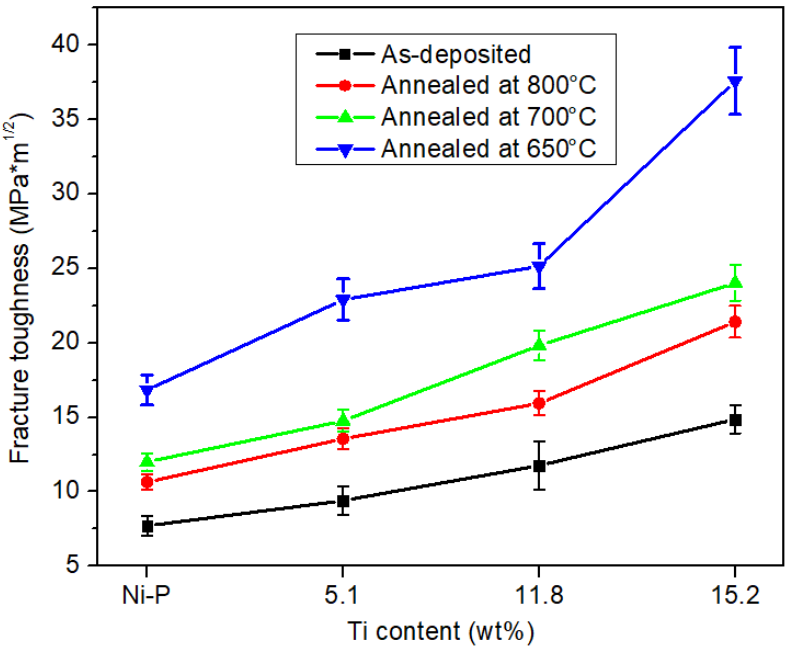

Figure 4-39 Fracture toughness of as-deposited and annealed coatings determined by constant load (40 N) scratch test

It has been observed that the annealed coatings have higher fracture toughness than as-deposited coatings (Figure 4-39). This is mainly because of the formation of superelastic NiTi within the composite coatings after annealing. NiTi alloy is well known for its high capability of absorbing impact or cracking energy due to martensitic phase transformation. Different toughening mechanisms observed inside the scratch track of 5.1 wt% Ti coating annealed at 650 °C for 2 hours (under a constant scratch normal load: 40 N) are shown in Figure 4-40. The black arrow indicates the direction of crack propagation. When a crack encounters a NiTi particle and attempts to pass through the particle, the crack wake is bridged by the particle. As the crack continues to propagate, the particle is pulled out from the Ni matrix (Figure 4-40 (a)), thereby lowering the driving force for crack propagation. After bridging, the cracking becomes less severe. Crack deflection attenuates the driving force for cracking by changing the direction of crack propagation. When a crack

approaches a NiTi particle, the interaction between the crack and the particle alters the path of crack propagating (Figure 4-40 (b)), which results in a loss in driving force for crack propagation. It is interesting to note that a crack is arrested by a NiTi particle in Figure 4-40 (c). When a crack encounters a NiTi particle, the stress at the crack tip induces martensitic phase transformation. Austenitic NiTi phase transforms to a detwinned martensitic phase with a large amount of superelastic deformation and an increase in the particle volume. The superelastic deformation consumes the energy for crack propagation; the increased volume results in a compressive field in the vicinity of the particle, which further reduces the driving energy for crack propagation. Eventually, the crack loses the driving energy and is arrested by the particle. The formation of superelastic NiTi considerably improves the toughness of the annealed composite coatings. As Ti content increases, the amount of NiTi phase rises, which results in improved fracture toughness.

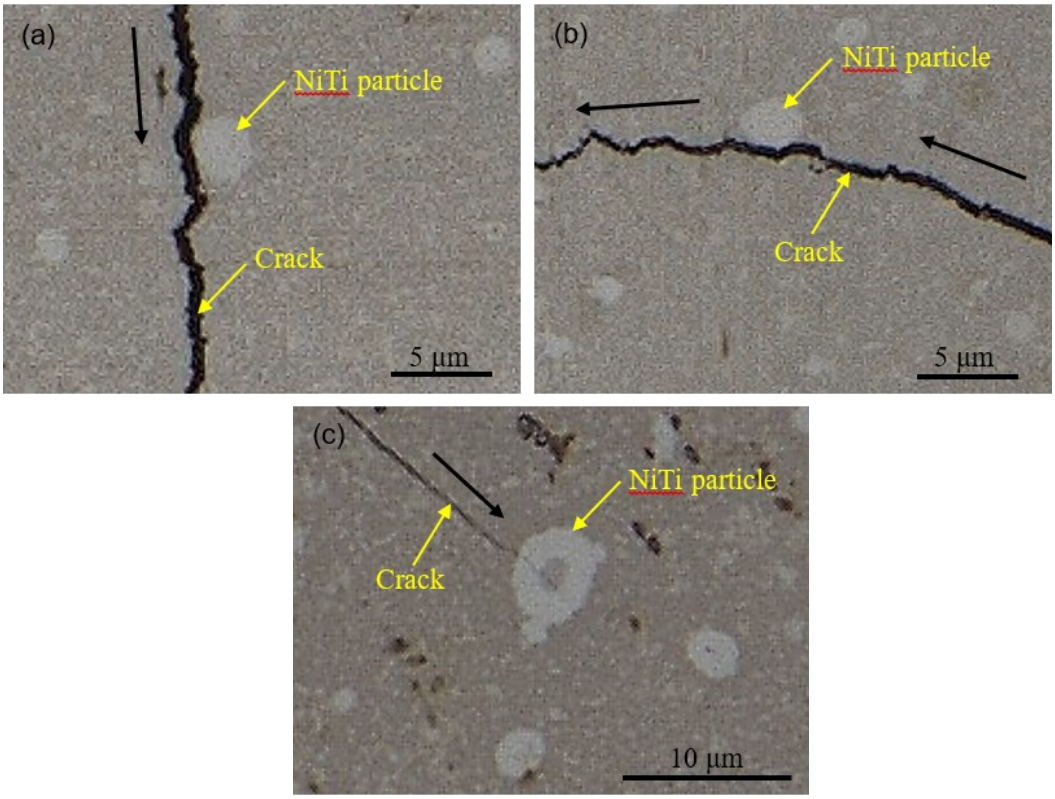

Figure 4-40 Different toughening mechanisms observed inside the scratch track of 5.1 wt% Ti coating annealed at 650 °C for 2 hours (under a constant scratch normal load: 40 N), (a) crack bridging, (b) crack deflection, (c) crack arresting

Multiple passes (5 passes, 10 passes, 20 passes and 40 passes) scratch tests under a constant load (9.8 N) were conducted on API X100 substrates and coatings annealed at 650 °C for 2 hours. Material volume loss was calculated using the equation 3.13 (Chapter 3). Here, the diameter of scratch indenter tip is 0.4 mm, the scratch length is 5 mm and the width of scratch scar was measured by optical microscope. The material volume losses calculated by the equation 3.13 against scratch travel distance of API X100 and coatings annealed at 650 °C for 2 hours are plotted in Figure 4-41 (a). Figure 4-41 (b) is a magnified figure of the marked part in Figure 4-41 (a). Because the length of a single scratch pass is 5 mm, the corresponding scratch distance values for 5 scratch passes, 10 scratch passes, 20 scratch passes, and 40 scratch passes are 25 mm, 50 mm, 100 mm, and 200 mm, respectively. Solid lines in Figures 4-41 (a) and (b) are the linear fitting lines. The fitting results are given in Table 4-7 . From Table 4-7, it can be seen that the lines fit well with the material volume loss data since all the R^2 values are larger than 90%. The slopes of fitting lines represent the wear rates (mm^3/mm) of materials. The wear rates of the coatings annealed at 650 °C for 2 hours are given in Figure 4-42.

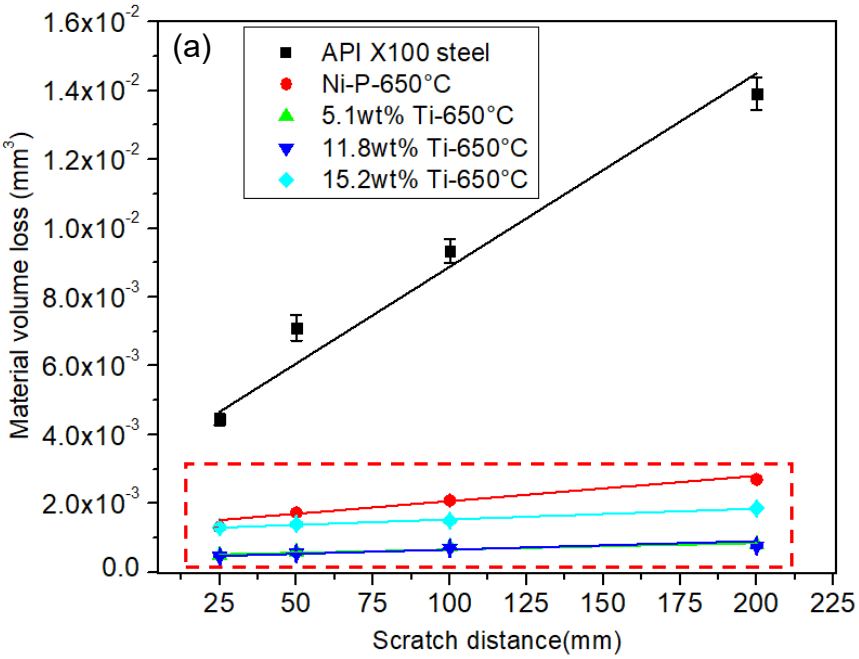

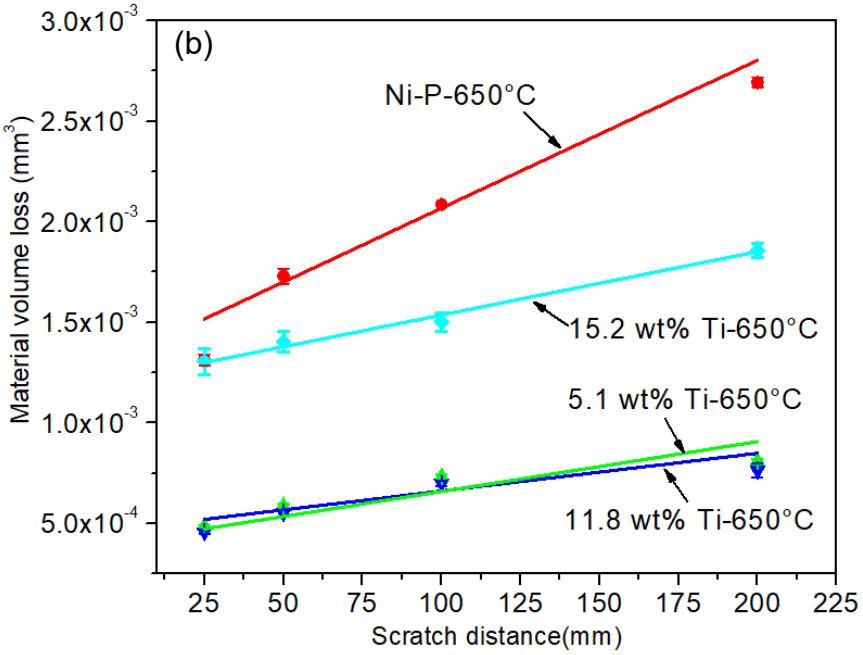

Figure 4- 41 (a) material volume loss of API X100 and coatings annealed at 650 °C for 2 hours as a function of scratch distance, (b) magnified figure of the marked part in (a)

Table 4-7 Linear fitting results of volume loss against scratch distance

Samples	Slope (mm^3/mm)	R^2
API X100	5.62×10^{-5}	96%
Ni-P-650°C	7.36×10^{-6}	92%
5.1wt% Ti-650°C	1.75×10^{-6}	93%
11.8wt% Ti-650°C	1.66×10^{-6}	94%
15.2wt% Ti-650°C	2.20×10^{-6}	99%

Figure 4-42 shows the wear rates of API X100, as-deposited coatings, and coatings annealed at different temperatures. The wear rates of as-deposited coatings as well as coatings annealed at 700°C and 800 °C for 5 hours are also shown in Figure 4-43 for comparative study. It is observed that API X100 exhibits the highest wear rate (5.62×10^{-5} mm^3/mm) due to its lowest hardness, whereas the 11.8 wt% Ti coating annealed at 650 °C for 2 hours has the lowest wear rate (1.66×10^{-6} mm^3/mm) due to the highest hardness and formation of superelastic NiTi within the coatings after annealing. In addition, for as-deposited coatings, the wear rate increases with increase in Ti content. On the other hand, for annealed coatings, the wear rate decreases as Ti content increases. Furthermore, compared to coatings annealed at 700°C and 800 °C for 5 hours, coatings annealed at 650°C for 2 hours have much lower wear rates. This is mainly because of the small grain size effect.

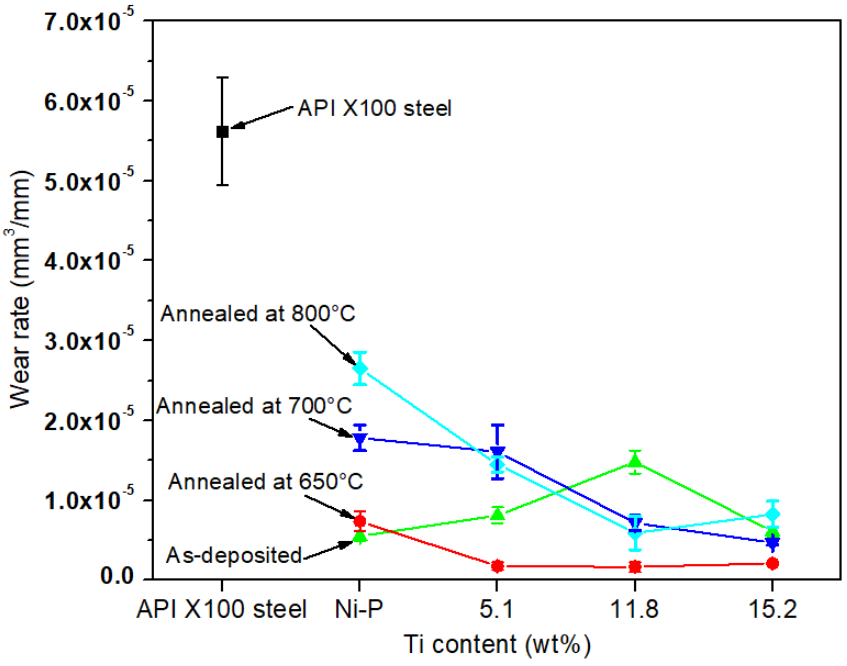

Figure 4-42 Wear rates of API X100, as-deposited coatings, and coatings annealed at different temperatures

4.2.3 Effect of Grain Size on Fracture Toughness

Fracture toughness as a function of grain size at different annealing temperatures is shown in Figure 4-43. It is observed that the fracture toughness of annealed Ni-P-Ti composite coatings decreases as the grain size increases. This increase in fracture toughness by reducing grain size can be ascribed to two major mechanisms. First, inter-grain sliding is produced at a crack tip due to the stress concentration near the tip, which results in edge dislocations at triple junctions of grain boundaries [159]. Second, edge dislocations initiated by stress concentration near a crack tip are arrested by the opposite grain boundaries [160]. These two mechanisms give rise to the blunting of cracks, which results in improved fracture toughness. Therefore, grain boundaries act as barriers in crack growth, resulting in blunting or arresting of cracks, which improve the fracture toughness. In addition, it is found that the fracture toughness of Ni increases with decrease in grain size until the grain size reaches 20 nm, then it becomes a constant [161]. In the present study, the grain size of Ni matrix is larger than 20 nm, fracture toughness increases as the grain size decreases due to the blunting effect of grain boundaries to microcracks.

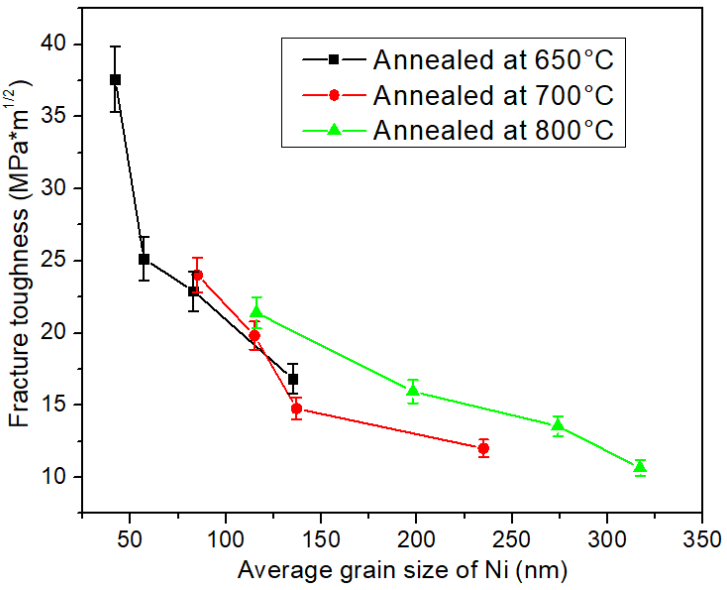

Figure 4-43 Fracture toughness as a function of grain size of Ni

4.2.4 Effect of Grain Size on Scratch Resistance

Wear rates as a function of grain sizes of Ni and Ni_3P are shown in Figure 4-44. The wear rates of annealed coatings decrease as the grain sizes of Ni and Ni_3P drops. For Ni matrix, the relationship between the strength (or hardness) and grain size is following Hall-Petch relationship [102]:

$$\sigma_y = \sigma_0 + kd^{-1/2} \quad (4.9)$$

Here, σ_y is the yield strength; σ_0 and k are constants, and d is the average grain size. From the equation 4.9, it is clear that as the grain size decreases, the yield strength (or hardness) increases. Therefore, in present study, the reduction in grain size not only promotes the toughness but also improves the strength of the annealed composite coatings.

Ni_3P precipitates serve as barriers to impede the motion of dislocations, which improves the strength of annealed coatings. When a moving dislocation encounters Ni_3P precipitates, it can not cut through them since the precipitates are much stronger than the Ni matrix. Therefore, the dislocation must bow between the Ni_3P precipitates. Eventually, a dislocation loop is left around each precipitate. The stress (τ) required for this bowing process is given by [162]:

$$\tau = \frac{2Gb}{l} \quad (4.10)$$

Here, G is the shear modulus of Ni matrix, b is the Burgers vector and l is the average distance between precipitates. For a given Ti content, as the grain size of Ni_3P decreases, the amount of Ni_3P precipitates increases, which results in a reduction in distance (l). According to equation 4.10, the stress required to bow the dislocation increases with the reduction in distance l, which gives rise to increased strength.

It is known that the scratch and wear resistance is dependent on hardness, strength and fracture toughness [124]. In general, materials having high hardness and fracture toughness exhibit high scratch and wear resistance. In the present study, as the annealing temperature

decreases, the grain size of Ni drops, which improves both the strength and fracture toughness of the Ni matrix. In addition, the grain size of Ni_3P decreases as the annealing temperature drops, which further increases the strength of the annealed coatings. High hardness and fracture toughness significantly contribute to the improvement of scratch and wear resistance.

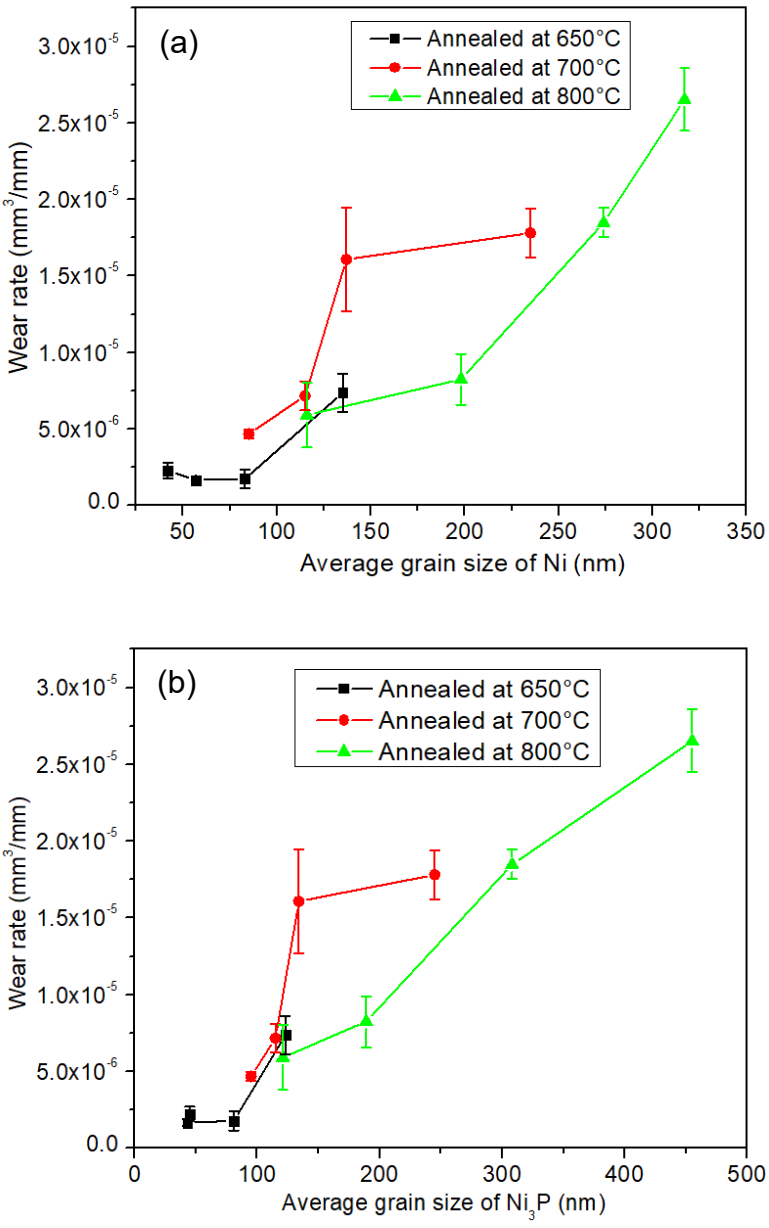

Figure 4-44 Wear rates as a function of grain sizes of (a) Ni and (b) Ni_3P

Since the coatings annealed at 650 °C for 2 hours have higher toughness, scratch and wear resistance compared to the coatings annealed at 700 °C and 800 °C for 5 hours, the following study will focus on the coatings annealed at 650 °C for 2 hours.

4.3 Nanoindentation Behavior of Coating Annealed at 650 °C

4.3.1 Nanoindentation Behavior

In order to confirm the superelastic effect on annealed Ti particles, Nanoindentation tests were conducted on annealed Ti particles and Ni-P matrix. Representative nanoindentation locations and corresponding load-depth curves of annealed 5.1 wt% Ti coating are shown in Figure 4-45. The nanoindentation tests were performed from the outside (Ni-P matrix) to the inside of an annealed Ti particle (Figure 4-45, indents: 1-5). It is observed that the size and the depth of indent increase as indentation moves from the outside to the inside of the particle. This indicates that the hardness decreases from the outside to the inside of the annealed particle. In addition, the load-depth curve 5 shows significant elastic recovery during the unloading process compared to the other curves.

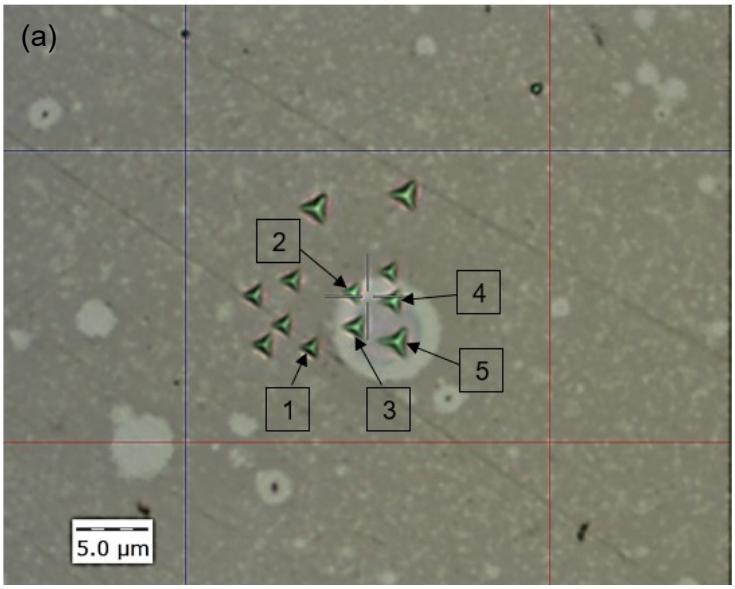

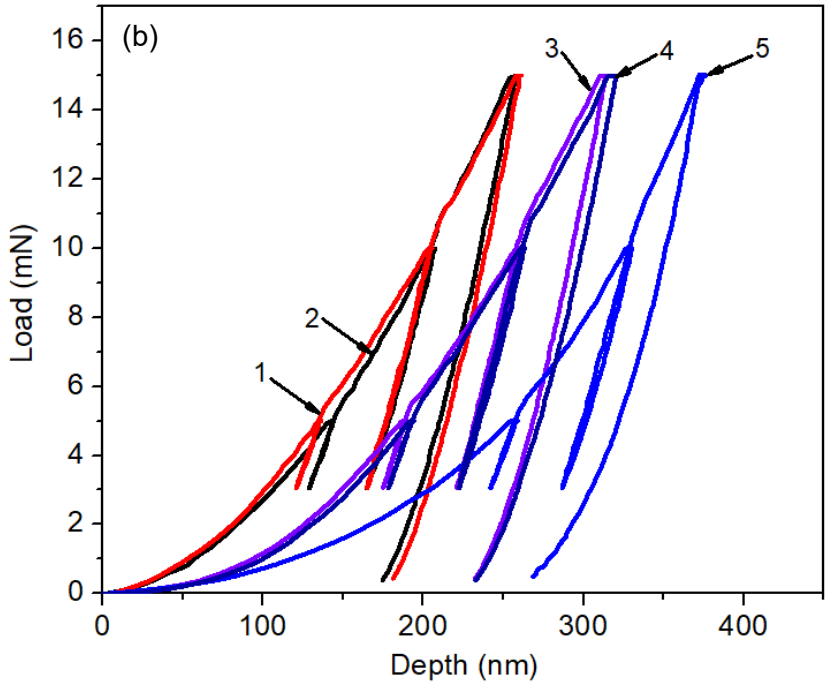

Figure 4-45 (a) representative nanoindentation locations and (b) corresponding nanoindentation load-depth curves of annealed 5.1 wt% Ti coatings

By comparing the nanoindentation locations (Figure 4-45 (a)) with EDS line scan and point scan locations (Figures 4-17 and 4-18), the different phases under nano-indent at different nanoindentation locations can be determined. As the indentation depth increases, the stress field may extend into neighboring phases. Therefore, to reduce the influence of neighboring phases on the nanoindentation testing results, the testing results (recovery ratio, hardness, and Young's modulus) acquired at the lowest applied load (5 mN) were chosen as representative results. The representative results are given in Table 4-8. The errors in Table 4-8 are the standard deviations of testing results (at 5 mN load) on three different particles. The recovery ratio was calculated by dividing the area under unloading curve to the total area under loading curve. It is observed that the recovery ratio increases

and the nanoindentation hardness decreases from the location 1 to the location 5 due to the presence of NiTi phase.

Table 4-8 Nanoindentation locations in Figure 4-46 (a) and corresponding possible phases nanoindentation tested on

Nanoindentation locations	Recovery ratio (%)	Nanoindentation hardness (GPa)	Possible phases nanoindentation tested on
1	31.5 ± 1.4	12.5 ± 0.3	Ni-P matrix
2	32.6 ± 0.8	13.7 ± 0.5	Ni_3Ti+Ni-P matrix
3	35.4 ± 1.9	8.1 ± 0.3	Ni_3Ti+NiTi
4	38.5 ± 1.5	7.0 ± 0.4	Ni_3Ti+NiTi
5	47.8 ± 2.3	3.4 ± 0.3	NiTi

The comparisons of Young's modulus (E) , hardness (H), and recovery ratio values derived from nanoindentation tests of annealed Ni-P matrix, Ni_3Ti, and NiTi (this study) with other studies are given in Tables 4-9, 4-10, and 4-11, respectively. The errors in Tables 4-9, 4-10, and 4-11are the standard deviations of testing results (at 5 mN load) on three different particles. From Table 4-9, the E and H values of annealed Ni-P coatings acquired from other studies are in a range of 191-233 GPa and 11-15 GPa, respectively. The E and H values obtained in the present study (nanoindentation location 1) are 220.7 ± 5.7 GPa and 12.5 ± 0.3 GPa, respectively, which are comparable to other studies. The E and H values of Ni_3Ti (nanoindentation location 2) are in agreement with other studies (Table 4-10). The E and H values of superelastic NiTi in the present study are 92.1 ± 8.3 and 3.4 ± 0.3 GPa, which are consistent with other studies (Table 4-11 E: 73-105 GPa, H: 2.4-4.4 GPa). The recovery ratio of superelastic NiTi phase is 47.8 ± 2.3 %, which is comparable to the values (36-52%) obtained in studies [163-166], but lower than the value (62.5%) acquired in another study [167] due to the different preparation methods and various heat treatment processes.

Table 4-9 Comparison of E and H values of annealed Ni-P matrix (nanoindentation location 1) with other studies measured by nanoindentation

Studies	E value (GPa)	H value (GPa)	h_{max} (nm)	Annealed temperature (°C)
This study	220.7 ± 5.7	12.5 ± 0.3	143.6 ± 11.5	650
Chen et al.[168]	230.4	13.5	150.0	500
Sribalaji et al.[169]	191.9	14.9	50.0	600
Salicio-Paz et al.[170]	220.6	11.1	180.0	400
Tien et al. [171]	233.0	12.3	150.0	500
Valentini et al. [172]	203.0	12.2	180.0	400

Table 4-10 Comparison of E and H values of Ni_3Ti (nanoindentation location 2) with other studies measured by nanoindentation

Studies	E value (GPa)	H value (GPa)
This study	262.9 ± 7.5	13.7 ± 0.5
Kulo et al.[173]	245.0	/
Cao et al. [174]	249.6	/
Yang et al. [175]	260.0	13.5

Table 4-11 Comparison of E, H, and recovery ratio values of superelastic NiTi (nanoindentation location 5) with other studies measured by nanoindentation on bulk NiTi alloys

Studies	E value (GPa)	H value (GPa)	h_{max} (nm)	Recovery ratio (%)
This study	92.1 ± 8.3	3.4 ± 0.3	258 ± 15	47.8 ± 2.3
Cameron et al. [167]	80.5	3.9	250	62.5
Laplanche et al. [176]	80.0	2.4	800	/
Micklich et al. [177]	98.0	3.0	200	/
Shastry et al. [164]	/	/	300	50.6
Wang et al. [165]	73.0	/	600-1000	42.0-52.0
Xu et al. [166]	73.7-92.8	2.5-4.4	80-110	32.5-48.5
Raju et al. [178]	85.0-105.0	3.8-4.4	261-312	31.0-40.0
Liu et al. [163]	/	3.5	380-550	36.0-47.0

4.3.2 The Origin of the High Recovery Ratio of NiTi Phase

It has been found that NiTi phase has high recovery ratio. This is mainly because of stress-induced reversible martensite phase transformation. The hardness measured on NiTi phase is equal to 3.4 ± 0.3 GPa at the lowest applied load (5 mN), which could be employed to represent the mean contact stress during nanoindentation test since the hardness was calculated using the equation 3.17 ($H = F_t / A$). It is known that the stress required to induce a martensitic phase transformation in superelastic NiTi alloy is in a range of 100-400 MPa at 25 °C [25, 142, 179], depending on the exact composition and heat treatment history of NiTi alloy. As a result, the mean contact stress at the applied load of 5 mN is higher than the required stress for the phase transformation. Therefore, during loading, the austenitic NiTi phase transforms to a detwinned martensitic phase along with a large recoverable superelastic strain. Then during the unloading, the detwinned martensitic phase transforms back to the austenitic phase accompanied with large strain recovering. For superelastic NiTi phase, the strain energy during loading is absorbed to induce martensitic phase transformation and stored in martensite variants, which is then consumed by the reverse phase transformation during unloading with large strain recovery [180]. On the other hand, for Ni matrix and Ni_3Ti, in order to relieve the strain energy during loading, plastic deformation occurs, which is unrecoverable [181]. This explains why NiTi phase has much higher recovery ratio than Ni matrix and Ni_3Ti.

4.4 Bending and Tensile Behavior

4.4.1 Bending Behavior

Bend tests were conducted on substrate, as-deposited, and annealed bilayer samples (coated samples). An acoustic emission sensor was used to record the changes in acoustic emission energy. Energy spikes associated with crack formation was detected by the acoustic emission sensor. The force associated with the first spike in acoustic emission curve was defined as first crack force. First crack force can be measured by superimposing the force-displacement and acoustic emission curves as seen in Figure 4-46. Compared to the substrate, a localized drop in bending force can be observed in the coating-substrate bilayer system, which is associated with the acoustic energy spike, providing evidence of crack formation. In addition, the first crack force of the as-deposited 11.8 wt% Ti coating is higher than that of as-deposited Ni-P coating. This means that the required force to initiate a crack on the as-deposited Ni-P-Ti coating is higher in comparison with the as-deposited Ni-P coating.

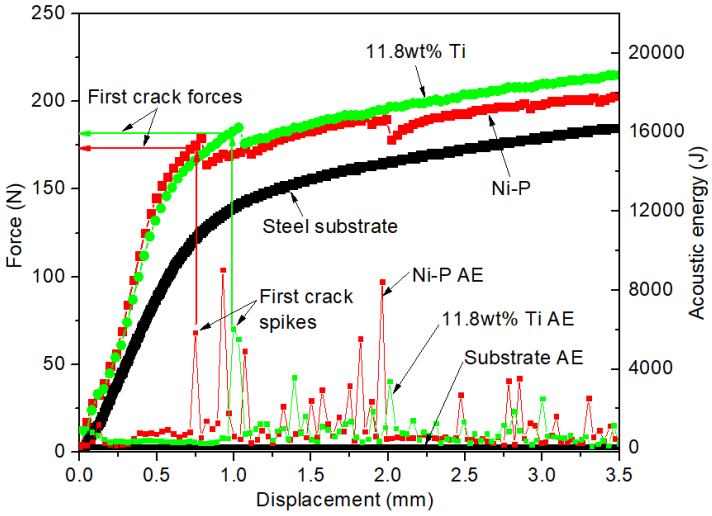

Figure 4-46 Representative force-displacement and acoustic emission data collected during bend tests of as-deposited coatings and substrate

The force-displacement and first crack force associated with the acoustic emission from bend tests on as-deposited coatings and annealed coatings can be seen in Figure 4-47. From Figure 4-47, for as-deposited or annealed coatings it can be observed that the first crack force increased with the increase in Ti content. Fracture morphology was studied using optical microscopy on bending test specimens at the maximum displacement (7 mm). Fracture morphology of as-deposited Ni-P coating and annealed 15.2 wt% Ti coating is shown in Figure 4-48. Large cracks and delamination are observed in the as-deposited Ni-P coating (Figure 4-48 (a)). From the cross-section view in Figure 4-48 (c), coating delamination can be seen in the as-deposited Ni-P coating. The delamination is associated with the sudden decrease of bending force found in the force-displacement curves shown in Figure 4-47. On the other hand, compared to the as-deposited Ni-P coating, no coating delamination or large cracks are observed in the annealed 15.2 wt% Ti coating shown in Figure 4-48 (b) and (d). The only observed phenomena are microcracks with a major crack width of 1.5-4 μm as shown in Figure 4-48 (b). Therefore, the optical microscopy observations on the bend specimens agree with the results of the first crack force shown in Figure 4-47. From the cross-section view of the annealed coating in Figure 4-48 (d), the diffusion between the coating and substrate may have occurred at the interface during annealing, resulting in improved interface strength of the annealed coating.

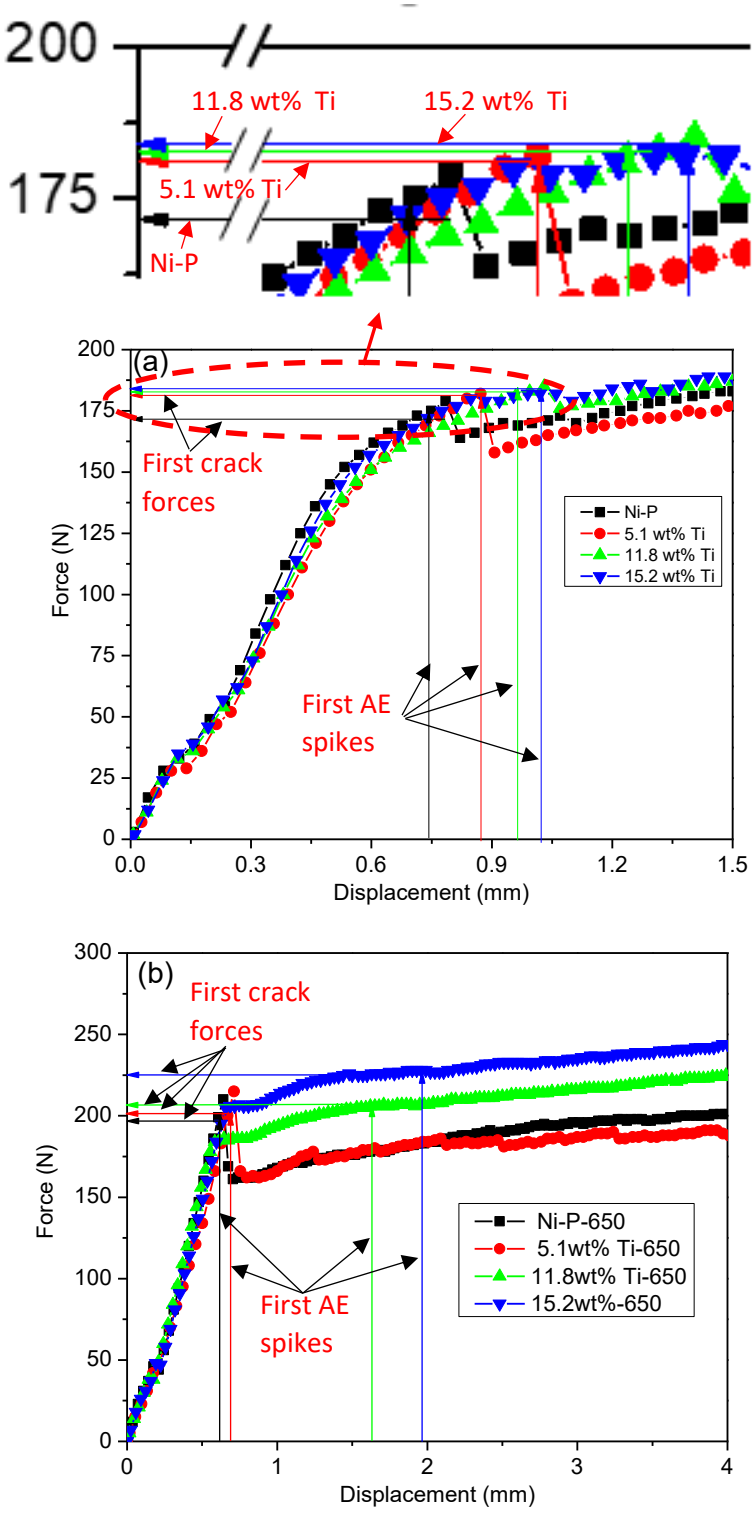
200
175
11.8 wt% Ti
15.2 wt% Ti
5.1 wt% Ti
Ni-P
(a)
First crack forces
First AE spikes
Force (N)
Displacement (mm)
Ni-P
5.1 wt% Ti
11.8 wt% Ti
15.2 wt% Ti
(b)
First crack forces
First AE spikes
Force (N)
Displacement (mm)
Ni-P-650
5.1wt% Ti-650
11.8wt% Ti-650
15.2wt%-650

Figure 4-47 Representative force-displacement and first crack force associated with acoustic emission of bend tests on (a) as-deposited coatings and (b) annealed coatings

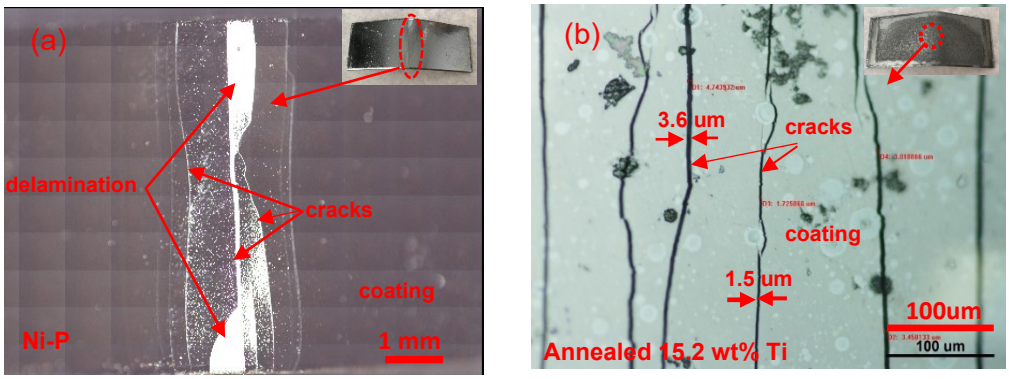

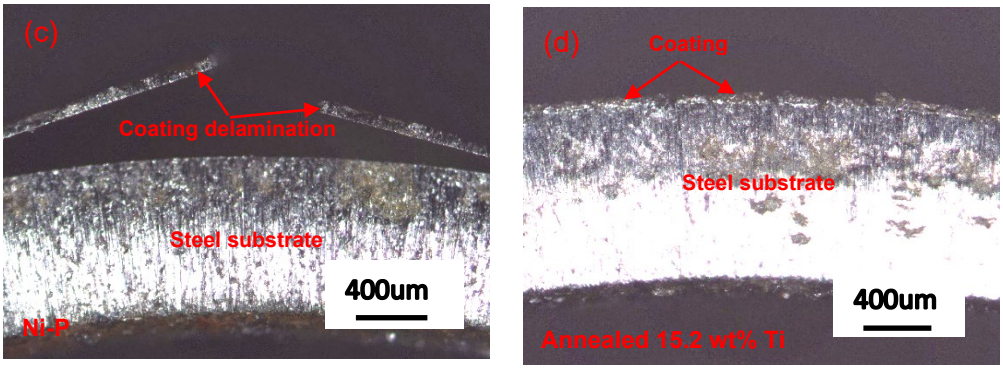

Figure 4- 48 Representative fracture morphology of as-deposited Ni-P coating as well as 15.2 wt% Ti coating annealed at 650°C after bend testing. (a) (b) surface view and (c) (d) cross-section view

4.4.2 Tensile Behavior of Standalone Coatings.

Figure 4-49 shows tensile stress-strain curves of as-deposited and annealed standalone coatings (thickness: approximately 100 μm). For the as-deposited coatings, the tensile strain increased with the increase of the Ti content. The same trend can also be observed on annealed coatings. In addition, as the Ti content increased, the fracture strength improved. To investigate the fracture morphology of coatings, optical microscope was adopted. Representative tensile cross-section fracture morphology of an as-deposited Ni-P coating and an annealed 15.2 wt% Ti coating is shown in Figure 4-49. Typical brittle

fracture morphology can be observed on an as-deposited Ni-P coating (Figure 4-50 (a)). The cross-section of an as-deposited Ni-P coating after the tensile test is observed to be perfectly flat without any signs of plastic deformation, seen in Figure 4-50 (a). On the other hand, annealed 15.2 wt% Ti shows limited plastic deformation (dimples), seen from Figure 4-50 (b), which is consistent with the stress-strain curve shown in Figure 4-49.

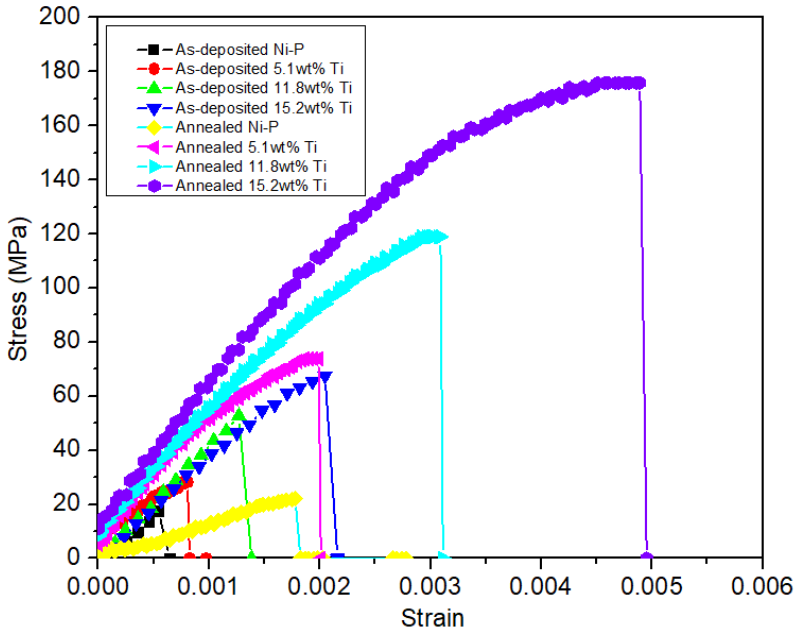

Figure 4-49 Representative tensile stress-strain curves of as-deposited standalone coatings as well as annealed standalone coatings at 650 °C

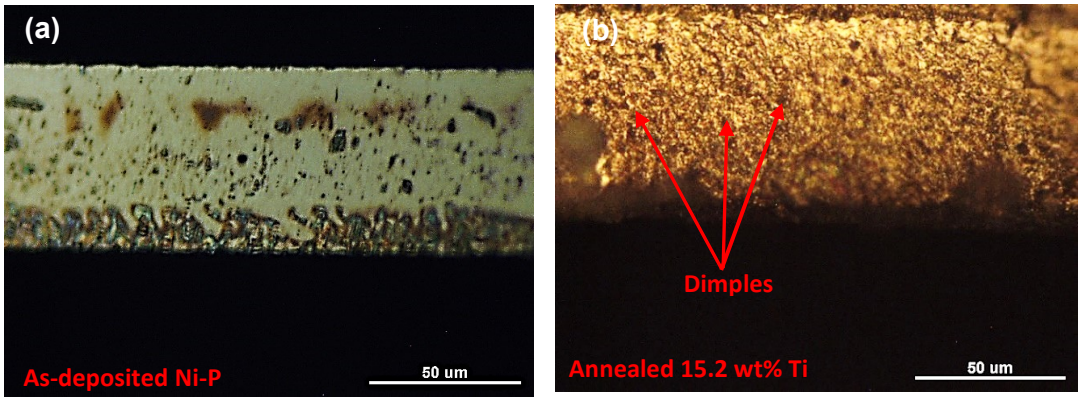

Figure 4-50 Representative tensile cross-section fracture morphology of (a) as-deposited Ni-P coating as well as (b) 15.2 wt% Ti coating annealed at 650 °C

4.4.3 Mechanical Properties of Coatings

A basic but important mechanical property of materials is Young's modulus; it indicates a material's resistance to elastic deformation, which is also a critical parameter used for computing elastic deflections. The Young's modulus for the composite coating is associated with the slope of the elastic deformation portion of the force-displacement and stress-strain curve for the bend and tensile tests, respectively. After the bend tests, the Young's moduli of the coatings were calculated using Equation 3.24 (chapter 3). On the other hand, the Young's moduli of the coatings determined from the tensile tests were obtained by computing the slope of the initial linear portion of the stress-strain curve. The Young's moduli of as-deposited and annealed coatings acquired from the bend and tensile tests can be seen in Figures 4-51 (a) and (b) respectively. From Figure 4-51 (a), it is observed that the Young's moduli of the as-deposited coatings decrease with an increase in Ti content. The reason for this decrease is that the Young's modulus of the Ti particles is lower than that of the Ni-P matrix, which decreases the composite coatings' Young's modulus [64]. However, the Young's moduli of the annealed coatings improve as the Ti content increases. The reason is that the annealed composite coatings contain Ni_3Ti precipitates which have higher Young's modulus compared to the annealed Ni-P matrix [182]. Therefore, the Ni_3Ti precipitates improve the annealed composite coatings' Young's modulus. The trend observed from the bend tests can also be seen from the tensile tests (Figure 4-51 (b)). In addition, it should be noted that the Young's moduli obtained from the bend tests are higher at around 170 GPa compared to the tensile tests due to the influence of the steel substrate. Although the Young's moduli are different, the trends between the as-deposited and annealed coatings are consistent between the two testing methods. Furthermore, the Young's modulus of as-deposited Ni-P coating determined from the tensile test is 42 GPa, which is in agreement with other studies (40-55 GPa) [12, 60,

183]. The Young's moduli of annealed Ni-P-Ti coatings are in a range of 35-80 GPa, which are comparable to other reported Ni-P based composite coatings (40-100 GPa) [61, 184].

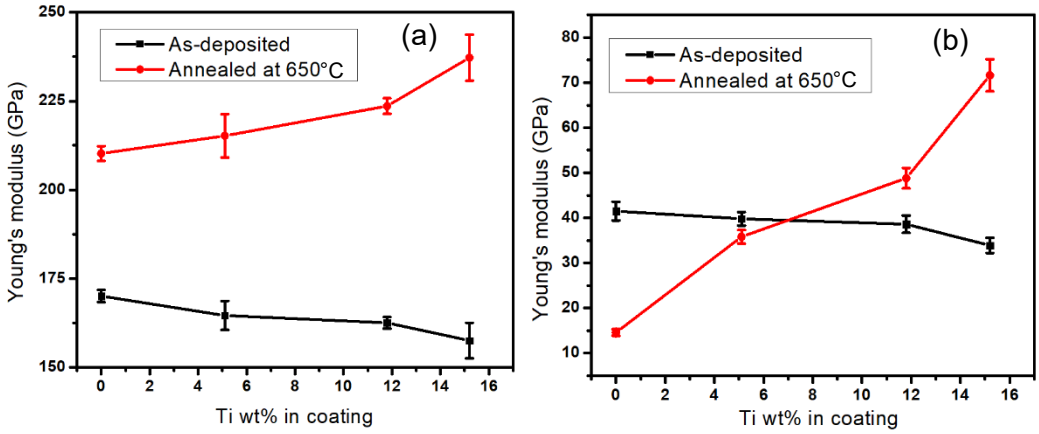

Figure 4-51 Young's moduli of as-deposited and annealed coatings acquired from (a) bend tests and (b) tensile tests

Toughness is the ability to absorb energy before material fracture and is a very important mechanical property of materials. Toughness is a property that indicates a material's resistance to fracture when a crack is present, which is especially critical for brittle coatings such as Ni-P. The toughness of the coating can be determined from both the bend and tensile tests. For the bend test, the toughness is the area under the force-displacement curve up to the first crack force. For the tensile test, the toughness is the area under the stress-strain curve up to the fracture point. The toughness of the as-deposited and annealed coatings acquired from the bend and tensile tests is shown in Figures 4-52 (a) and (b) respectively. From Figure 4-52 (a), it is noted that the toughness of the as-deposited and annealed coatings increases with an increase in Ti content in the coatings. A similar trend can be also observed in Figure 4-52 (b). This increase can be attributed to the ductile particles toughening mechanisms, including crack deflection, crack bridging, and microcracking. In addition, it is important to note that the toughness of the annealed coatings is improved compared to the as-deposited coatings. The reasons for this are twofold. First, after annealing, the initially amorphous coatings transformed to a crystalline structure which increased the probability of plastic deformation, resulting in enhanced

toughness. Secondly, the dominant phase in NiTi intermetallic particles is the NiTi austenite phase after annealing, which can undergo phase transformation under stress. During the phase transformation process, the driving energy for crack initiation and propagation was absorbed, which considerably improved the toughness of the coating by the transformation toughening mechanism [185]. Furthermore, the toughness of the coatings acquired from the tensile tests is different from that obtained from the bend tests. Three reasons contribute to this difference. Firstly, toughness is determined at the point of the first crack for the bend tests whereas toughness is computed up to the fracture point of the standalone coatings for the tensile tests. Secondly, the bend tests were conducted on the coating-substrate bilayers, where the effect of the steel substrate on the coatings' toughness cannot be ignored. On the other hand, the tensile tests were performed on the standalone coatings with no effect of the steel substrate. Lastly, the toughness results come from two different measure methods. Although the toughness is different, the trends between the as-deposited and annealed coatings are consistent between the two testing results.

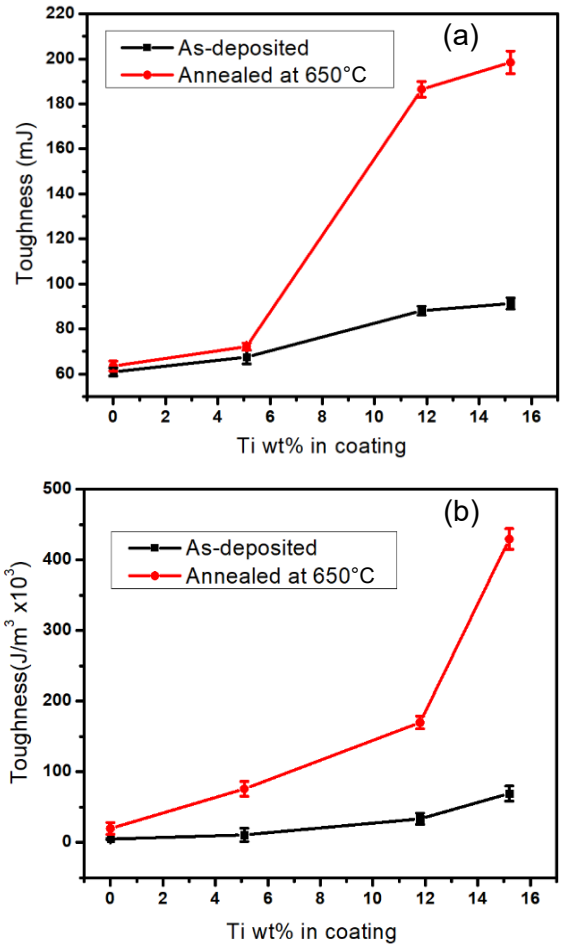

Figure 4-52 Toughness of as-deposited and annealed coatings acquired from (a) bend tests and (b) tensile tests

To investigate the different toughening mechanisms operating in coatings, optical microscopy was adopted to observe the annealed 15.2 wt% Ti specimen after bend testing. Figure 4-53 shows different toughening mechanisms that occurred after a bend test in an annealed 15.2 wt% Ti specimen. Crack deflection can be seen in Figures 4-53 (a), (b), and (e), in which a crack propagated towards a NiTi particle which altered the crack propagation path causing a loss in the crack driving force. Crack bridging is observed in Figures 4-53 (c), (d), and (f), where a crack passed through a NiTi intermetallic particle and the stress at the crack tip attempted to deform the particle. The particle could either be

pulled out of the Ni-P matrix or prevent the crack from advancing, which is dependent upon the crack size, as seen in Figures 4-53 (d) and (c), respectively. Microcracks can be observed in Figures 4-53 (a), (b), and (e) where they branch out from a major crack. This branching reduces the driving force of the major crack and the propagation of the microcracks are stopped by the NiTi particles through transformation toughening mechanism. When a major crack or microcrack propagates toward a NiTi particle as seen in Figure 4-53 (c), the stress at the crack tip induces a NiTi phase transformation. The austenitic NiTi phase transformed to a detwinned martensitic phase with a large superelastic deformation and energy absorption. This phase transformation allows for the reduction in the crack driving force where the cracks are subsequently arrested by the particles, as seen in Figures 4-53 (a), (b), (c), and (e). These toughening mechanisms interacted with each other which operated synergistically and simultaneously to improve the toughness of the annealed composite coatings considerably compared to the as-deposited coatings. It is believed that these toughening mechanisms function more effectively at higher particle content to improve the toughness of composite materials [138, 139]. For this reason, the annealed 15.2 wt% Ti coating has the highest toughness compared to the other coatings with less Ti content.

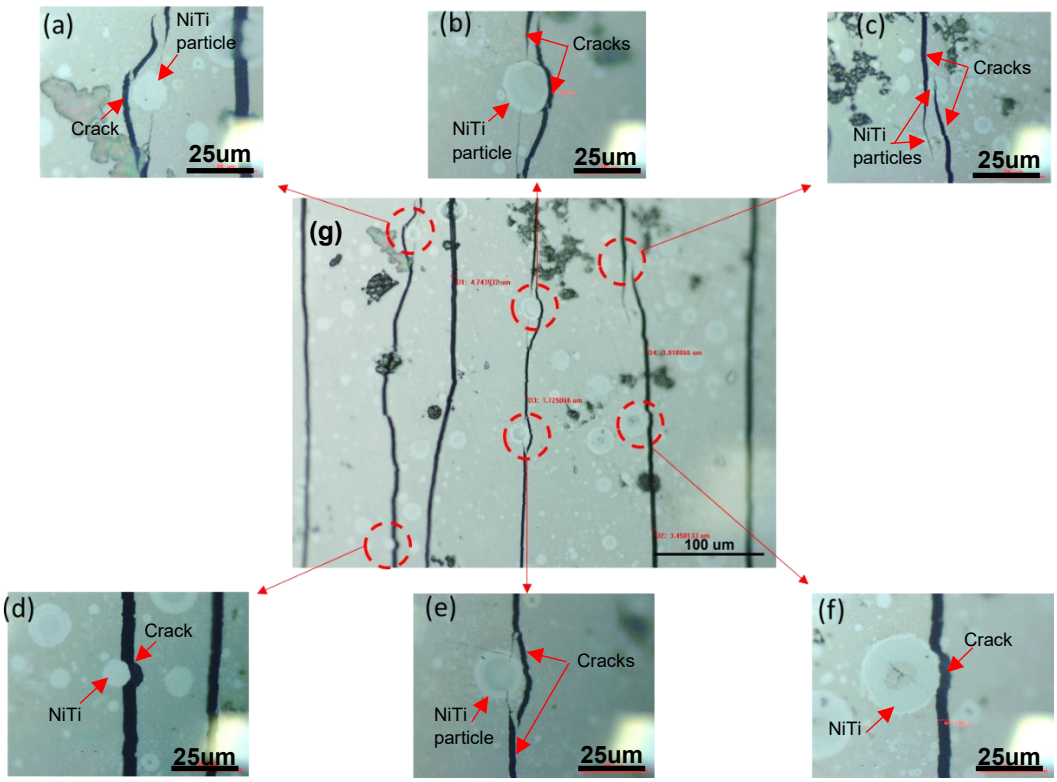

Figure 4-53 Different toughening mechanisms in 15.2 wt% Ti specimen annealed at 650°C after bend test

Fracture strength is another critical property to investigate for brittle materials, termed as the stress at which the material fractures. Fracture strength is often measured with large variation [186] and is dependent upon the size and shape of the specimen, loading rate, test method, and environment [187]. For bend tests, fracture strength is calculated using equation 3.26 (Chapter 3). For the tensile test, fracture strength is the stress in the stress-strain curve at the fracture point. Fracture strength of as-deposited and annealed coatings acquired from bend and tensile tests can be seen in Figures 4-54 (a) and (b) respectively. From Figure 4-54 (a), it is observed that the fracture strength of the as-deposited and annealed coatings improved as the Ti content increased, which are consistent with the results obtained from the tensile tests, as seen in Figure 4-54 (b). The reason is that the toughening by particles operated more effectively as the Ti content increased. However, the fracture strength acquired from the bending tests is higher than that attained from the

tensile tests due to the different size of the specimens [187], different test methods [187], as well as the effect of the steel substrate on coatings required for the bend tests. Although the fracture strength is different, the trends between the as-deposited and annealed coatings are consistent between the two testing methods. In addition, it can be observed that the fracture strength of the coatings increased after annealing compared to the as-deposited coatings due to the crystallization of the coatings and the transformation toughening mechanism. Furthermore, it is noted that the fracture strength of the coatings acquired from the bend tests is found to be within a range of 300-550 MPa, which is in agreement with published results [2, 19]. However, the tensile strength (fracture strength) of the electroless Ni-P or Ni-P composite standalone coatings has rarely been reported due to the difficulties of preparing the standalone coatings.

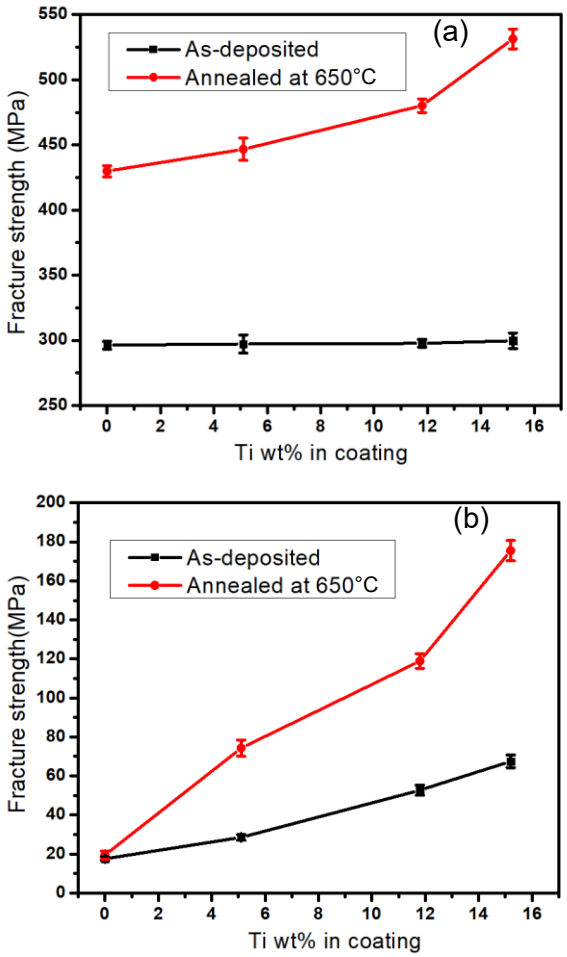

Figure 4-54 Fracture strength of as-deposited and annealed coatings acquired from (a) bend tests and (b) tensile tests

4.5 Coatings under Hertzian Contact

4.5.1 Hertzian Indentation Behavior

In order to investigate the indentation fracture behavior of the coatings, the indentation morphology was examined using optical microscopy. Combining the indentation test with acoustic emission allows for the first crack force to be determined. The spikes in an acoustic emission curve are associated with the formation of cracks. The force associated with the first spike in an acoustic emission curve is defined as the first crack force [2]. The load-displacement and acoustic emission curves as well as indentation morphology of the coatings are shown in Figure 4-55. Figure 4-55 (a) shows the load-displacement and acoustic emission curves of indentation testing for the as-deposited Ni-P coating, and Figures 4-55 (b) and (c) present the surface and cross-section views of the indent after indentation testing on the as-deposited Ni-P coating. From Figure 4-55 (a), the first crack force can be determined by superimposing the load-displacement curve with the acoustic emission curve. The first crack force determined from Figure 4-55 (a) is 176 N. This result is in line with the results obtained in previous studies [2, 19]. This indicates that the required indentation force to initiate a crack in the as-deposited Ni-P coating is 176 N. Radial cracks and coating delamination are observed at the edge of the indent, as shown in Figure 4-55 (b). Hertzian cracks and coating delamination are also seen from the coatings cross-section view, as shown in Figure 4-55 (c). Compared to as-deposited Ni-P coating, the first crack initiation occurred under a higher load of 320 N for the as-deposited 15.2 wt% Ti coating as determined from Figure 4-55 (d). In addition, from Figure 4-55 (d), it is observed that the amplitude of acoustic emission signal during the indentation testing process on the as-deposited 15.2 wt%Ti coating is lower than that of the as-deposited Ni-P coating; this suggests that the fracture energy released during the indentation process of the as-deposited 15.2wt%Ti coating is lower compared to the as-deposited Ni-P coating. Furthermore, the crack density and crack size diminish in comparison with the as-deposited Ni-P coating, as observed in Figures 4-55 (b) and (e). This reduction in crack density and crack size indicates the improved toughness of the as-deposited 15.2wt%Ti coating in comparison to the as-deposited Ni-P coating.

The load-displacement and acoustic emission curves as well as indentation morphology of the coatings annealed at 650°C are also summarized in Figure 4-55. From Figure 4-55 (g), the first crack load of indentation testing on annealed Ni-P coating was measured to be 208 N, which shows limited improvement compared to as-deposited Ni-P coating (176 N). The amplitude of acoustic emission for the first crack of indentation testing on the annealed Ni-P coating is a little lower than that of the testing on the as-deposited Ni-P coating, shown in Figure 4-55 (g). Radial cracks, Hertzian cracks and coating delamination are observed in the annealed Ni-P coating after indentation testing, shown in Figures 4-55 (h) and (j), respectively. On the other hand, the 15.2 wt% Ti coating annealed at 650°C exhibits the highest first crack force (986 N) and the lowest associated acoustic emission amplitude (28 dB) compared to other coatings, as observed in Figure 4-55 (j). Only very fine radial cracks are observed on the coating surface after indentation testing, seen in Figure 4-55 (k). These observations indicate that the 15.2 wt% Ti coating annealed at 650°C possesses the highest toughness in comparison with other coatings. Furthermore, it is also important to note that the 15.2 wt% Ti coating annealed at 650°C presents the smallest indentation depth and indent size compared to other coatings under the same maximum load (2000N), seen from Figures 4-55 (j), (k), and (l). This attenuation in indentation depth and indent size is due to the superelastic effect of the NiTi phase in annealed Ti particles.

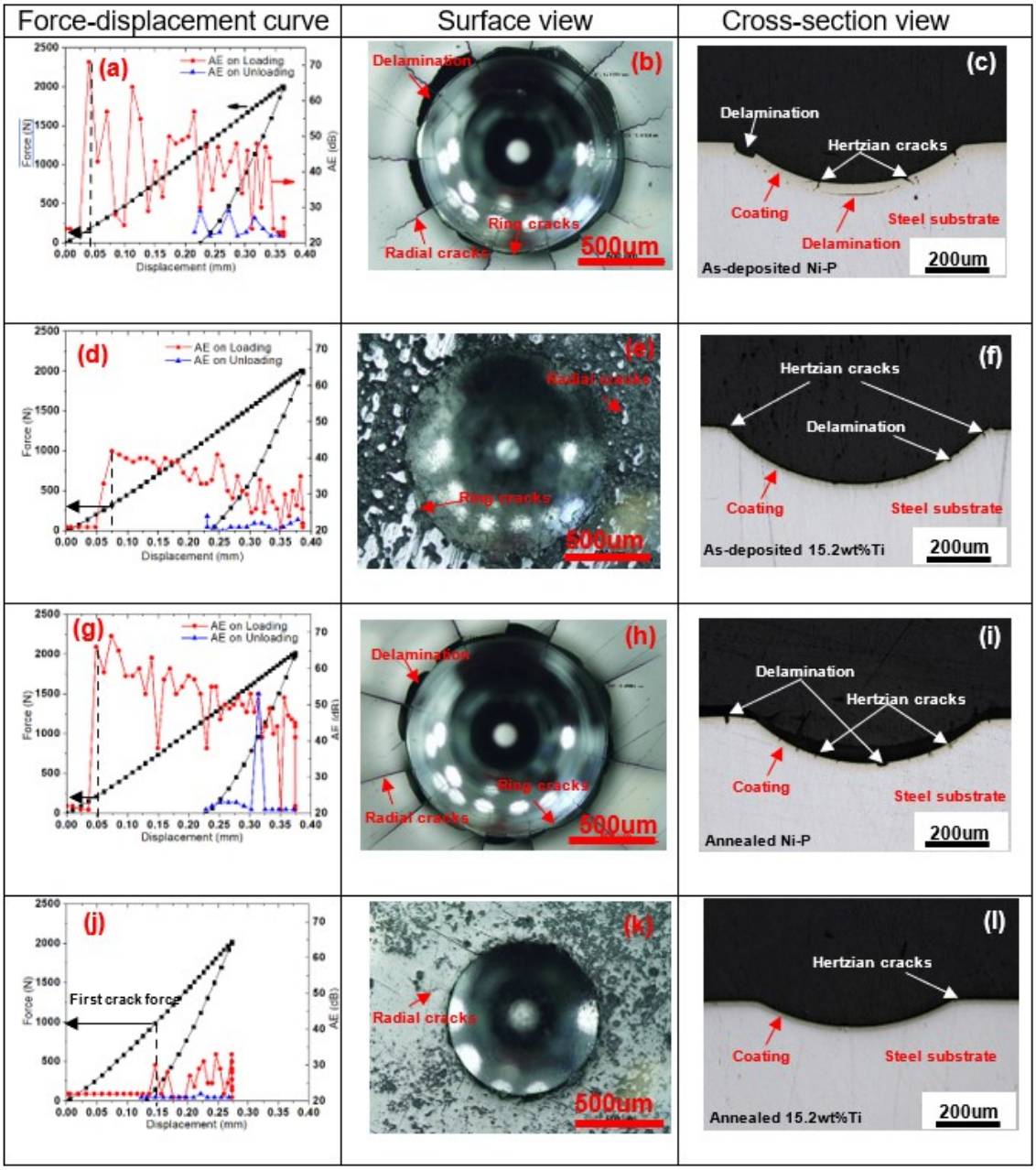

Figure 4-55 Load-displacement curves and indentation behaviors of coatings under a maximum load 2000 N. (a) (b) (c) as-deposited Ni-P, (d) (e) (f) as-deposited Ni-P-15.2wt%Ti, (g) (h) (i) Ni-P annealed at 650°C, (j) (k) (l) Ni-P-15.2wt%Ti annealed at 650°C

In order to investigate the details of indentation behavior of the coatings, the average radial crack width at the edge of the indent and the AE amplitude of the first crack in the coatings after indentation were compared, as shown in Figure 4-56 (a). It can be seen that the AE amplitude of the first crack and the average radial crack width diminish with the increase of Ti content within the coatings, respectively. These provide strong evidence for the improved toughness of the coatings with increasing Ti content. In addition, the first crack force of the coatings is shown in Figure 4-56 (b). From Figure 4-56 (b), for the as-deposited or annealed coatings, the first crack force rises as the Ti content in coating increases. This indicates as Ti content in the coating increases, a larger applied force is required to initiate a crack in the composite coating.

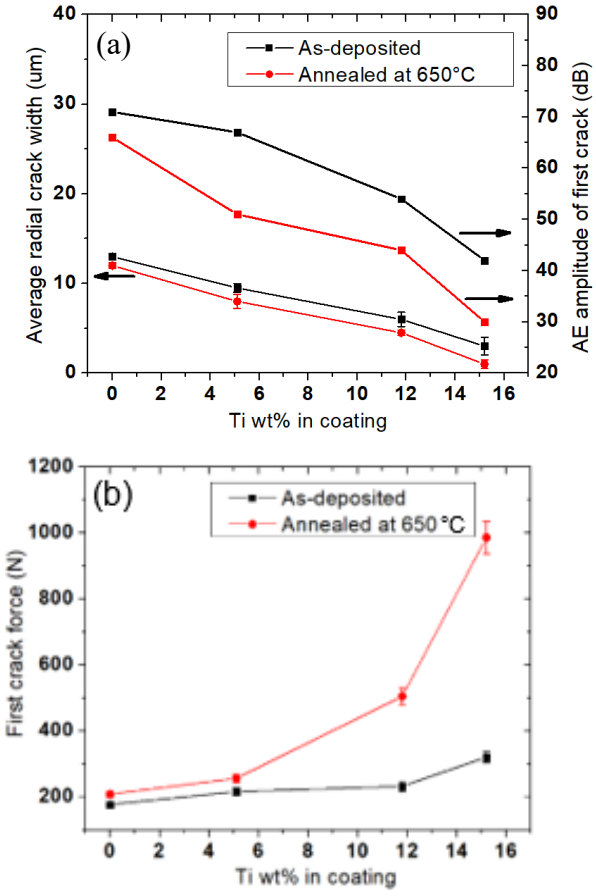

Figure 4-56 Indentation behavior of the coatings as a function of Ti content in coatings: (a) the average radial crack width at the edge of the indent as well as AE amplitude of the first

crack as a function of Ti content in the coating under a maximum load of 2000 N (b) first crack force as a function of Ti content under a maximum load of 2000 N

The toughness of the coating can be determined from the indentation tests. For the indentation test, the toughness is the area under the force-displacement curve up to the first crack force. The toughness of the as-deposited and annealed coatings as a function of Ti content acquired from indentation tests is shown in Figure 4-57. It is noted that the toughness of the as-deposited and annealed coatings were enhanced with increase in Ti content in the coatings. This increase can be attributed to toughening mechanisms induced by the relatively ductile Ti particles, including crack deflection, crack bridging, and microcracking [108]. In addition, it is important to note that the toughness of the annealed coatings significantly improved compared to the as-deposited coatings. The reasons for this are twofold. First, after annealing, the amorphous coatings transform to a crystalline structure which increase the possibility of plastic deformation, resulting in improved toughness. Secondly, the dominant phase resulted from the Ni-Ti solid diffusion during annealing is the superelastic austenitic NiTi phase, which is capable of undergoing reversible martensitic phase transformation under stress. During the phase transformation process, the driving energy for crack initiation and propagation is absorbed by the transformation, which considerably improves the toughness of the coating by the transformation toughening mechanism [185].

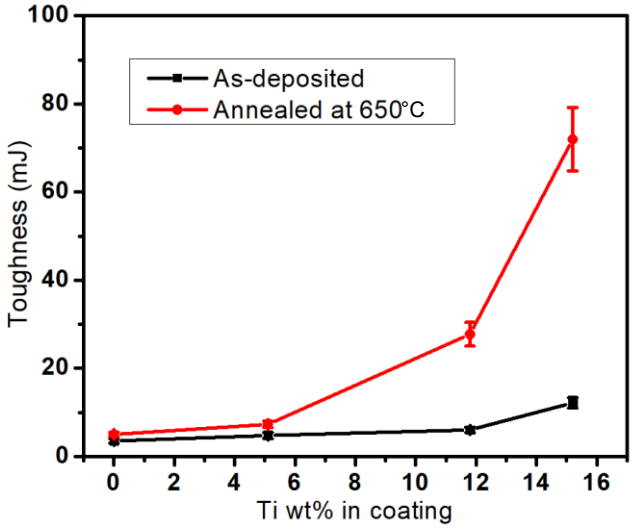

Figure 4-57 Toughness of the as-deposited and annealed coatings determined from indentation tests

To investigate the different cracking mechanisms in different coatings, optical microscopy was adopted to examine the coatings after indentation testing. Figure 4-58 shows different cracking mechanisms on as-deposited and annealed coatings, where the black arrow indicates the direction of crack propagation. Severe cracking and coating delamination are observed in the as-deposited Ni-P coating (Figure 4-58 (a)) due to its low toughness. When a crack encounters a Ti particle (Figure 4-58 (b)), the crack passes through and tears apart the Ti particle since the Ti particle does not have sufficient toughness to absorb the driving energy of the crack. On the other hand, this phenomenon is not observed in annealed 15.2 wt% Ti coating due to the high toughness of superelastic NiTi particles. Different toughening mechanisms are observed in annealed 15.2 wt% Ti coatings. Crack bridging is observed in Figure 4-58 (c), where a NiTi intermetallic particle slows down the propagating crack by bridging its wake. As the crack advances, the particle is pulled out from the Ni-P matrix, which lowers the driving force for crack propagation. After bridging, the crack is less severe as it continues to propagate. Crack deflection can be seen in Figure 4-58 (d), in which a crack propagates towards a NiTi particle which alters the path of crack propagation, causing a loss in driving force of the crack. Crack branching can be observed in Figure 4-58 (e), where fine cracks are branched out from a major crack. This branching reduces the driving force of the major crack and the severity of cracking. It is also interesting to observe that a crack is arrested by a NiTi particle in Figure 4-58 (f) due to transformation toughening.

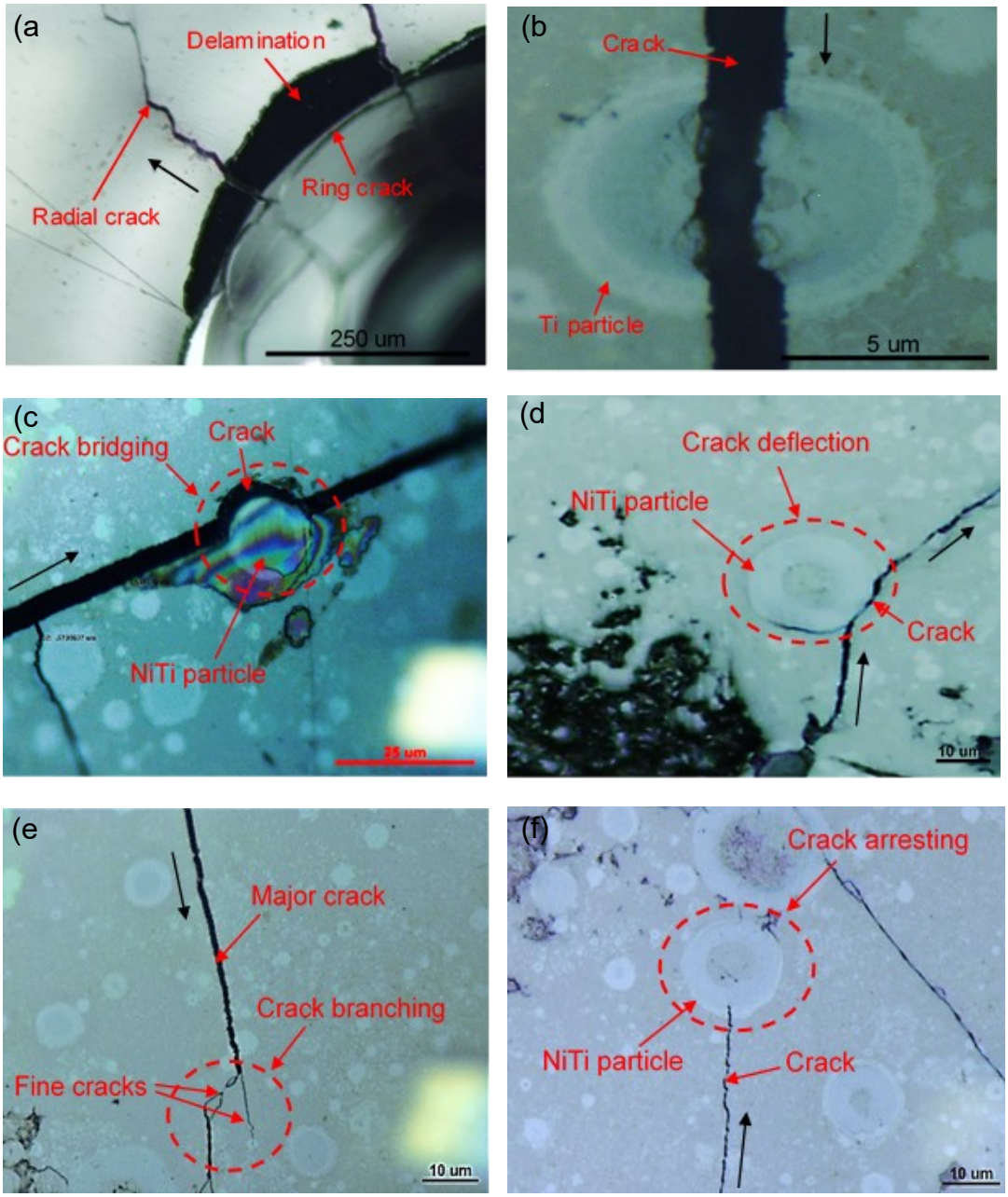

Figure 4-58 (a) Severe cracking and delamination in as-deposited Ni-P coating, (b) cracking in as-deposited 15.2 wt% Ti coating, (c) cracking bridging in annealed 15.2 wt% Ti coating, (d) crack deflection in annealed 15.2 wt% Ti coating, (e) crack branching in annealed 15.2 wt% Ti coating, (f) crack arresting in annealed 15.2 wt% Ti coating.

It has been confirmed that the toughness of the annealed coatings is improved compared to the as-deposited coatings, as observed in Figure 4-58. The toughness of the annealed coatings is enhanced with increase in Ti content within the coatings. This is mainly due to the formation of superelastic NiTi particles after annealing. The improvement of Ni-P coatings' toughness from the formation of superelastic NiTi particles is achieved through following different toughening mechanisms such as crack deflection, crack bridging, crack branching, crack arresting, and transformation toughening, observed in Figure 4-59. The superelastic NiTi particles within the brittle Ni-P matrix have the capacity to absorb the energy required for crack initiation and advancement, resulting in a reduction of crack driving force. Crack deflection from NiTi particles allows for the attenuation of the crack driving force by changing the crack propagation path [144]. Akin to crack deflection, crack bridging lowers the crack driving force through superelastic deformation or even pulling out of NiTi particles from the Ni-P matrix. Crack driving energy can be absorbed by the bridging process, where the crack propagation is inhibited and the crack closes [147]. Stress around a crack tip can be relieved through microcracking which diminishes the driving force of the crack [150]. The energy of a large crack can be consumed by branching fine cracks, consequently dwindling the driving force of the large crack, preventing the crack from advancing [150]. Crack arresting can transpire by transformation toughening when a crack encounters a superelastic NiTi particle. From this encounter, a stress-induced phase transformation is initiated where the austenitic parent phase transforms to a detwinned martensitic phase, accompanying with a large amount of energy absorption as well as an increase in the particle's volume. The energy absorption decreases the driving force of the propagating crack and the increased volume results in compressive stresses around the crack tip. These compressive stresses further reduce the driving force for crack propagation and subsequently decreases the stress intensity at the crack tip. Transformation toughening mechanism from the superelastic NiTi alloy has proven to effectively improve the toughness of brittle materials [149]. These different toughening mechanisms interact with each other, which function synergistically and concurrently to considerably improve the toughness of the annealed composite coatings compared to the as-deposited coatings. It is believed that these toughening mechanisms operate more effectively at higher particle

content to improve the toughness of composite materials [138, 139]. For this reason, the toughness of annealed coatings increases with increase in Ti content, and the annealed 15.2 wt% Ti coating has higher toughness compared to the other coatings with less Ti content.

To investigate the indentation behavior of the coatings, η values were calculated from the load-displacement curves of the indentation tests. Liu et al. [163] first employed the η values to investigate the indentation behavior of superelastic NiTi alloy. They defined η as the ratio of the recoverable deformation energy to the total deformation energy [163]. They also pointed out that η indicates a material's capability to absorb the deformation energy during an indentation process with no permanent damage and is a measure of the effectiveness of the elasticity after the indentation tests [163]. Recoverable deformation energy (W_{rc}) is the area under an unloading curve up to the maximum applied force in the force-displacement curve of an indentation test, whereas the total deformation energy (W_t) is the area under a loading curve up to the maximum applied force in the force-displacement curve of an indentation test; W_{rc}, W_t and η can be computed by the following equations [163]:

$$W_{rc} = \int_{D_r}^{D_{max}} F dD \tag{4.11}$$

$$W_t = \int_{0}^{D_{max}} F dD \tag{4.12}$$

$$\eta = \frac{W_{rc}}{W_t} \tag{4.13}$$

Where F is the applied indentation load; D is the penetration depth; D_r is the residual depth after unloading; D_{max} is the maximum penetration depth.

The values of η for the as-deposited and annealed coatings determined from the indentation force-displacement curves are summarized in Table 4-12. It is known that a material with higher η value has greater ability to absorb deformation energy and withstand more deformation with less damage [163]. From Table 4-12, it is observed that the as-deposited

15.2 wt% Ti coating has higher η values compared to the as-deposited Ni-P coating. This means that the as-deposited 15.2 wt% Ti coating can absorb more deformation energy without cracking in comparison to the as-deposited Ni-P coating. On the other hand, for the annealed coatings, it can be observed that the annealed Ni-P coating exhibits higher η value in comparison with as-deposited Ni-P coating. This suggests that the ability of the annealed Ni-P coating to absorb deformation energy is improved compared to the as-deposited Ni-P coating. In addition, it is important to note that the 15.2 wt% Ti coating annealed at 650 °C has the highest η value compared to other coatings. Among the four different coatings in Table 4-12, only the annealed 15.2 wt% Ti coating contains the superelastic NiTi particles, which can undergo martensitic transformation under stress and can absorb the deformation energy during the phase transformation process. Therefore, this coating can accommodate the largest amount of deformation without cracking or damage compared to the other coatings. This result is consistent with the result of the coating's toughness (Figure 4-57). Furthermore, the η value (52.4%) of the annealed 15.2 wt% Ti coating determined in the present study is higher than that (47%) of the annealed superelastic NiTi alloy reported in the literature [163]. The reason for this difference is that the spherical-shape indenter was employed in the present study whereas a pyramidal-shape indenter was utilized in the literature [163]. Under pyramidal-shape indenter, more plastic deformation occurs due to the higher stress compared to the spherical-shape indenter, which lowers the η value.

Table 4-12 η values for different coatings determined from the indentation tests

Specimens	η (%)
As-deposited Ni-P	37.6
As-deposited 15.2 wt% Ti	39.6
Ni-P annealed at 650°C	38.3
15.2 wt% Ti annealed at 650°C	52.4

4.5.2 Hertzian Stress Distribution Analysis and Indentation Behavior

Large Hertzian cracks as well as coating delamination have been observed in the as-deposited Ni-P (Figure 4-55 (c)). On the other hand, for the annealed 15.2 wt% Ti coating, only small Hertzian cracks are observed at the edge of the indent, as shown in Figure 4-55 (l). To investigate these different indentation behaviors of the coatings, Hertzian stress distribution of as-deposited Ni-P coating as well as 15.2 wt% Ti coating annealed at 650°C was calculated under different applied loads.

The Hertzian stress distribution of indentation testing on the as-deposited Ni-P coating was computed using equations 3.27-3.36 (Chapter 3). The Young's modulus (42 GPa) of the as-deposited Ni-P coating acquired from the tensile test and the Poisson's ratio (0.25) reported in the literature [60] were employed to calculate the Hertzian stress distribution. The Poisson's ratio and Young's modulus of the WC-6Co spherical indenter are 0.3 and 650 GPa, respectively [115]; the radius of the indenter is 0.795mm. The first crack force (176N) for the as-deposited Ni-P coating acquired from the indentation test was used to calculate the stress distribution. The cross-sectional micrographs as well as Hertzian stress distribution analysis of indentation testing of as-deposited Ni-P coating are shown in Figure 4-59. It is observed that the two first Hertzian cracks were symmetrical around the axis of the applied load, shown in Figure 4-59 (a). These first Hertzian cracks are associated with the first crack force (176 N). Figure 4-59 (b) shows the stress distribution of the principal stress σ_1 calculated under the first crack force (176 N). From Figure 4-59 (b), it can be seen that the maximum tensile stress (780 MPa) is located at the edge of the contact circle. This maximum tensile stress initiated the ring crack on the coating surface under the first crack force. As the applied load increases, the ring crack commences propagating into the coating along the σ_3 trajectory [94].

In addition, coating delamination is observed below the coating surface at a depth of 51μm, shown in Figure 4-59 (a). This delamination is caused by the maximum shear stress (1470 MPa) since the coating and the coating/substrate interface lie within maximum shear stress zone under the first crack force (176N), shown in Figure 4-59 (c). The maximum shear

stress first induces a lateral crack at the depth of 51 μm, as the applied indentation load increases, the lateral crack begins to advance along the direction parallel to the coating surface under the maximum shear stress until the coating is delaminated. However, as the applied indentation load gradually rises to the maximum applied load (2000 N), the maximum shear stress zone shifts into the steel substrate at a depth of 300 μm, as seen in Figure 4-59 (d); the coating, on the other hand, is in a much lower shear stress zone (457-865 MPa) compared to that (1289-1470 MPa) under the first crack force (176N). These results of Hertzian stress distribution analysis are consistent with the experimental results of the indentation tests.

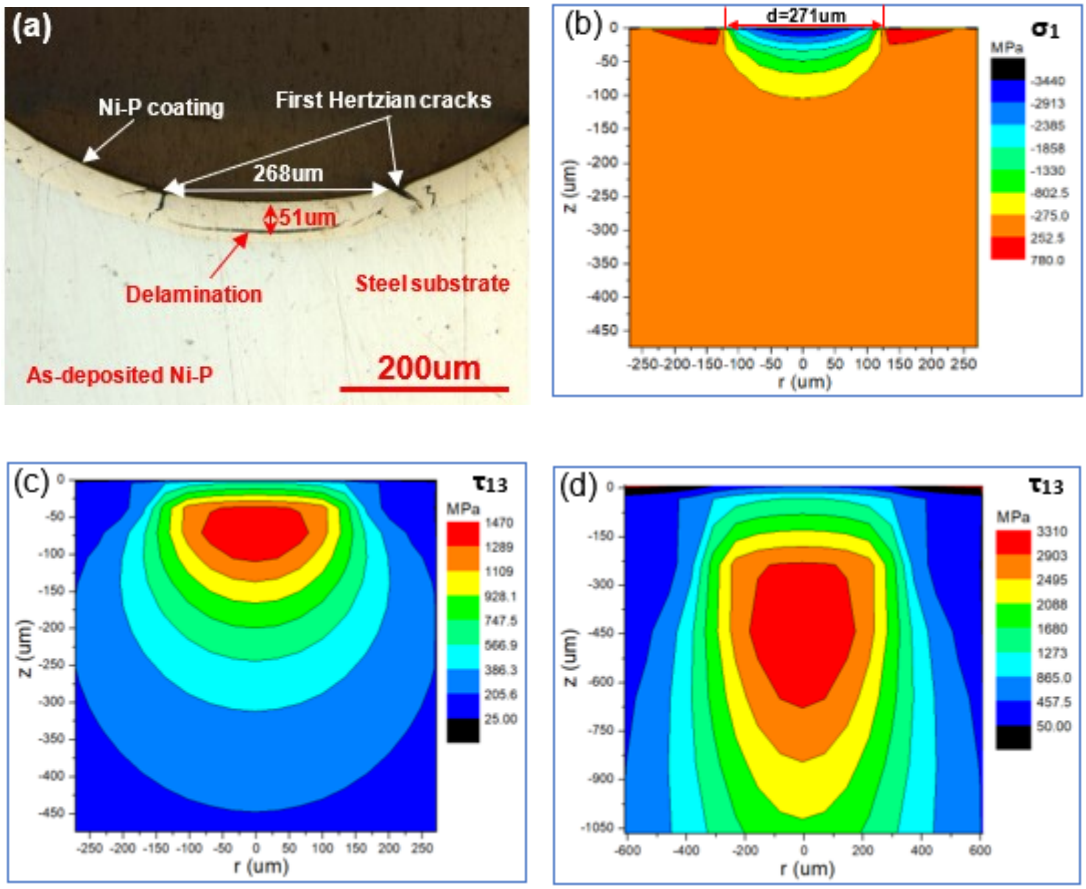

Figure 4-59 Indentation behavior as well as Hertzian stress distribution analysis of indentation testing on as-deposited Ni-P coating. (a) cross-section view of the indent, (b) σ_1 under the first crack force (176 N), (c) τ_{13} under the first crack force (176 N), (d) τ_{13} under the maximum force (2000 N)

In order to investigate the indentation behavior of 15.2 wt% Ti coating annealed at 650°C, the Hertzian stress distribution was computed using equations 3.27-3.36 (Chapter 3) under the maximum load (2000 N). The Young's modulus (72 GPa) of the annealed 15.2 wt% Ti coating acquired from the tensile test and the Poisson's ratio (0.3) reported in the literature [188] were employed to calculate the stress distribution. The Poisson's ratio and Young's modulus of the WC-6Co spherical indenter are 0.3 and 650GPa, respectively [115]; the radius of the indenter is 0.795mm. The Hertzian stress distribution analysis of indentation testing on 15.2 wt% Ti coating annealed at 650°C under the maximum indentation load (2000 N) is shown in Figure 4-60. From Figure 4-60 (a), it is observed that the maximum tensile stress (1950 MPa) of σ_1 is located at the edge of the contact circle. This indicates that the Hertzian crack is expected to initiate at the edge of the indent due to the maximum tensile stress, as observed in Figure 4-61. Figure 4-61 shows the cross-section view of the indent after the indentation testing on the annealed 15.2 wt% Ti coating. From Figures 4-61 (a) and (b), it is noted that the ring cracks initiate at the edge of the indent under the maximum tensile stress. These ring cracks then propagate into the coating, along σ_3 trajectory [94]. However, this propagation of the ring cracks is shielded by the superelastic NiTi particles through the transformation toughening mechanism, as observed in Figure 4-61 (b). It is known that the stress required to induce a martensitic transformation of a NiTi alloy is found to be within the range of 100-400 MPa at 25 °C [24, 141, 142], depending on the exact composition and heat treatment history of the NiTi alloy. The compressive stress below the contact surface is found to be within in the range of 1825-14600 MPa, as shown in Figure 4-60 (b), which is much higher than the stress required for the phase transformation. Therefore, under the compressive stress, the phase transformation in the NiTi particles occurs where the austenitic phase transforms to a detwinned martensitic phase, accompanied by a large superelastic deformation and energy absorption; this energy absorption lowers the driving force of the cracks and relieves the stress concentration. Also, during the phase transformation process, the volume of the NiTi particles enlarges, which produces a compressive stress field around the NiTi particles. This compressive stress field has the capability to close the cracks. Therefore, the propagation of the Hertzian cracks is blocked by the NiTi particles through the transformation toughening mechanism, observed in Figures 4-61 (a) and (b).

In addition, under the maximum indentation load (2000 N), it is observed that the maximum shear stress zone is in the steel substrate at a depth of 100 μm (coating thickness: approximately 50 μm) and the shear stress in the coating is in a range of 1195-1753 MPa, as seen in Figure 4-61 (c). Compared to the as-deposited Ni-P coating, under the same maximum indentation load (2000 N), the 15.2 wt% Ti coating annealed at 650°C withstands much higher tensile stress (σ_1) and shear stress (τ_{13}). Furthermore, lower crack density and no coating delamination are observed in the annealed 15.2 wt% Ti coating in comparison with the as-deposited Ni-P coating due to the transformation toughening mechanism. The transformation toughening significantly enhances the toughness of the annealed composite coating, which makes it possible for the annealed 15.2 wt% Ti composite coating to allow higher stresses and accommodate a larger amount of deformation with less cracking and damage compared to the as-deposited Ni-P coating.

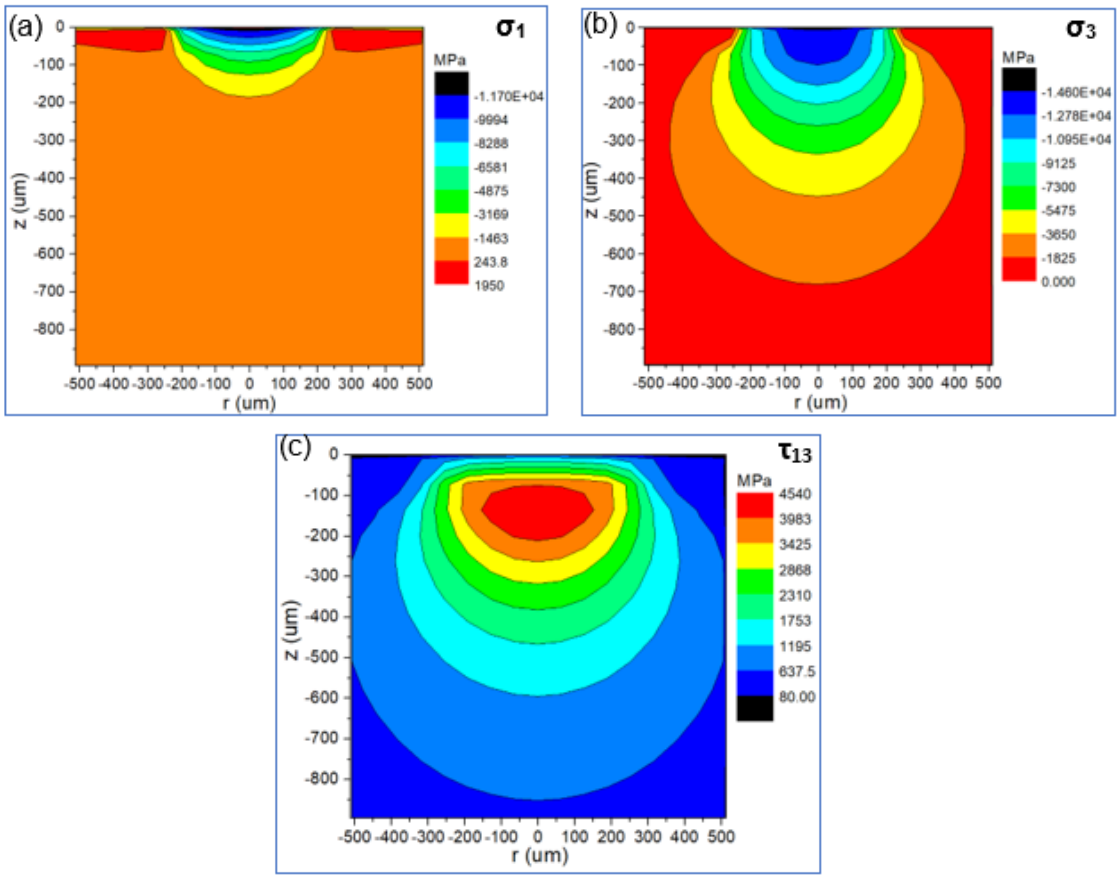

Figure 4-60 Hertzian stress distribution of indentation testing on 15.2 wt% Ti coating annealed at 650°C under the maximum indentation load (2000 N) (a) σ_1 (b) σ_3 (c) τ_{13}

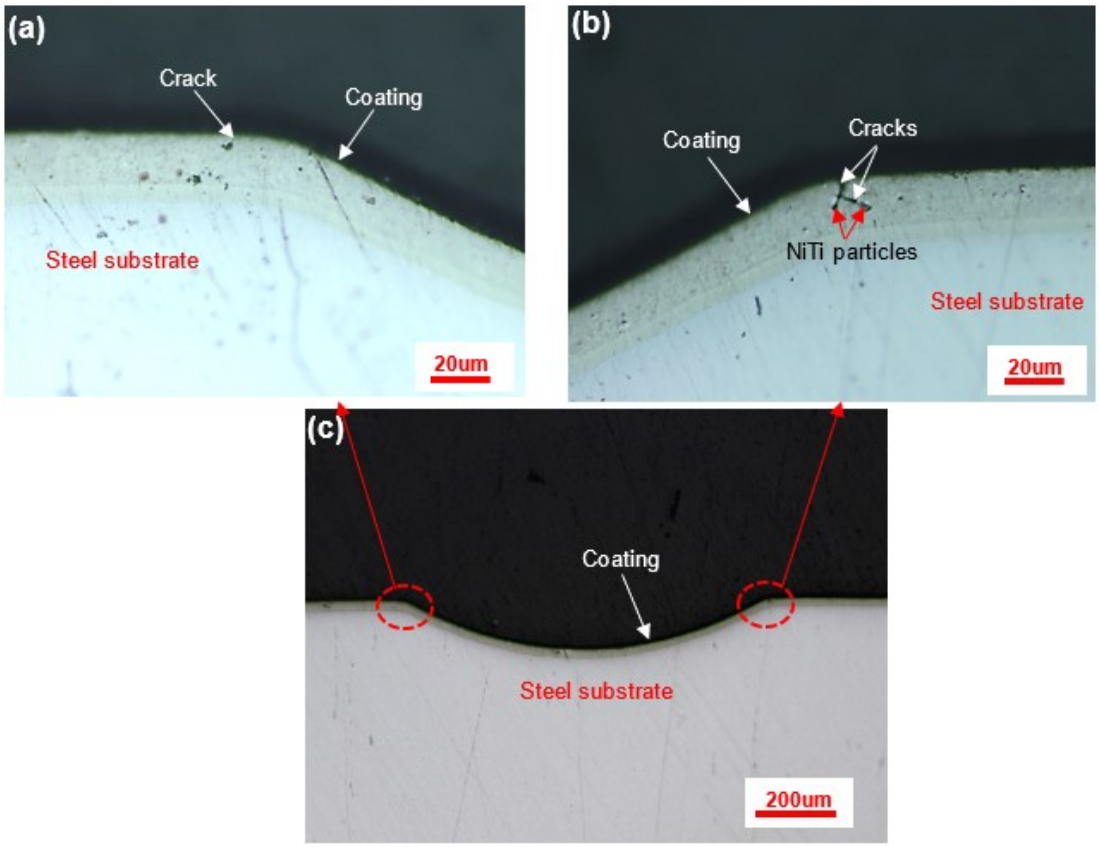

Figure 4-61 Cross-section view of 15.2 wt% Ti coating annealed at 650°C after indentation testing under the maximum load (2000N). (a) (b) high magnification of the indent edge; (c) low magnification of the indent

4.6 Single Particle Erosion Behavior

4.6.1 Single Particle Erosion Investigation

In order to investigate the coatings under impact loading (dynamic loading), single particle erosion tests were performed. Single particle erosion can cast light on particle impact and material removal mechanisms that are not possible to be studied by traditional multiparticle erosion tests. The single particle erosion tests were conducted at various impact angles (30°,

45°, 60° and 90°). Figures 4-62 (a) and (b) show the impact crater volume of as-deposited and annealed coatings as a function of impact angle, respectively. For as-deposited and annealed coatings, the impact crater volume increases with an increase in impact angles and the highest impact crater volume is reached at 90°. This is mainly because the impact energy increases as impact angles increase. For ductile materials, erosion is typically highest at low impact angle as a result of cutting mechanisms. However, the cutting mechanism is induced as a result of sharp particles impacts, which is not the case in this study. Therefore, increasing displacement volume with impact angle is expected when spherical impact particles are used in the present study.

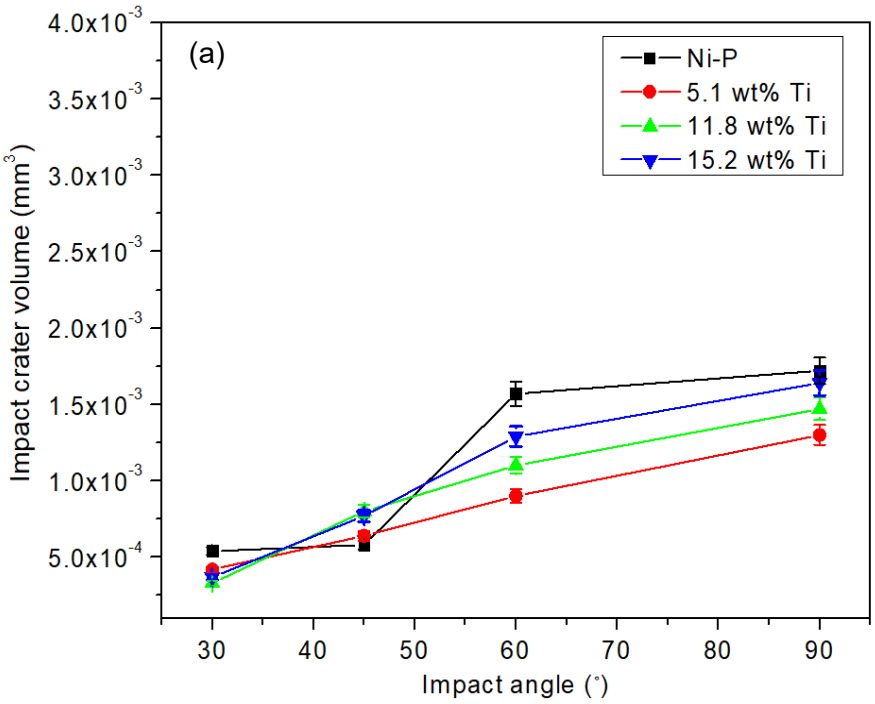

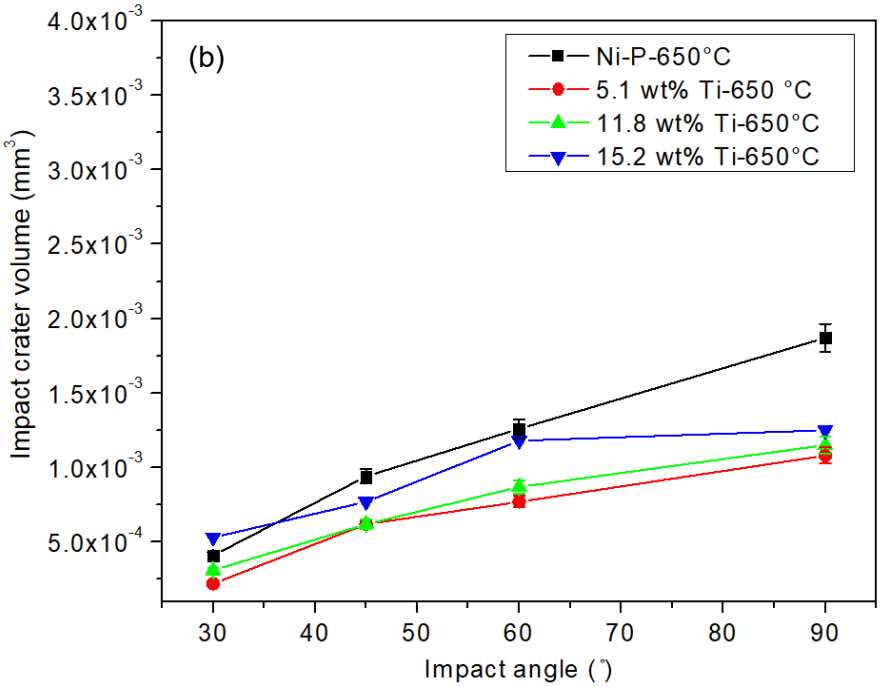

Figure 4-62 Impact crater volume as a function of impact angle tested at impact velocity of 52 m/s, (a) as-deposited coatings and (b) coatings annealed at 650°C

Figure 4-63 shows the wear scar of as-deposited coatings after impact at 52 m/s. It can be seen that the erosive crater generated at low angle (30°) impact is elliptical in shape, whereas the wear scar at high angle (90°) impact is circular. The displaced volume at high impact angle is larger compared to low impact angle scar. This is mainly because, at high impact angle, most of the kinetic energy is absorbed by the deformation of the coatings. On the other hand, at low impact angle, majority of the kinetic energy is converted to the thermal energy due to frictional force [189]. This observation is consistent with the impact crater volume result (against impact angle Figure 4-62). From Figure 4-63, different types of cracks are observed in the vicinity of the impact crater. Both Hertzian and radial cracks are present in the as-deposited Ni-P coating at both low and high angle impacts (Figures 4-63 (a) and (b)). However, only Hertzian type cracks are observed in the composite Ni-P-Ti coatings. It is believed that the Hertzian cracks initiate on the coating surface and is associated with the maximum tensile radial stress [89]. On the other hand, radial cracks are generated at the edge of a crater due to the maximum tensile hoop stress [190]. When the

applied stress is in excess of a critical value, Hertzian crack and radial crack initiate on the coating surface. It is interesting to note that at low impact angle (< 45°), the Hertzian cracks are only present behind where the erodent particle initially touches the coating surface but not exhibited on the other side where the impact particle leaves the surface (Figure 4-63). This observation is analogous to the Hertzian cracking observed during scratch testing process due to the tensile stress just behind the sliding indenter [4, 108]. Furthermore, in comparison with the as-deposited Ni-P coating, cracking becomes less severe as Ti content increases for the Ni-P-Ti composite coatings. This suggests that the toughness of the Ni-P-Ti composite coatings is improved with the increase of the Ti concentration within the coatings [108].

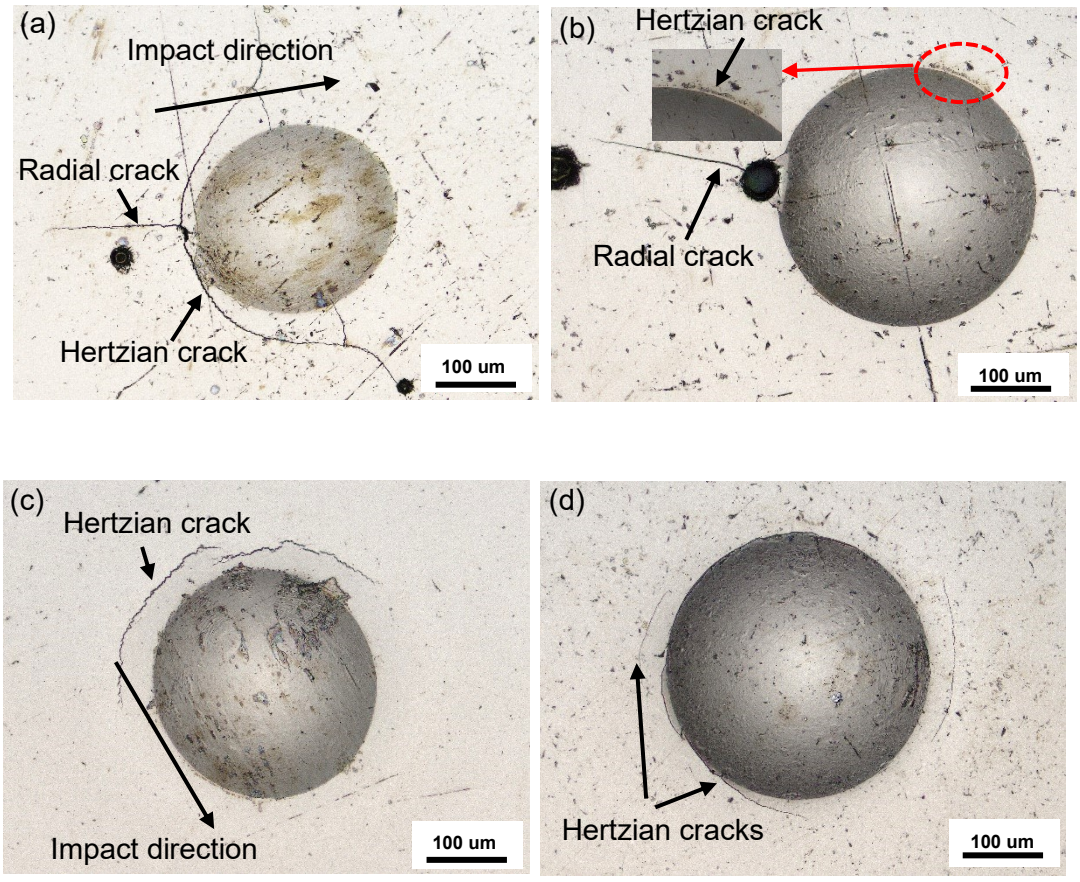

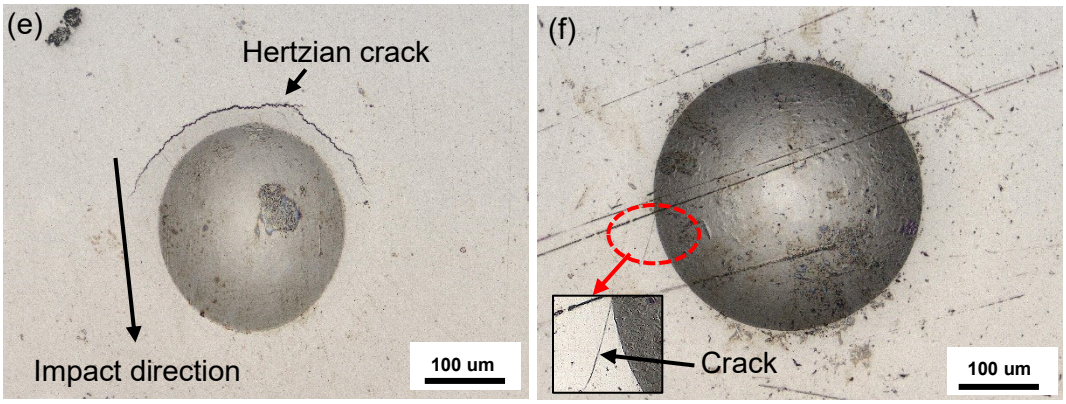

Figure 4-63 Wear scar of as-deposited coatings after impact at 52 m/s. (a) (b) as-deposited Ni-P coating, (c) (d) as-deposited 11.8 wt% Ti coating, (e) (f) as-deposited 15.2 wt% Ti coating, (a) (c) (e) low angle impact (30°) and (b) (d) (f) high angle impact (90°)

The erosion behavior of annealed coatings tested at impact velocity 52 m/s is shown in Figure 4-64. From Figures 4-64 (a) and (b), Hertzian crack and radial crack are observed on annealed Ni-P coating surface in the vicinity of the impact crater. On the other hand, for annealed 11.8 wt% Ti coating, only one small radial crack is present at high impact angle and no crack is observed at the low impact angle (Figures 4-64 (c) and (d)). Crack shielding by a NiTi particle as well as crack closing is observed in Figure 4-64 (d). It is worth noting that there is no crack observed at both low and high angle impacts for the annealed 15.2 wt% Ti coating under the same magnification (Figures 4-64 (c) and (f)). This indicates that the toughness of the annealed Ni-P-Ti coatings is superior to that of the annealed Ni-P coating. This improved toughness is a result of the transformation toughening derived from NiTi particles.

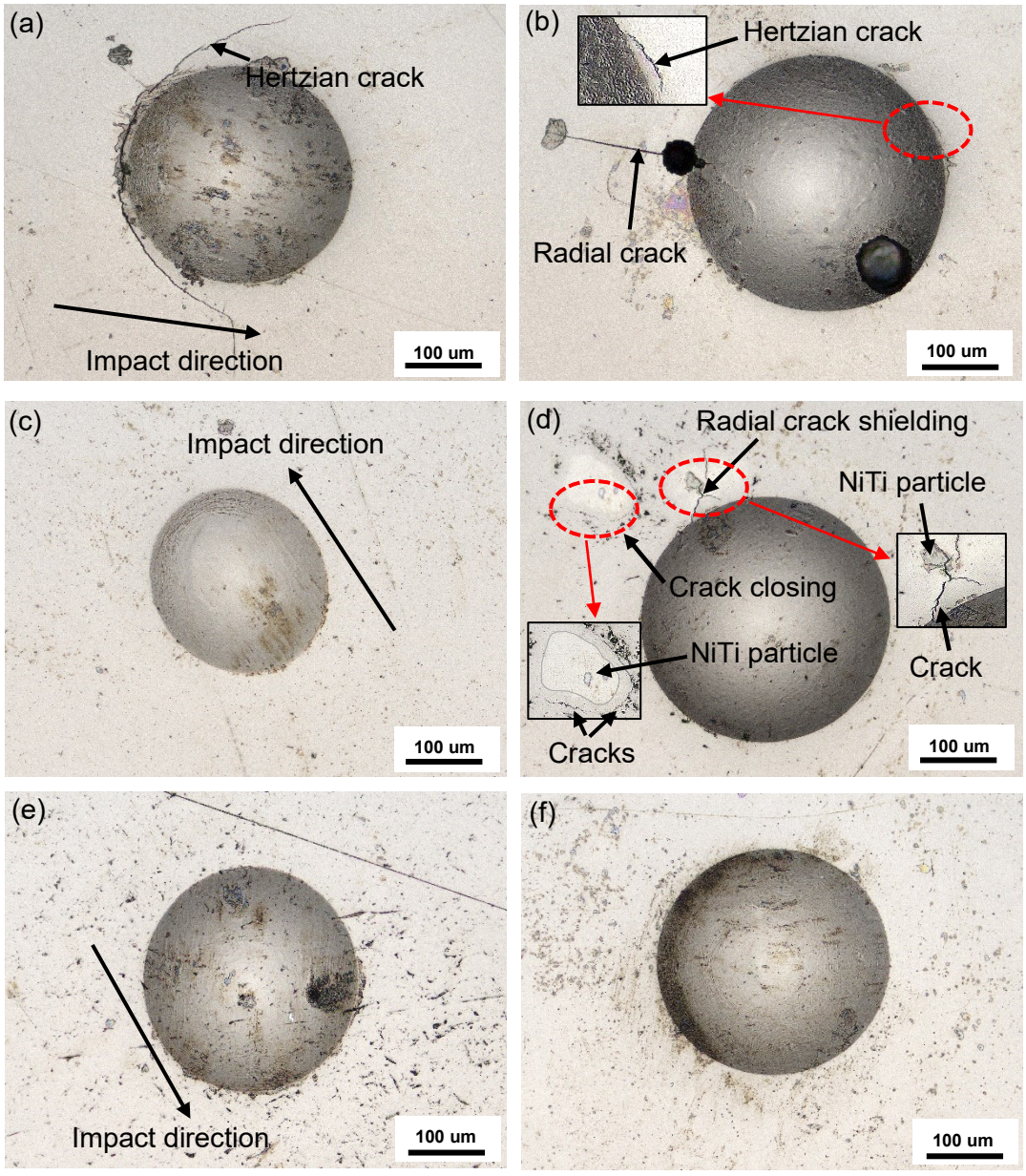

Figure 4-64 Wear scar of annealed coatings (650°C) after impact at 52 m/s. (a) (b) annealed Ni-P coating; (c) (d) annealed 11.8 wt% Ti coating; (e) (f) annealed 15.2 wt% Ti coating. (a) (c) (e) low impact angle (30°) and (b) (d) (f) high impact angle (90°).

The 3D images and depth profiles of impact craters of as-deposited and annealed coatings after single particle impact testing are shown in Figures 4-65 to 4-68. The as-deposited 15.2 wt% Ti coating exhibits pile-up at both low and high angle impacts, whereas no obvious pile-up is observed on the as-deposited Ni-P coating after the impact testing (Figures 4-65 and 4-66). This indicates that the as-deposited 15.2 wt% Ti coating is more ductile than the as-deposited Ni-P coating. For as-deposited Ni-P coating, significant portion of the impact energy is transformed into the driving energy for cracks initiation and propagation, whereas the kinetic energy is converted into the plastic deformation to form the pile-up lips for the more ductile as-deposited 15.2 wt% Ti coating especially at the low angle impact [100]. For low impact angle, the pile-up is created in front of the impinging particle and accumulated at the edge of the impact crater where the impact particle leaves the coating surface. On the other hand, the material pile-up is more uniform in the vicinity of the impact crater at the normal impact. The pile-up is also observed on the annealed 11.8 wt% Ti and 15.2 wt% Ti coatings after impact (Figures 4-67 and 4-68). However, the pile-up is more prominent on the annealed 15.2 wt% Ti coating than other as-deposited and annealed coatings. The reason for this prominent pile-up is that after annealing, the brittle amorphous Ni-P matrix transforms to the ductile crystalline coating within which superelastic NiTi particles are embedded. These NiTi particles improve the toughness and ductility of the annealed Ni-P-Ti composite coatings by transformation toughening. This is in agreement with the observations of wear scars of coatings (Figure 4-64).

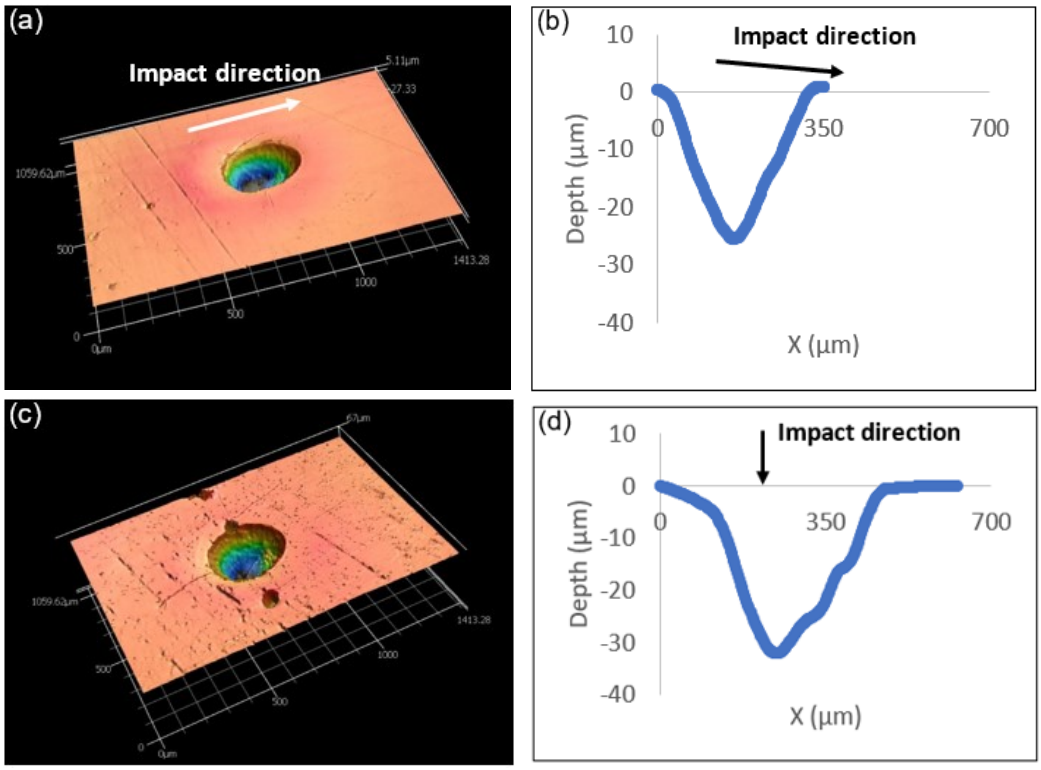

Figure 4-65 3D surface and depth profiles of as-deposited Ni-P coating (a), (b) at low impact angle (30°) and (c), (d) at high impact angle (90°)

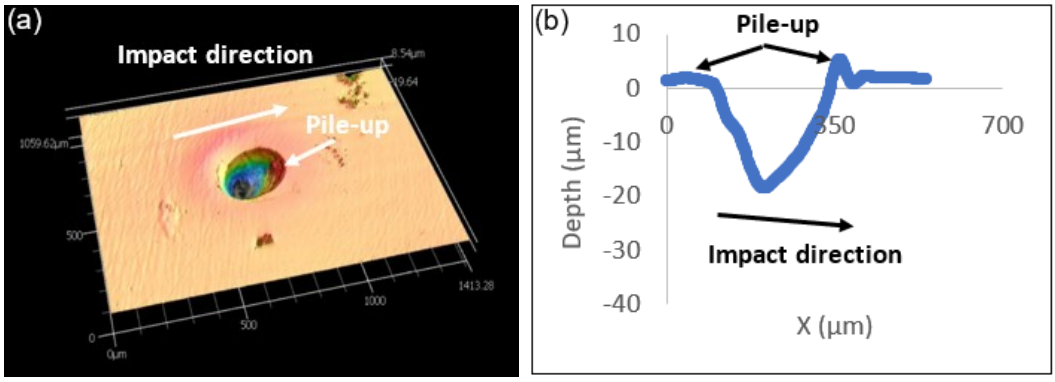

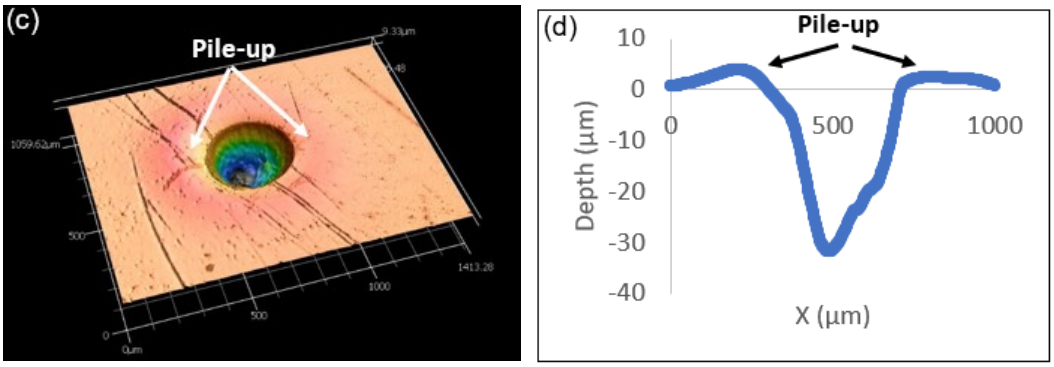

Figure 4- 66 3D surface and depth profiles of as-deposited 15.2 wt% Ti coating (a), (b) at low impact angle (30°) and (c), (d) at high impact angle (90°)

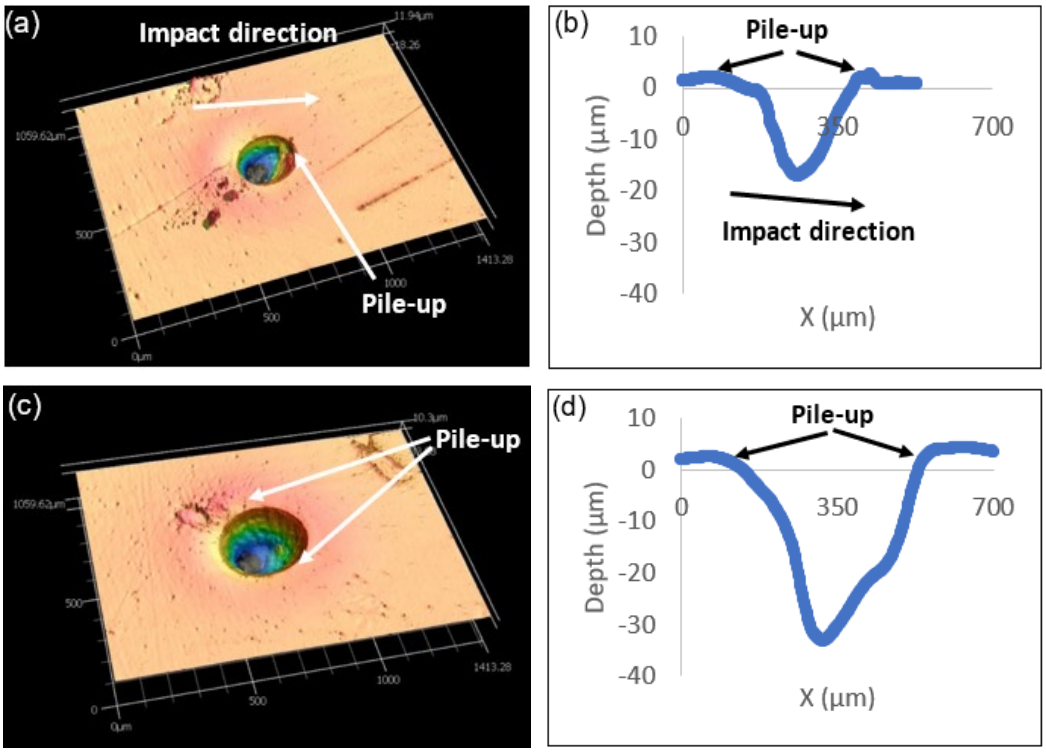

Figure 4- 67 3D surface and depth profiles of annealed 11.8 wt% Ti coating (a), (b) at low impact angle (30°) and (c), (d) at high impact angle (90°)

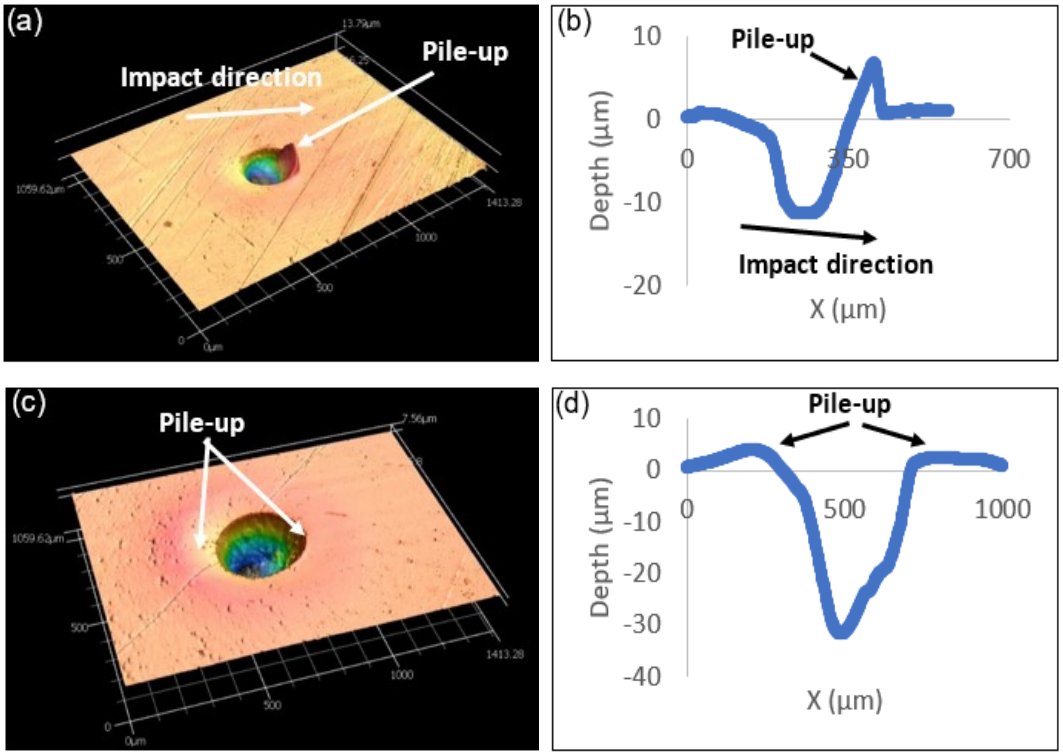

Figure 4- 68 3D surface and depth profiles of annealed 15.2 wt% Ti coating (a), (b) at low impact angle (30°) and (c), (d) at high impact angle (90°)

4.6.2 Toughening and Erosion Mechanisms

In order to investigate the toughening mechanisms of annealed 11.8 wt% Ti coating after the single particle testing, laser confocal microscopy was employed. Crack shielding and crack closing induced by transformation toughening have been observed at the edge of the impact crater, as already seen in Figure 4-64 (d). Hence, to substantiate that the applied stress during the impact process is adequate to induce austenite to martensite transformation in NiTi, firstly, the mean impact force (P) during the impact process was estimated by assuming an ideal case scenario and using the following equations $W = Pd$ and $E = ½ mv^2$. Here, W is the work done to create an impact crater; d is the depth of the impact crater; E is the kinetic energy of the impact particle; m and v are the mass and

velocity of the impact particle, respectively. Li et al. investigated and simulated the single particle erosion behavior of AISI 4340 annealed steel and established that the plastic work was found to be in a range of 76-84% of the kinetic energy of the impact particle [191]. In the present study, if 76-84% of kinetic energy is converted into the plastic work to generate an impact crater, the mean impact force is found to range between 11.8-23.7 N for different impact angles. Using the above argument, the mean contact pressure during the impact process was computed using equations 3.36-3.39 (Chapter 3). The radius of the impact ball is 500 μm. The Young's modulus (50 GPa) of annealed 11.8 wt% Ti coating obtained from tensile test and the Poisson's ratio 0.3 reported in the literature [192] were utilized to calculate the mean contact pressure. Assuming that $v_2 = 0.26$, $E_2 = 650$ GPa for the WC-Co impact ball [115], the mean contact pressure for the single particle impact is found to be within a range from 2.4 GPa to 3.0 GPa. It is known that the stress required to induce a martensitic phase transformation in superelastic NiTi alloy falls within a range of 100-400 MPa at 25 °C [24, 141, 142], depending on the exact composition and heat treatment history of the NiTi alloy. Therefore, the mean contact pressure for the impact testing is higher than the stress required to induce phase transformation in NiTi alloy. Hence, transformation toughening by NiTi particles is expected to occur.

Additionally, in order to confirm that the impact stress outside of the impact crater is sufficient to prompt a martensitic phase transformation, the stress distribution at the normal impact was computed using the equations 3.27, 3.29, 3.30, 3.31, 3.35, 3.36 (Chapter 3). The stress (σ_1) distribution during the normal impact process of annealed 11.8 wt% Ti coating is shown in Figure 4-69 (a). It is observed that in the contact area or in the impact crater, the stress has a negative sign that means the stress is compressive stress, which is found to range between 445-3640 MPa. This stress range is sufficient to induce a martensitic phase transformation in NiTi, as discussed above. By comparing Figures 4-69 (a) and (b), it is estimated that NiTi particle A is under a tensile stress within a range of 548-582 MPa and NiTi particle B is also under a tensile stress but within a lower stress range of 420-537 MPa. Therefore, the applied stresses on particles A and B are higher than the critical stress. Hence, the transformation toughening is expected to occur in NiTi particles A and B. From Figure 4-69 (c), during the impact process, a radial crack initiates

at the edge of the impact crater and propagates outward, when the crack approaches the NiTi particle A, the austenitic phase within the particle A transforms to a martensitic phase accompanied by a large superelastic deformation. Synchronously, the volume of the particle A expands due to the phase transformation, which develops a compressive stress field in the vicinity of particle A. The superelastic deformation and the compressive stress field result in a reduction in the driving force for the crack propagation and ultimately the crack is arrested by the NiTi particle A, as seen in Figure 4-69 (c). From Figure 4-69 (d), it is interesting to observe that the cracks in the vicinity of the NiTi particle B propagating around the particle are closed by the compressive stress field due to the transformation toughening mechanism.

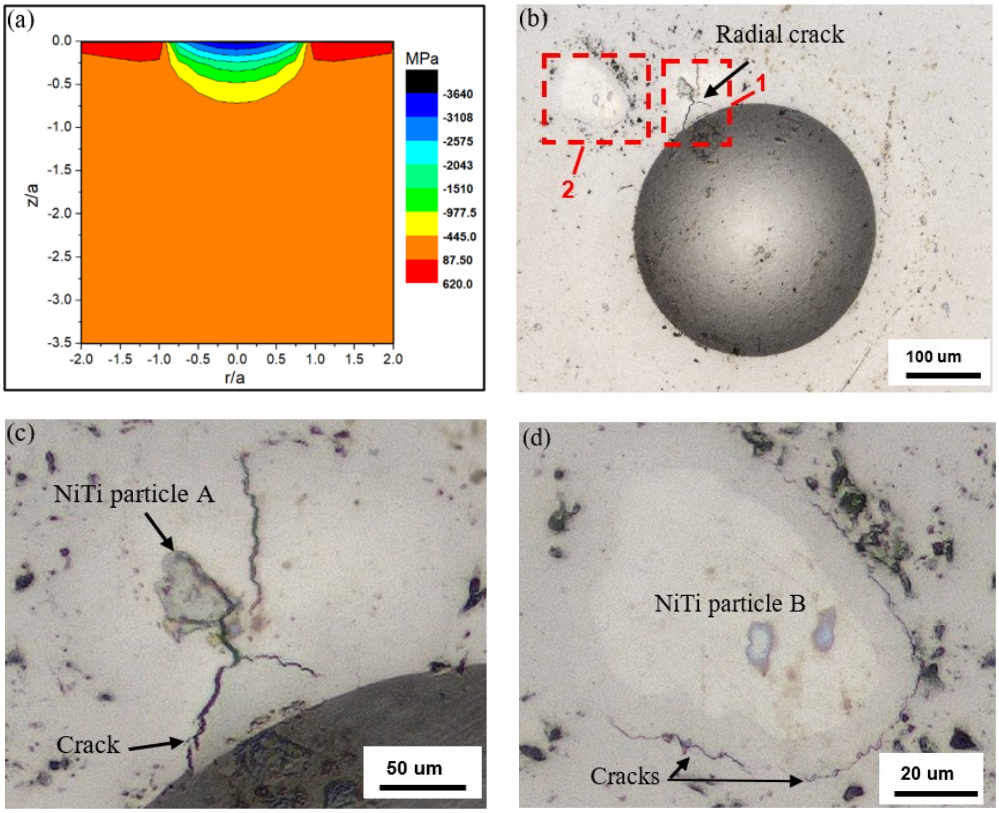

Figure 4-69 Hertzian stress (σ_1) distribution during the impact process as well as transformation toughening observed in annealed (650°C) 11.8 wt% Ti coating. (a) σ_1 stress distribution, (b) transformation toughening (c) magnified micrograph of square area 1 in (b), (d) magnified micrograph of square area 2 in (b).

Both Hertzian and radial cracks are present in the vicinity of the impact crater on as-deposited Ni-P coating, whereas no cracks are observed in the vicinity of impact crater on annealed 15.2 wt% Ti coating at both low and high angles impacts (Figures 4-63 and 4-64). In order to further investigate the toughening mechanisms during impact process, the samples were sectioned after impact. Figure 4-70 shows cross-sectional micrographs (using confocal laser microscope) of the impact craters of as-deposited Ni-P and annealed 15.2 wt% Ti coatings. The insets in Figures 4-70 (a) and (b) are the magnified micrographs of the marked parts, respectively. From Figures 4-70 (a) and (b), Hertzian cracks are observed on cross-section of impact craters of as-deposited Ni-P coating at both low and normal angles. On the other hand, under the same magnification, no cracks are observed on the cross-section of impact craters of annealed 15.2 wt% Ti coating at both low and normal angles. This prominent difference is due to the transformation toughening mechanism. For as-deposited coating, during impact process, ring cracks first initiated on the coating surface due to the maximum tensile stress [89], as already seen in Figures 4-63 (a) and (b). Below the surface, ring cracks propagated along σ_3 trajectory forming cone cracks [94]. However, for annealed 15.2 wt% Ti coating, during the impact process, the average impact stress is higher than the critical stress, as discussed above. The phase transformation is anticipated to transpire, which results in an absorption of impact energy and a compressive stress in the vicinity of NiTi particles. The energy absorption and compressive stress field significantly improve the toughness of the coating, which in turn prevent the initiation of cracks during the impact process. In addition, compared to the as-deposited Ni-P coating, the size and depth of impact crater are smaller for annealed 15.2 wt% Ti coating due to the superelastic effect of NiTi phase, which imparts a higher elastic recovery to the composite coating.

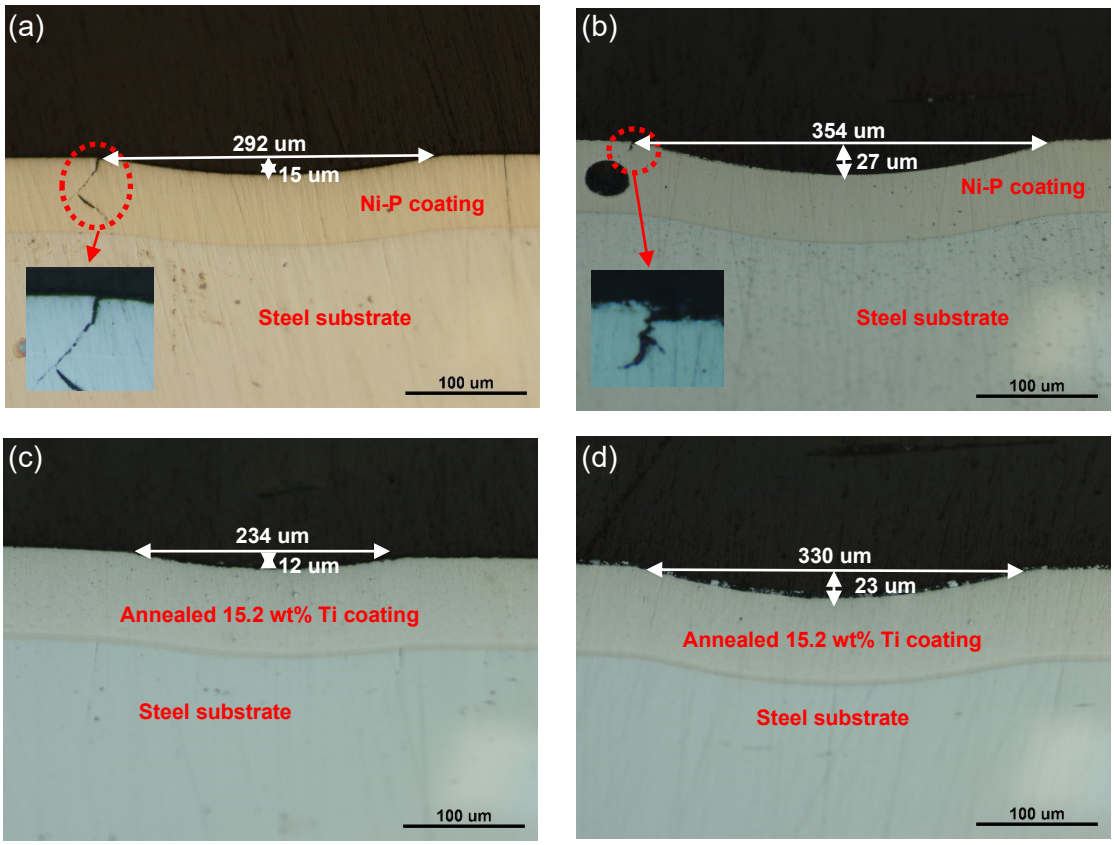

Figure 4-70 Cross-sectional micrographs of impact craters of as-deposited Ni-P and annealed 11.5 wt% Ti coatings. (a) and (c) low angle impact (30°), (b) and (d) normal impact (90°).

It is found that the ductility and toughness of the as-deposited Ni-P-Ti coatings are higher compared to the as-deposited Ni-P coating. The toughness of the as-deposited coatings increases with an increase in Ti content (Figure 4-63). This is mainly because of the effect of Ti particles on the ductility and toughness of the coatings. Ti particles are softer and more ductile than the Ni-P matrix, which enhance the ductility and toughness of the Ni-P-Ti composite coatings [64, 193]. Jason et al. investigated the mechanical properties of the Mg-based bulk metallic glass composites and found that the compressive strain is improved to 7.2 % by incorporating 20 vol.% of Fe particles into the Mg-based bulk metallic glass matrix due to the fact that Fe particles are capable of branching dominant shear band into multiple shear bands and mitigating the stress concentration [138]. In another research,

Jang et al. observed that the Ti particles impart exceptional plasticity to the Mg-based bulk metallic glass composites and the compressive plasticity is enhanced from 12 % to 25 % strain by decreasing the mean Ti particle size from 89 ± 20 μm to 50 ± 17 μm when adding 40 vol.% Ti particles into the brittle Mg-base bulk metallic glass matrix [139]. This is mainly because smaller particle size decreases the inter-particle spacing or mean free path, which in turn prompts a prominent improvement in plasticity and toughness of the Mg-based bulk metallic glass composites [139]. In the present study, as the Ti content increases within the as-deposited coatings, the volume fraction of Ti particles within the coatings is enhanced, which in turn results in a reduction of the interparticle spacing between Ti particles. Therefore, according to Jang et al.'s argument [139], the toughness of as-deposited Ni-P-Ti coatings improves with the increase in Ti content due to the reduction of the interparticle spacing of the Ti particles.

After annealing, the Ti particles embedded in the Ni-P matrix react with Ni to form NiTi intermetallic alloy. Both toughness and ductility of the annealed coatings are further improved compared to the as-deposited coatings, as already observed in Figure 4-64. This further improvement in toughness can be attributed to the ductile NiTi particle toughening mechanisms derived from the stress-induced phase transformation. When the erosive particle impacts the surface of the annealed Ni-P-Ti composited coating, the impact stress calculated using Hertzian contact theory is higher than the stress required for phase transformation, which facilitates the martensitic phase transformation. The austenite phase within the NiTi metallic particles transforms to a martensite phase accompanied by a large amount of energy absorption and an increase in the volume of the particle [4]. This volume increase yields a compressive stress field in the vicinity of the NiTi metallic particles. When a crack advances to a NiTi intermetallic particle, the intermetallic particle has the capability to absorb the driving energy for the crack propagation, which lowers the driving force for the crack advancement, then the crack can either be deflected or bridged by the particle [108] or even shielded or arrested by the particles due to the compressive stress field. NiTi alloy is known for its superelasticity and excellent energy absorption ability [163]. Hao et al. prepared a transforming nanocomposite material that possesses large elastic strain, low modulus, and high strength by incorporating Nb nanowires in a NiTi matrix that exhibits a large superelastic strain through stress-induced martensitic

transformation [194]. In addition, due to the martensitic phase transformation, a 600% increase in energy absorption is observed by W. Zhang et al. in an E-glass composite material employing shape memory NiTi alloy as the reinforcement material [195]. The superelasticity and high energy absorption ability of NiTi are the dominant reasons why annealed Ni-P-Ti coatings exhibit outstanding toughness and ductility, which in turn completely converts the erosion behavior of the coatings from a brittle erosion behavior for as-deposited Ni-P coating to a ductile erosion behavior for the annealed 15.2 wt% Ti coating.

4.7 Static Corrosion Performance

4.7.1 Potentiodynamic Polarization Behavior of Coatings

To study the static corrosion behavior, potentiodynamic polarization (PP) and electrochemical impedance spectroscopy (EIS) tests were conducted on as-deposited and annealed samples in a 3.5 wt% sodium chloride solution. In addition, the as-received and annealed 1018 steel substrates were also tested as references. Representative potentiodynamic polarization curves for as-deposited and annealed samples are shown in Figure 4-71. Compared to AISI 1018 steel substrate, Ni-P and Ni-P-Ti coatings exhibit much higher corrosion potential. The corrosion current density (i_{corr}) and corrosion potential (E_{corr}) were extracted from polarization curves using Tafel extrapolation. Corrosion rate (CR) premised on corrosion current density was calculated using the following equation [196]:

$$CR = \frac{i_{corr} \times EW}{D} \times 3270 \qquad 4.14$$

Where *EW* is the equivalent weight, *D* is the density of the sample.

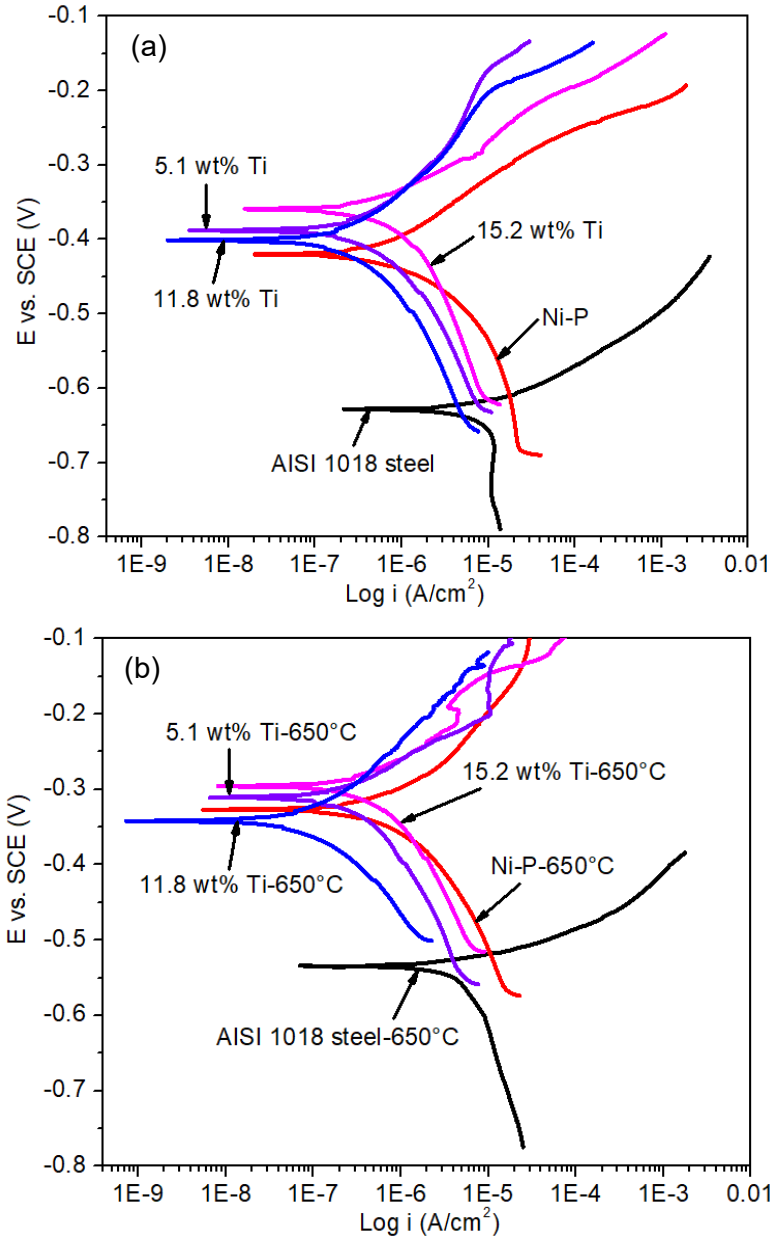

Figure 4-71 Representative polarization curves of (a) as-deposited and (b) annealed samples at 650°C.

The corrosion characteristics of as-deposited samples are given in Table 4-13. Compared to as-received AISI 1018 steel, as-deposited Ni-P coating shows a much lower corrosion

rate. The corrosion rate of as-deposited Ni-P coating is approximately two orders of magnitude lower than that of the as-received AISI 1018 steel. Several reasons contribute to this exceptional corrosion resistance of the as-deposited Ni-P coating. First, this excellent corrosion resistance is due to its amorphous structure (Figure 4-6). Amorphous materials generally have high corrosion resistance due to the absence of grains and grain boundaries that are high energy sites and are susceptible to corrosion [66]. Second, the enriched elemental phosphorus in the coating (Figure 4-15 (c)) functions as barriers to impede the anodic dissolution of Ni [197]. Third, the formation of hypophosphite anions on the coating surface due to the reaction between elemental phosphorus and water shields the surface from the corrosive environment and attenuate corrosion action [198]. Additionally, the reducing nature of the hypophosphite anions may help mitigate the dissolution of Ni [198]. Last and most importantly, Ni can form passivation film (NiO) on surface, which blocks the further corrosion.

As-deposited Ni-P-Ti coatings exhibit higher corrosion resistance in comparison with as-deposited Ni-P coating (Table 4-13). The corrosion resistance of as-deposited Ni-P-Ti coatings improves as the Ti content increases from 5.1 wt% to 11.8 wt% within the coatings. On the other hand, the corrosion resistance of the as-deposited Ni-P-Ti coating decreases slightly when the Ti concentration reaches 15.2 wt%. Therefore, among the tested coatings, the Ni-P-Ti coating containing 11.8 wt% Ti has the highest corrosion resistance.

The corrosion characteristics of annealed samples are given in Table 4-14. The corrosion resistance of annealed AISI 1018 steel is superior to that of as-received AISI 1018 steel due to the removal of work hardened surface derived from the manufacturing process by annealing. The work hardened surface is highly vulnerable to corrosion, which suffers much rapid corrosion during the polarization test [199]. The corrosion rate of annealed Ni-P coating is one order of magnitude lower compared to the annealed AISI 1018 steel. In comparison with annealed Ni-P coating, annealed Ni-P-Ti coatings possess higher corrosion resistance. The corrosion resistance of annealed Ni-P-Ti coatings enhances with an increase in Ti content up to 11.8 wt%, whereas it slightly deteriorates when the Ti content rises to 15.2 wt%. The highest corrosion resistance is achieved on the annealed

11.8 wt% Ti coating. This result is in line with the trend for as-deposited Ni-P-Ti coatings observed in Table 4-13. Additionally, compared to the as-deposited coatings, the corrosion resistance of the annealed coatings is inferior due to crystallization of the Ni-P and depletion of elemental phosphorus on the coating surface by forming Ni_3P precipitates during annealing [200].

Table 4-13 Corrosion characteristics of as-deposited coatings derived from polarization curves

As-deposited	E_{corr} (V)	i_{corr} (A/cm^2)	CR (mm/year)
AISI 1018 steel	-0.629±0.021	1.55 ±0.15 × 10^{-5}	1.80±0.17
Ni-P	-0.419±0.025	1.06±0.13 × 10^{-6}	9.01±0.15 × 10^{-2}
5.1 wt% Ti	-0.387±0.011	3.20±0.10 × 10^{-7}	2.91±0.14 × 10^{-2}
11.8 wt% Ti	-0.391±0.009	2.80±0.09 × 10^{-7}	2.50±0.15 × 10^{-2}
15.2 wt% Ti	-0.359±0.013	4.31±0.11 × 10^{-7}	4.10±0.13 × 10^{-2}

Table 4-14 Corrosion characteristics of annealed coatings derived from polarization curves

Annealed	E_{corr} (V)	i_{corr} (A/cm^2)	CR (mm/year)
AISI 1018 steel-650°C	-0.542±0.032	1.43±0.17 × 10^{-5}	1.66±0.15
Ni-P-650°C	-0.327±0.023	1.32±0.14 × 10^{-6}	1.10±0.13 × 10^{-1}
5.1 wt% Ti-650°C	-0.304±0.013	4.11±0.13 × 10^{-7}	3.60±0.15 × 10^{-2}
11.8 wt% Ti-650°C	-0.335±0.015	3.58±0.15 × 10^{-7}	3.31±0.14 × 10^{-2}
15.2 wt% Ti-650°C	-0.295±0.013	4.72±0.13 × 10^{-7}	4.50±0.13 × 10^{-2}

In order to investigate the anti-corrosion mechanisms of as-deposited and annealed coatings, the porosity density (P.D.) of the coatings based on polarization testing was estimated by the following equation [201]:

$$P.D. = \frac{R_s}{R_c} \times 10^{-\frac{\Delta E}{\beta_\alpha}} \quad 4.15$$

Where, R_s is the polarization resistance of the AISI 1018 steel substrate, R_c is the polarization resistance of the coated samples, ΔE is the potential difference between the AISI 1018 steel substrate and the coated samples, and β_α is the slope of anodic Tafel extrapolation for the AISI 1018 steel substrate.

The porosity density of as-deposited and annealed coatings derived from the equation 4.15 are listed in Table 4-15. From Table 4-15, as-deposited Ni-P coating has higher porosity density compared to as-deposited Ni-P-Ti coatings. As Ti content increases to 11.8 wt% within the coating, the porosity density of as-deposited Ni-P-Ti coatings decreases due to the accommodation of nano-Ti particles to fit and fill the micro and nano pores in the Ni-P matrix [69]. However, the porosity density slightly increases as the Ti concentration continues to increase to 15.2 wt% due to the possible agglomeration of the particles [123, 124]. The lowest porosity density is realized on the as-deposited 11.8 wt% Ti coating that has the highest corrosion resistance (Table 4-13). An akin trend is also observed on the annealed coatings. The annealed Ni-P coating possesses the highest porosity density (9.27%). As the Ti content rises to 11.8 wt%, the porosity density of the annealed Ni-P-Ti coatings declines to 4.17%, whereas the porosity density rises to 5.44% with the Ti content increasing to 15.2 wt%. In addition, the polarization resistance (R_c) is found to be inversely proportional to the porosity density as seen in Table 4-13. The higher is the value of polarization resistance, the lower is the porosity density. The highest polarization resistance is attained on the as-deposited 11.8 wt% Ti coating that has the optimal corrosion resistance. Furthermore, by comparison with as-deposited coatings, the porosity density of annealed coatings is slightly increased due to the formation of pores by releasing a small amount of hydrogen during the annealing process and Kirkendall effect during annealing [35, 68].

Hasannaeimi et al. [37] investigated the annealing process of Ni-Ti coatings and noticed that some nano or micro pores are observed in the annealed coatings. They proposed that these pores may be a result of the Kirkendall effect due to the difference in the diffusivity of Ni and Ti atoms (Ni diffuses faster than Ti [51]). Therefore, as expected, the nano or micro pores can be observed on the Ni side, which increases the porosity density of the annealed coatings [68]. This increased porosity density undermines the corrosion resistance of the annealed coatings.

Table 4-15 Porosity density of as-deposited and annealed coatings estimated based on polarization testing

As-deposited	β_a (mV)	Rs/Rc (Ωcm^2)	P.D. (%)
1018 steel	120±11	2684±235	/
Ni-P	103±7	22799±947	8.11±0.25
5.1 wt% Ti	182±5	60678±1984	3.58±0.13
11.8 wt% Ti	147±7	64132±1846	3.17±0.12
15.2 wt% Ti	90±5	36779±712	4.80±0.15
1018 steel-650°C	118±8	2949±157	/
Ni-P-650°C	135±5	19019±455	9.27±0.33
5.1 wt% Ti-650°C	185±7	40208±789	4.90±0.17
11.8 wt%Ti-650°C	188±9	49365±1367	4.17±0.14
15.2 wt%Ti-650°C	198±3	30774±547	5.44±0.13

4.7.2 Electrochemical Impedance Spectroscopy Behavior of Coatings

To further study the anti-corrosion property of the coatings, electrochemical impedance spectroscopy (EIS) tests were implemented in a 3.5 wt% sodium chloride solution. The as-received and annealed 1018 steel were also examined for comparative study. Representative Nyquist and Bode/phase angle plots of as-deposited and annealed samples are shown in Figures 4-72 and 4-73, respectively. The dots characterize the experimental data, while the solid lines typify the fitted data that were generated using an equivalent electrical circuit. From Figures 4-72 (a) and 4-73 (a), capacitive semicircles are observed that are associated with the electrochemical arrangement between the electric-double layer capacitance and the charge transfer resistance [88]. The inductive loops related to the active dissolution process of the coating [202] are not observed inasmuch as the EIS tests were conducted at an open circuit state. From Figure 4-72 (a), It is also worth noting that the diameter of the capacitive semicircle for the as-deposited Ni-P-Ti coatings is larger compared to as-deposited Ni-P coating, and the diameter achieves a maximum value on the as-deposited 11.8 wt% Ti coating. Likewise, in comparison with the annealed Ni-P coating, an increase in diameter of the capacitive semicircle on the annealed Ni-P-Ti coatings is also observed (Figure 4-73 (a)). The maximum diameter value is obtained on the annealed 11.8 wt% Ti coating (Figure 4-73 (a)). Bode/phase angle plots of as-deposited and annealed samples are shown in Figures 4-72 (b) and 4-73 (b), respectively. It is observed that the shape of the phase angle plots of as-deposited and annealed Ni-P and Ni-P-Ti coatings does not change, while the peak positions and the maximum values vary. Compared to as-deposited Ni-P coating, the peak positions of the phase angle for as-deposited Ni-P-Ti coatings shift to higher frequencies (Figure 4-72 (b)). Compared to as-deposited Ni-P coating, the maximal values of the phase angle for as-deposited Ni-P-Ti coatings are higher, and the maximum phase angle is achieved on as-deposited 11.8 wt% Ti coating. Similar trends are also observed on the annealed coatings (Figure 4-73 (b)). These results are consistent with the observations in Fayyad et al.'s work [203].

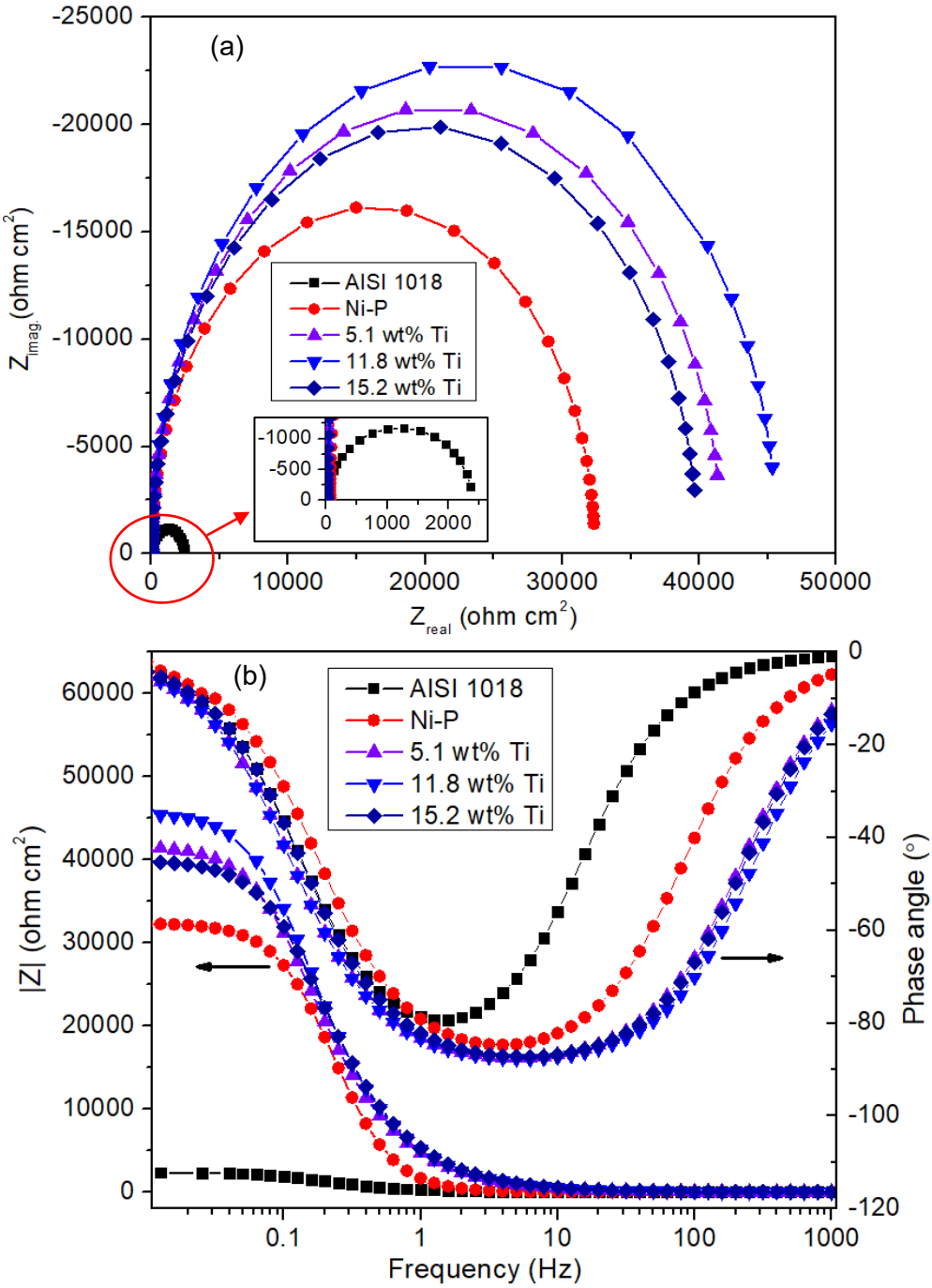

Figure 4-72 Representative (a) Nyquist and (b) Bode/phase angle plots of as-deposited samples.

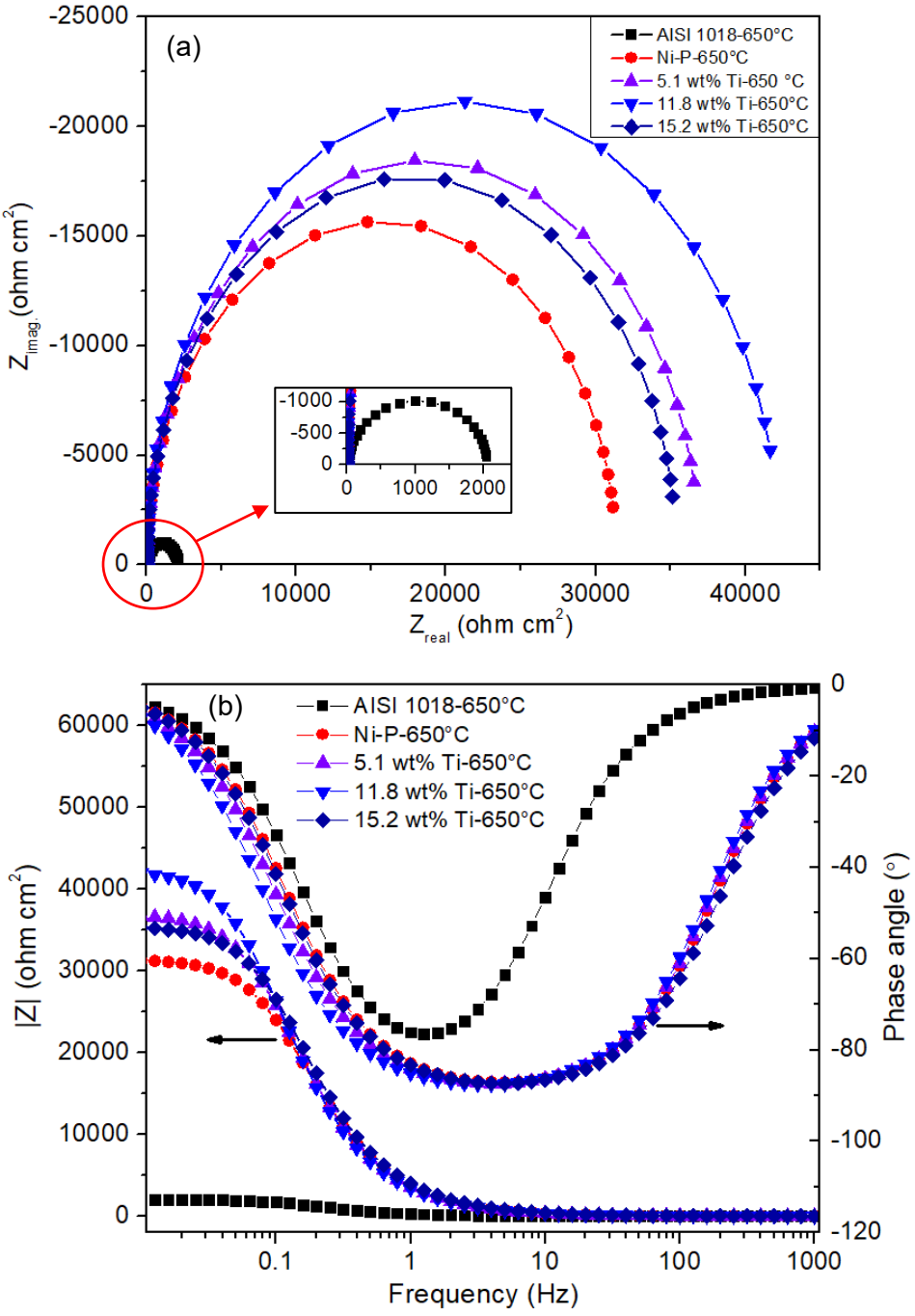

Figure 4-73 Representative (a) Nyquist and (b) Bode/phase angle plots of annealed samples.

The equivalent electrical circuit employed for fitting the EIS testing data is shown in Figure 4-74. In the equivalent electrical circuit, R_s is the solution resistance, CPE is the double layer constant phase element and R_{ct} is the charge transfer resistance or polarization resistance [204]. The charge transfer resistance (R_{ct}) is associated with the corrosion resistance of coatings, high value of the R_{ct} implies the high protective ability of the coatings [68, 204]. The CPE is related to the porosity density of coatings, lower value of the CPE suggests lower porosity density [69]. The fitting results using equivalent electrical circuit are given in Table 4-16. Compared to as-received 1018 steel, the charge transfer resistance of as-deposited Ni-P coating is one order of magnitude higher, suggesting that the as-deposited Ni-P coating possesses much higher corrosion resistance. As-deposited Ni-P-Ti coatings present superior charge transfer resistance compared to as-deposited Ni-P coating, and as the Ti content within the coating increases up to 11.8 wt%, the charge transfer resistance rises. However, the charge transfer resistance slightly drops when further increases the Ti concentration to 15.2 wt%, though the charge transfer resistance is still higher than that of the as-deposited Ni-P coating. An analogous trend of the charge transfer resistance is observed on the annealed coatings, as seen in Table 4-16. In addition, the charge transfer resistance of the annealed coatings is inferior to that of the as-deposited coatings, which indicates that the corrosion resistance of the coatings is compromised after annealing. The inferences derived from the EIS tests are in agreement with the results obtained from the polarization tests.

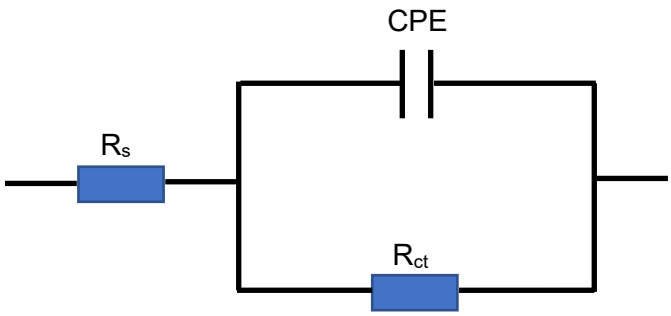

Figure 4-74 Equivalent electrical circuit for fitting EIS data

Table 4-16 Fitting results of EIS experimental data using equivalent electrical circuit

As-deposited	R_s (Ωcm^2)	CPE ($\mu F/cm^2$)	R_{ct} (Ωcm^2)
1018 steel	20.86±0.14	510±15	2132±175
Ni-P	21.29±0.25	35±5	32865±675
5.1 wt% Ti	20.93±0.17	29±3	41733±1283
11.8 wt% Ti	18.60±0.15	20±2	45778±1394
15.2 wt% Ti	22.54±0.32	32±4	39935±654
1018 steel-650°C	28.60±0.45	520±13	2452±213
Ni-P-650°C	20.06±0.16	47±4	31457±944
5.1wt% Ti-650°C	19.77±0.27	43±5	37846±676
11.8wt% Ti-650°C	19.73±0.13	36±7	42653±1185
15.2wt% Ti-650°C	19.24±0.21	45±3	36465±537

The porosity density (P.D.) estimated from the EIS tests premised on the faradic capacity (CPE) was first proposed by Creus et al. [201]. They suggested that the porosity density can be estimated from the faradic capacity (CPE) of the coated steel and the significant reduction in faradic capacity is due to the presence of more anti-corrosion coatings on the steel substrate [201]. They also implied that should the coating be denser, the lower is the faradic capacity value. Therefore, the porosity density can be estimated by dividing the capacity value of the coatings by that of the steel substrate [201]. The porosity density estimated from the EIS data is given in Table 4-17. As-deposited Ni-P-Ti coatings have lower porosity density in comparison with as-deposited Ni-P coating. For both as-deposited and annealed Ni-P-Ti coatings, as Ti concentration increases to 11.8 wt% within the coatings, the porosity density decreases; nevertheless, the porosity density slightly increases when the Ti concentration rises to 15.2 wt%, and the lowest porosity density is attained at the Ti concentration of 11.8 wt%. Although the specific values of porosity density obtained from EIS tests are of a little difference from those acquired from the potentiodynamic polarization (PP) tests (Table 4-15) due to the different testing and

calculation methods [201], the trend of the porosity density is similar in the two different tests.

Table 4-17 Porosity density estimated from EIS tests

As-deposited	P.D. (%)	Annealed	P.D. (%)
Ni-P	6.86±0.25	Ni-P-650	9.04±0.33
5.1 wt% Ti	5.69±0.13	5.1 wt% Ti-650°C	8.27±0.27
11.8 wt% Ti	3.92±0.14	11.8 wt% Ti-650°C	6.92±0.19
15.2 wt% Ti	6.27±0.17	15.2 wt% Ti-650°C	8.65±0.22

In order to identify the corrosion products on the coatings' surface, XRD tests were employed to characterize the samples after corrosion tests. XRD patterns of as-deposited and annealed samples are shown in Figure 4-75. Fe_2O_3 and NiO XRD peaks are observed on the XRD patterns of AISI 1018 steel substrate and as-deposited Ni-P coating (Figure 4-75 (a)), respectively. However, for as-deposited Ni-P coating, the NiO XRD peaks overlapped with the amorphous Ni-P peaks. For annealed samples, Fe_2O_3 and NiO XRD peaks are also observed on the XRD patterns of annealed AISI 1018 steel substrate and annealed Ni-P coating (Figures 4-75 (b) and (c)), respectively. For annealed Ni-P coating, the NiO XRD peaks overlapped with the Ni_3P XRD peaks. The XRD tests results suggest that the Fe_2O_3 are the main corrosion product on the as-received and annealed AISI 1018 steel substrate after corrosion tests, and the NiO is the dominant corrosion product on the as-deposited and annealed Ni-P coatings.

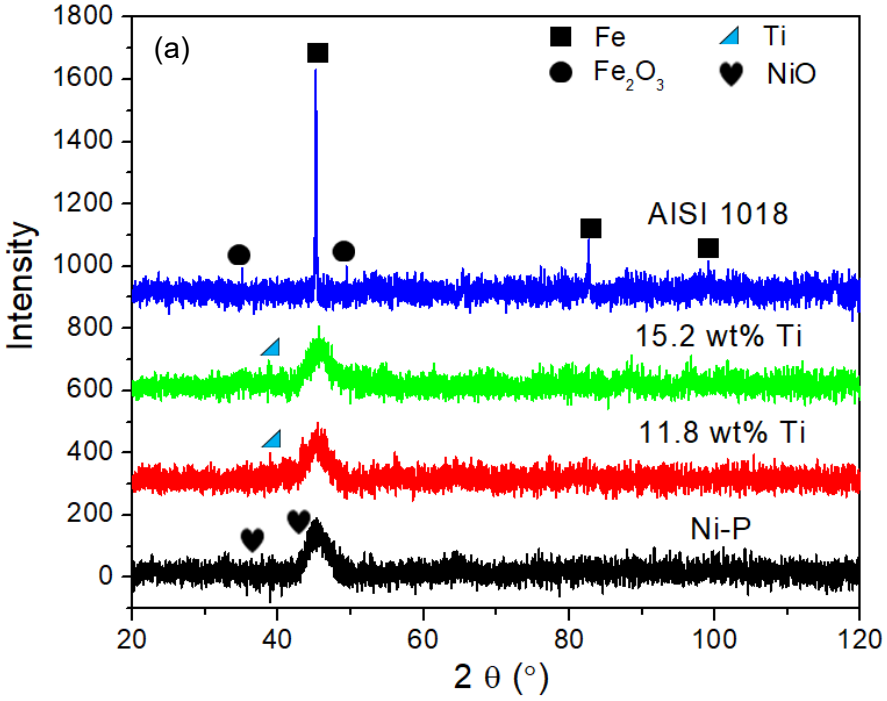
(a)
Fe
Ti
Fe_2O_3
NiO
AISI 1018
15.2 wt% Ti
11.8 wt% Ti
Ni-P
Intensity
2 θ (°)

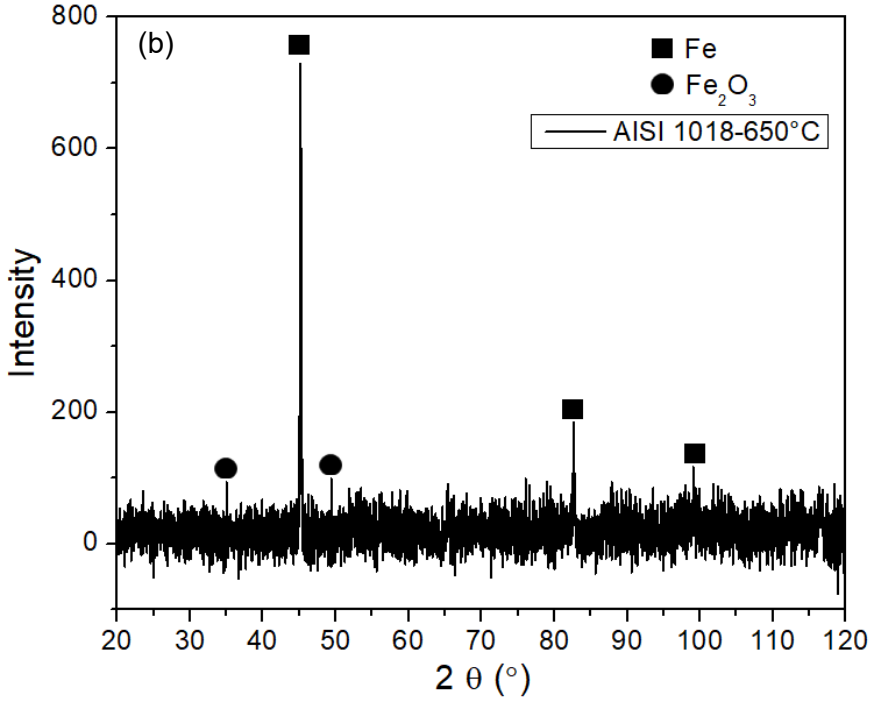
(b)
Fe
Fe_2O_3
AISI 1018-650°C
Intensity
2 θ (°)

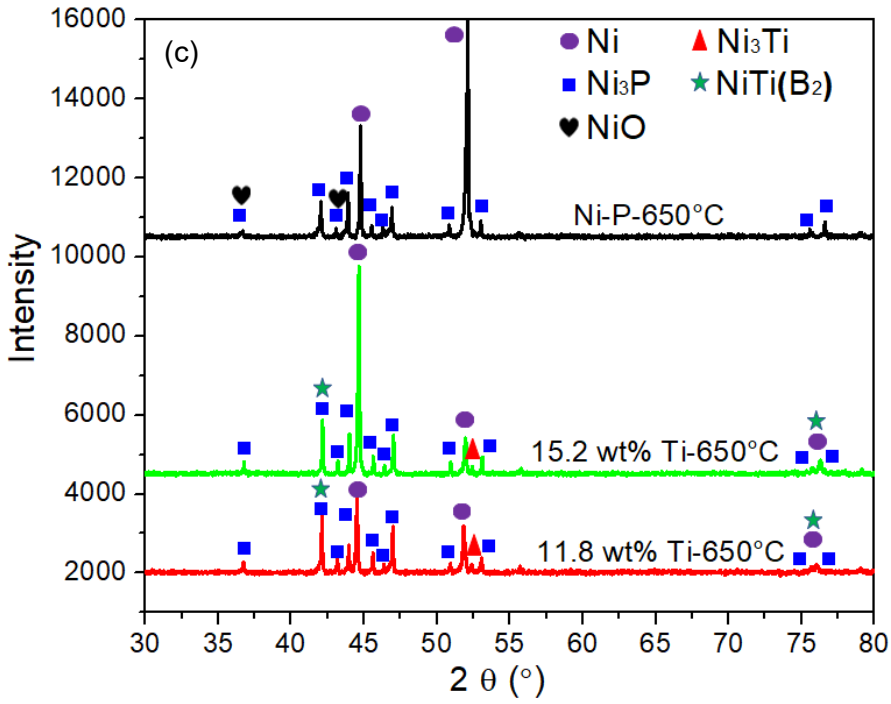

Figure 4-75 XRD patterns of as-deposited and annealed samples after corrosion tests, (a) as-deposited samples, (b) annealed AISI 1018 substrate, (c) annealed coatings.

To separate NiO XRD peaks from other XRD peaks and identify the NiO phase, slow scan XRD tests (step size: 0.01 deg/s) were employed. Figures 4-76 and 4-77 show the slow scan XRD patterns of as-deposited and annealed coatings, respectively. Standard XRD patterns of NiO [205] and Ni_3P [133] are also shown in Figures 4-76 and 4-77. For as-deposited coatings, NiO peaks are observed on the XRD patterns of as-deposited Ni-P coating, while no NiO peaks are detected on the XRD patterns of as-deposited Ni-P-Ti coatings (Figures 4-76 (a) and (b)). Similarly, for annealed coatings, NiO peaks are exhibited on the XRD patterns of annealed Ni-P coating, however, no NiO peaks are observed on the XRD patterns of annealed Ni-P-Ti coatings (Figure 4-77). Therefore, the slow scan XRD test results indicate that the main corrosion product on the as-deposited and annealed Ni-P coatings is the NiO, however, no NiO phase is formed on the as-deposited and annealed Ni-P-Ti coatings.

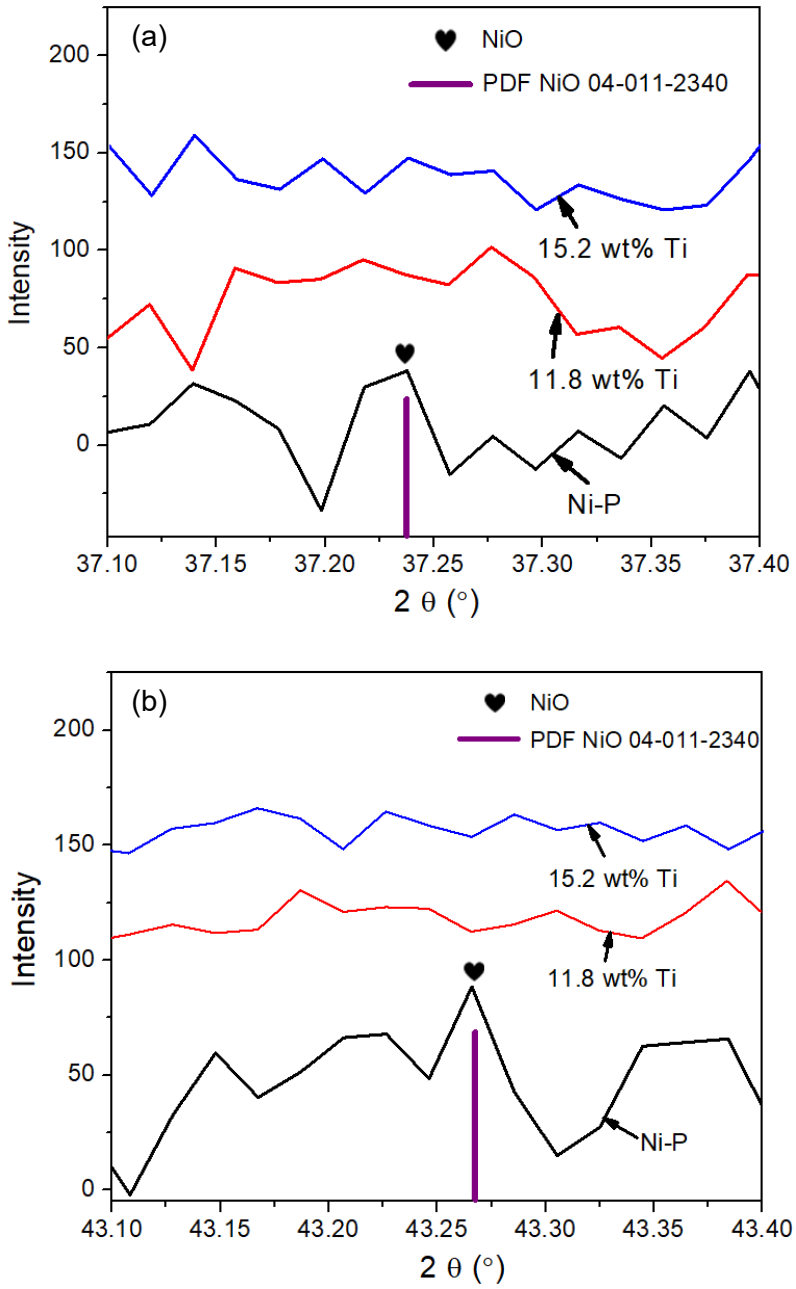

Figure 4-76 Slow scan XRD patterns of as-deposited coatings after corrosion tests (a) 2 theta angle range 37.10-37.40° (b) 2 theta angle range 43.10-43.40°

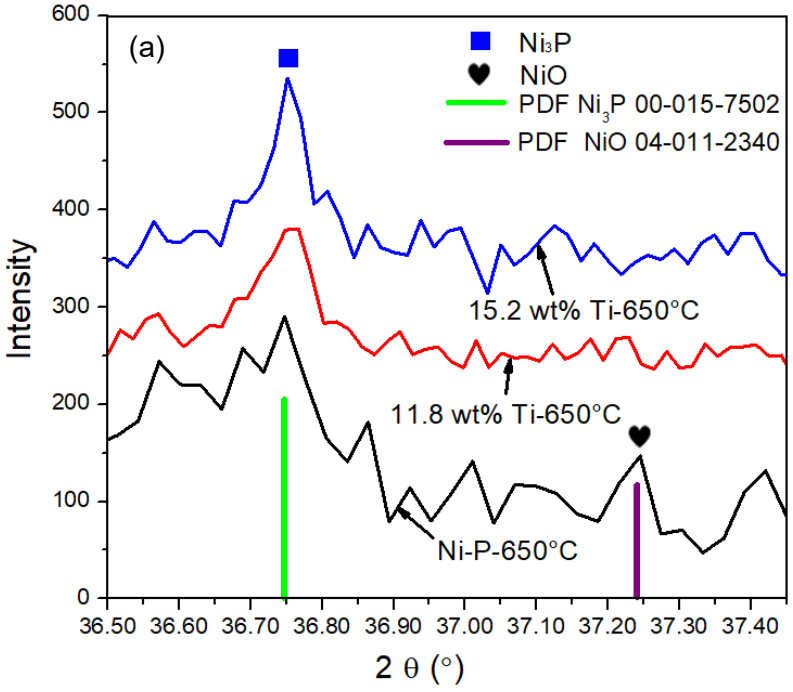
(a)
Ni3P
NiO
PDF Ni3P 00-015-7502
PDF NiO 04-011-2340
15.2 wt% Ti-650°C
11.8 wt% Ti-650°C
Ni-P-650°C
Intensity
2 θ (°)
600
500
400
300
200
100
0
36.50
36.60
36.70
36.80
36.90
37.00
37.10
37.20
37.30
37.40

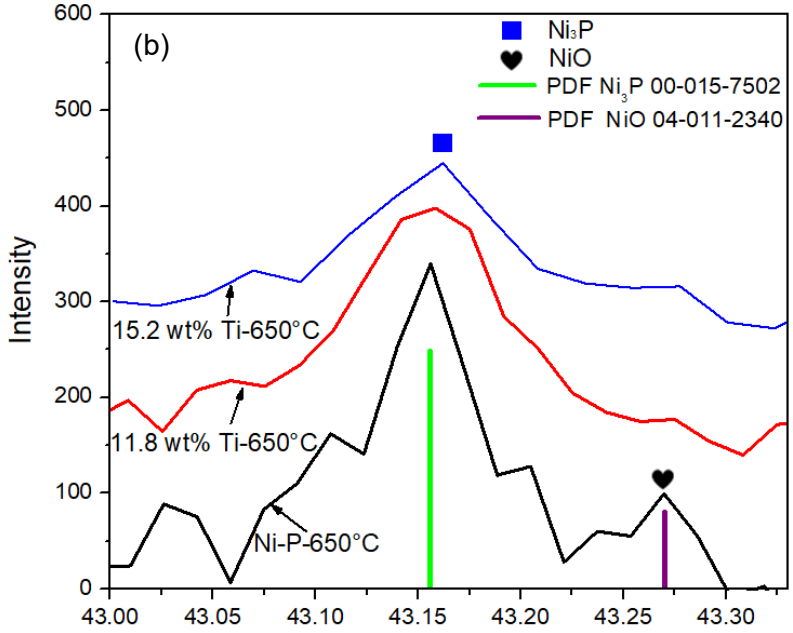
(b)
Ni3P
NiO
PDF Ni3P 00-015-7502
PDF NiO 04-011-2340
15.2 wt% Ti-650°C
11.8 wt% Ti-650°C
Ni-P-650°C
Intensity
600
500
400
300
200
100
0
43.00
43.05
43.10
43.15
43.20
43.25
43.30

Figure 4-77 Slow scan XRD patterns of annealed coatings after corrosion tests (a) 2 theta angle range 36.50-37.45° (b) 2 theta angle range 43.00-43.33°

Visual inspection of AISI 1018 steel, Ni-P and Ni-P-Ti coatings after polarization corrosion test is shown in Figure 4-78. For as-received and annealed AISI 1018 steel substrates, severe corrosion is widespread over the entire exposed surface. Compared to AISI 1018 steel, as-deposited and annealed Ni-P coatings show a much less corroded surface. On the other hand, as-deposited and annealed Ni-P-Ti coatings display uniform corroded and shiny metal surface after corrosion tests. No severe material degradation appears on the surface of as-deposited and annealed Ni-P-Ti coatings in visual inspection. Visual inspection of the different samples after corrosion test confirms the electrochemical testing results.

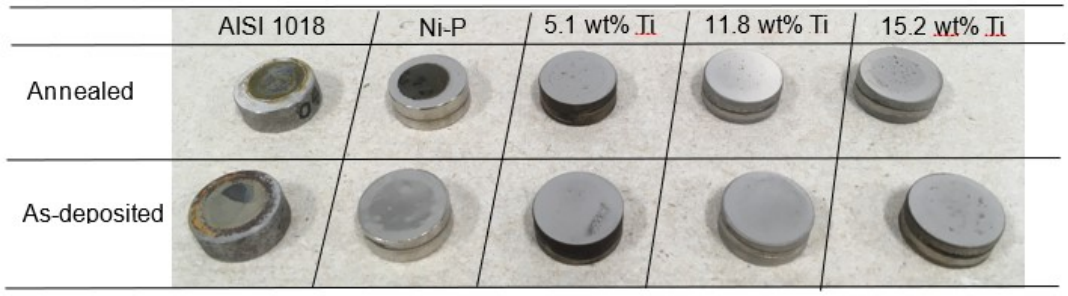

Figure 4-78 Visual inspection of sample surface after corrosion test

To further investigate the corrosion behavior of AISI 1018 steel, as-deposited and annealed Ni-P and Ni-P-Ti coatings, SEM and EDS examinations were conducted. Surface morphology micrographs and EDS test results of AISI 1018 steel substrate after corrosion test are shown in Figure 4-79. Severe corrosion morphologies are observed on AISI 1018 steel substrate (Figures 4-79 (a) and (b)). Cracks are also observed on the surface after corrosion test (Figure 4-79 (b)), reflecting the brittle nature of corrosion-product layer. From EDS test results (Figures 4-80 (c), (d), (e)), the sample surface appears to be severely oxidized. The oxygen content on the sample surface is very high (61.19 at%). Based on the XRD test results (Figure 4-79 (a)), this oxidation layer is identified to be Fe_2O_3. Minor amount of sodium and chlorine elements are also detected (Figure 4-79 (e)). This is

probably due to the penetration of corrosive solution (NaCl) into cracks. The EDS results are consistent with the XRD results.

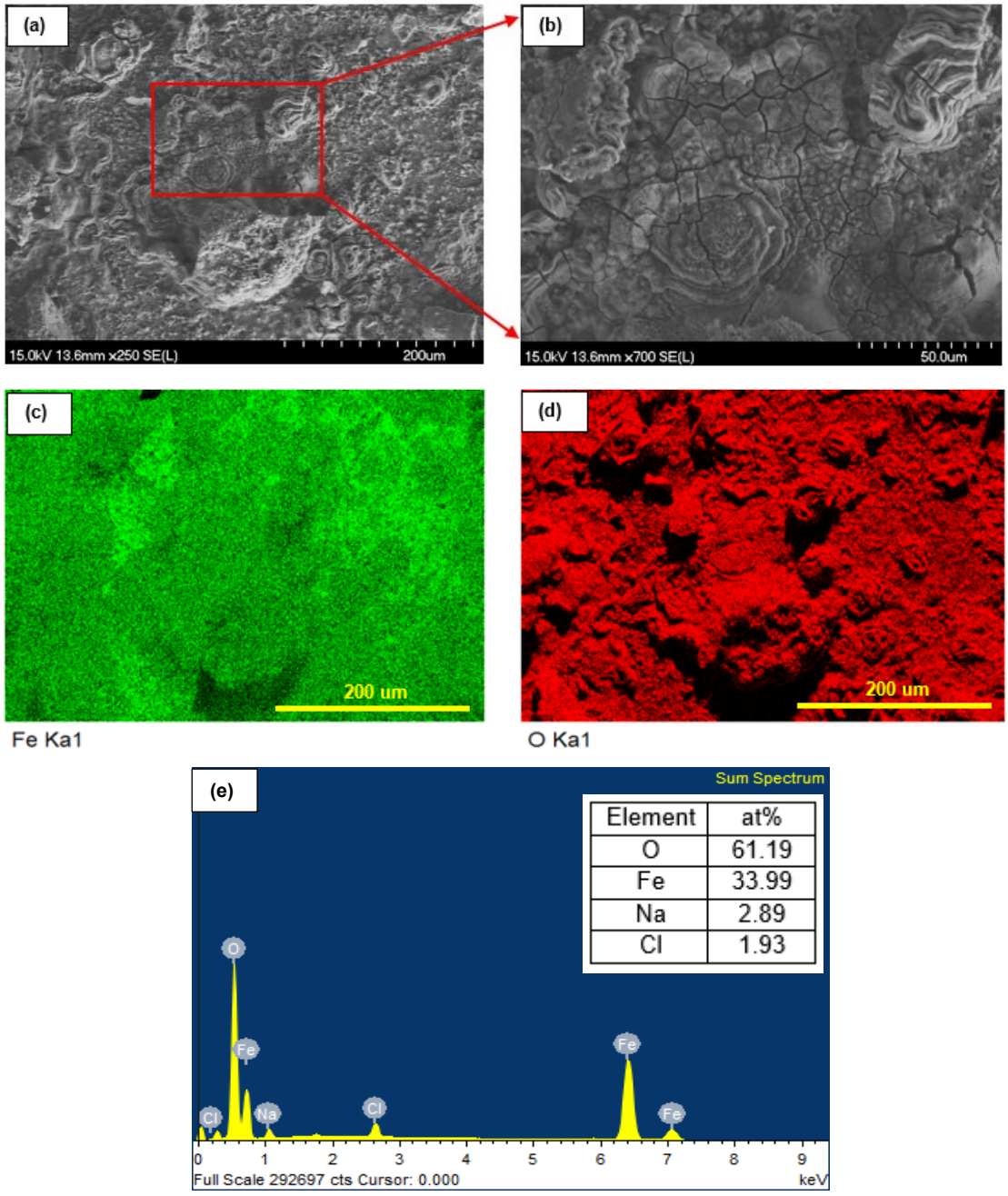

Figure 4-79 Surface SEM micrographs and EDS results of AISI 1018 steel substrate after corrosion test, (a) (b) surface SEM micrographs, (c) (d) EDS element map of Fe and O of area (a), (e) EDS spectrum of area (a)

Compared to AISI 1018 steel, milder corrosion with some pitting morphologies are observed on as-deposited and annealed Ni-P coatings (Figures 4-80 and 4-81 (a) and (b)). It is known that as-deposited Ni-P coatings have relatively high porosity due to hydrogen evolution during the oxidation of sodium hypophosphite in the electroless plating process [134]. These pore morphologies on as-deposited and annealed Ni-P coatings have been confirmed in Figure 4-13. These pores are vulnerable sites for pitting corrosion (Figures 4-80 and 4-81). For as-deposited and annealed Ni-P coatings, once a localized corrosion initiates at a small surface area with a defect (e.g. a small area with a pore), then the rest of surface area acts as cathode, which leads to a large cathode to anode area ratio. This large cathode to anode area ratio results in severe pitting corrosion (Figures 4-80 and 4-81 (a) and (b)) and high corrosion rates (Tables 4-13 and 4-14). From EDS test results (Figures 4-80 and 4-81 (c)-(f)), an oxidation layer is formed on the surface of as-deposited (oxygen content: 37.11 at%) and annealed (oxygen content: 38.82 at%) Ni-P coatings after corrosion test. Based on XRD test results (Figures 4-76 and 4-77), this oxidation layer is NiO. Therefore, the EDS results are in a good agreement with the XRD results.

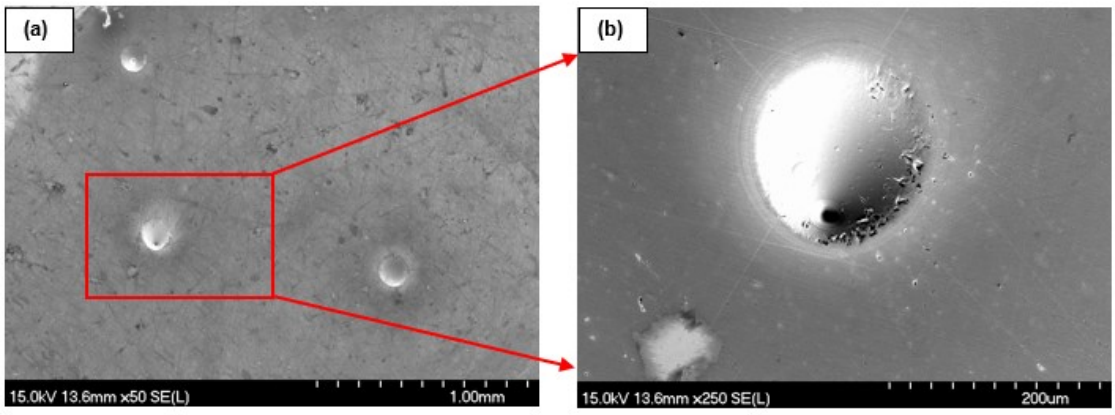

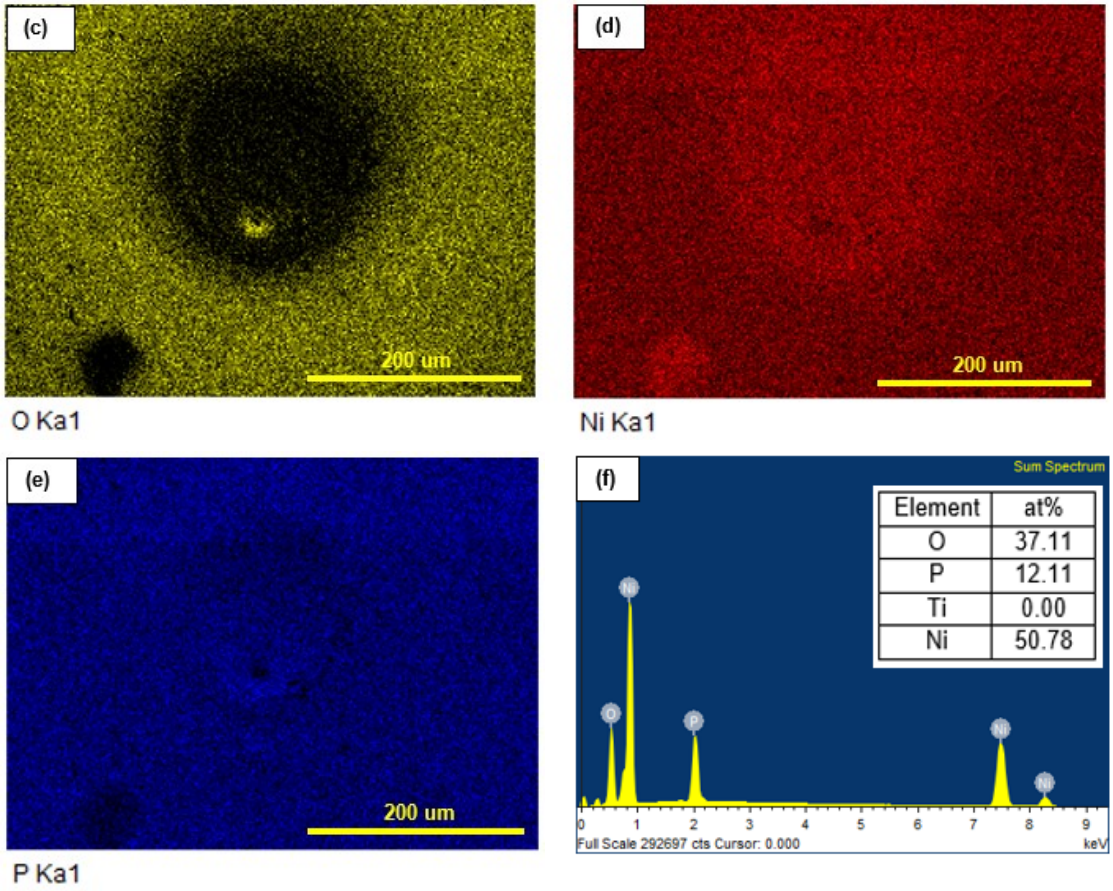

Figure 4-80 Surface SEM micrographs and EDS results of as-deposited Ni-P coating after corrosion test, (a) (b) surface SEM micrographs, (c) (d) (e) EDS element maps of area (b), (f) EDS spectrum of area (b)

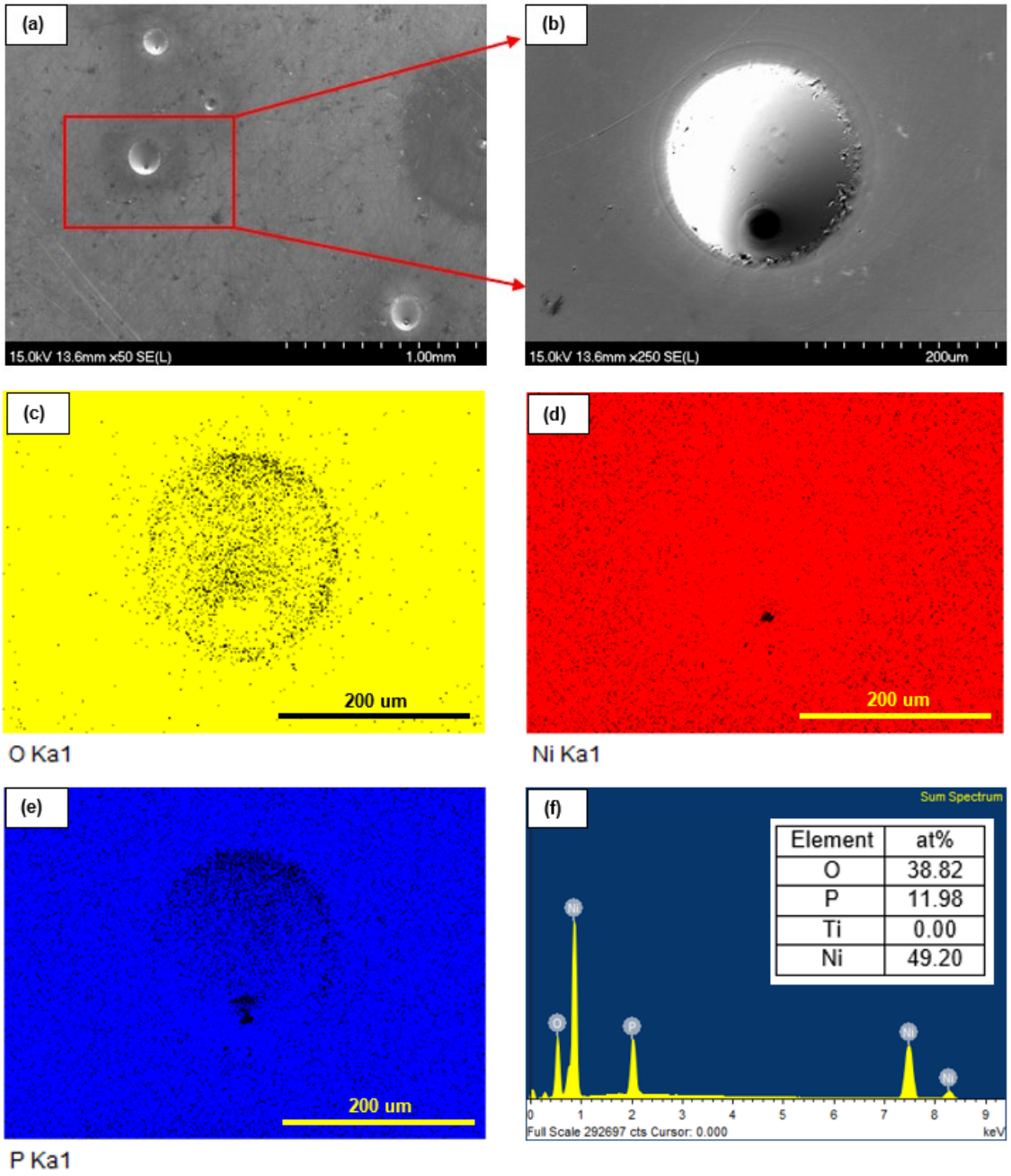

Figure 4-81 Surface SEM micrographs and EDS results of annealed Ni-P coating after corrosion test, (a) (b) surface SEM micrographs, (c) (d) (e) EDS element maps of area (b), (f) EDS spectrum of area (b)

On the other hand, unlike the as-deposited Ni-P coatings, as-deposited 11.8 wt% Ti coating undergoes uniform corrosion (Figures 4-82 (a) and (b)), which gives rise to a much lower corrosion rate (Table 4-13). Several anti-corrosion mechanisms may contribute to the improved corrosion resistance of as-deposited Ni-P-Ti coatings in comparison with as-deposited Ni-P coating. Firstly, for as-deposited Ni-P-Ti coatings, the uniformly distributed Ti particles (Figure 4-82 (f)) could prevent the localized corrosion by producing many uniformly distributed micro corrosion cells [206]. In the micro corrosion cells, the uniformly distributed Ti particles act as cathode and Ni acts as anode, since Ti is more noble than Ni in the galvanic series [207]. This arrangement significantly reduces the cathode to anode area ratio, which prevents pitting corrosion and decreases corrosion rate (Figures 4-82 (a) and (b)). Secondly, for as-deposited Ni-P coatings, the observed pores on the surface (Figure 4-13 (a)) are favorable sites for pitting corrosion (Figure 4-80 (b)); on the other hand, Ti nanoparticles have the capability to accommodate themselves to occupy the nano and micro pores in the Ni-P matrix (Figure 4-13 (a)), thus improving the impenetrability of as-deposited Ni-P-Ti coatings (Figure 4-82 (b)) [69]. From porosity density results in Table 4-15, it is observed that the porosity density of the as-deposited Ni-P-Ti coatings is much lower than that of the as-deposited Ni-P coating and the lowest porosity density is achieved on the 11.8 wt% Ti coating that possesses the highest corrosion resistance. This inference is further substantiated by the EIS testing results, as seen in Table 4-17. Thirdly, Ti nanoparticles exhibit a high tendency to form a thin layer of TiO_2 (Figures 4-82 (c) and (g)) on the particle surface in a corrosive environment due to high surface energy, as confirmed in the XRD patterns of as-received Ti powder (Figure 4-6). Furthermore, there is higher tendency to form TiO_2 than NiO, which is also confirmed by other researchers [203, 208]. This inert TiO_2 layer may impede anodic current, thus reduce the dissolution of Ni [69, 209]. In addition, compared to as-deposited Ni-P coating (oxygen content: 37.11 at%), the oxygen content is only 1.55 at% on the surface for as-deposited 11.8 wt% Ti coating. This is probably the reason why the NiO XRD peaks are not detected on the as-deposited 11.8 wt% Ti coating, and also suggests that the as-deposited 11.8 wt% Ti coating has high corrosion resistance.

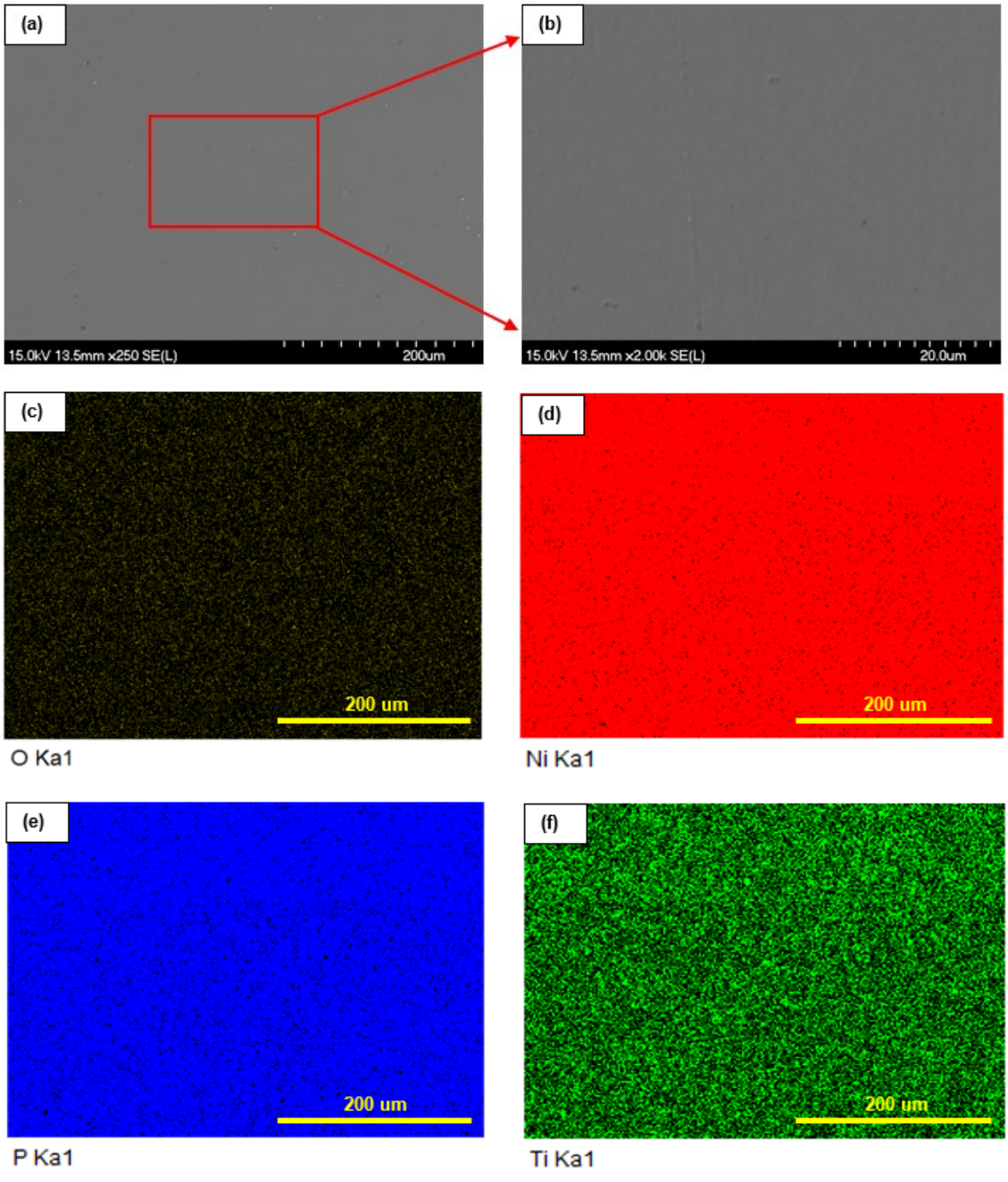
(a)
15.0kV 13.5mm x250 SE(L)
200um
(b)
15.0kV 13.5mm x2.00k SE(L)
20.0um
(c)
200 um
O Ka1
(d)
200 um
Ni Ka1
(e)
200 um
P Ka1
(f)
200 um
Ti Ka1

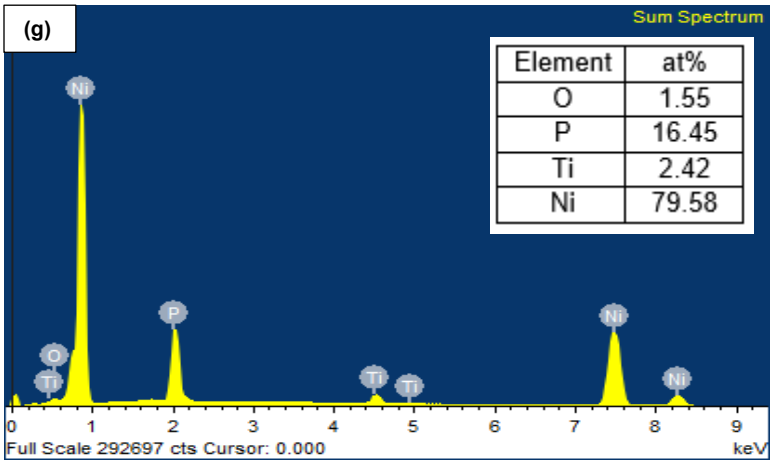

Figure 4-82 Surface SEM micrographs and EDS results of as-deposited 11.8 wt% Ti coating after corrosion test, (a) (b) surface SEM micrographs, (c) (d) (e) (f) EDS element maps of area (a), (g) EDS spectrum of area (a)

Similarly, annealed 11.8 wt% Ti coating shows a uniformly corroded surface (Figures 4-83 (a) and (b)), which has much higher corrosion resistance than annealed Ni-P coating (Table 4-14). This is mainly due to the formation of NiTi phase within the annealed 11.8 wt% Ti coatings (Figure 4-11) and low porosity density (Table 4-15). NiTi alloy is known for its high corrosion resistance and is more noble than crystallized Ni in the galvanic series [207]. Therefore, the uniformly distributed NiTi particles (Figures 4-83 (d) and (f)) within annealed Ni-P-Ti coatings act as cathode and the crystallized Ni acts as anode, which reduces cathode to anode area ratio and corrosion rate compared to annealed Ni-P coating. In addition, the porosity density of annealed Ni-P-Ti coatings is lower than annealed Ni-P coating (Table 4-15). Lower porosity density indicates high impenetrability of the coating (Figures 4-83 (a) and (b)), which blocks the penetration of electrolyte into the coating and improves corrosion resistance. Furthermore, Fayyad et al. suggested that titanium oxide formed on the surface of NiTi particles during electrochemical corrosion process improves the corrosion resistance of annealed Ni-P-NiTi coatings [203]. A minor amount (1.72 at%) of oxygen element is detected on the surface of annealed 11.8 wt% Ti coating. This may

explain why the NiO XRD peak is not observed on the annealed 11.8 wt% Ti coating, and also suggest the high corrosion resistance of the annealed 11.8 wt% Ti coating.

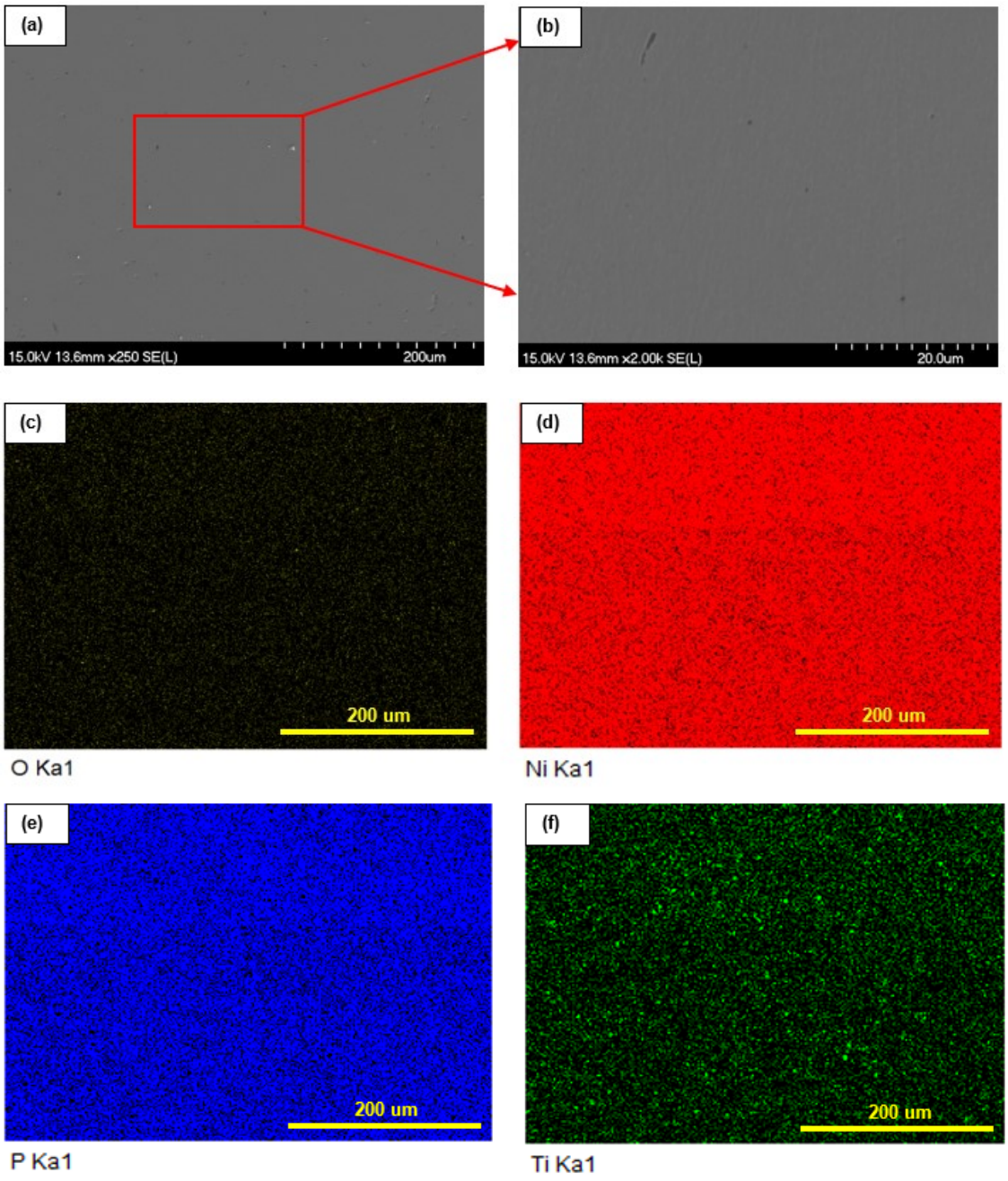

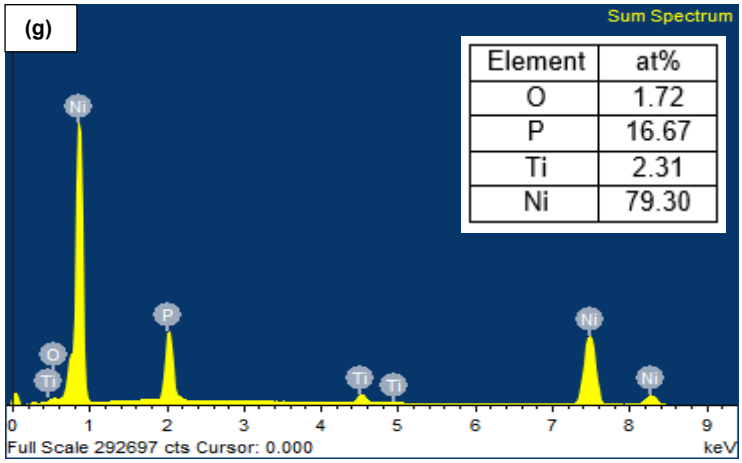

Figure 4-83 Surface SEM micrographs and EDS results of annealed 11.8 wt% Ti coating after corrosion test, (a) (b) surface SEM micrographs, (c) (d) (e) (f) EDS element maps of area (a), (g) EDS spectrum of area (a)

Base on the aforementioned test results, corrosion characteristics of different coatings are summarized in Table 4-18

Table 4-18 Corrosion characteristics of different coatings

Coatings	Corrosion characteristics
As-deposited Ni-P	• Pitting corrosion • high corrosion rate • high porosity density • formation of NiO layer on surface • Large cathode to anode area ratio
As-deposited Ni-P-Ti	• Uniform corrosion • Low corrosion rate • Small cathode to anode area ratio due to uniformly distributed Ti particles acting as cathode • Low porosity density due to the addition of Ti particle
Annealed Ni-P coating	• Pitting corrosion • High porosity density • formation of NiO layer on surface • high corrosion rate due to crystallization • Large cathode to anode area ratio
Annealed Ni-P-Ti coating	• Uniform corrosion • Low corrosion rate • Uniformly distributed NiTi particles act as cathode and Ni acts as anode, which decrease cathode to anode area ratio • Low porosity density • Ni Matrix crystallization decreases corrosion resistance compared to as-deposited Ni-P-Ti.

4.7.3 Effect of An Accidental Scratch on Static Corrosion Behavior

During installation and maintenance, an accidental scratch on coated components may lead to accelerated corrosion during operation. Cracking and fracture of protective coatings during scratching may lower the corrosion resistance, shorten the lifetime of the coatings, and even expose the vulnerable steel substrate under the coatings to a corrosive environment. Therefore, to investigate the influence of an accidental scratch on the corrosion resistance of the protective coatings, constant load of 40 N scratch tests were performed on API X100 steel, as-deposited and annealed Ni-P and Ni-P-Ti coatings. The material volume loss after scratch tests was calculated using the equation 3.13 (Chapter 3) The diameter of scratch indenter tip (0.4 mm); the scratch length is 3 mm; the width of scratch scar was measured by laser confocal microscope. The volume loss values of API X100 steel substrate, as-deposited and annealed coatings are shown in Figure 4-84 (a). The relative scratch resistance, calculated by dividing the volume loss of the substrate by that of the coatings, was used to rank the scratch resistance of different coatings in comparison with the reference material (API X100 steel) [210]. The relative scratch resistance of API X100 steel substrate, as-deposited and annealed coatings is shown in Figure 4-84 (b). The relative scratch resistance of as-deposited 11.8wt% Ti coating is higher than that of as-deposited Ni-P coating due to its higher toughness [4]; Similarly, compared to annealed Ni-P coating, annealed 11.8 wt% Ti coating has higher relative scratch resistance. In addition, the relative scratch resistance of annealed Ni-P coating is lower than that of as-deposited Ni-P coating due to its lower hardness. The relative scratch resistance data also clearly shows that the scratch resistance of the annealed 11.8 wt% Ti coating is significantly higher than that of the as-deposited 11.8 wt% Ti coating due to its high hardness and the formation of superelastic NiTi phase. Superelastic NiTi phase is known for its high scratch and wear resistance [211, 212]. The presence of the NiTi phase within the Ni-P-Ti coating after annealing improves its scratch resistance. Hence, the highest relative scratch resistance is achieved on annealed 11.8 wt% Ti coating, which is 5 times of the reference material.

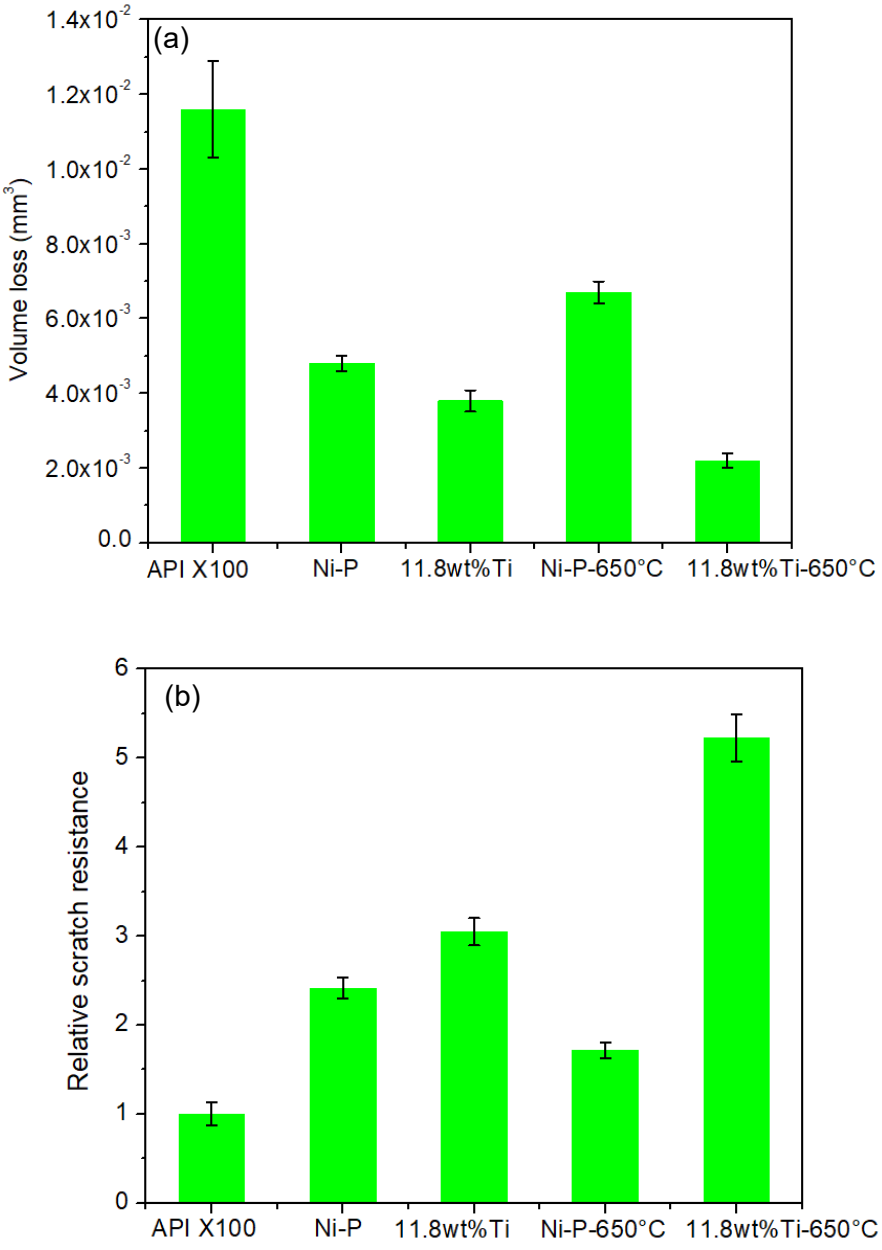

Figure 4-84 (a) volume loss and (b) relative scratch resistance of API X100 substrate, as-deposited and annealed coatings

In order to investigate the effects of scratching on corrosion resistance of coatings, potentiodynamic polarization (PP) and electrochemical impedance spectroscopy (EIS)

tests were performed on the coatings after scratch tests. Coatings surfaces with scratch scars (length: 3 mm) were exposed to a 3.5 wt% sodium chloride solution at room temperature. As-received API X100 steel substrate with a scratch scar was also tested for comparison. Representative PP curves of as-deposited and annealed coatings with scratch scars are shown in Figure 4-85. As expected, Ni-P and Ni-P-Ti coatings exhibit higher corrosion potential in comparison with the API X100 steel substrate. The corrosion potential (E_{corr}) and corrosion current density ((i_{corr}) were extracted from polarization curves using Tafel extrapolation. The corrosion rate (CR: mm/year) based on corrosion current density was calculated using the equation 4.14.

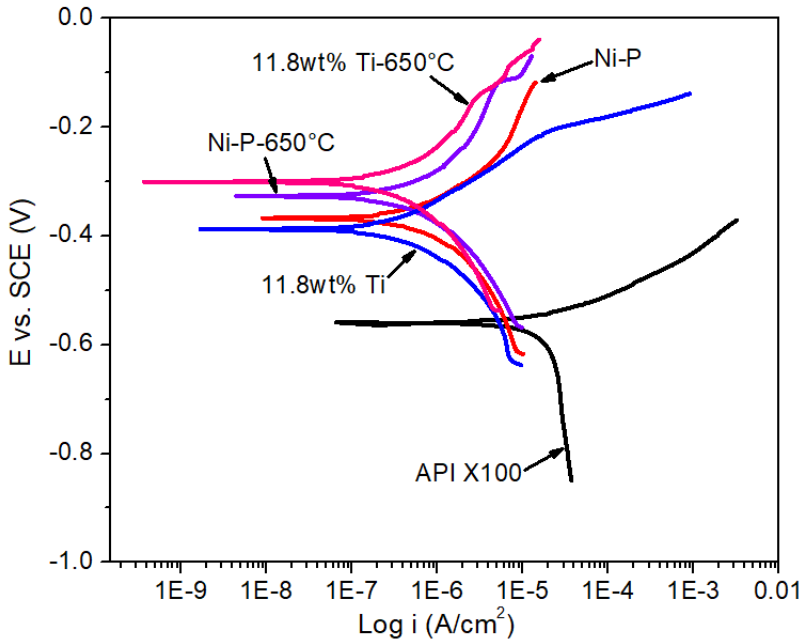

Figure 4-85 Representative polarization curves of as-deposited and annealed coatings with scratch scars

The corrosion characteristics of as-deposited and annealed coatings with scratch scars are summarized in Table 4-19. Compared to API X100 steel substrate, the corrosion current density of as-deposited Ni-P coating is one order of magnitude lower. Furthermore, the corrosion current density of as-deposited 11.8 wt% Ti coating is lower than that of the as-

deposited Ni-P coating. Similarly, the annealed 11.8 wt% Ti coating exhibits lower corrosion current density than annealed Ni-P coating. Compared to the as-deposited Ni-P coating, the annealed Ni-P coating shows lower corrosion current density due to its higher toughness. The annealed 11.8 wt% Ti coating also exhibits lower corrosion current density in comparison with the as-deposited 11.8 wt% Ti coating due to its improved toughness and high scratch resistance as a result of the formation of superelastic NiTi phase within the coating after annealing. The lowest corrosion current density is achieved on the annealed 11.8 wt% Ti coating.

Table 4-19 Corrosion characteristics of as-deposited and annealed coatings with scratch scars

Samples	E_{corr} (V)	i_{corr} (A/cm^2)
API X100 steel	-0.557±0.027	1.59±0.12 × 10^{-5}
Ni-P	-0.378±0.009	1.60±0.11 × 10^{-6}
11.8 wt% Ti	-0.381±0.011	3.96±0.07 × 10^{-7}
Ni-P-650°C	-0.317±0.007	1.47±0.09 × 10^{-6}
11.8 wt% Ti-650°C	-0.310±0.005	3.80±0.05 × 10^{-7}

The corrosion rates of as-deposited and annealed coatings with scratch scars are shown in Figure 4-86. The error bars in Figure 4-86 are the standard deviations of the tests results of three samples. Compared to API X100 steel substrate, the corrosion rate of as-deposited Ni-P coating is approximately one order of magnitude lower. The corrosion rate of as-deposited 11.8 wt% Ti coating is lower than that of as-deposited Ni-P coating.

Similar observations are also seen on annealed coatings (Figure 4-86). Annealed Ni-P coating shows one order of magnitude higher corrosion resistance than the API X100 steel substrate. The corrosion resistance of annealed 11.8 wt% Ti coating is approximately one order of magnitude higher than that of the annealed Ni-P coating due to its high scratch resistance.

Compared to the as-deposited Ni-P coating, the annealed Ni-P coating has higher corrosion resistance due to its improved toughness (Figure 4-86). Similarly, the corrosion resistance of the annealed 11.8 wt% Ti coating is higher than that of the as-deposited 11.8 wt% Ti coating. The highest corrosion resistance is reached on the annealed 11.8 wt% Ti coating among tested coatings.

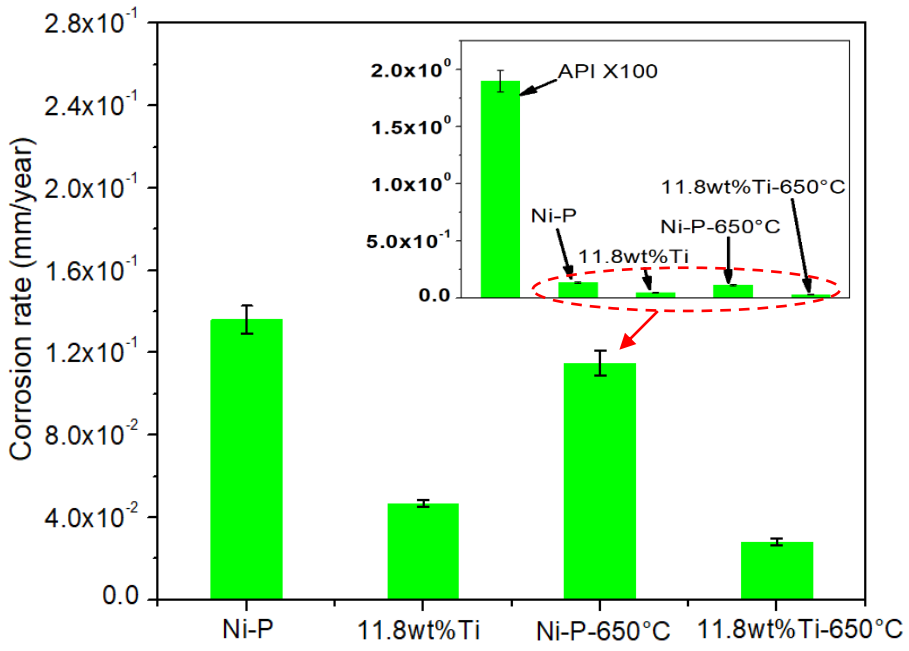

Figure 4-86 Corrosion rates of as-deposited and annealed coatings with scratch scars

To further investigate the corrosion performance of different coatings with scratch scars, electrochemical impedance spectroscopy (EIS) tests were conducted on as-deposited and annealed coatings with scratch scars. The as-received API X100 steel substrate with a scratch scar was also tested as a reference. The same equivalent electrical circuit (Figure 4-74) was utilized for fitting the EIS testing data. Representative Nyquist and Bode/phase angle plots of as-deposited and annealed coatings with scratch scars are shown in Figure 4-87. The dots characterize the experimental data, and the solid lines typify the fitted data that were generated using the equivalent electrical circuit. Capacitive semicircles related

to the electrochemical arrangement between the electric-double layer capacitance and the charge transfer resistance [88] are observed in Figures 4-87 (a). On the other hand, the inductive loops associated with the active dissolution of the coatings are not observed since the EIS tests were conducted at a low AC potential (10 mV) in a 3.5 wt% sodium chloride solution. In addition, compared to as-deposited Ni-P coating, the diameter of the capacitive semicircle for as-deposited 11.8 wt% Ti coating is larger (Figure 4-87). Similarly, an increase in diameter of the capacitive semicircle of the annealed 11.8 wt% Ti coating is also observed in comparison with annealed Ni-P coating (Figure 4-87). Bode/phase angle plots of as-deposited and annealed coatings with scratch scars are shown in Figure 4-87 (b). It is worth noting that the shape of the phase angle plots of as-deposited Ni-P and 11.8 wt% Ti coatings does not change, whereas the maximum values and peak positions vary. The peak position of the phase angle of the as-deposited 11.8 wt% Ti coating moves to higher frequency in comparison to the as-deposited Ni-P coating (Figure 4-87 (b)). The maximum phase angle value of the as-deposited 11.8 wt% Ti coating is higher than that of the as-deposited Ni-P coating. Similar trends are also observed on the annealed coatings (Figure 4-87 (b)).

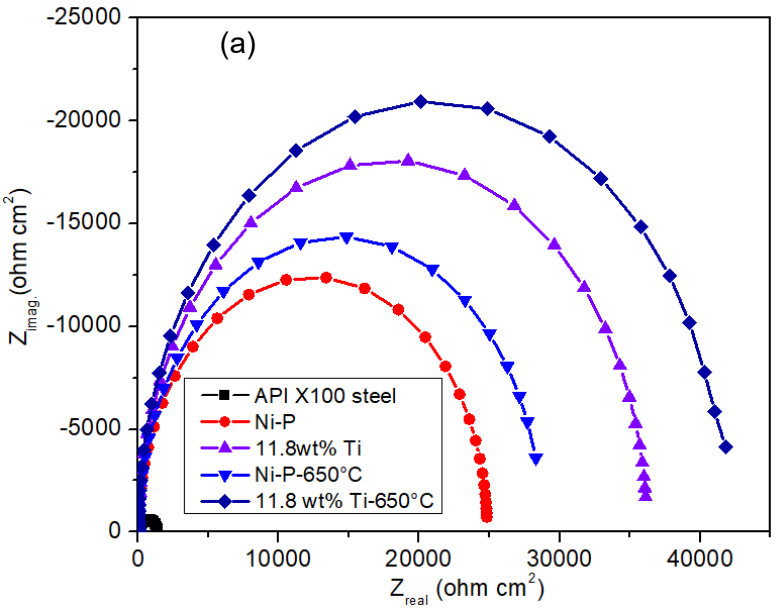

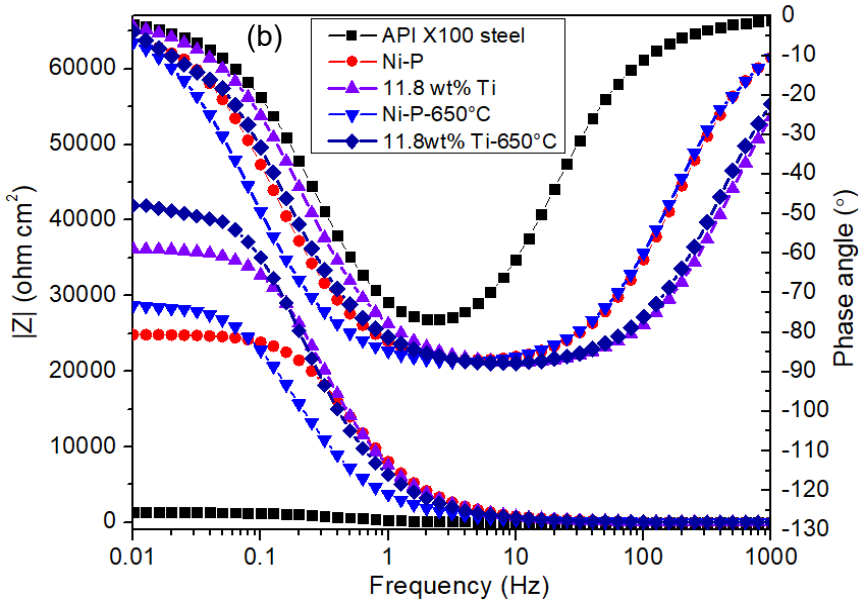

Figure 4-87 Representative (a) Nyquist and (b) Bode/phase angle plots of as-deposited and annealed coatings with scratch scars

Charge transfer resistance (R_{ct}) of as-deposited and annealed coatings with scratch scars is shown in Figure 4-88. Charge transfer resistance is closely related to corrosion resistance, high charge transfer resistance values represent high corrosion resistance [68, 204]. The charge transfer resistance value of API X100 steel is one order of magnitude lower than that of as-deposited Ni-P coating. Compared to as-deposited Ni-P coating, as-deposited 11.8 wt% Ti coating has higher charge transfer resistance. Similarly, the charge transfer resistance of annealed 11.8 wt% Ti coating is higher than that of annealed Ni-P coating. In addition, annealed Ni-P coating shows higher charge transfer resistance than the as-deposited Ni-P coating. The annealed 11.8 wt% Ti coating also exhibits higher charge transfer resistance in comparison with the as-deposited 11.8 wt% Ti coating due to the formation of the NiTi phase. The highest charge transfer resistance is achieved on the annealed 11.8 wt% Ti coating among the tested coatings. The results of charge transfer resistance are in good agreement with the corrosion rates results (Figure 4-86).

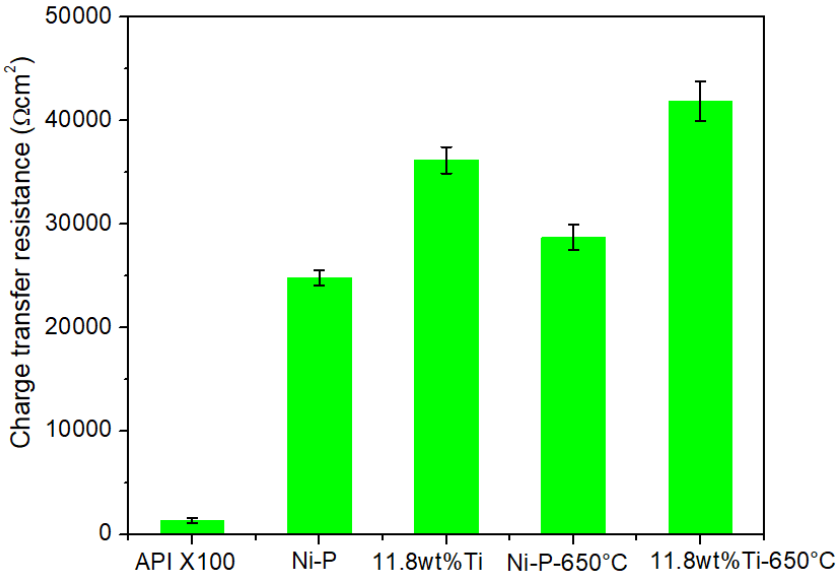

Figure 4-88 Charge transfer resistance of as-deposited and annealed coatings with scratch scars

The presence of superelastic NiTi phase in the annealed 11.8 wt% Ti coating has been confirmed by XRD and EDS. NiTi is known for its high scratch and wear resistance due to its superelastic effect [213, 214]. For conventional metallic materials, in order to relieve the strain energy during scratch or wear, plastic deformation occurs [213]. On the other hand, for superelastic NiTi alloy, the strain energy is absorbed to induce martensitic phase transformation and stored in martensite variants, which improves the scratch resistance [212]. It is found that the addition of superelastic NiTi into composite materials can improve their scratch and impact resistance [215].

In the present study, it is observed that the annealed 11.8 wt% Ti coating exhibits higher scratch resistance than other coatings (Figure 4-84 (b)). This improvement in scratch resistance by the formation of superelastic NiTi within the coatings can be ascribed to two factors. First, the presence of superelastic NiTi particles inhibits the nucleation and propagation of microcracks during scratching due to transformation toughening

mechanism [214]. Second, the stress-induced martensitic phase transformation can absorb strain energy, which prevents severe plastic deformation [212]. Therefore, the presence of superelastic NiTi phase in the annealed Ni-P-Ti coating improves its scratch resistance. In order to confirm the applied stress during scratching process was sufficient to induce the martensitic phase transformation, the average contact stress (p_0) was calculated using the equations 3.27-3.40. Here, P is the applied load (40 N). R is the radius of the scratch indenter (200 μm). Assuming that $v_1 = 0.3$ [216] and $E_1 = 50$ GPa acquired from tensile test for the annealed 11.8 wt% Ti coating and $v_2 = 0.25$, $E_2 = 1050$ GPa for the scratch indenter [115], then the average contact stress is equal to 3.3 GPa, which is higher than the stress (100-400 MPa [24, 141, 142]) required for martensitic phase transformation at 25 °C. Hence, during the scratching process, stress-induced martensitic phase transformation is expected within the annealed 11.8 wt% Ti coating.

Scratch tests were performed on as-deposited and annealed Ni-P and Ni-P-Ti coatings under a high constant load (40 N). After scratch tests, the scratch scars were examined under laser confocal microscope. The laser confocal micrographs of scratch scars on as-deposited Ni-P and annealed Ni-P-Ti coatings are shown in Figure 4-89. Severe cracking is observed on the as-deposited Ni-P coating after scratch test (Figure 4-89 (a)). Hertzian cracks cross the scratch scar and some cracks even propagate outside of the scratch scar. On the other hand, no obvious cracks are observed inside or outside of the scratch scar on the annealed 11.8 wt% coating (Figure 4-89 (b)). At higher magnification, very fine cracks (crack size: 2-5 μm) are observed at the edge of the scratch scar on the annealed 11.8 wt% Ti coating (Figure 4-89 (c)). In comparison with the as-deposited Ni-P coating, cracks observed on the annealed 11.8 wt% Ti coating are less, finer, and shallower due to the transformation toughening induced by superelastic NiTi particles. Transformation toughening induced by a superelastic NiTi particle is shown in Figure 4-89 (d). During the scratching process, the applied stress is higher than the required stress for martensitic phase transformation, which has confirmed by the calculation of average contact stress. When a crack encounters a NiTi particle, austenite phase in the NiTi particle transforms to a detwinned martensite phase, resulting in a large amount of energy absorption and an increase in the particle's volume [216, 217]. The energy absorption decreases the driving

force for crack propagation and the increased volume results in a compressive stress field around the crack tip. The compressive stress field further reduces the driving force for crack propagation and subsequently decreases the stress intensity at the crack tip. Ultimately, the crack completely loses driving force and is prevented by the superelastic NiTi particle. Transformation toughening significantly improves the toughness of the annealed Ni-P-Ti coating.

From a corrosion point of view, cracks on coatings surface increase the porosity of the coatings, which are favorable sites for pitting corrosion. The presence of cracks on the coatings increases the available surface area for localized corrosion and decreases the corrosion resistance of the coatings. Compared to the as-deposited Ni-P coating, the annealed 11.8 wt% Ti coating exhibits less, finer, and shallower cracks on the coating surface after scratch test, which significantly reduces the available surface area for localized corrosion. Also, finer and shallower cracks retard the penetration of electrolyte into the coating and prevent the exposure of the more vulnerable steel substrate to a corrosive environment compared to larger and deeper cracks on the as-deposited Ni-P coating. Therefore, due to the presence of superelastic NiTi particles, the corrosion resistance of the Ni-P coating is significantly improved during an accidental scratch event.

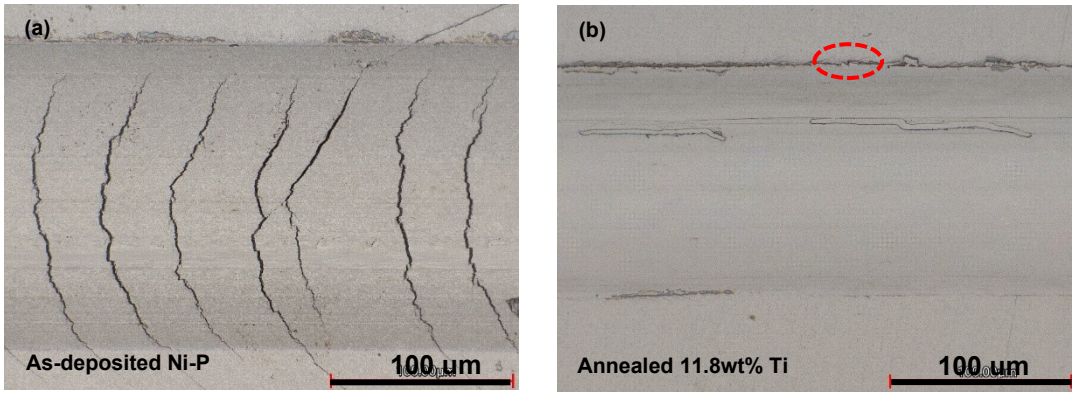

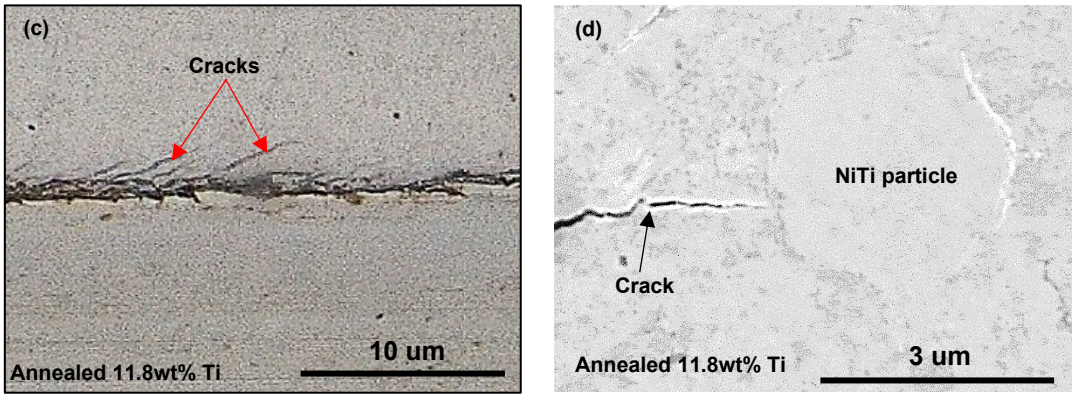

Figure 4-89 Laser confocal surface micrographs of scratch scars (a) as-deposited Ni-P coating, (b) annealed 11.8 wt% coating and (c) magnified micrograph of the marked area in Figure (b), (d) SEM micrograph of transformation toughening observed on annealed 11.8 wt% Ti coating

In order to confirm that the presence of cracks on coating surface increases the available surface area (cracks and pores area) for localized corrosion, the porosity density (P.D.) of the coatings with scratch scars based on polarization testing was estimated by the equation 4.15 (Section 4.7). The parameters utilized to calculate the porosity density of as-deposited Ni-P coating and annealed 11.8 wt% Ti coating with scratch scars are listed in Table 4-20.

Table 4-20 Parameters utilized to calculate the porosity density of as-deposited Ni-P and annealed 11.8 wt% Ti coatings with scratch scars

Samples	β_a (mV)	R_s or R_c (Ωcm^2)	ΔE (V)
API X100 steel	194±11	2821±157	/
Ni-P	78±9	12994±534	0.179±0.013
11.8wt%Ti-650°C	119±13	49365±1754	0.247±0.009

Porosity density is highly related to the corrosion resistance of coatings since the cracks and pores on coating surface are the favorable sites for pitting corrosion. Porosity density is reversely proportional to the corrosion resistance [69]. The higher is porosity density, the lower is the corrosion resistance. Porosity density of as-deposited Ni-P coating and annealed 11.8 wt% Ti coating with scratch scars calculated using the equation 4.15 is shown in Figure 4-90. Compared to as-deposited Ni-P coating, annealed 11.8 wt% Ti coating has much lower porosity density. This is mainly because of two factors. Firstly, for the as-deposited Ni-P coating, some pores are formed on the coating surface due to the evolution of hydrogen during the oxidation of sodium hypophosphite in the electroless plating process [134]. These pores increase the porosity density of the as-deposited Ni-P coating. For the annealed 11.8 wt% coating, on the other hand, nano-Ti particles could fill the pores in the Ni-P matrix during electroless plating, which decrease its porosity density. Secondly, Large, and dense cracks are observed on the as-deposited Ni-P coating after scratch test (Figure 4-89 (a)). These cracks significantly increase the porosity density of the as-deposited Ni-P coating. On the other hand, cracking on the annealed 11.8 wt% Ti coating is much less severe than on the as-deposited Ni-P coating (Figure 4-89 (b)) due to transformation toughening (Figure 4-89 (d)). Transformation toughening induced by superelastic NiTi particles improves the toughness of the annealed 11.8 wt% Ti coating, which results in less, finer, and shallower cracks on the coating surface after scratch test in comparison with the as-deposited Ni-P coating. Therefore, lower porosity density is observed on the annealed 11.8 wt% Ti coating that has higher corrosion resistance compared to the as-deposited Ni-P coating during an accidental scratch event due to the presence of superelastic NiTi phase.

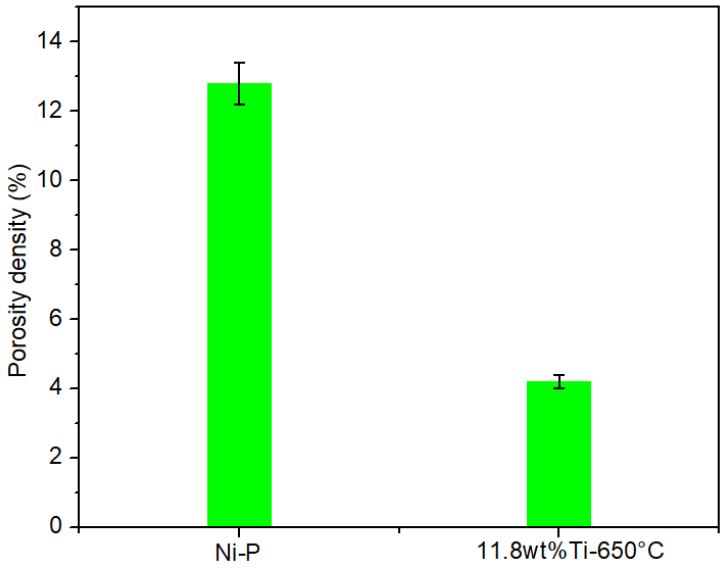

Figure 4-90 Porosity density of as-deposited Ni-P and annealed 11.8 wt% Ti coatings with scratch scars.

4.8 Erosion-Corrosion Behavior

4.8.1 Erosion-Corrosion Behavior of As-deposited Coatings

To study the pure corrosion resistance of AISI 1018 steel, Ni-P and Ni-P-Ti coatings, potentiodynamic polarization (PP) tests were conducted in 3.5 wt% sodium chloride solution (in the absence of abrasive particles) under flowing condition (900 rpm). Potentiodynamic polarization curves for tested samples are shown in Figure 4-91. Compared to AISI 1018 steel, the potentiodynamic polarization curves of Ni-P and Ni-P-Ti coatings shift to a higher potential position. The corrosion current density (i_{corr}) and corrosion potential (E_{corr}) were extracted from polarization curves using Tafel extrapolation. Corrosion rate (CR: mm/year) was calculated using the equation 4.15.

Table 4-21 shows corrosion characteristics of AISI 1018 steel, Ni-P and Ni-P-Ti coatings derived from polarization curves. Compared to AISI 1018 steel, Ni-P coating shows a much lower corrosion rate. The corrosion rate of Ni-P coating is approximately one-third of the AISI 1018 steel. Several reasons may contribute to this exceptional corrosion resistance. First, Ni-P amorphous coating exhibits superior corrosion resistance relative to the crystalline counterparts due to the absence of grains and grain boundaries [66]. Secondly, the dissolution rate of P is much lower than that of Ni, resulting in an enrichment of the elemental P surface [197]. This phosphorus enriched layer functions as a barrier that blocks the primary dissolution sites and prohibits the anodic dissolution [197]. Thirdly, as the dissolution process advances, the enriched phosphorus in the surface reacts with water to form hypophosphite anions [198]. These hypophosphite anions are absorbed on the coating surface, which shields the coating surface from water, prevents the formation of nickel hydrate, hinders the anodic dissolution of Ni and eventually passivates the coating surface [197, 203]. Also, the highly reducing nature of the hypophosphite anions may help prevent the dissolution of Ni [197]. Lastly, Ching [218] observed that phosphorus can function as an acceptor that is capable of receiving approximately 0.6 electrons from Ni in a Ni-20P alloy, which forms a chemical binding between Ni and P, resulting in higher activation

energy for Ni dissolution during corrosion process compared to pure Ni coating. Diegle et al [197] confirmed that this donor-acceptor behavior may improve the activation energy for the anodic dissolution of Ni, which results in enhanced corrosion resistance of the Ni-20P amorphous alloy. Furthermore, the formation of passive film (NiO) on coating surface under flowing condition also contributes to the high corrosion resistance [219].

The corrosion rates of Ni-P-Ti coatings are approximately one order of magnitude lower than that of Ni-P coating (Table 4-21). As the Ti content increases, the corrosion rate of Ni-P-Ti coatings decreases and the lowest corrosion rate is achieved on the 15.2 wt% Ti coating (Table 4-21), which indicates that the corrosion resistance is improved as the Ti content rises. Several anti-corrosion mechanisms are proposed to explain the enhancement of the corrosion resistance of Ni-P-based composite coatings in comparison with Ni-P coating. Abdel [206] studied the corrosion resistance of Ni-TiO_2 composite coating and indicated that TiO_2 particles play a pivotal role in enhancing the corrosion resistance. Firstly, the inert TiO_2 particles act as barriers to refine the microstructure of the Ni matrix during deposition, thereby lowering the corrosion rate [206]. Secondly, the uniformly dispersed TiO_2 particles prevent localized corrosion by producing uniformly distributed corrosion micro cells [206]. In the present study, Ti particles were incorporated in the Ni-P matrix. Ti nanoparticles exhibit a higher tendency than Ni to form a oxide layer on the surface [203, 208]. Therefore, the anti-corrosion mechanisms proposed by Abdel [206] could be employed to explain the improved corrosion resistance of Ni-P-Ti coatings. In addition, it is believed that nanoparticles can accommodate themselves to fill the nano and micropores in the Ni-P matrix, thus improving the impermeability of the coatings [69]. Hence, considering the anti-corrosion mechanisms discussed above, superior corrosion resistance of Ni-P-Ti coatings may be due to the formation of TiO_2 layer, barrier effect and decreased porosity density.

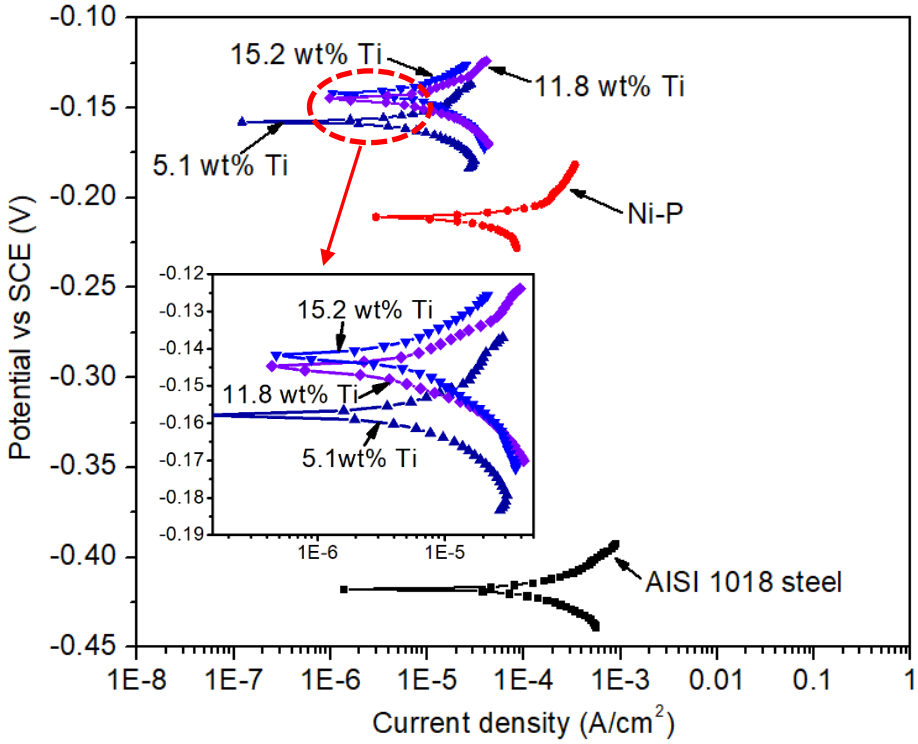

Figure 4-91 Representative potentiodynamic polarization curves (in the absence of abrasive particle) for AISI 1018 steel, Ni-P and Ni-P-Ti coatings under flowing condition (900 rpm).

Table 4-21 Corrosion characteristics of tested samples derived from polarization curves in the absence of abrasive particles under flowing condition (900 rpm)

Samples	E_{corr} (V)	i_{corr} (μA/cm^2)	CR (mm/year)
AISI 1018 steel	-0.415 ± 0.005	92.1 ± 0.7	10.70 ± 0.08
Ni-P	-0.219 ± 0.004	33.1 ± 0.5	2.81 ± 0.05
5.1 wt% Ti	-0.157 ± 0.007	4.8 ± 0.2	4.21 ± 0.03 × 10^{-1}
11.8 wt% Ti	-0.143 ± 0.002	4.5 ± 0.1	4.11 ± 0.02 × 10^{-1}
15.2 wt% Ti	-0.141 ± 0.003	3.4 ± 0.2	3.24 ± 0.03 × 10^{-1}

To investigate the effects of abrasive particles on corrosion resistance, total corrosion rates were measured using potentiodynamic polarization (PP) technique in 3.5 wt% NaCl solution in the presence of abrasive particles under flowing condition (900 rpm). Figure 4-92 shows potentiodynamic polarization curves for tested samples in the presence of abrasive particles. The corrosion potential of Ni-P and Ni-P-Ti coatings is much higher than AISI 1018 steel, which indicates higher corrosion resistance in the presence of abrasive particles. Compared to the polarization curves of Ni-P-Ti coatings in the absence of abrasive particles (Figure 4-91), the corrosion potential of the coatings in Figure 4-92 is less noble due to the presence of abrasive particles. Tafel extrapolation was employed to extract the corrosion potential (E_{corr}) and corrosion current density (i_{corr}) from potentiodynamic polarization curves. Corrosion rates were calculated using the equation 4-15. Corrosion characteristics of AISI 1018 steel, Ni-P and Ni-P-Ti coatings are summarized in Table 4-22.

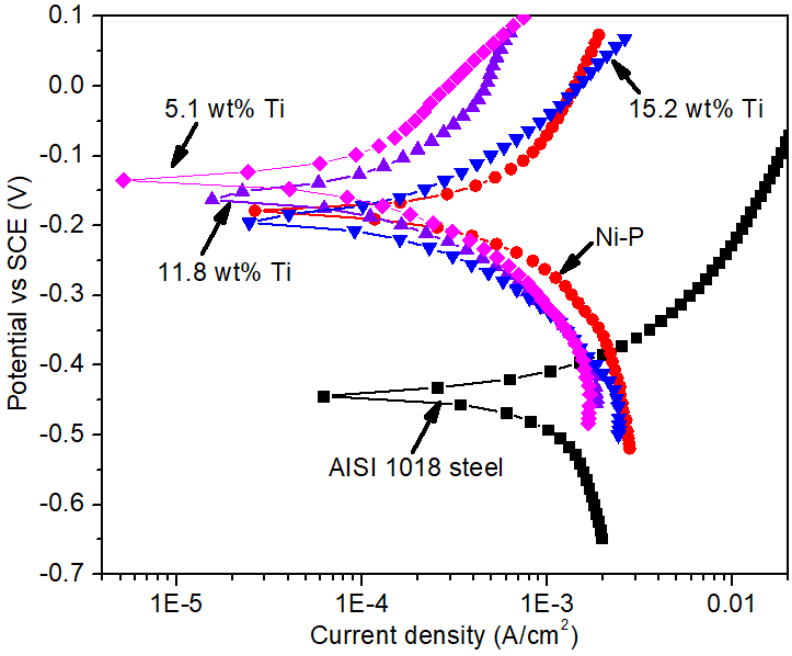

Figure 4-92 Potentiodynamic polarization curves (in the presence of abrasive particle) for AISI 1018 steel, Ni-P and Ni-P-Ti coatings under flowing condition (900 rpm)

Total corrosion rates of AISI 1018 steel and Ni-P coating in presence of abrasive particles (Table 4-22) are approximately one order of magnitude higher than the pure corrosion rates in absence of abrasive particles (Table 4-21), while the difference in corrosion rates increases to two orders of magnitude for Ni-P-Ti coatings. In comparison with as-deposited Ni-P coating, as-deposited Ni-P-Ti coatings exhibit a much lower total corrosion rate. The total corrosion rates of as-deposited 5.1 wt% Ti, 11.8 wt% Ti, and 15.2 wt% Ti coatings are only 26.0%, 29.6%, and 33.7% of the as-deposited Ni-P coating, respectively. It is important to note that, in the presence of erosive particles, a slight decrease in corrosion resistance was observed as Ti content increases. Erosive particles remove passive films, which expose the fresh and more vulnerable surface to the corrosive solution [220, 221]. In the absence of abrasive particles, Ti particles exposed to the corrosive solution have a high tendency to form an oxide layer, which protects the coating from corrosion [203, 208]. However, in the presence of abrasive particles, as the Ti content increases, more TiO_2 layers are formed on the Ti particles' surface, which are then removed by abrasive particles, resulting in a higher corrosion rate.

Table 4-22 Corrosion characteristics of samples derived from polarization curves in the presence of abrasive particles under flowing condition (900 rpm)

Samples	E_{corr} (V)	i_{corr} ($\mu A/cm^2$)	CR (mm/year)
AISI 1018 steel	-0.448 ± 0.005	800 ± 7	92.8 ± 0.6
Ni-P	-0.169 ± 0.004	437 ± 5	49.6 ± 0.5
5.1 wt% Ti	-0.136 ± 0.005	137 ± 3	12.9 ± 0.3
11.8 wt% Ti	-0.146 ± 0.003	162 ± 2	14.7 ± 0.2
15.2 wt% Ti	-0.170 ± 0.002	174 ± 3	16.7 ± 0.4

The total erosion-corrosion (E-C) rate (K_{ec}), erosion only rate (K_{eo}), corrosion only rate (K_{co}), total synergy rate (K_s), and the synergistic components (erosion enhanced corrosion rate (ΔK_c) and corrosion enhanced erosion rate (ΔK_e)) of AISI 1018, Ni-P and Ni-P-Ti coatings are displayed in Figure 4-93.

Due to its higher hardness, Ni-P coating exhibits superior pure erosion resistance to AISI 1018 steel (Figure 4-93). Additionally, the addition of Ti improves the pure erosion resistance. Although the hardness of Ni-P-Ti coatings slightly drops as Ti content increases, the toughness increases due to the ductile particle toughening [108]. Jang et al suggested that the shear banding energy can be absorbed and the principal shear band can be branched into small shear bands by the dispersed ductile Ti particles, which in turn decreases stress concentration and improves toughness [222]. This increase in the toughness may improve the erosion resistance of the Ni-P-Ti coatings [108].

During erosion-corrosion, Ni-P coating displays a lower material loss rate than the AISI 1018 steel (Figure 4-93). On the other hand, the total erosion-corrosion rates of 5.1 wt% Ti, 11.8 wt% Ti and 15.2 wt% Ti coatings are only 50.7%, 36.3%, and 31.9% of that of Ni-P coating, respectively, suggesting that the total erosion-corrosion resistance improves with the increase in Ti content. The total erosion-corrosion resistance is dependent on pure corrosion, pure erosion, and synergy resistance. As the Ti content increases within the composite coatings, the total synergy rate and pure erosion rate decrease, which results in a lower total erosion-corrosion rate.

The total synergy rate decreases as Ti content increases up to 11.8 wt% which is then increased slightly when the Ti content is 15.2 wt% (Figure 4-93). Compared to pure erosion or pure corrosion, the synergistic effect is more complex. Synergy is composed of erosion enhanced corrosion and corrosion enhanced erosion contribution. It is worth noting that the corrosion enhanced erosion rate is much higher than the erosion enhanced corrosion rate, which suggests that corrosion enhanced erosion is dominant in the total synergy. Corrosion increases the surface roughness of the material. Erosion is highly dependent on the impact

angle, which varies as the surface roughness increases, thus resulting in a higher erosion rate [221, 223]. As Ti content increases, more Ti particles fill the pores in the Ni-P matrix, which increases the impermeability of composite coatings and thus improving the corrosion resistance. For Ni-P-Ti coating with 15.2 wt% Ti, both erosion enhanced corrosion and corrosion enhanced erosion are equally responsible for higher synergy contribution.

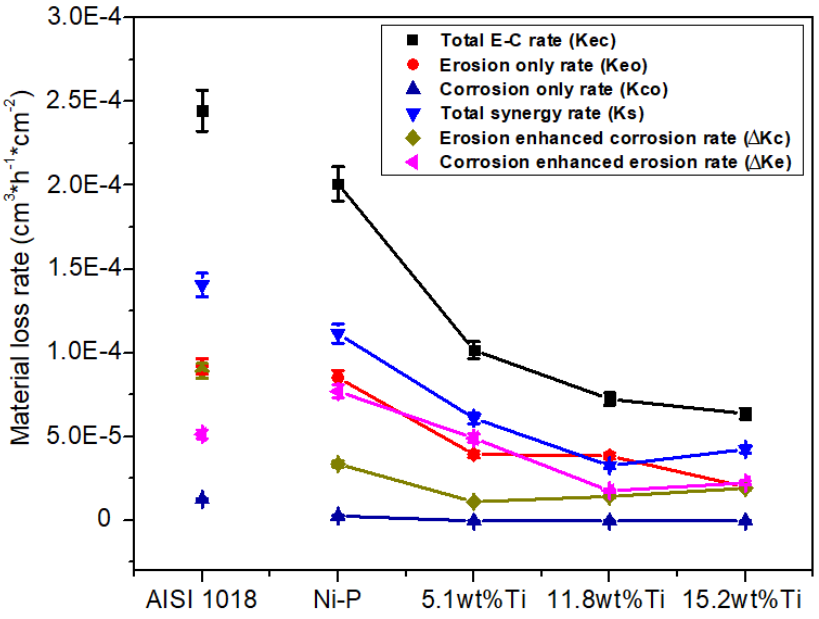

Figure 4-93 Material loss rate contributions of different components during erosion-corrosion

In order to study the corrosion mechanisms of composite coatings, the porosity density (P.D.) of the coatings based on polarization testing was estimated using the equation 4.15. Porosity density of coatings during pure corrosion in the absence of abrasive particles under flowing condition (900 rpm) derived from the equation 4.15 are summarized in Table 4-23. Ni-P coating has much higher porosity density due to the formation of hydrogen during the oxidation of $NaPO_2H_2$ in the electroless plating process [134]. The porosity density value of Ni-P coating is 2.55 %, which is close to the value (2.40%) reported in the literature [69]. The porosity density of Ni-P-Ti coating is one order of magnitude lower

than that of Ni-P coating. This is mainly because Ti nanoparticles can accommodate themselves to fit and fill the micro or nano-pores in the Ni-P matrix [69]. As the Ti content increases, more Ti particles fill the pores that result in lower porosity density. This explained why the corrosion resistance of Ni-P-Ti coatings improves with the increase in Ti content. Gheshlaghi et al. found that the corrosion resistance of Ni-P coating is considerably increased by the addition of WO_3 nanoparticles and suggested that the impermeability of the coating is improved by filling the pores with nanoparticles [209]. Allahkaram et al. calculated the porosity density of Ni-P-nanodiamond composite coatings and found that the porosity density decreases as the nanodiamond content increases within the coatings, which results in improved corrosion resistance [69]. The porosity density results are well consistent with the pure corrosion results (Table 4-21).

Table 4-23 Porosity density of coatings during pure corrosion in the absence of abrasive particles under flowing condition (900 rpm)

Samples	β_a (mV)	R_s or R_c (Ω cm^2)	P.D. (%)
1018 steel	17.3 ± 1.9	44.6 ± 1.7	/
Ni-P	15.6 ± 1.7	129.9 ± 1.5	2.55 ± 0.05
5.1 wt%Ti	19.3 ± 1.5	895.4 ± 1.2	0.16 ± 0.03
11.8 wt% Ti	20.3 ± 1.2	922.6 ± 1.4	0.13 ± 0.02
15.2 wt% Ti	15.4 ± 1.3	988.7 ± 1.3	0.12 ± 0.03

The porosity density of the coatings during corrosion in the presence of abrasive particles under flowing condition (900 rpm) derived from the equation 4.15 are summarized in Table 4-24. The coatings exhibit much higher porosity density in the presence of abrasive particles than in the absence of abrasive particles (Table 4-23). The impacts of abrasive particles cause a high strain layer on the coating surface, which is more anodic and highly vulnerable to corrosion [220]. During the corrosion process, the abrasive particles break

the passive NiO film and expose the fresh surface to the corrosive environment. Due to the breakdown of the protective film, pits are initiated at the surface, which increase the porosity density. Compared to Ni-P coating, Ni-P-Ti coatings have much lower porosity density due to their higher erosion resistance. As the Ti content increases, the porosity density of the composite coatings increases slightly, which is consistent with the total corrosion results presented in Table 4-22.

Table 4-24 Porosity density of coatings during corrosion in the presence of abrasive particles under flowing condition (900 rpm)

Samples	β_a (mV)	Rs or Rc (Ω cm^2)	P.D. (%)
1018 steel	141.6 ± 3.5	57.4 ± 5.5	/
Ni-P	501.9 ± 4.7	141.6 ± 4.3	29.01 ± 0.05
5.1 wt%Ti	284.1 ± 2.5	304.9 ± 5.9	11.96 ± 0.03
11.8 wt% Ti	217.7 ± 3.4	242.2 ± 3.6	12.33 ± 0.05
15.2 wt% Ti	241.5 ± 2.8	212.8 ± 5.2	13.04 ± 0.02

To investigate the surface morphologies during erosion-corrosion, the AISI 1018 steel samples' surface before and after erosion-corrosion for 30 mins was examined using SEM and EDS. Based on EDS results, it is confirmed that iron oxide (Fe_xO_y) layer (at% of Fe: 33%, at% of O: 67%) is formed on the surface after erosion-corrosion test (Figure 4-94). Figure 4-95 (a) shows the optical micrograph of AISI 1018 steel before erosion-erosion, which shows the surface is smooth and flat. After erosion-corrosion, severe surface degradation is observed (Figures 4-95 (b), (c) and (d)). During erosion-corrosion, an oxide layer is formed on the AISI 1018 steel surface due to corrosion. As the thickness of the oxide layer increases, it becomes brittle. This brittle oxide layer then undergoes cracking and fracture due to abrasive particle impact (Figures 4-95 (c) and (d)). The removal of the oxide layer exposes the fresh iron surface to corrosion, which accelerates the material loss rate.

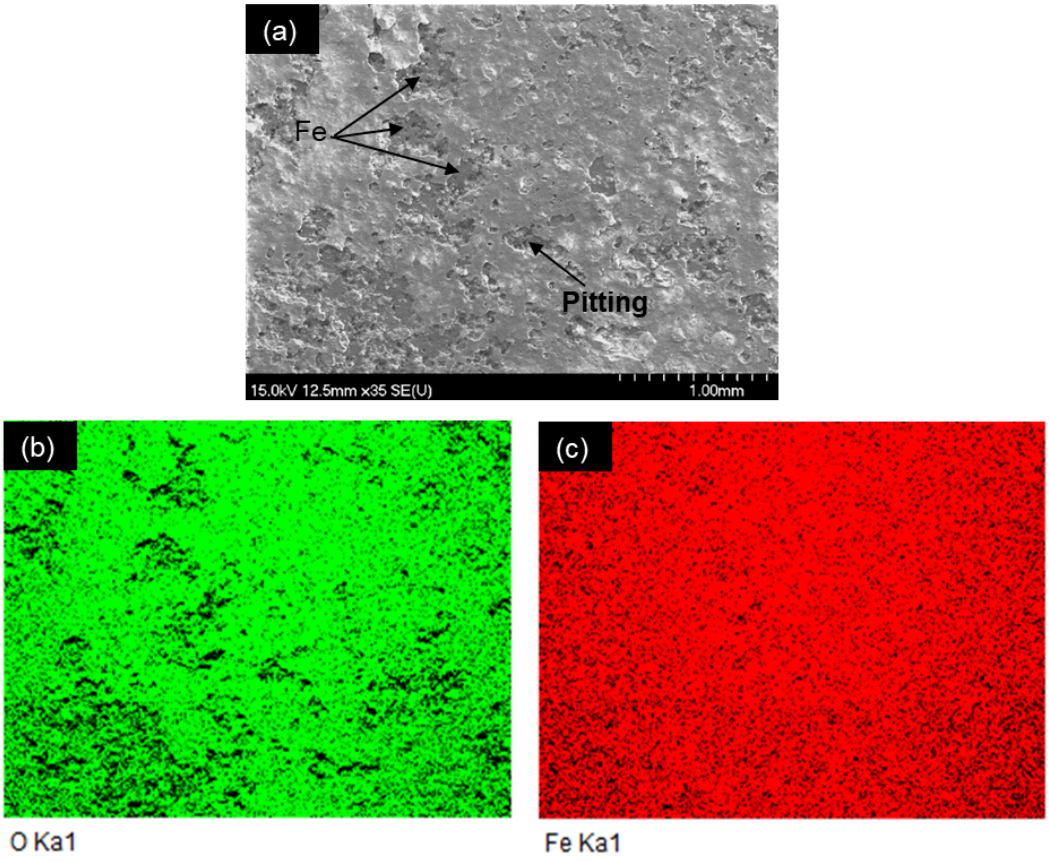

Figure 4-94 (a) SEM micrograph, (b) and (c) corresponding EDS element maps of AISI 1018 steel after erosion-corrosion for 30 mins.

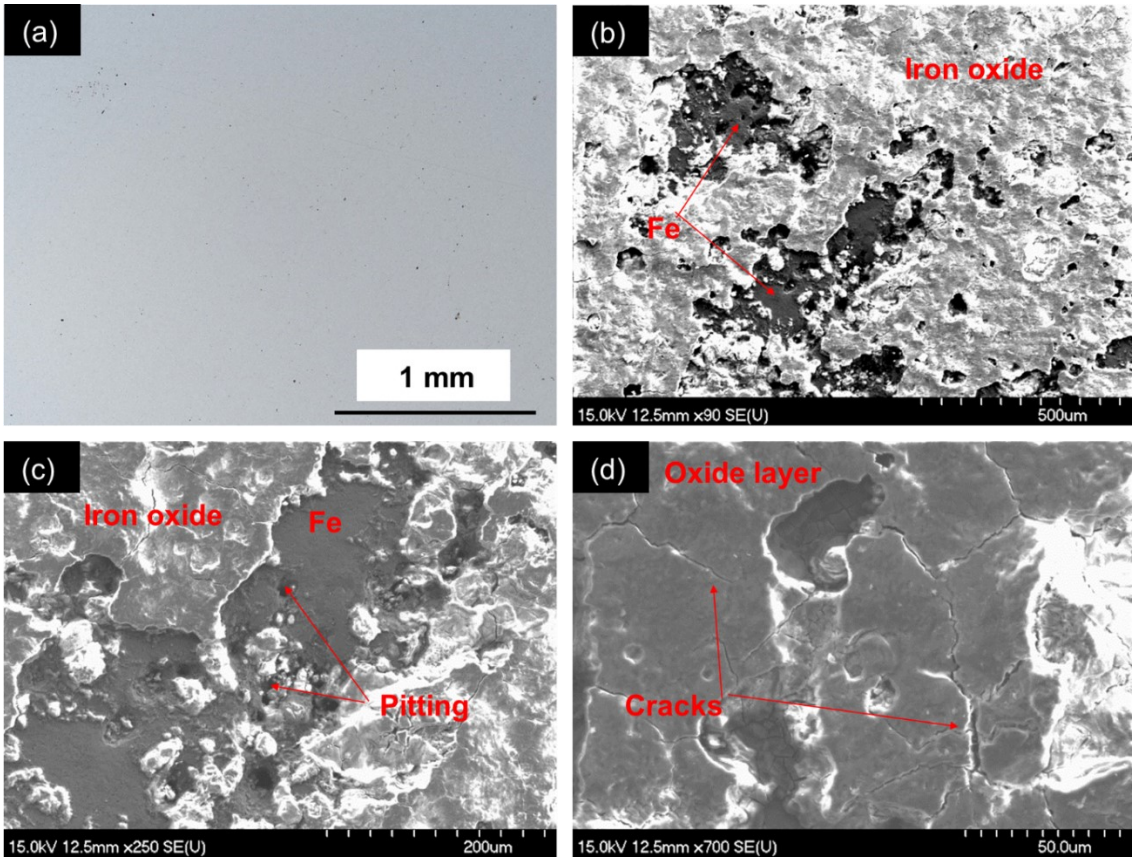

Figure 4-95 (a) optical micrograph of AISI 1018 steel before erosion-corrosion and (b), (c), (d) SEM micrographs of AISI 1018 steel after erosion-corrosion for 30 mins

Figure 4-96 (a) shows the surface morphology of Ni-P coating before erosion-corrosion test. A nodular structure and pores are observed on the coating surface. Figures 4-96 (b)-(d) show the SEM micrographs of Ni-P coating after erosion-corrosion (for 30 mins). Abrasive particle impact results in cracking and fracture due to the low toughness of the coating (Figure 4-96 (b)). The fracture fragments were then removed by the following erosive particles, creating cavities. These cavities are extremely vulnerable to localized corrosion. Scratching by the sharp edge of abrasive particles causes cracking and fracture on the coating surface (Figures 4-96 (c) and (d)). There is also some evidence of pitting and smoothing of scar edges as a result of localized corrosion (Figure 4-96 (c)) due to the high strain. These high strain sites became more anodic compared to unstrained sites on

the coating surface. For Ni-P coating, cracking and fracture caused by the abrasive particles are the dominant wear mechanisms. Localized corrosion at degraded sites is the governing corrosion mechanism during erosion-corrosion.

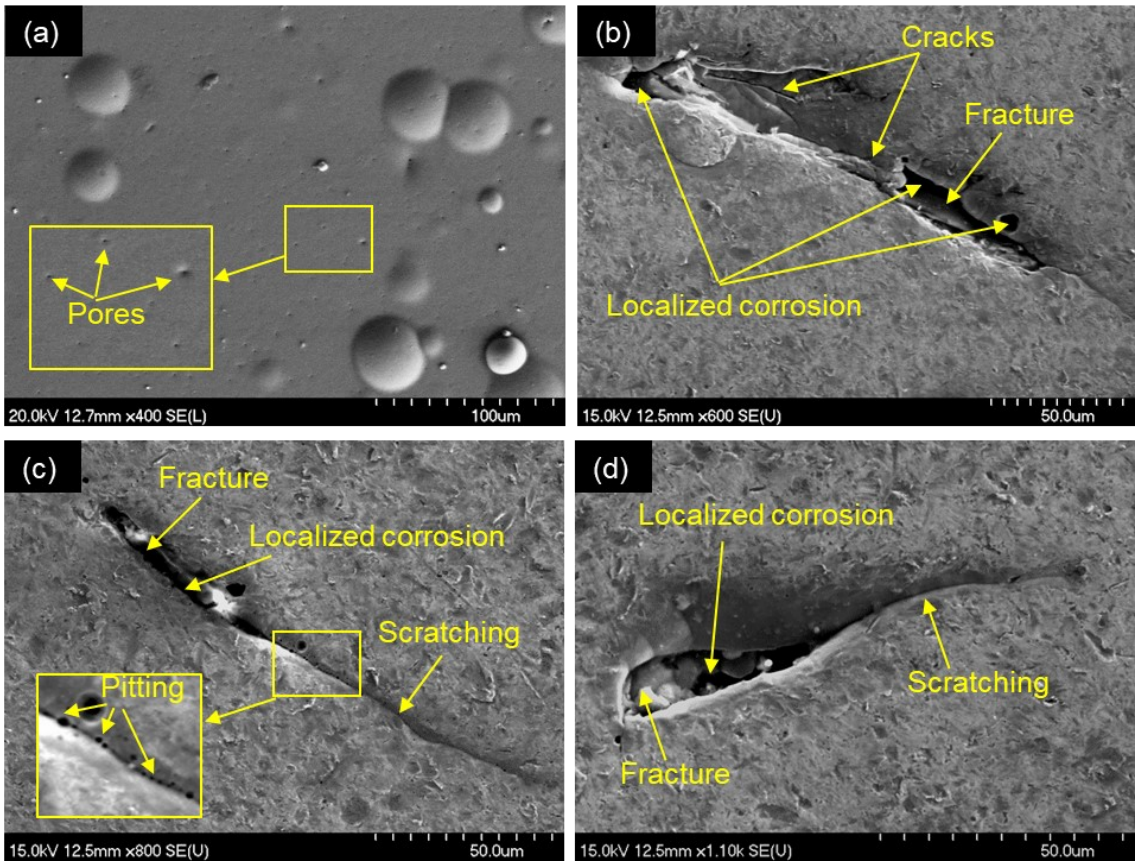

Figure 4-96 SEM micrographs of (a) Ni-P coating before and (b), (c), (d) after erosion-corrosion for 30 mins

SEM micrograph of 15.2 wt% Ti coating before erosion-corrosion test is shown in Figure 4-97 (a). Compared to Ni-P coating (Figure 4-96 (a)), 15.2 wt% Ti coating contains more refined nodular structure and a denser surface. Because of its homogenously distributed Ti particles, 15.2 wt% Ti coating undergoes uniform degradation during erosion-corrosion (Figure 4-97 (b)). Due to its improved toughness, micro-scratching and low angle micro-cutting caused by the abrasive particles are the dominant wear mechanisms. During scratching, abrasive particle pushes the material to the sides and in front of its sliding direction (Figures 4-97 (c) and (e)). The heavily strained material at the rim or at the end

of the scar is then removed by subsequent impacts. During low angle micro-cutting (Figure 4-97 (d)), an angular particle moves forwards, indenting the surface and cuts a small portion of material. In some cases, the corrosive solution penetrates the subsurface layer through the microfracture or microcracks, which corrodes the subsurface layer. Then the unsupported top layer is removed by the subsequent impacts causing spallation (Figure 4-97 (f)).

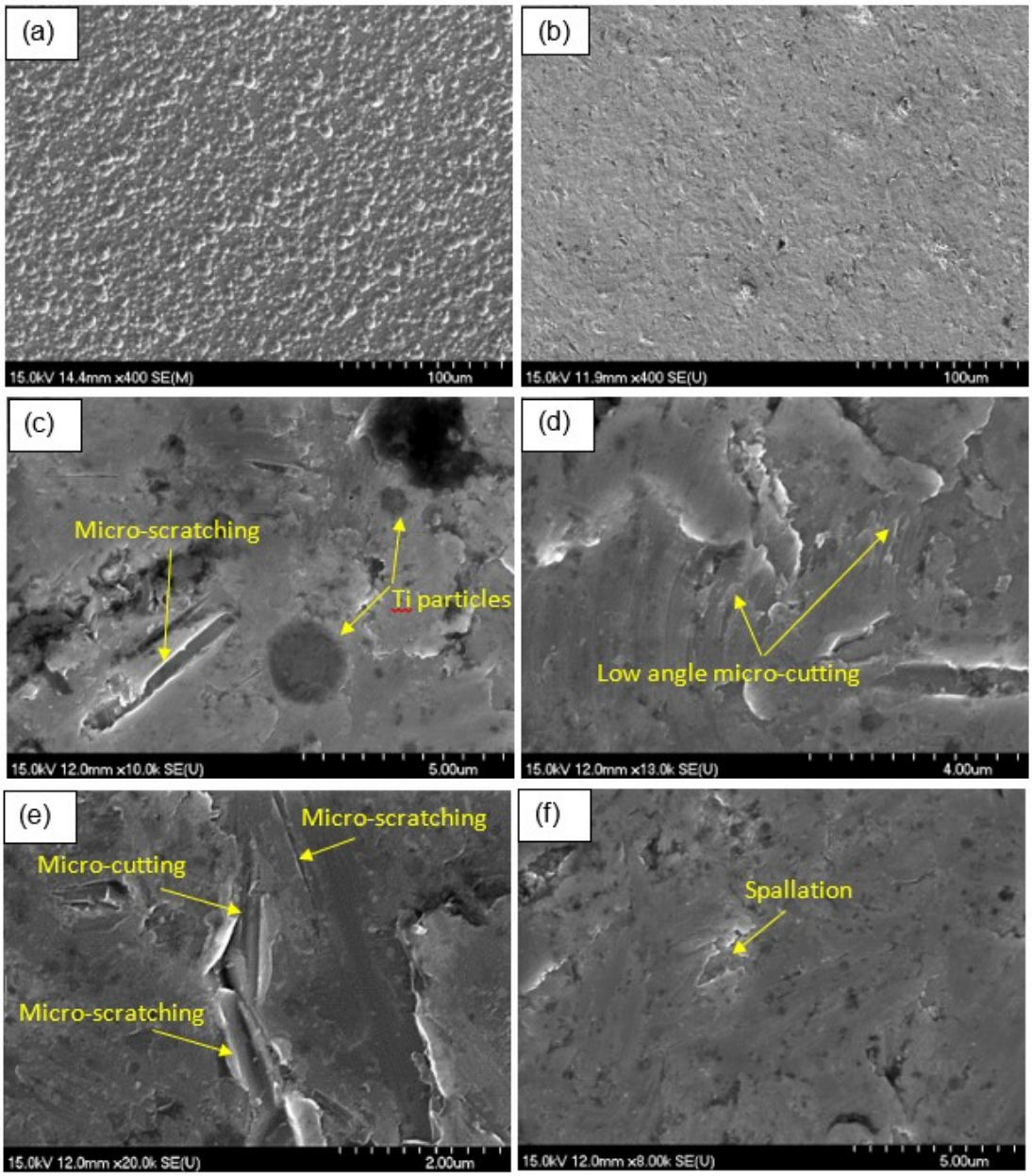

Figure 4-97 SEM micrographs of (a) 15.2 wt% Ti coating before and (b)-(f) after erosion-corrosion for 30 mins

To further study the erosion-corrosion mechanisms of AISI 1018, Ni-P and Ni-P-Ti coatings, the cross-sections of samples after erosion-corrosion were examined under optical microscopy and SEM. Figure 4-98 shows the cross-sections of different samples after erosion-corrosion for 30 mins. From Figure 4-98 (a), it is observed that AISI 1018 steel undergoes severe pitting corrosion. Figure 4-98 (b) shows the EDS map of one pit, the green color represents iron and the red color is oxygen. EDS confirms that the oxidation product (EDS results: at% of Fe: 33%, at% of O: 67%) is formed, which undergoes cracking and fracture (Figures 4-98 (c) and (d)). For AISI 1018 steel, an oxide film (thickness: 2-3 μm) is formed on the surface, which is then removed by abrasive particle impact. Due to the breakdown of the oxide film, pits initiate at the surface. These pits continue to grow and are filled with corrosion products. Because of the brittle nature of the corrosion product, it is then removed easily and contributes to the total material loss rate.

The cross-section micrograph of Ni-P coating is shown in Figure 4-98 (e). The insets are the magnified micrographs of marked parts. Abrasive particle impact causes cracking of the coating. These cracks propagate to the subsurface of the coating which results in the fracture of the coating. Then the following impacts remove the fracture debris and cause material loss (Figure 4-98 (e)). Therefore, cracking and fracture are the dominant material removal mechanisms for the Ni-P coating. On the other hand, after 30 mins erosion-corrosion, the thickness of 15.2 wt% Ti coating is uniform, no cracks or fracture is observed on cross-section (Figure 4-98 (f)). This suggests that 15.2 wt% Ti coating undergoes uniform material degradation and has higher toughness compared to Ni-P coating. Micro-indentation or localized material removal (micro-cutting and micro-scratching) is observed on the cross-section (Figure 4-98 (g)). No microcracks are present in the vicinity of indent even at high magnification (20 K times) due to the ductile Ti particle toughening (Figure 4-98 (h)). During erosion-corrosion, micro-cracking and fracture contribute to a higher material loss for Ni-P coating, whereas Ni-P-Ti coatings undergo material degradation with lower material loss due to improved toughness.

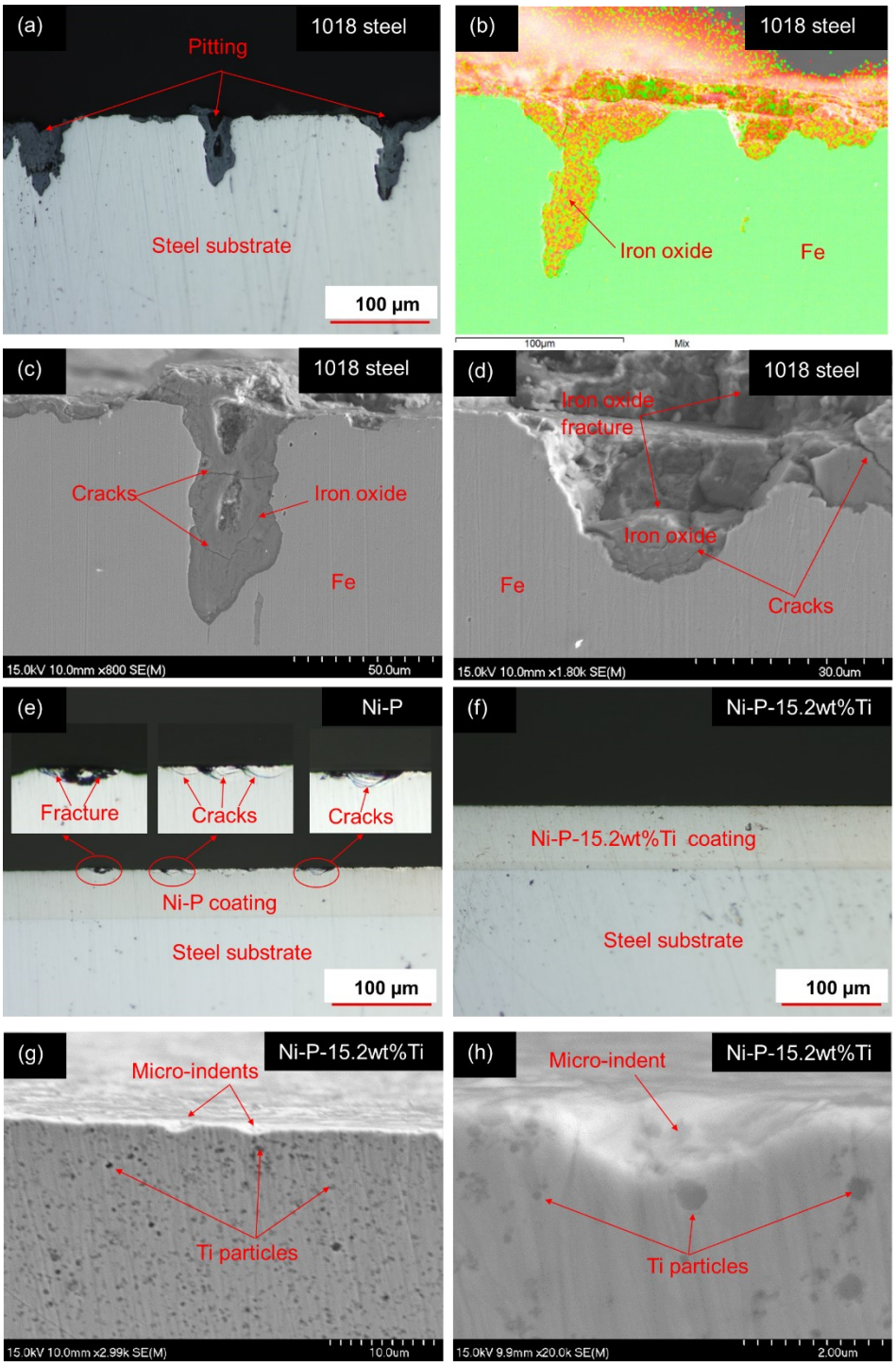
(a)
1018 steel
Pitting
Steel substrate
100 µm
(b)
1018 steel
Iron oxide
Fe
100µm
Mix
(c)
1018 steel
Cracks
Iron oxide
Fe
15.0kV 10.0mm x800 SE(M)
50.0um
(d)
1018 steel
Iron oxide
fracture
Iron oxide
Fe
Cracks
15.0kV 10.0mm x1.80k SE(M)
30.0um
(e)
Ni-P
Fracture
Cracks
Cracks
Ni-P coating
Steel substrate
100 µm
(f)
Ni-P-15.2wt%Ti
Ni-P-15.2wt%Ti coating
Steel substrate
100 µm
(g)
Ni-P-15.2wt%Ti
Micro-indents
Ti particles
15.0kV 10.0mm x2.99k SE(M)
10.0um
(h)
Ni-P-15.2wt%Ti
Micro-indent
Ti particles
15.0kV 9.9mm x20.0k SE(M)
2.00um

Figure 4-98 (a) optical cross-section micrograph of 1018 steel; (b) EDS cross-section map of 1018 steel; (c), (d) SEM cross-section micrographs of 1018 steel; (e) optical cross-section micrograph of Ni-P coating; (f) optical cross-section micrograph of Ni-P-15.2wt% Ti coating; (g),(h) SEM cross-section micrographs of Ni-P-15.2wt% Ti coating

To investigate the role of Ti particles during erosion-corrosion, examinations of 15.2 wt% Ti coating surface using SEM and EDS element maps were performed after erosion-corrosion. Figure 4-99 (a) shows the SEM micrograph of 15.2 wt% Ti coating after erosion-corrosion for 30 mins. Corresponding EDS element maps are given in Figures 4-99 (b)-(e). It is important to note that Ti particles are uniformly distributed in the Ni-P matrix. Oxygen was detected on the coating surface after erosion-corrosion, which suggests that an oxide layer is formed on the surface. Es-Souni et al. [208] proposed that titanium and titanium alloys exhibit a high tendency to form a layer of TiO_2 on the surface. Fayyad et al. [203] also confirmed the formation of titanium oxide on the surface of NiTi nanoparticles.

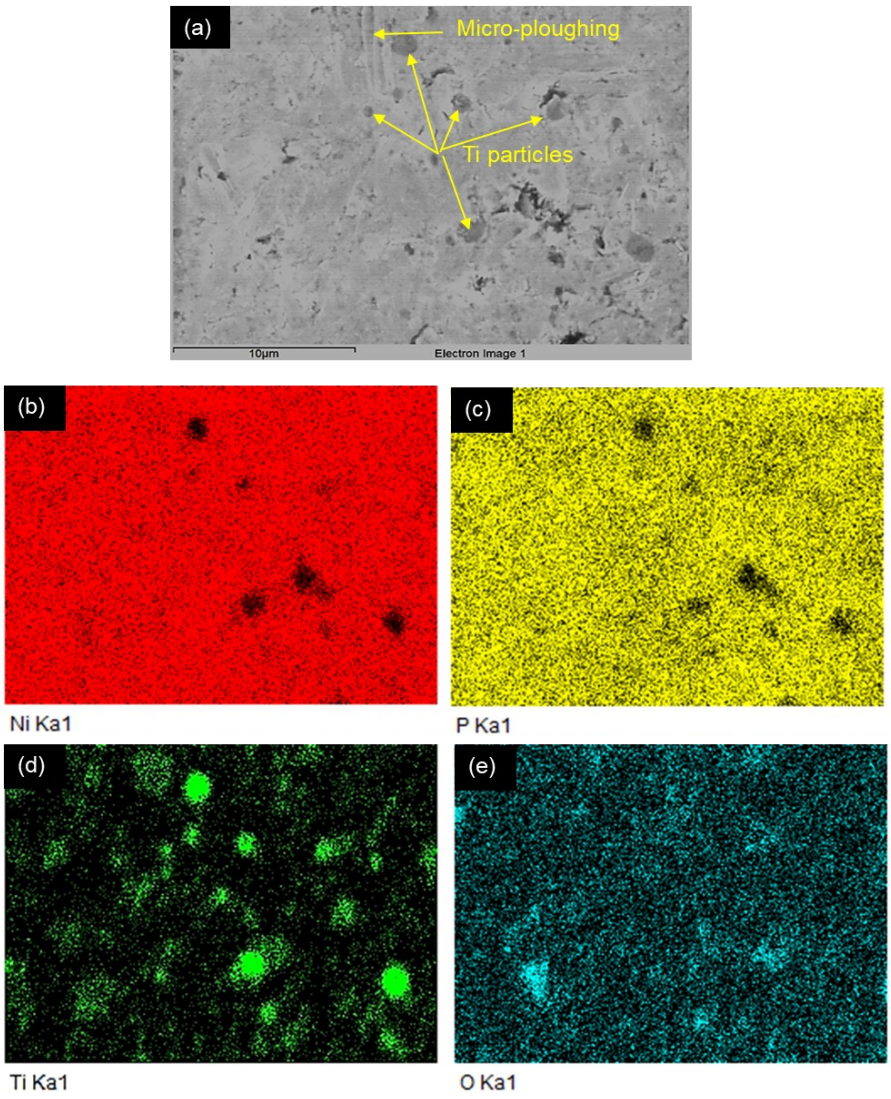

Figure 4-99 (a) SEM micrograph, and (b)-(e) EDS element maps of 15.2 wt% Ti coating after erosion-corrosion for 30 mins

SEM micrographs in Figure 4-100 illustrates the effects of Ti particles on various material removal processes. Ti particle acts as a barrier in front of the sliding abrasive particle. As observed in Figure 4-100 (a), the micro-scratching path is deflected by a Ti particle. When an abrasive particle slides over a Ti particle during micro-scratching (Figure 4-100 (b)) or micro-cutting (Figure 4-100 (c)), the kinetic energy of the abrasive particle is absorbed by the Ti particle through elastic or plastic deformation. The abrasive particle loses the kinetic

energy, which results in a significant reduction in driving force for micro-scratching or micro-cutting. Ultimately, the micro-scratching or micro-cutting is impeded by the Ti particle. In addition, micro-cracks caused by micro-cutting are blocked by Ti particle, as observed in 4-100 (d). Ti particles block microcracks propagation initiated in brittle Ni-P matrix as a result of micro-cutting/scratching by abrasive particles, which improve the erosion-corrosion resistance of Ni-P-Ti coatings.

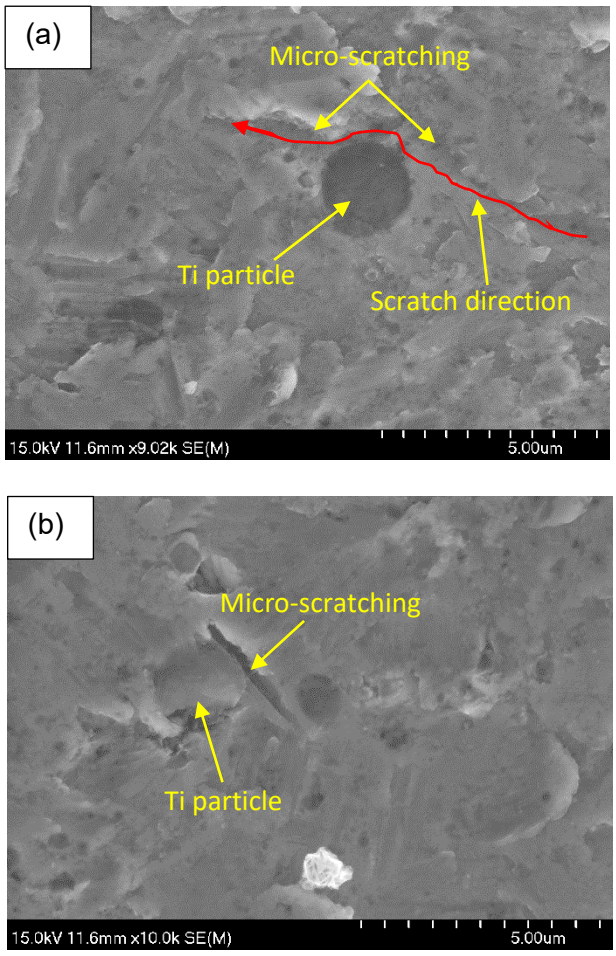

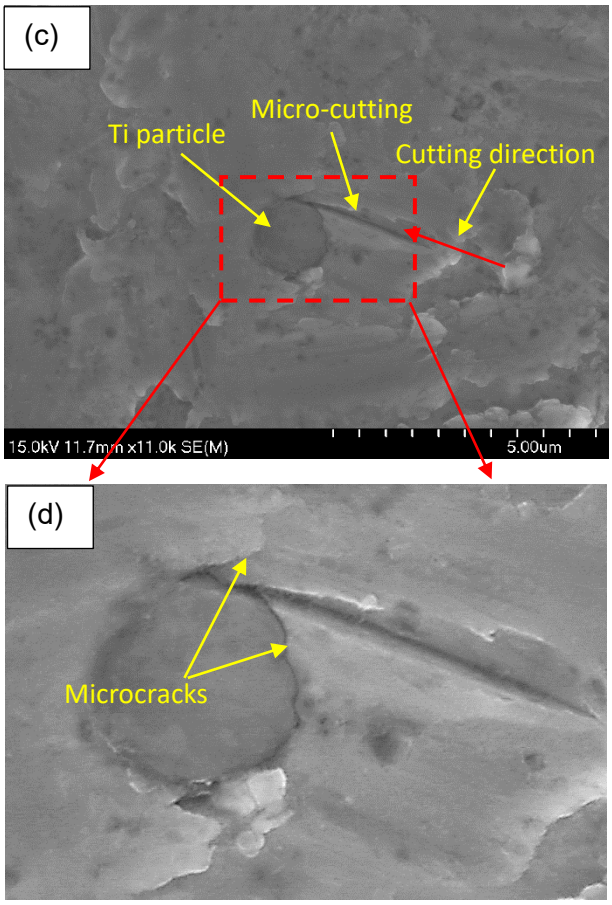

Figure 4-100 SEM micrographs of interactions between Ti particles and various material removal mechanisms

4.8.2 Erosion-Corrosion Behavior of Annealed Coatings

The material loss rates ($cm^3 \cdot h^{-1} \cdot cm^{-2}$) during erosion-corrosion (Kec), pure erosion (Keo), pure corrosion (Kco), and synergy effect (Ks) for AISI 1018 steel substrate, as-deposited and annealed coatings are shown in the Figure 4-101. Figure 4-101 gives an overall comparison between the steel substrate and all as-deposited and annealed coatings. The AISI 1018 steel substrate shows the highest material loss rate during the erosion-corrosion process, while the lowest material loss rate during the erosion-corrosion rate is achieved

on the annealed 5.1 wt% Ti coating. In addition, compared to the as-deposited coatings, the annealed coatings have lower material loss rates. Furthermore, the erosion-corrosion rate of as-deposited Ni-P coating is approximately 6 times higher than that of annealed 5.1 wt% Ti coating. In order to facilitate the following discussion and avoid repetition, the focus will be on the comparison between annealed Ni-P and annealed 5.1 wt% Ti coatings since the annealed 5.1 wt% Ti coating has the highest erosion-corrosion resistance and the erosion-corrosion mechanisms of as-deposited coatings have been discussed in the section 4.8.1. Next, the corrosion behavior in the absence and in the presence of abrasive particles, the wear mechanisms during erosion-corrosion process of annealed Ni-P and annealed 5.1 wt% Ti coatings will be discussed.

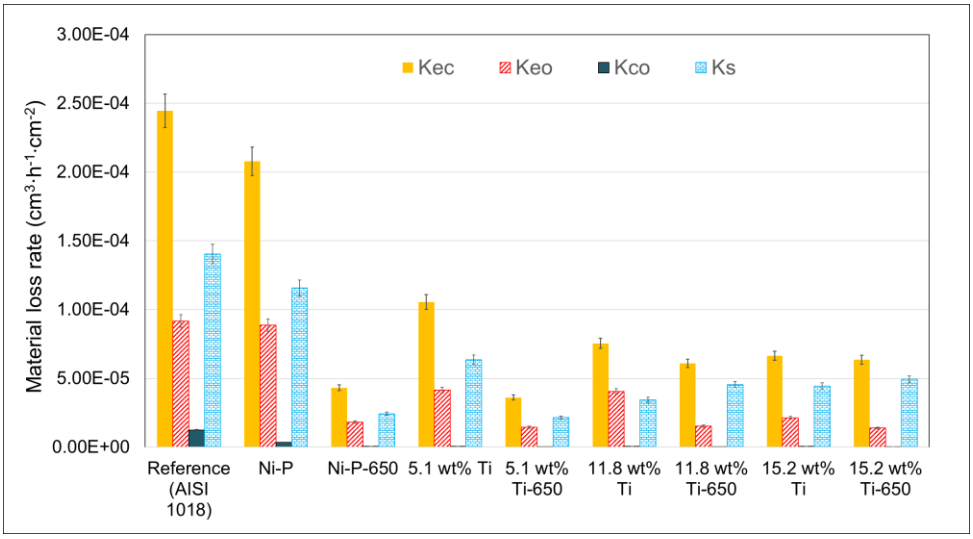

Figure 4-101 Material loss rates during erosion-corrosion (Kec), pure erosion (Keo), pure corrosion (Kco), and synergy effect (Ks) for AISI 1018 steel substrate, as-deposited and annealed coatings.

To investigate the pure corrosion behavior of annealed coatings, potentiodynamic polarization (PP) tests were performed in 3.5 wt% NaCl solution in the absence of abrasive particles under flowing condition (900 rpm). The tests were repeated twice to confirm the repeatability and reproducibility. The test results were averaged, and the standard deviations were utilized as error bars. Representative potentiodynamic polarization curves

of annealed Ni-P and 5.1 wt% Ti coatings in the absence of abrasive particles under flowing condition (900 rpm) are shown in Figure 4-102. Tafel extrapolation was employed to extract corrosion current density (i_{corr}) and corrosion potential (E_{corr}). Current density (i_{corr}) was then used to calculate corrosion rate (CR: mm/year) using equation 4.14.

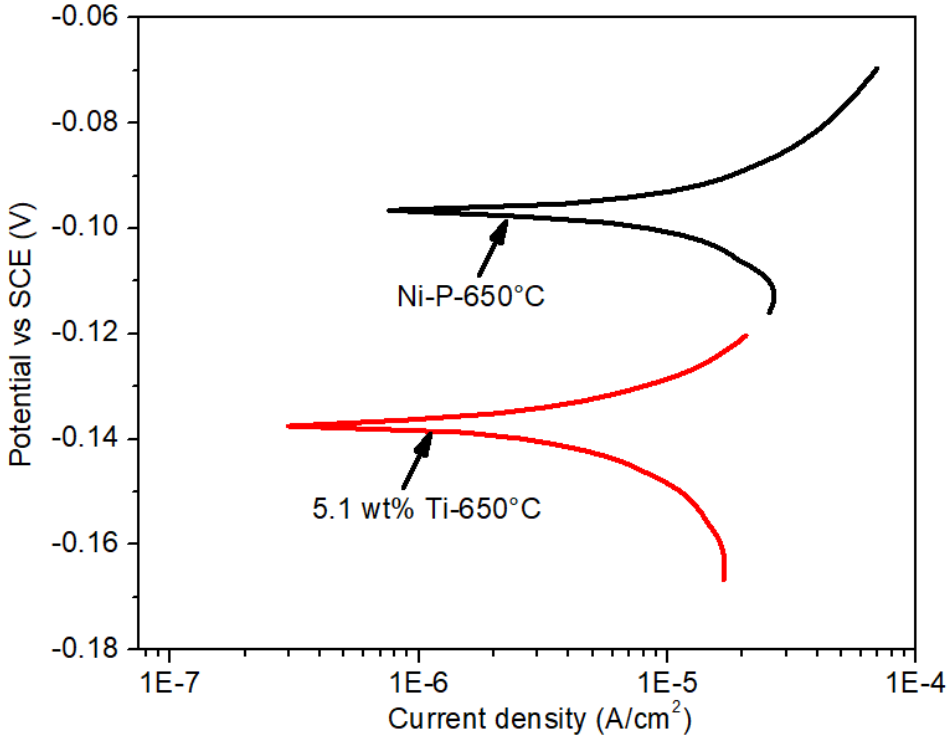

Figure 4-102 Potentiodynamic polarization curves of annealed Ni-P and 5.1 wt% Ti coatings in the absence of abrasive particles under flowing condition (900 rpm)

Corrosion characteristics of annealed Ni-P and 5.1 wt% Ti coatings in the absence of abrasive particles under flowing condition (900 rpm) are given in Table 4-25. Compared to annealed Ni-P coating, annealed 5.1 wt% Ti coating has lower corrosion rate, which is only 23% of that of annealed Ni-P coating. Two factors contribute to the high corrosion resistance of annealed 5.1 wt% Ti coating. First, nanoparticles occupy the micro or nano pores in Ni-P matrix, which increase the impenetrability of annealed 5.1 wt% Ti coating. Second, under flowing condition, annealed 5.1 wt% Ti coating has higher cavitation resistance than annealed Ni-P coating as a result of the formation of superelastic NiTi phase.

Table 4-25 Corrosion characteristics of annealed Ni-P and 5.1 wt% Ti coatings in the absence of abrasive particles under flow condition (900 rpm).

Samples	E_{corr} (V)	i_{corr} (μA/cm^2)	CR (mm/year)
Ni-P-650°C	-0.096 ± 0.014	6.0 ± 0.3	0.61± 0.07
5.1 wt% Ti-650°C	-0.139 ± 0.013	1.8 ± 0.2	0.14± 0.05

To study the influence of abrasive particles on the corrosion behavior of the annealed coatings, potentiodynamic polarization tests were conducted in 3.5 wt% NaCl solution in the presence of abrasive particles under flowing condition (900 rpm). The tests were repeated twice to confirm the repeatability and reproducibility. The test results were averaged, and the standard deviations were employed as error bars. Representative potentiodynamic polarization curves of annealed coatings in the presence of abrasive particles under flowing condition (900 rpm) are shown in Figure 4-103.

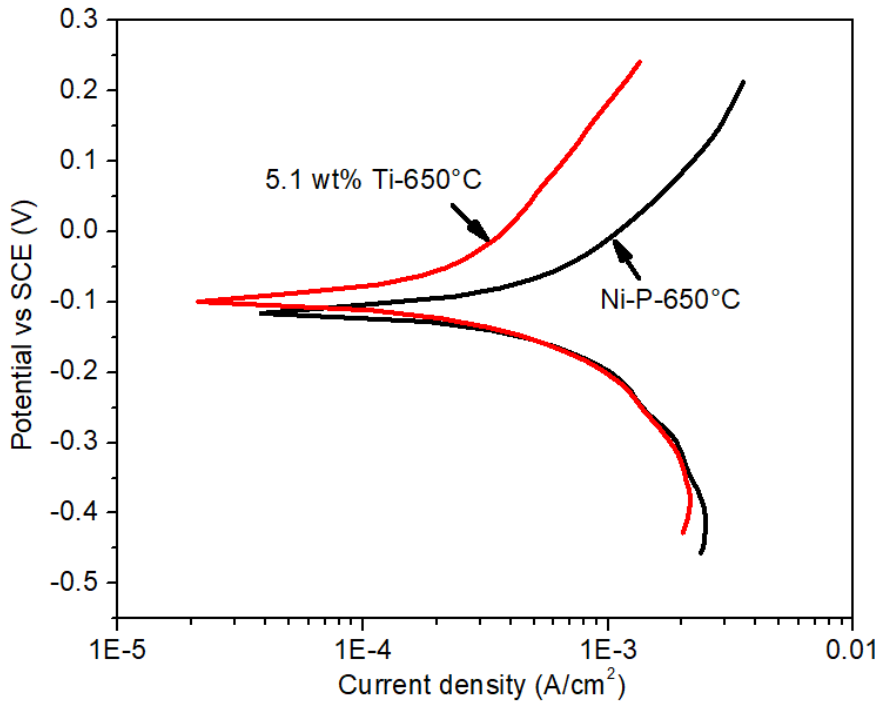

Figure 4-103 Representative potentiodynamic polarization curves of annealed Ni-P and 5.1 wt% coatings in the presence of abrasive particles under flowing condition (900 rpm)

Corrosion potential (E_{corr}) and corrosion current density (i_{corr}) were extracted from potentiodynamic polarization curves using Tafel extrapolation. Corrosion rates were calculated using the equation 4.14. Corrosion characteristics of annealed Ni-P and 5.1 wt% Ti coatings in the presence of abrasive particles under flowing condition (900 rpm) are given in Table 4-26. In the presence of abrasive particles under flowing condition, the corrosion rate of annealed 5.1wt% Ti coating is only 53% of that of annealed Ni-P coating. This is mainly due to the formation of superelastic NiTi phase in annealed 5.1 wt% Ti coating. For annealed Ni-P coating, abrasive particles result in a high strained surface, which is susceptible to corrosion. On the other hand, for annealed 5.1 wt% Ti coating, during impacts, NiTi austenite phase transforms to a detwinned martensite phase with large recoverable deformation (i.e., the coating absorbs the impact energy of the impacting particles). During unloading (particles leave surface), the detwinned martensite phase transforms back to austenite phase accompanied by deformation recovery, resulting in an unstrained surface, thus lowing the corrosion rate of annealed 5.1 wt% Ti coating in the presence of abrasive particles.

Table 4-26 Corrosion characteristics of annealed Ni-P and 5.1 wt% Ti coatings in the presence of abrasive particles under flowing condition (900 rpm)

Samples	E_{corr} (V)	i_{corr} (μA/cm^2)	CR (mm/year)
Ni-P-650°C	-0.123 ± 0.007	220 ± 5	18.7 ± 0.4
5.1 wt% Ti-650°C	-0.101 ± 0.005	113 ± 3	10.1 ± 0.2

The materials mass loss due to pure erosion and erosion-corrosion was measured using a high precision micro-balance (accuracy: 0.01 mg). The total synergy rate was calculated

using the equation 3.43. The total erosion-corrosion rate (*Kec*), erosion only rate (or pure erosion rate *Keo*), corrosion only rate (or pure corrosion rate *Kco*), and total synergy rate (*Ks*) annealed Ni-P and 5.1 wt% Ti coatings are shown in Figure 4-104.

According to the equation 3.41 (Chapter 3), the total erosion-corrosion rate depends on the pure erosion rate, pure corrosion rate, and synergic rate. It is observed that the pure corrosion has the least contribution to the total erosion-corrosion, while synergistic effect has the highest contribution to the total erosion-corrosion among all the components (Figure 4-104). Therefore, synergistic effect plays a dominant role in erosion-corrosion. In addition, compared to pure erosion and pure corrosion, the synergistic effect is more complex. Synergy consists of erosion enhanced corrosion and corrosion enhanced erosion contributions. Annealed 5.1 wt% Ti coating shows lower synergy rate in comparison with annealed Ni-P coating as a result of the formation of superelastic NiTi phase. The formation of superelastic NiTi phase improves both the corrosion and erosion resistance of annealed 5.1 wt% Ti coating (Figure 4-104: Keo and Kco). For annealed Ni-P coating, due to its low erosion resistance, abrasive particles readily remove the thin protective layer (NiO) on the coating surface, which exposes a fresh and more vulnerable surface to corrosion. For annealed 5.1 wt% Ti coating, the thin protective layer is difficult to remove by abrasive particles due to its high erosion resistance, resulting in high corrosion resistance during erosion-corrosion. Additionally, for annealed Ni-P coating, corrosion produces rough surface, which increases erosion rate during erosion-corrosion since erosion is sensitive to impact angle. An increase in surface roughness changes the local impact angle, which results in high erosion rate. Compared to annealed Ni-P coating, annealed 5.1 wt% Ti coating has higher corrosion resistance (Figure 4-104), which generates a smoother surface after corrosion, resulting in lower erosion rate during erosion-corrosion.

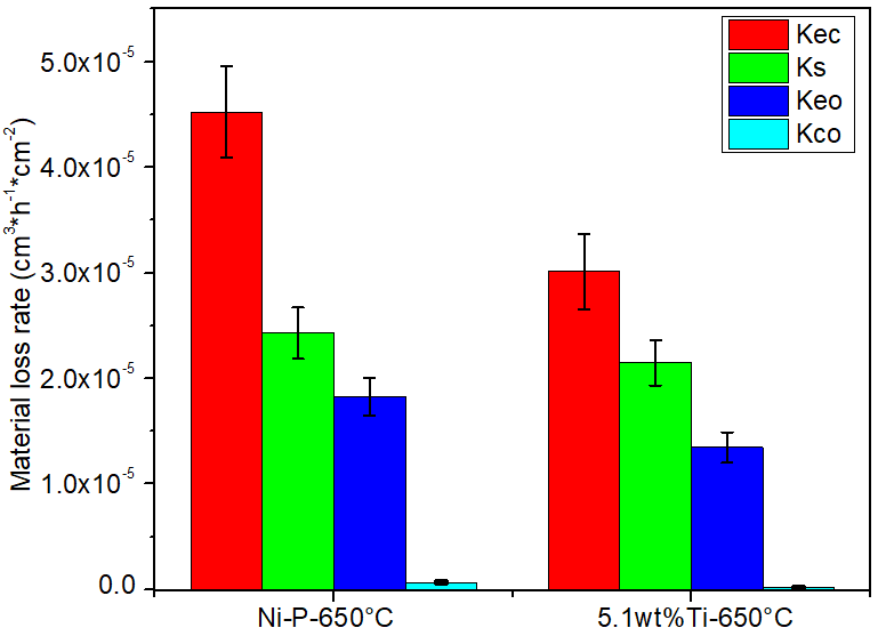

Figure 4-104 Material loss rate contribution of different components during erosion-corrosion of annealed Ni-P and 5.1 wt% Ti coatings, Kec: total erosion-corrosion rate, Ks: synergy rate, Keo: pure corrosion rate, Kco: pure erosion rate.

In order to identify different wear mechanisms during erosion-corrosion, the coatings' surface after erosion-corrosion tests was examined using SEM. The representative surface SEM micrographs of annealed Ni-P and 5.1 wt% Ti coatings after erosion-corrosion tests are shown in Figure 4-105.

Unlike the as-deposited Ni-P coating, annealed Ni-P coating undergoes a more ductile erosion process due to its low hardness and improved toughness (Figure 4-105). Among all the as-deposited and annealed coatings, annealed Ni-P coating has the lowest Vickers hardness, as confirmed in Figure 4-23. After annealing, the toughness of Ni-P coating improved due to crystallization, as also confirmed by other studies [108, 216]. Micro-cutting and plastic deformation are observed on the annealed Ni-P coating surface after erosion-corrosion test (Figures 4-105 (a) and (b)). During erosion-corrosion, silicon oxide abrasive particles strike the coating surface at a relatively high velocity, some small sharp

particles embed into the coating (Figures 4-105 (a) and (b)). Energy dispersive spectroscopy (EDS) examination on the surface of the particle and the matrix confirms that the embedded particles are silicon oxide (Figure 4-106). Nickel and phosphorus are also detected on the surface of the embedded particles (Figure 4-106), which suggests that the embedded particles were covered by Ni-P debris due to the subsequent repeated impacts. These embedded particles play an important role during the erosion-corrosion process. First, the embedded particles increase the hardness of the annealed Ni-P coating due to the high hardness (Vickers hardness: 10.9 GPa [224]) of silicon oxide particles. This improves the erosion-corrosion resistance of the annealed Ni-P coating. Second, the embedded particles increase the weight of the annealed Ni-P coating, which results in a relatively low material loss rate. These two factors contribute to the measured erosion-corrosion resistance of annealed Ni-P coating.

Compared to annealed Ni-P coating, no embedded abrasive particles are observed on the surface of annealed 5.1 wt% Ti coating due to its higher hardness, as confirmed by Vickers hardness test. A smooth surface with shallow micro-indents and micro-scratching scars is observed on annealed 5.1 wt% Ti coating after erosion-corrosion test (Figures 4-105 (c) and (d)). The SEM surface micrographs confirm that annealed 5.1 wt% Ti coating has higher erosion-corrosion resistance than annealed Ni-P coating. This is mainly due to its higher hardness and the formation of superelastic NiTi phase within the coating after annealing. Superelastic NiTi alloy has high impact and wear resistance due to its stress-induced martensite phase transformation [214, 217]. For conventional metals and alloys, to release or relieve the impact energy, plastic deformation occurs. However, for NiTi alloy, the impact energy is utilized to induce a martensitic phase transformation and stored in martensite variants [212], which improves its impact resistance.

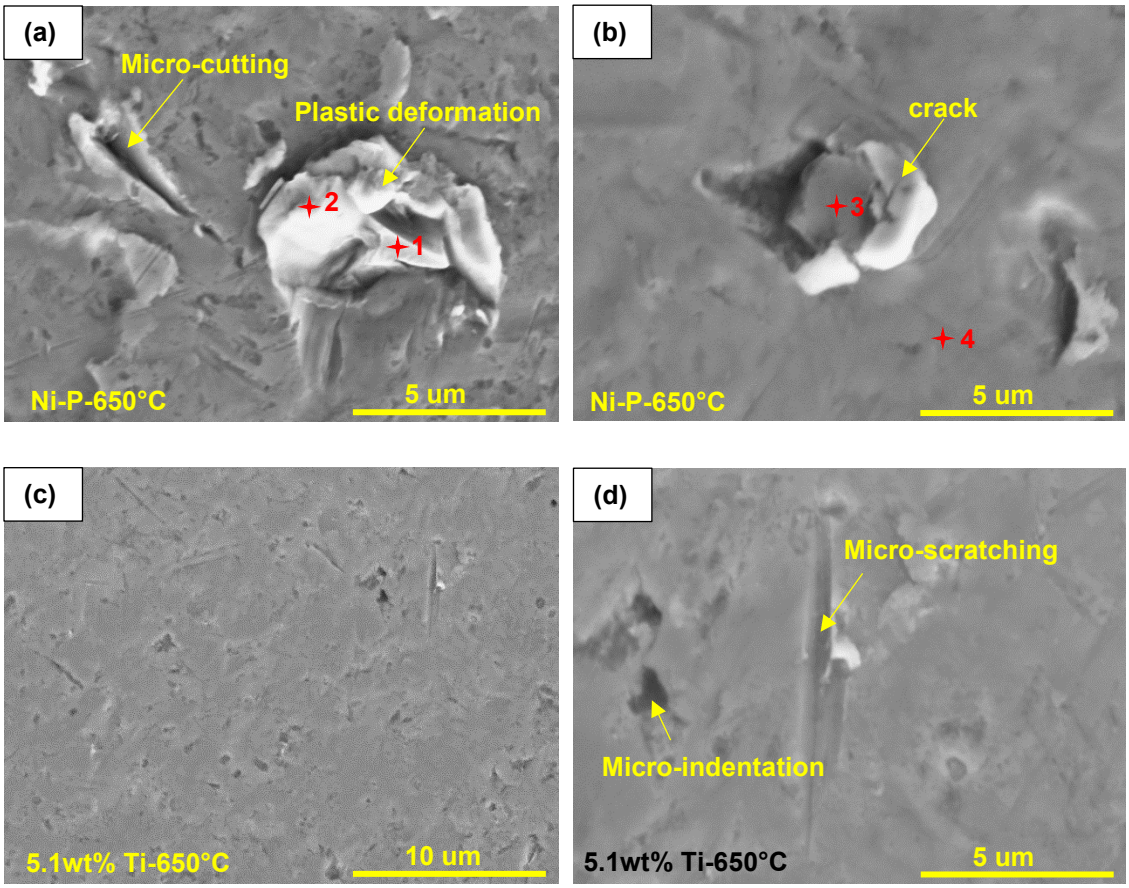

Figure 4-105 Representative surface SEM micrographs of annealed Ni-P and 5.1 wt% Ti coatings after erosion-corrosion tests, (a) and (b) annealed Ni-P coating, (c) and (d) annealed 5.1 wt% Ti coating.

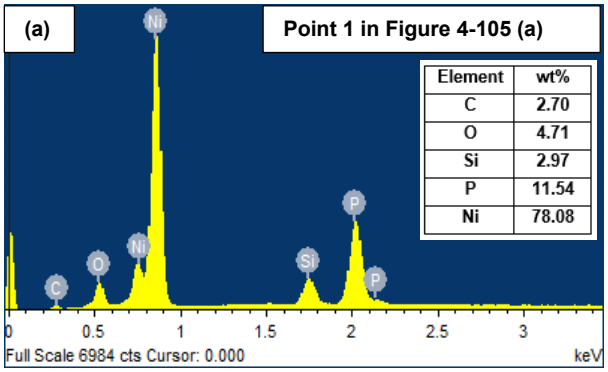
(a)
Point 1 in Figure 4-105 (a)
Element wt%
C 2.70
O 4.71
Si 2.97
P 11.54
Ni 78.08
Ni
O
C
Ni
Si
P
P
0 0.5 1 1.5 2 2.5 3
Full Scale 6984 cts Cursor: 0.000
keV

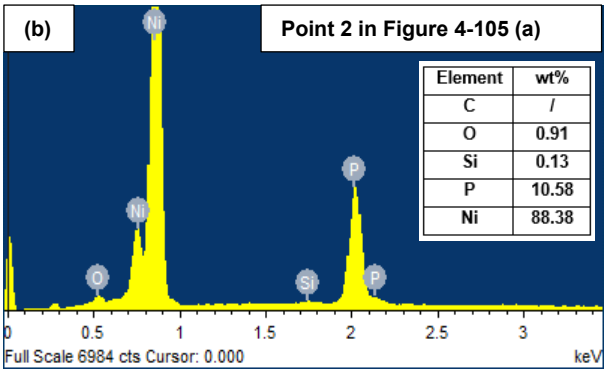
(b)
Point 2 in Figure 4-105 (a)
Element wt%
C /
O 0.91
Si 0.13
P 10.58
Ni 88.38
Ni
O
Ni
Si
P
P
0 0.5 1 1.5 2 2.5 3
Full Scale 6984 cts Cursor: 0.000
keV

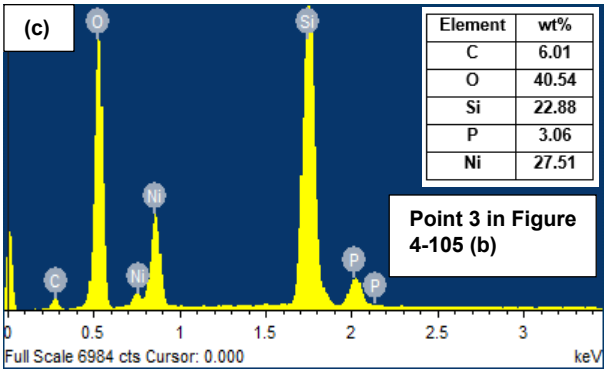
(c)
Element wt%
C 6.01
O 40.54
Si 22.88
P 3.06
Ni 27.51
Point 3 in Figure 4-105 (b)
O
Si
Ni
C
Ni
P
P
0 0.5 1 1.5 2 2.5 3
Full Scale 6984 cts Cursor: 0.000
keV

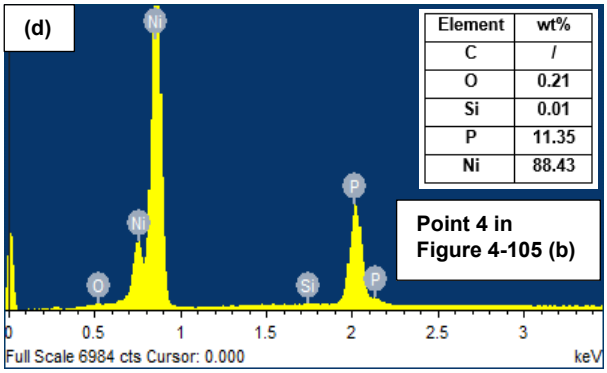
(d)
Element wt%
C /
O 0.21
Si 0.01
P 11.35
Ni 88.43
Point 4 in Figure 4-105 (b)
Ni
Ni
P
O
Si
P
0 0.5 1 1.5 2 2.5 3
Full Scale 6984 cts Cursor: 0.000
keV

Figure 4-106 Point EDS results in Figures 4-105 (a) and (b) on annealed Ni-P coating after erosion-corrosion test

To further study the erosion-corrosion mechanisms of different coatings, the annealed samples after 30 minutes erosion-corrosion tests were sectioned and then examined under SEM. SEM micrographs of cross-sections of annealed Ni-P and 5.1 wt% Ti coatings after 30 mins erosion-corrosion tests are shown in Figure 4-107. Unlike the as-deposited Ni-P coating (Figure 4-96), annealed Ni-P coating does not show severe cracking and fracture (Figure 4-107 (a)). However, under high magnification, minor coating delamination is observed on the cross-section due to repeated impacts (Figure 4-107 (b)). For annealed 5.1 wt% Ti coating, a coating with uniform thickness and intact surface is observed after erosion-corrosion (Figures 4-107 (c) and (d)) due to the formation of superelastic NiTi phase within the coating after annealing. Under very high magnification, only micro-size indents are observed on the cross-section, which confirms the high erosion-corrosion resistance of annealed 5.1 wt% Ti coating as a result of the formation of superelastic NiTi particles within the coating. During the impact process, NiTi particles within the annealed 5.1 wt% coating absorbs the kinetic energy of impact particles, which is then stored in the martensitic phase during phase transformation process. After the impact particles leave the surface, the martensitic phase transforms back to austenitic phase with deformation recovery. The formation of NiTi particles within the annealed 5.1 wt% Ti coating significantly improves its erosion-corrosion resistance.

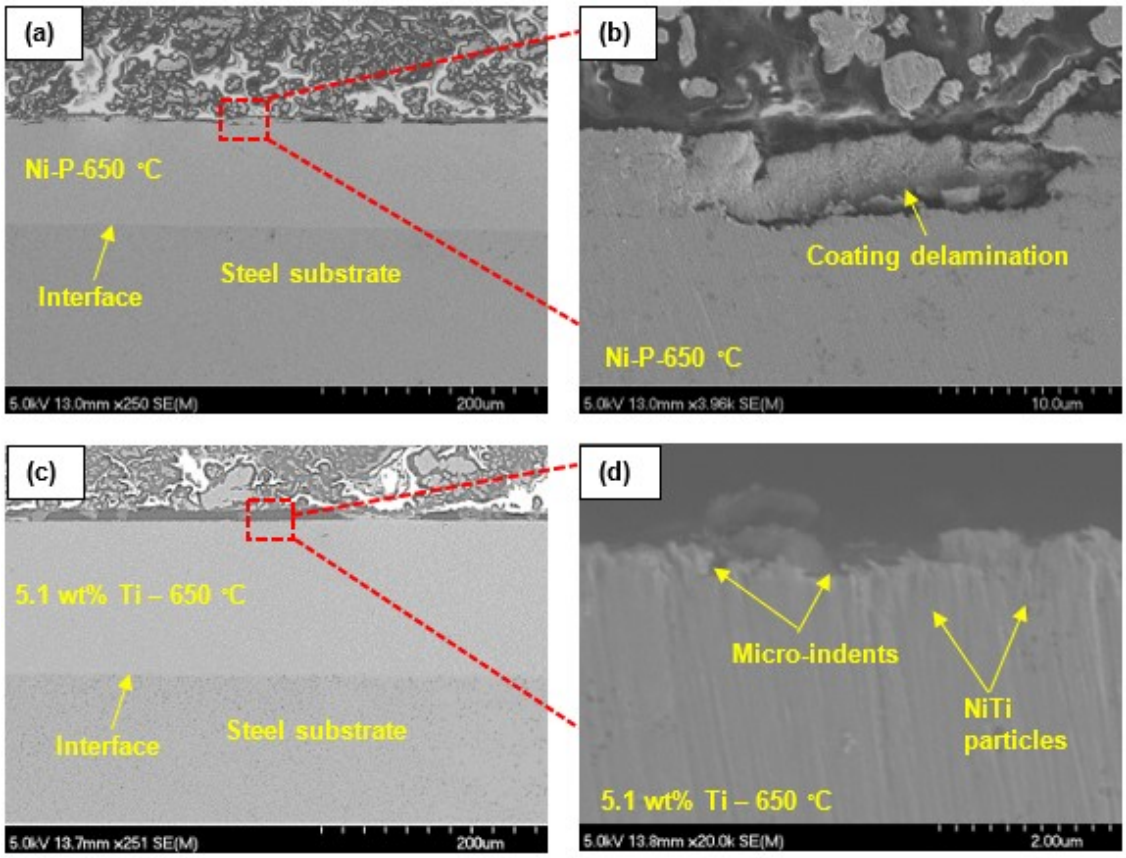

Figure 4-107 SEM micrographs of cross-sections of annealed Ni-P and 5.1 wt% Ti coatings after 30 mins erosion-corrosion tests, (a) and (b) annealed Ni-P coating, (c) and (d) annealed 5.1 wt% Ti coating.

4.8.3 Comparison Between Static and Dynamic Corrosion

Corrosion is sensitive to environment, materials in different environments may have different performance. To investigate the corrosion behavior of as-deposited and annealed coatings, corrosion tests were carried out under different conditions, including static corrosion (Section 4.7.1), dynamic corrosion in the absence of abrasive particles (Section 4.8.1), dynamic corrosion in the presence of abrasive particles (Section 4.8.2) using potentiodynamic polarization in 3.5 wt% NaCl solutions. The corrosion rates of as-deposited and annealed Ni-P and 5.1 wt% Ti coatings under different conditions are given in Table 4-27.

The static corrosion resistance of annealed coatings is slightly lower than that of as-deposited coatings (Table 4-27). For example, the average static corrosion rate of annealed 5.1 wt% Ti coating is 3.6×10^{-2} mm/year, which is higher than that of as-deposited 5.1 wt% Ti coating (2.9×10^{-2} mm/year). This is mainly due to the presence of grain boundaries as a result of crystallization after annealing, which are vulnerable sites for corrosion. However, annealed 5.1 wt% Ti coating still has much higher static corrosion resistance than as-deposited Ni-P coating.

Compared to static corrosion rates, the dynamic corrosion rates in the absence of abrasive particles under flowing condition (900 rpm) are two to three orders of magnitude higher (Table 4-27). This is mainly because of the flowing condition. The flowing NaCl solution causes cavitation on coating surface, which accelerates corrosion rates. Unlike static corrosion, it is interesting to note that the dynamic corrosion rate of annealed coatings is lower than that of as-deposited coatings (e.g. annealed 5.1 wt% Ti coating: 0.14 mm/year vs as-deposited 5.1 wt% Ti coating: 0.42 mm/year) due to their improved toughness after annealing. In addition, in the absence of abrasive particles, the lowest dynamic corrosion rate is reached on annealed 5.1 wt% Ti coating, which is only 5% of that of as-deposited Ni-P coating.

Compared to dynamic corrosion rates in the absence of abrasive particles (Table 4-27), dynamic corrosion rates in the presence of abrasive particles are approximately one order

of magnitude higher. This indicates that the dynamic corrosion rate was significantly increased by the presence of erosive particles. In the absence of erosive particles, the passive oxide film (NiO) prevents the coating from further corrosion [223]. On the other hand, in the presence of erosive particles, the passive film is removed by abrasive particles, which exposes more vulnerable fresh surface to the corrosive solution [225]. In addition, the high strained sites on the coating surface due to the impacts of abrasive particles are the susceptible sites for corrosion since they are more anodic than the unstrained sites. These factors result in higher dynamic corrosion rates in the presence of abrasive particles compared to the dynamic corrosion rates in the absence of abrasive particles. Unlike the static corrosion, annealed coatings have higher dynamic corrosion resistance than as-deposited coatings in the presence of abrasive particles due to their increased toughness (e.g. annealed 5.1 wt% Ti coating: 10.1 mm/year vs as-deposited 5.1 wt% Ti coating: 12.9 mm/year). The lowest dynamic corrosion rate in the presence of abrasive particles is achieved on annealed 5.1 wt% Ti coating among all the tested coatings, which is only 20% of that of as-deposited Ni-P coating.

Table 4-27 Comparison between static and dynamic corrosion rates

Coatings	Static corrosion rate (mm/year)	Dynamic corrosion rate (mm/year, in the absence of abrasive particles, under flowing condition 900 rpm)	Dynamic corrosion (mm/year, in the presence of abrasive particles, under flowing condition 900 rpm)
Ni-P	$9.01\pm0.15 \times 10^{-2}$	2.81 ± 0.05	49.6 ± 0.5
5.1 wt% Ti	$2.91\pm0.14 \times 10^{-2}$	0.42 ± 0.03	12.9 ± 0.3
Ni-P-650°C	$1.10\pm0.13 \times 10^{-1}$	0.61 ± 0.07	18.7 ± 0.4
5.1 wt% Ti-650°C	$3.60\pm0.15 \times 10^{-2}$	0.14 ± 0.05	10.1 ± 0.2

4.9 Summary

Various tests i.e., scratch, bending, tensile, Hertzian indentation, dynamic corrosion, and erosion-corrosion were performed on as-deposited and annealed coatings. Table 4-28 summarizes the performance of different coatings under various experimental conditions with respect to as-deposited Ni-P coating. This Table can also be used as reference when applying annealed Ni-P-Ti coatings to various industrial applications under different environmental conditions.

Table 4-28 Percent improvement of the best performing coatings with respect to as-deposited Ni-P coating for different tests

Properties	Best coating	Percent improvement (%)
Vickers hardness	Annealed 11.8 wt% Ti coating (650°C)	17%
Scratch Hardness	Annealed 11.8 wt% Ti coating (650°C)	19%
First crack load (Scratch test)	Annealed 15.2 wt% Ti coating (650°C)	442%
Scratch toughness	Annealed 15.2 wt% Ti coating (650°C)	400%
Scratch resistance	Annealed 11.8 wt% Ti coating (650°C)	69%
First crack load (Bending test)	Annealed 15.2 wt% Ti coating (650°C)	32%
Bending toughness	Annealed 15.2 wt% Ti coating (650°C)	207%
Bending strength	Annealed 15.2 wt% Ti coating (650°C)	75%

Properties	Best coating	Percent improvement (%)
Tensile toughness	Annealed 15.2 wt% Ti coating (650°C)	1233%
Tensile strength	Annealed 15.2 wt% Ti coating (650°C)	800%
First crack load (Hertzian indentation test)	Annealed 15.2 wt% Ti coating (650°C)	467%
Hertzian indentation Toughness	Annealed 15.2 wt% Ti coating (650°C)	1300%
Elastic recovery ratio (Hertzian indentation test)	Annealed 15.2 wt% Ti coating (650°C)	39%
Dynamic corrosion resistance (without abrasive particles)	Annealed 5.1 wt% Ti coating (650°C)	1940%
Dynamic corrosion resistance (with abrasive particles)	Annealed 5.1 wt% Ti coating (650°C)	400%
Erosion-corrosion resistance	Annealed 5.1 wt% Ti coating (650°C)	170%

Chapter 5 Conclusions

In the present study, Ni-P-NiTi composited coatings were successfully prepared on low carbon steel substrates (API X 100 and AISI 1018) by co-depositing Ni-P and Ti nanoparticles followed by annealing as-deposited Ni-P-Ti coatings. The following conclusions can be drawn from the present study:

1. It was found that the Ti content within as-deposited Ni-P-Ti coatings increases as the Ti amount in the plating solution rises, while the deposition rate decreases with the increase of Ti content within the plating solution. Ti particles agglomeration was observed at the highest Ti content (21.8 wt%).

2. The formation of NiTi phase within Ni-P-Ti coatings after annealing was confirmed by slow scan XRD, point and line scan EDS. The superelastic effect of NiTi phase within the annealed Ni-P-Ti coatings was also evidenced by nanoindentation test.

3. Annealed Ni-P-Ti coatings exhibit higher toughness and scratch resistance compared to as-deposited Ni-P-Ti coatings.

4. Ni-P-Ti coatings annealed at 650 °C for 2 hours have higher Vickers hardness, toughness, and scratch resistance than coatings annealed at 800 °C and 700 °C for 5 hours due to the higher amount of NiTi phase and smaller grain size.

5. The scratch toughness of annealed 15.2 wt% Ti coating (650 °C for 2 hours) is 7 times higher than that of as-deposited Ni-P coating and the scratch resistance of annealed 5.1 wt% Ti coating (650 °C for 2 hours) is 4 times higher than that of as-deposited Ni-P coating.

6. Toughness and fracture strength of annealed Ni-P-Ti coatings improve with the increase in Ti content owing to the formation of intermetallic NiTi phase and precipitation strengthening.

7. The tensile strength and bend strength of annealed 15.2 wt% Ti coating (650 °C for 2 hours) are 4 times and 1.8 times higher than those of as-deposited Ni-P coating, respectively.

8. The elastic recovery ratio of annealed 15.2 wt% Ti coating (650 °C for 2 hours) obtained from Hertzian indentation is 1.5 times higher that of as-deposited Ni-P coating.

9. The static corrosion rate of annealed 11.8 wt% Ti coating (650 °C for 2 hours) is only 30% of that of as-deposited Ni-P coating. The dynamic corrosion rate of annealed 5.1 wt% Ti coating in the absence of abrasive particles under flowing condition (900 rpm) is only 5% of that of as-deposited Ni-P coating. The dynamic corrosion rate of annealed 5.1 wt% Ti coating in the presence of abrasive particles under flowing condition is only 20% of that of as-deposited Ni-P coating.

10. The erosion-corrosion rate of as-deposited Ni-P coating is approximately 6 times higher than that of annealed 5.1 wt% Ti coating. Among different Ti concentrations (5.1 wt%, 11.8 wt%, and 15.2 wt%) of annealed Ni-P-Ti coatings, annealed 5.1 wt% Ti coating has the highest erosion-corrosion resistance, which can be recommended for applications that require high erosion-corrosion resistance.

11. Different toughening mechanisms (crack deflection, crack bridging, transformation toughening) induced by superelastic NiTi particles are observed and confirmed in the annealed Ni-P-Ti coatings under aforementioned various tests, i.e., scratch, bend, indentation, single particle erosion, and erosion-corrosion tests.

12. Among the various toughening mechanisms, transformation toughening, due to the reversible martensitic transformation of superelastic NiTi, plays the most significant role in enhancing the behavior of the coatings.

13. Annealed Ni-P-Ti composites are attractive potential coatings for industrial applications in which high scratch, dent, corrosion, and erosion-corrosion resistance are required.

Most significant contributions:

1. Developed an economical method to produce Ni-P-NiTi composite coatings.

2. Successfully confirmed the formation of superelastic NiTi phase after annealing by slow scan XRD, point and line scan EDS, and nanoindentation.

3. Investigated and identified different toughening mechanisms induced by superelastic NiTi phase.

4. Significantly improved the toughness of Ni-P coating, hence, enhanced the mechanical properties, corrosion, and erosion-corrosion behavior of Ni-P coating.

The following work is recommended to further understand and investigate the behavior of as-deposited and annealed Ni-P-Ti coatings:

1. The microstructure of the as-deposited and annealed Ni-P-Ti coatings may be further studied using transmission electron microscopy (TEM), especially to identify the different phases formed within nano-size Ti particles after annealing.

2. The surface of the coatings after static corrosion and erosion-corrosion tests may be further explored to identify corrosion products and mechanisms using X-ray photoelectron spectroscopy (XPS).

3. The corrosion resistance of the coatings may be further investigated in acidic or alkali solutions during a long period (eg. 5 days, 10 days, 15 days, 20 days) using PD or/and EIS techniques.

4. Advanced models may be built to simulate and analyze single particle erosion, erosion-corrosion process for as-deposited and annealed Ni-P-Ti composite coatings using Finite Element analysis.

5. The effect of particle size on toughening mechanism may be further investigated by TEM.

6. The suitability of plating Ni-P-NiTi coatings on other substrates (eg. Cu, Al) may need to be further studied.

Publications (first author) generated from the thesis include:

1. Improved Erosion-Corrosion Resistance of Electroless Ni-P Coating by the Formation of Superelastic NiTi Nanoparticles, Conference of Metallurgists 2021, Canada, submitted.

2. Effects of Ti Content and Annealing on Corrosion Resistance of Electroless Ni-P-Ti Composite Coatings, Journal of Bio- and Tribo-Corrosion, under review, (2021).

3. The benefit of superelastic NiTi addition on corrosion performance of electroless Ni-P coating during an accidental scratch event, Journal of Bio- and Tribo-Corrosion, 7:12 (2021) 1-13.

4. Investigation of Erosion-Corrosion Resistance of Electroless Ni-P-Ti composite coatings, Journal of Bio- and Tribo-Corrosion, 6:107 (2020) 1-17.

5. Effects of Ti content and annealing temperatures on fracture toughness and scratch resistance of electroless Ni-P-Ti coatings, Journal of Materials Engineering and Performance, 29 (2020) 5807-5821.

6. Microstructure Development and Nanoindentation Behavior of Annealed Ni-P-Ti Coatings, Surface Engineering, 37 (2020) 527-535.

7. Hertzian Indentation Behavior of Ni-P-Ti coatings, Metallurgical and Materials Transactions A, 51 (2020) 3674-3691.

8. Investigation of the Mechanical Behavior of Electroless Ni-P-Ti Composite Coatings, ASME: Journal of Engineering materials and technology, 142 (2020) 031006-031018.

9. Investigation of Single-Particle Erosion Behavior of Electroless Ni-P-Ti Composite Coatings, Journal of Materials Engineering and Performance, 29 (2020) 1671-1683.

10. Synthesis, and Characterization of Scratch Resistant Ni-P-Ti Based Composite Coating, Tribology Transactions, 62 (2019) 880-896.

Appendix A – Calculation Details for Hertzian Stress Distribution

When using the equations 3.27-3.36 to calculate Hertzian stress distribution, there are four mathematic singularity points need to be considered:

(1) When Z=0, R<1, then L=0, Z/L = ?.

(2) When Z=0, R>1, then $\frac{\sigma_r}{\sigma_0}$ = ?.

(3) When R=r/a=0, the part [- $\frac{1\text{-}2\nu}{3R^2}$(1- $\frac{Z^3}{L^3}$)] in the equation 3.28 is close to infinity.

(4) When R=Z=0, L=0, then $\frac{\sigma_r}{\sigma_0}$ = ?, $\frac{\sigma_\theta}{\sigma_0}$=?

These four singularity points need to be solved before calculating the Hertzian stress.

For the singularity point 1, if Z =0, R < 1,

$$L = [\frac{1}{2}(R^2 + Z^2 - 1 + \sqrt{(R^2 + Z^2 - 1)^2 + 4Z^2})]^{\frac{1}{2}}$$

$$= (R^2 - 1)^{1/2}$$

If R < 1, then $(R^2 - 1) < 0$, therefore, for R < 1, L = $(R^2 - 1) = 0$.

$$R^2 = (1 + L^2)(1 - \frac{Z^2}{L^2}) \rightarrow \frac{Z^2}{L^2} = 1 - R^2 \rightarrow \lim_{Z\rightarrow 0, L\rightarrow 0} \frac{Z}{L} = (1 - R^2)^{1/2}$$

Considering the part $-\frac{L^3R^2Z}{(L^4+Z^2)(1+L^2)^2}$ in the equation 3.27, if Z =0, L =0, R<1, then

$$\lim_{Z\rightarrow 0, L\rightarrow 0} -\frac{L^3R^2Z}{(L^4 + Z^2)(1 + L^2)^2} \rightarrow \frac{0}{0}$$

Therefore, we need to consider the reciprocal of the whole part:

$$-\frac{(L^4+Z^2)(1+L^2)^2}{L^3R^2Z} = -\frac{L^4+2L^6+L^8+Z^2+2L^2Z^2+L^4Z^2}{L^3R^2Z} = -\frac{L}{ZR^2} + \frac{2L^3}{ZR^2} + \frac{L^5}{ZR^2} + \frac{Z}{L^3R^2} + \frac{2Z}{LR^2} + \frac{LZ}{R^2}$$

When Z =0, L =0, R<1, $\frac{Z}{L} = (1 - R^2)^{1/2} \rightarrow \frac{L}{Z} = \frac{1}{(1-R^2)^{1/2}}$, put into the above equation:

$$= -(\frac{1}{R^2(1-R^2)^{1/2}} + \frac{2L^2}{R^2}\frac{1}{(1-R^2)^{1/2}} + \frac{L^4}{R^2}\frac{1}{(1-R^2)^{1/2}} + \frac{1}{L^2R^2}(1-R^2)^{1/2} + \frac{2}{R^2}(1-R^2)^{1/2} + \frac{LZ}{R^2})$$

$\lim_{Z\to 0,L\to 0} \frac{2L^2}{R^2}\frac{1}{(1-R^2)^{1/2}} \to 0;$

$\lim_{Z\to 0,L\to 0} \frac{L^4}{R^2}\frac{1}{(1-R^2)^{1/2}} \to 0$

$\lim_{Z\to 0,L\to 0} \frac{1}{L^2R^2}(1-R^2)^{1/2} \to \infty$

$\lim_{Z\to 0,L\to 0} \frac{LZ}{R^2} \to 0$

Therefore,

$\lim_{Z\to 0,L\to 0} -\frac{(L^4+Z^2)(1+L^2)^2}{L^3R^2Z} \to \infty$

$\lim_{Z\to 0,L\to 0} -\frac{L^3R^2Z}{(L^4+Z^2)(1+L^2)^2} \to \frac{1}{\infty} \to 0$

Therefore,

$\frac{\sigma_r}{\sigma_0} = -\frac{L^3R^2Z}{(L^4+Z^2)(1+L^2)^2}$-(1-2ν)[$\frac{Z}{L(1+L^2)}$ - $\frac{1}{3R^2}$(1-$\frac{Z^3}{L^3}$)]+$\frac{Z}{L}$[L(1+ν)arctan($\frac{1}{L}$)-(1-ν) $\frac{L^2}{1+L^2}$ - 2ν]

$= -(1-2\nu)[\,(1-R^2)^{1/2} - \frac{1}{3R^2}(1-(1-R^2)^{3/2}) + (1-R^2)^{1/2} * (-2\nu)$

$= (1-2\nu)\,\frac{1}{3R^2}(1-(1-R^2)^{3/2}) - (1-R^2)^{1/2}$

$\frac{\sigma_\theta}{\sigma_0} = -\frac{1-2\nu}{3R^2}(1-\frac{Z^3}{L^3})+\frac{Z}{L}[L(1+\nu)\arctan(\frac{1}{L})-(1-\nu)\frac{L^2}{1+L^2} - 2\nu]$

$= -\frac{1-2\nu}{3R^2}(1-(1-R^2)^{3/2}) - 2\nu(1-R^2)^{1/2}$

$\lim_{Z\to 0,L\to 0} \frac{\sigma_z}{\sigma_0} = -\frac{Z^3}{L(L^4+Z^2)} \to \frac{0}{0}$ therefore, we consider:

$\frac{\sigma_0}{\sigma_z} = -\frac{L(L^4+Z^2)}{Z^3} = -\frac{L^5+LZ^2}{Z^3} = -(L^2\,\frac{L^3}{Z^3} + \frac{L}{Z}) = -\frac{1}{(1-R^2)^{1/2}}$

Therefore,

$\lim_{Z\to 0,L\to 0} \frac{\sigma_z}{\sigma_0} = -\frac{Z^3}{L(L^4+Z^2)} \to -(1-R^2)^{1/2}$

$\lim_{Z\to 0,L\to 0} \frac{\tau_{zr}}{\sigma_0} = -\frac{LRZ^2}{(1+L^2)(L^4+Z^2)} \to \frac{0}{0}$ therefore, we consider:

$\frac{\sigma_0}{\tau_{zr}} = -\frac{(1+L^2)(L^4+Z^2)}{LRZ^2} = -\frac{L^4+L^6+Z^2+L^2Z^2}{LRZ^2} = -(\frac{L}{R}\frac{L^2}{Z^2} + \frac{L^3}{R}\frac{L^2}{Z^2} + \frac{1}{LR} + \frac{L}{R})$

$= -(\frac{L}{R}\frac{1}{1-\mathrm{R}^2} + \frac{L^3}{R}\frac{1}{1-\mathrm{R}^2} + \frac{1}{LR} + \frac{L}{R})$

$\lim_{L\to 0}\frac{L}{R}\frac{1}{1-\mathrm{R}^2} \to 0$; $\lim_{L\to 0}\frac{L^3}{R}\frac{1}{1-\mathrm{R}^2} \to 0$; $\lim_{L\to 0}\frac{1}{LR} \to \infty$; $\lim_{L\to 0}\frac{L}{R} \to 0$;

Therefore, $\lim_{Z\to 0, L\to 0}\frac{\sigma_0}{\tau_{zr}} = -\frac{(1+L^2)(L^4+Z^2)}{LRZ^2} \to \infty$;

$\lim_{Z\to 0, L\to 0}\frac{\tau_{zr}}{\sigma_0} = -\frac{LRZ^2}{(1+L^2)(L^4+Z^2)} \to \frac{1}{\infty} \to 0$

Summary: when Z=0, L=0, R<1, $\frac{Z}{L} = (1-R^2)^{1/2}$

$\frac{\sigma_r}{\sigma_0} = (1-2\nu)\frac{1}{3\mathrm{R}^2}(1-(1-\mathrm{R}^2)^{3/2}) - (1-\mathrm{R}^2)^{1/2}$

$\frac{\sigma_\theta}{\sigma_0} = -\frac{1-2\nu}{3R^2}(1-(1-\mathrm{R}^2)^{3/2}) - 2\nu(1-\mathrm{R}^2)^{1/2}$

$\frac{\sigma_z}{\sigma_0} = -(1-R^2)^{1/2}$

$\frac{\tau_{zr}}{\sigma_0} = 0$

For the singularity point 2, if Z =0, R >1,

$L = [\frac{1}{2}(R^2+Z^2-1+\sqrt{(R^2+Z^2-1)^2+4Z^2})]^{\frac{1}{2}}$

$= (R^2-1)^{1/2}$

Then R >1, therefore, $L = (R^2-1)^{1/2}$, when Z = 0,

$\frac{\sigma_r}{\sigma_0} = -\frac{L^3R^2Z}{(L^4+Z^2)(1+L^2)^2} - (1-2\nu)[\frac{Z}{L(1+L^2)} - \frac{1}{3R^2}(1-\frac{Z^3}{L^3})] + \frac{Z}{L}[L(1+\nu)\arctan(\frac{1}{L}) - (1-\nu)\frac{L^2}{1+L^2} - 2\nu]$

$= \frac{1-2\nu}{3R^2}$

$\frac{\sigma_\theta}{\sigma_0} = -\frac{1-2\nu}{3R^2}(1-\frac{Z^3}{L^3}) + \frac{Z}{L}[L(1+\nu)\arctan(\frac{1}{L}) - (1-\nu)\frac{L^2}{1+L^2} - 2\nu]$

$= -\frac{1-2\nu}{3R^2}$

$$\frac{\sigma_z}{\sigma_0} = -\frac{Z^3}{L(L^4+Z^2)} = 0$$

$$\frac{\tau_{zr}}{\sigma_0} = -\frac{LRZ^2}{(1+L^2)(L^4+Z^2)} = 0$$

For the singularity point 3, if R = 0,

$$L = [\frac{1}{2}(R^2+Z^2-1+\sqrt{(R^2+Z^2-1)^2+4Z^2})]^{\frac{1}{2}}$$

$$= [\tfrac{1}{2}(Z^2-1+\sqrt{(Z^2-1)^2+4Z^2})]^{\frac{1}{2}}$$

$$= [\frac{1}{2}(Z^2-1+\sqrt{Z^4-2Z^2+1+4Z^2})]^{\frac{1}{2}}$$

$$= [\frac{1}{2}(Z^2-1+\sqrt{Z^4+2Z^2+1})]^{\frac{1}{2}}$$

$$= [\frac{1}{2}(Z^2-1+\sqrt{(Z^2+1)^2})]^{\frac{1}{2}}$$

= Z

However, $\lim_{R\to 0} -\frac{1-\frac{Z^3}{L^3}}{3R^2} \rightarrow \frac{0}{0}$

Since $R^2 = (1+L^2)(1-\frac{Z^2}{L^2})$, therefore,

$$-\frac{1-\frac{Z^3}{L^3}}{3R^2} = -\frac{1-\frac{Z^3}{L^3}}{3(1+L^2)\left(1-\frac{Z^2}{L^2}\right)}$$

$$= -\frac{1}{3(1+L^2)} \frac{1-\frac{Z^3}{L^3}}{(1-\frac{Z^2}{L^2})}$$

$$= -\frac{1}{3(1+L^2)} \frac{(1-\frac{Z}{L})(1+\frac{Z}{L}+\frac{Z^2}{L^2})}{(1-\frac{Z}{L})(1+\frac{Z}{L})}$$

$$= -\frac{1}{3(1+L^2)} (1+\frac{\frac{Z^2}{L^2}}{1+\frac{Z}{L}})$$

$$= -\frac{1}{3(1+L^2)} (1+\frac{\frac{Z^2}{L^2}}{1+\frac{Z}{L}})$$

Since R=0, L=Z, Then,

$$-\frac{1-\frac{Z^3}{L^3}}{3R^2} = -\frac{1}{3(1+L^2)}\left(1+\frac{\frac{Z^2}{L^2}}{1+\frac{Z}{L}}\right) = -\frac{1}{2}\frac{1}{1+Z^2}$$

$$\frac{\sigma_r}{\sigma_0} = -\frac{L^3R^2Z}{(L^4+Z^2)(1+L^2)^2}\text{-}(1\text{-}2\nu)\left[\frac{Z}{L(1+L^2)} - \frac{1}{3R^2}\left(1-\frac{Z^3}{L^3}\right)\right]+\frac{Z}{L}\left[L(1+\nu)\arctan\left(\frac{1}{L}\right)\text{-}(1\text{-}\nu)\frac{L^2}{1+L^2} - 2\nu\right]$$

$$= -(1-2\nu)\left[\frac{1}{1+Z^2}-\frac{1}{2(1+Z^2)}\right]+\left[Z(1+\nu)\arctan\frac{1}{Z}-(1-\nu)\frac{Z^2}{1+Z^2}-2\nu\right]$$

$$= -(1-2\nu)\frac{1}{2(1+Z^2)}]+\left[Z(1+\nu)\arctan\frac{1}{Z}-(1-\nu)\frac{Z^2}{1+Z^2}-2\nu\right]$$

$$= Z(1+\nu)\arctan\frac{1}{Z}-\left[(1-2\nu)\frac{1}{2(1+Z^2)}\right]+(1-\nu)\frac{Z^2}{1+Z^2}+2\nu]$$

$$= Z(1+\nu)\arctan\frac{1}{Z}-\left[\frac{1-2\nu+2(1-\nu)Z^2+4\nu(1+Z^2)}{2(1+Z^2)}\right]$$

$$= Z(1+\nu)\arctan\frac{1}{Z}-\left[\frac{1-2\nu+2Z^2+2\nu Z^2}{2(1+Z^2)}\right]$$

$$= Z(1+\nu)\arctan\frac{1}{Z}-\left[\frac{1-2\nu+2Z^2+2\nu Z^2+2-2}{2(1+Z^2)}\right]$$

$$= Z(1+\nu)\arctan\frac{1}{Z}-\left[\frac{-1+2(1+\nu)+2Z^2(1+\nu)}{2(1+Z^2)}\right]$$

$$= Z(1+\nu)\arctan\frac{1}{Z}-\left[\frac{2(1+Z^2)(1+\nu)-1}{2(1+Z^2)}\right]$$

$$\frac{\sigma_\theta}{\sigma_0} = -\frac{1-2\nu}{3R^2}\left(1-\frac{Z^3}{L^3}\right)+\frac{Z}{L}\left[L(1+\nu)\arctan\left(\frac{1}{L}\right)\text{-}(1\text{-}\nu)\frac{L^2}{1+L^2}\text{-}2\nu\right]$$

$$= -(1-2\nu)\frac{1}{2(1+Z^2)}]+\left[Z(1+\nu)\arctan\frac{1}{Z}-(1-\nu)\frac{Z^2}{1+Z^2}-2\nu\right]$$

$$\frac{\sigma_z}{\sigma_0} = -\frac{Z^3}{L(L^4+Z^2)}$$

$$= -\frac{Z^3}{Z(Z^4+Z^2)} = \frac{-1}{1+Z^2}$$

$\frac{\tau_{zr}}{\sigma_0} = -\frac{LRZ^2}{(1+L^2)(L^4+Z^2)} = 0$

Summary: when R = 0, L = Z,

$$\lim_{R\to 0} -\frac{1-\frac{Z^3}{L^3}}{3R^2} = -\frac{1}{2}\frac{1}{1+Z^2}$$

$$\frac{\sigma_r}{\sigma_0} = \frac{\sigma_\theta}{\sigma_0} = Z(1+\nu)\arctan\frac{1}{Z} - \left[\frac{2(1+Z^2)(1+\nu)-1}{2(1+Z^2)}\right]$$

$\frac{\sigma_z}{\sigma_0} = \frac{-1}{1+Z^2}$

$\frac{\tau_{zr}}{\sigma_0} = 0$

For the singularity point 4, if R = 0, Z = 0,

When R = 0, L = Z,

$$\frac{\sigma_r}{\sigma_0} = \frac{\sigma_\theta}{\sigma_0} = Z(1+\nu)\arctan\frac{1}{Z} - \left[\frac{2(1+Z^2)(1+\nu)-1}{2(1+Z^2)}\right]$$

$\frac{\sigma_z}{\sigma_0} = \frac{-1}{1+Z^2}$

$\frac{\tau_{zr}}{\sigma_0} = 0$

Then if Z =0,

$$\frac{\sigma_r}{\sigma_0} = \frac{\sigma_\theta}{\sigma_0} = Z(1+\nu)\arctan\frac{1}{Z} - \left[\frac{2(1+Z^2)(1+\nu)-1}{2(1+Z^2)}\right]$$

$= -\frac{2(1+\nu)-1}{2}$

$= -\frac{1+2\nu}{2}$

$\frac{\sigma_z}{\sigma_0} = \frac{-1}{1+Z^2} = -1$

$\frac{\tau_{zr}}{\sigma_0} = 0$

Appendix B – Additional Figures

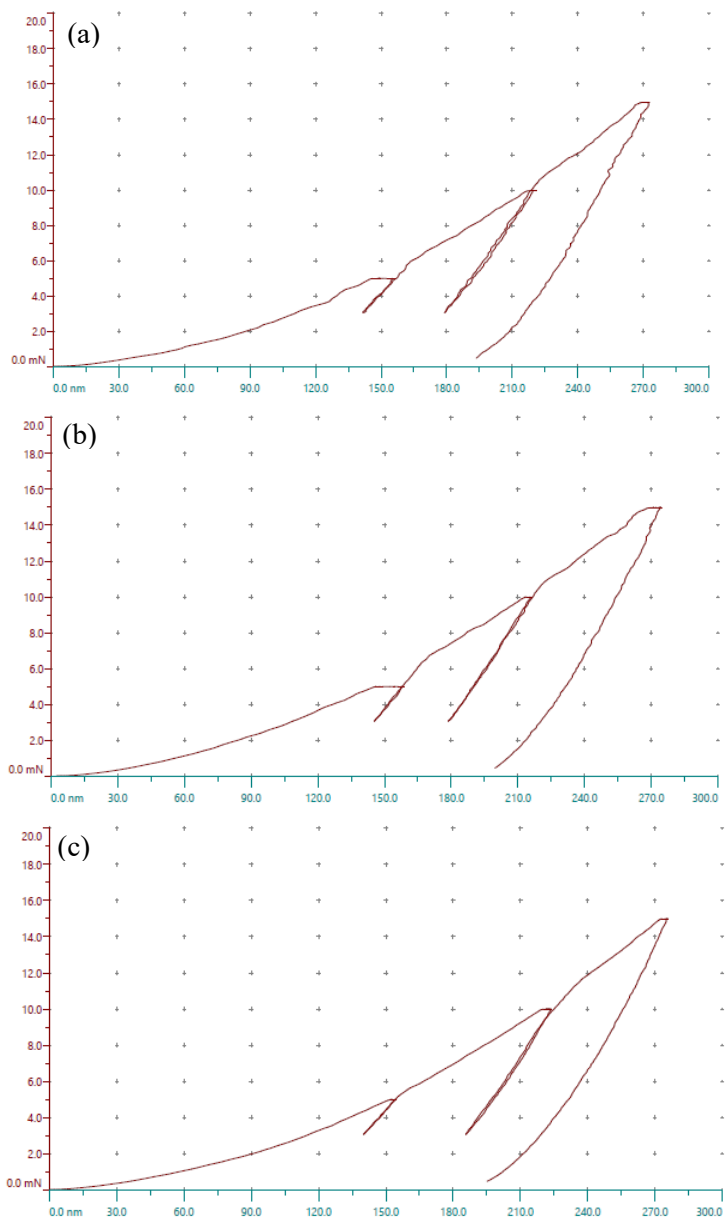

Figure B-1 Nanoindentation curves of annealed 5.1 wt% Ti coating on Ni-P matrix at three different locations (a), (b), and (c).

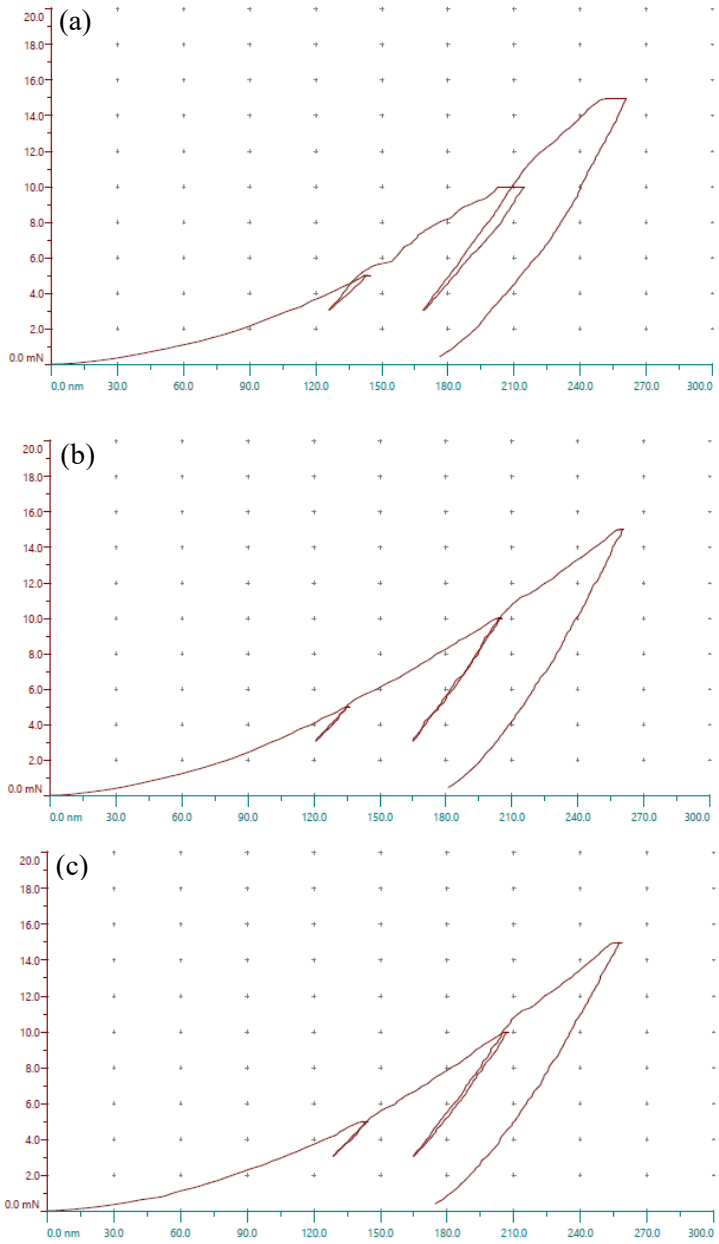

Figure B-2 Nanoindentation curves of annealed 5.1 wt% Ti coating on Ni_3Ti phase at three different locations (a), (b), and (c)

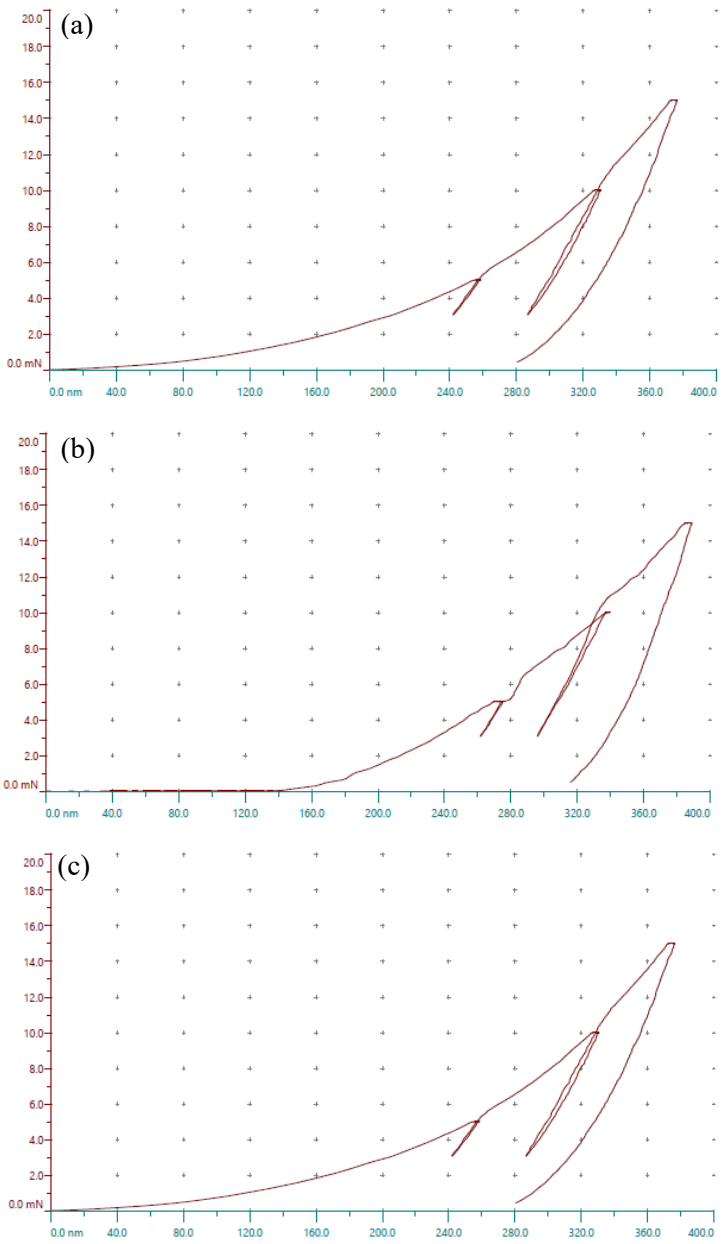

Figure B-3 Nanoindentation curves of annealed 5.1 wt% Ti coating on NiTi phase at three different locations (a), (b), and (c)

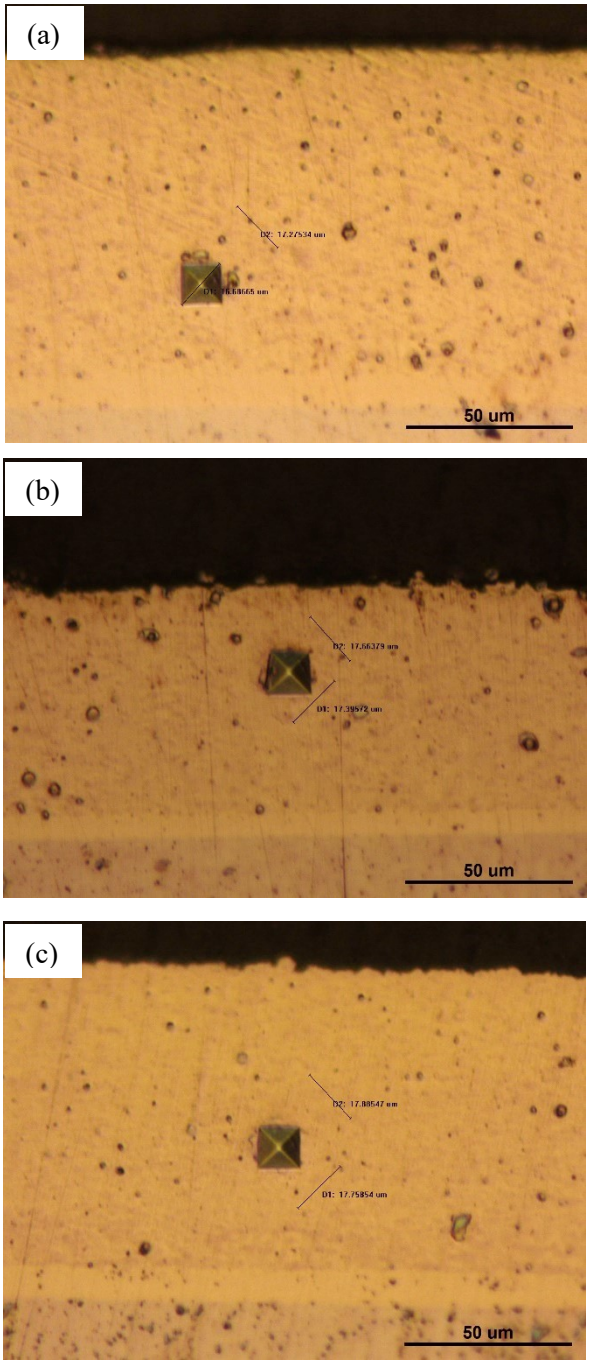

Figure B-4 Vickers hardness indentation tests on different as-deposited Ni-P-Ti coatings (a) 5.1 wt % Ti (b) 11.8 wt% Ti (c) 15.2 wt% Ti

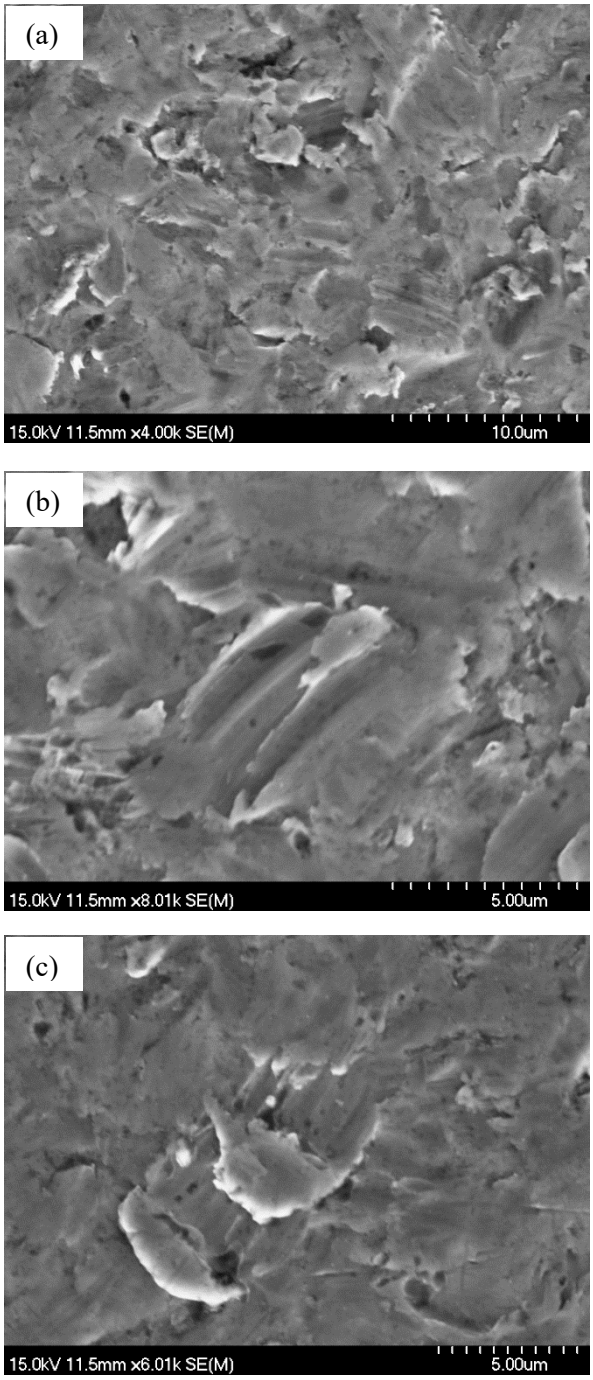

Figure B-5 Surface SEM micrographs of annealed 15.2 wt% Ti coating after Erosion-Corrosion test (a) general surface (b) micro-ploughing (c) micro-cutting

References:

[1] D. Gandy, Carbon Steel Handbook, Electri Power Research Institute, (2007) 1-172.

[2] C. Wang, Z. Farhat, G. Jarjoura, M.K. Hassan, A.M. Abdullah, Indentation and bending behavior of electroless Ni-P-Ti composite coatings on pipeline steel, Surface and Coatings Technology, 334 (2018) 243-252.

[3] T.R. Tamilarasan, U. Sanjith, M. Siva Shankar, G. Rajagopal, Effect of reduced graphene oxide (rGO) on corrosion and erosion-corrosion behaviour of electroless Ni-P coatings, Wear, 390-391 (2017) 385-391.

[4] M. MacLean, Z. Farhat, G. Jarjoura, E. Fayyad, A. Abdullah, M. Hassan, Fabrication and investigation of the scratch and indentation behaviour of new generation Ni-P-nano-NiTi composite coating for oil and gas pipelines, Wear, 426-427 (2019) 265-276.

[5] C. Wang, Indentation and Fracture Behaviour of Electroless Ni-P-based Composite Coatings, Halifax: Dalhousie University, (2017).

[6] T.C. Bayram, N. Orbey, R.Y. Adhikari, M. Tuominen, FP-based formulations as protective coatings in oil/gas pipelines, Progress in Organic Coatings, 88 (2015) 54-63.

[7] I. Taubkin, A.V. Sukhov, T. Rudakova, Analysis of the behavior of a protective polymer coating for gas pipelines under the action of applied heat, International Polymer Science and Technology 32 (2004) 22-32.

[8] D. Vojtěch, M. Novák, M. Zelinková, P. Novák, A. Michalcová, T. Fabián, Structural evolution of electroless Ni–P coating on Al–12wt.% Si alloy during heat treatment at high temperatures, Applied Surface Science, 255 (2009) 3745-3751.

[9] C.K. Lee, Structure, electrochemical and wear-corrosion properties of electroless nickel–phosphorus deposition on CFRP composites, Materials Chemistry and Physics, 114 (2009) 125-133.

[10] X. Xiu-qing, M. Jian, B. Zhen-quan, F. Yao-rong, M. Qiu-rong, Z. Wen-zhen, The corrosion behavior of electroless Ni–P coating in Cl−/H2S environment, Applied Surface Science, 258 (2012) 8802-8806.

[11] A. Brenner, G. E. Riddell, Nickel plating on steel by chemical reduction, Journal of Research of the National Bureau of Standards, 37 (1946) 31-34.

[12] G.O. Mallory, J. B. Hajdu, Electroless Plating: Fundamentals And Applications, William Andrew Publishing, (1990) 1-56.

[13] K.H. Krishnan, S.John, K.N. Sriivasan, J. Praveen, M. Ganesan, P.M. Kavimani, An Overall Aspect of Electroless Ni-P Depositions—A Review Article, Metallurgical and Materials Transactions A, 37A (2006) 1917-1926.

[14] C. Wang, Z. Farhat, G. Jarjoura, M.K. Hassan, A.M. Abdullah, Indentation and erosion behavior of electroless Ni-P coating on pipeline steel, Wear, 376-377 (2017) 1630-1639.

[15] M. Islam, M.R. Azhar, N. Fredj, T.D. Burleigh, O.R. Oloyede, A.A. Almajid, S. Ismat Shah, Influence of SiO2 nanoparticles on hardness and corrosion resistance of electroless Ni–P coatings, Surface and Coatings Technology, 261 (2015) 141-148.

[16] M. Palaniappa, S.K. Seshadri, Friction and wear behavior of electroless Ni–P and Ni–W–P alloy coatings, Wear, 265 (2008) 735-740.

[17] S. Duari, A. Mukhopadhyay, T.K. Barman, P. Sahoo, Study of wear and friction of chemically deposited Ni-P-W coating under dry and lubricated condition, Surfaces and Interfaces, 6 (2017) 177-189.

[18] C.J. Lin, K.C. Chen, J.L. He, The cavitation erosion behavior of electroless Ni–P–SiC composite coating, Wear, 261 (2006) 1390-1396.

[19] C. Wang, Z. Farhat, G. Jarjoura, M.K. Hassan, A.M. Abdullah, E.M. Fayyad, Investigation of fracture behavior of annealed electroless Ni-P coating on pipeline steel using acoustic emission methodology, Surface and Coatings Technology, 326 (2017) 336-342.

[20] M. MacLean, Z. Farhat, G. Jarjoura, E. Fayyad, A. Abdullah, M. Hassan, Fabrication and investigation of the scratch and indentation behaviour of new generation Ni-P-nano-NiTi composite coating for oil and gas pipelines, Wear, 426/427 (2019) 265-276.

[21] S. Angioni, M. Meo, A. Foreman, Impact damage resistance and damage suppression properties of shape memory alloys in hybrid composites—a review, smart materials and structures, 20 (2011).

[22] https://www.us-nano.com/nanopowders.

[23] W.J. Buehler, J.V. Gilfrich, R.C. Wiley, Effect of Low-Temperature Phase Changes on the Mechanical Properties of Alloys near Composition TiNi, Journal of Applied Physics, 34 (1963) 1475-1477.

[24] M.M. Sherif, O.E. Ozbulut, Tensile and superelastic fatigue characterization of NiTi shape memory cables, Smart Materials and Structures, 27 (2018) 015007.

[25] Y. Chen, O. Tyc, L. Kadeřávek, O. Molnárová, L. Heller, P. Šittner, Temperature and microstructure dependence of localized tensile deformation of superelastic NiTi wires, Materials & Design, 174 (2019) 107797-107797.

[26] K. Guda Vishnu, A. Strachan, Phase stability and transformations in NiTi from density functional theory calculations, Acta Materialia, 58 (2010) 745-752.

[27] K. Otsuka, X. Ren, Physical metallurgy of Ti–Ni-based shape memory alloys, Progress in Materials Science, 50 (2005) 511-678.

[28] M. Shahirnia, Deformation Behaviour of TiNi Shape Memory Alloy under Tensile and Compressive Loads .pdf, thesis (2011).

[29] D.C. Lagoudas, Shape Memory Alloys Modeling and Engineering Applications, Springer (2008).

[30] L.C. Brinson, I. Schmidt, R. Lammering, Stress-induced transformation behavior of a polycrystalline NiTi shape memory alloy: micro and macromechanical investigations via in situ optical microscopy, Journal of the Mechanics and Physics of Solids, 52 (2004) 1549-1571.

[31] L. Hu, Y. Xue, F. Shi, Intermetallic formation and mechanical properties of Ni-Ti diffusion couples, Materials & Design, 130 (2017) 175-182.

[32] M.A. Whitney, A study of the sintering behavior of Ni-Ti powder compacts using differential scanning calorimetry, University of Waterloo, thesis, (2007).

[33] D. Feng, S. Chen, W. Fan, L.F. Hu, Q. Meng, Phase transformation and mechanical performance of interface between Ti/Ni Diffusion bonding couples activated by electric field., Rare Metal Materials and Engineering, 44 (2015) 349-354.

[34] J. Laeng, Z. Xiu, X. Xu, X. Sun, H. Ru, Y. Liu, Phase formation of Ni–Ti via solid state reaction, Physica Scripta, T129 (2007) 250-254.

[35] A.D. Smigelkas, E.O. Kirkendall, Zinc diffusion in alpha brass, Trans. AIME, 171 (1947) 130-134.

[36] G.F. Bastin, G.D. Rieck, Diffusion in the Ti-Ni system: occurrence and growth of the various intermetallic compunds, Metallurgical Transactions 5(1974) 1817-1831.

[37] V. Hasannaeimi, T. Shahrabi, S. Sanjabi, Fabrication of NiTi layer via co-electrodeposition of nickel and titanium, Surface and Coatings Technology, 210 (2012) 10-14.

[38] B.Y. Li, L.J. Rong, Y.Y. Li, Porous NiTi alloy prepared from elemental powder sintering, Journal of Materials Research, 13 (2011) 2847-2851.

[39] A.V. Yakubovich, A.V. Verkhovtsev, M. Hanauske, A.V. Solov'yov, Computer simulation of diffusion process at interfaces of nickel and titanium crystals, Computational Materials Science, 76 (2013) 60-64.

[40] G.F. Bastin, G.D. Rieck, Diffusion in the Titanium-Nickel System: II. Calculations of Chemical and Intrinsic Diffusion Coefficients, Metallugical Transactions, 5 (1974) 1827-1831.

[41] X. Shao, X. Guo, Y. Han, Z. Lin, J. Qin, W. Lu, D. Zhang, Preparation of TiNi films by diffusion technology and the study of the formation sequence of the intermetallics in Ti–Ni systems, Journal of Materials Research, 29 (2014) 2707-2716.

[42] A.E. Pazy Puente, D.C. Dunand, Synthesis of NiTi microtubes via the Kirkendall effect during interdiffusion of Ti-coated Ni wires, Intermetallics, 92 (2018) 42-48.

[43] N. Barbat, K. Zangeneh-Madar, Fabrication and characterization of NiTi shape memory alloy synthesized by Ni electroless plating of titanium powder, Advanced Powder Technology, 29 (2018) 1005-1013.

[44] M. Abdoos, A.A. Amadeh, M. Adabi, Formation and wear mechanism of nickel titanium intermetallics during heat treatment of nickel coating on Ti-6Al-4V substrate, Transactions of the IMF, 97 (2019) 146-154.

[45] B.Y. Tay, C.W. Goh, Y.W. Gu, C.S. Lim, M.S. Yong, M.K. Ho, M.H. Myint, Porous NiTi fabricated by self-propagating high-temperature synthesis of elemental powders, Journal of Materials Processing Technology, 202 (2008) 359-364.

[46] S. Wisutmethangoon, N. Denmud, L. Sikong, Characteristics and compressive properties of porous NiTi alloy synthesized by SHS technique, Materials Science and Engineering: A, 515 (2009) 93-97.

[47] X. Li, X. Chen, C. Zhang, J. Luo, Preparation of self-lubricating NiTi alloy and its self-adaptive behavior, Tribology International, 130 (2019) 43-51.

[48] C.Y. Tang, L.N. Zhang, C.T. Wong, K.C. Chan, T.M. Yue, Fabrication and characteristics of porous NiTi shape memory alloy synthesized by microwave sintering, Materials Science and Engineering: A, 528 (2011) 6006-6011.

[49] S.V. Divinski, I. Stloukal, L. Kral, C. Herzig, Diffusion of Titanium and Nickel in B2 NiTi, Defect and Diffusion Forum, 289-292 (2009) 377-382.

[50] D. Liu, M. Peterlechner, J. Fiebig, S. Trubel, M. Wegner, Y. Du, Z. Jin, G. Wilde, S.V. Divinski, Grain boundary diffusion and precipitates in B2 Ti−50.2 at.% Ni alloy, Intermetallics, 61 (2015) 30-37.

[51] A.E. Pazy Puente, D.C. Dunand, Shape-memory characterization of NiTi microtubes fabricated through interdiffusion of Ti-Coated Ni wires, Acta Materialia, 156 (2018) 1-10.

[52] R.G. Brenner A, Nickel Plating on Steel by Chemical Reduction JOURNAL OF RESEARCH 37 (1946) 31-34.

[53] Hersch P, study of the mechanism of the electroless deposition of nickel Transaction of Institue of Metal Finishing 33 (1955) 417420.

[54] J. Sudagar, J. Lian, W. Sha, Electroless nickel, alloy, composite and nano coatings – A critical review, Journal of Alloys and Compounds, 571 (2013) 183-204.

[55] R.H. Guo, S.X. Jiang, C.W.M. Yuen, M.C.F. Ng, J.W. Lan, G.H. Zheng, Influence of deposition parameters and kinetics of electroless Ni-P plating on polyester fiber, Fibers and Polymers, 13 (2012) 1037-1043.

[56] H.R. Molla, H. Modarress, M. Abdouss, Electroless nickel–phosphorus deposition on carbon steel CK-75 and study of the effects of some parameters on properties of the deposits, Journal of Coatings Technology and Research, 9 (2009) 183-188.

[57] Z. Chen, X. Xu, C.C. Wong, S. Mhaisalkar, Effect of plating parameters on the intrinsic stress in electroless nickel plating, Surface and Coatings Technology, 167 (2003) 170-176.

[58] P. Sahoo, S.K. Das, Tribology of electroless nickel coatings – A review, Materials & Design, 32 (2011) 1760-1775.

[59] J. K. Luo, A.J. Flewitt, S. M. Spearing, N. A. Fleck, W. I. Milne, Young's modulus of electroplated Ni thin film for MEMS applications, Materials Letters, 58 (2004) 2306-2309.

[60] S. Guo, L. Li, G. Zhang, W. Wang, X. Zhao, Stress analysis at the interface between Ni–P coating and SiCp/Al substrate of space mirror, Applied Surface Science, 255 (2009) 3691-3695.

[61] S. Karthikeyan, L. Vijayaraghavan, S. Madhavan, A. Almeida, Study on the Mechanical Properties of Heat-Treated Electroless NiP Coatings Reinforced with Al2O3 Nano Particles, Metallurgical and Materials Transactions A, 47 (2016) 2223-2231.

[62] C.A. León-Patiño, J. García-Guerra, E.A. Aguilar-Reyes, Tribological characterization of heat-treated Ni-P and Ni-P-Al2O3 composite coatings by reciprocating sliding tests, Wear, 426-427 (2019) 330-340.

[63] A. Hadipour, M. Rahsepar, H. Hayatdavoudi, Fabrication and characterisation of functionally graded Ni-P coatings with improved wear and corrosion resistance, Surface Engineering, 35 (2018) 883-890.

[64] J.N. Balaraju, T.S.N. Sankara Narayanan, S.K. Seshadri, Electroless Ni–P composite coatings, Journal of Applied Electrochemistry, 33 (2003) 807-816.

[65] D.K. Schotter, The effects of heat treatment on microindentation hardness, abrasion and corrosion resistance of electroless nickel coatings, thesis, (1988).

[66] J. Qi, B. Huang, Z. Wang, H. Ding, J. Xi, W. Fu, Dependence of corrosion resistance on grain boundary characteristics in a high nitrogen CrMn austenitic stainless steel, Journal of Materials Science & Technology, 33 (2017) 1621-1628.

[67] K.M. Shartal, G.J. Kipouros, Electroless Nickel Phosphorus Plating on AZ31, Metallurgical and Materials Transactions B, 40 (2009) 208-222.

[68] B. Jiang, S.L. Jiang, A.L. Ma, Y.G. Zheng, Effect of Heat Treatment on Erosion-Corrosion Behavior of Electroless Ni-P Coatings in Saline Water, Materials and Manufacturing Processes, 29 (2014) 74-82.

[69] H. Mazaheri, S.R. Allahkaram, Deposition, characterization and electrochemical evaluation of Ni–P–nano diamond composite coatings, Applied Surface Science, 258 (2012) 4574-4580.

[70] M.A. Islam, Z.N. Farhat, Effect of impact angle and velocity on erosion of API X42 pipeline steel under high abrasive feed rate, Wear, 311 (2014) 180-190.

[71] G.W. Stachowiak, A.W. Batchelor, Engineering Tribology, Oxford: Elsevier Inc. , (2014).

[72] C.J. Lin, K.C. Chen, J.L. He, The cavitation erosion behavior of electroless Ni–P–SiC composite coating, Wear, 261 (2006) 1390-1396.

[73] C.J. Chen, K.L. Lin, The Deposition and Crystallization Behaviors of Electroless Ni-Cu-P Deposits, Journal of the Electrochemical Society 146 (1999) 137-140.

[74] I. Mukhopadhyay, C.L. Aravinda, D. Borissov, W. Freyland, Electrodeposition of Ti from TiCl4 in the ionic liquid l-methyl-3-butyl-imidazolium bis (trifluoro methyl sulfone) imide at room temperature: study on phase formation by in situ electrochemical scanning tunneling microscopy, Electrochimica Acta, 50 (2005) 1275-1281.

[75] G.R. Hu, Y.X Liu, J.H. Yang, Electroless plating composite coatings of Ni-Ti-Re on the surface of diamond, journal of central south University of Technology 6(1999) 13-15.

[76] J.N. Balaraju, Kalavati, K.S. Rajam, Influence of particle size on the microstructure, hardness and corrosion resistance of electroless Ni–P–Al_2O_3 composite coatings, Surface and Coatings Technology, 200 (2006) 3933-3941.

[77] S. Sadreddini, A. Afshar, Corrosion resistance enhancement of Ni-P-nano SiO2 composite coatings on aluminum, Applied Surface Science, 303 (2014) 125-130.

[78] Y. Liu, Q. Zhao, Study of electroless Ni–Cu–P coatings and their anti-corrosion properties, Applied Surface Science, 228 (2004) 57-62.

[79] T. Rabizadeh, S.R. Allahkaram, Corrosion resistance enhancement of Ni–P electroless coatings by incorporation of nano-SiO2 particles, Materials & Design, 32 (2011) 133-138.

[80] J.N. Balaraju, V. Ezhil Selvi, K.S. Rajam, Electrochemical behavior of low phosphorus electroless Ni–P–Si3N4 composite coatings, Materials Chemistry and Physics, 120 (2010) 546-551.

[81] A. Araghi, M.H. Paydar, Electroless deposition of Ni–P–B4C composite coating on AZ91D magnesium alloy and investigation on its wear and corrosion resistance, Materials & Design, 31 (2010) 3095-3099.

[82] Y.Y. Tsaia, F.B. Wub, Y.I. Chena, P.J. Penga, J.G. Duhb, S.Y. Tsaic, Thermal stability and mechanical properties of Ni–W–P electroless deposits, Surface and Coatings Technology, 146-147 (2001) 502-507.

[83] M.A. Shoeib, M.M. Kamel, S.M. Rashwan, O.M. Hafez, Corrosion behavior of electroless Ni-P/TiO_2 nanocomposite coatings, Surface and Interface Analysis, 47 (2015) 672-680.

[84] L. Song, Y. Wang, W. Lin, Q. Liu, Primary investigation of corrosion resistance of Ni-P/TiO_2 composite film on sintered NdFeB permanent magnet, Surface and Coatings Technology, 202 (2008) 5146-5150.

[85] U. Matik, Structural and wear properties of heat-treated electroless Ni-P alloy and Ni-P-Si_3N_4 composite coatings on iron based PM compacts, Surface and Coatings Technology, 302 (2016) 528-534.

[86] D. Vojtěch, Properties of Hard Ni–P–$Al_2O_3$and Ni–P–SiC Coatings on Al-Based Casting Alloys, Materials and Manufacturing Processes, 24 (2009) 754-757.

[87] B. Bozzini, P.L. Cavallotti, G. Parisi, Corrosion and erosion-corrosion of electrodeposited Ni–P/B_4C composites, British Corrosion Journal, 36 (2013) 49-55.

[88] J.A. Calderón, J.E. Henao, M.A. Gómez, Erosion–corrosion resistance of Ni composite coatings with embedded SiC nanoparticles, Electrochimica Acta, 124 (2014) 190-198.

[89] G.M.P. Robert F. Cook, Direct Observation and Analysis of Indentation Cracking in Glasses and Ceramics, Journal of American Ceramic Society, 73 (1990) 787-817.

[90] H. Hertz, Hertz's Miscellaneous Papers, Thesis, (1896) 1-383.

[91] B.R. Lawn, Indentation of Ceramics with Spheres: A Century after Hertz, Journal of American Ceramic Society, 81 (1998) 1977-1994.

[92] A.C. Fischer-Cripps, Predicting Hertzian fracture, Journal of Materials Science, 32 (1997) 1277-1285.

[93] C. Kocer, R.E. Collins, Angle of Hertzian Cone Cracks, Journal of American Ceramic Society, 81 (1998) 1736-1742.

[94] F. Frank, On the theory of Hertzian fracture, proceeding of the Royal Society of London. Series A. Mathematical and Physical Sciences, 299 (1967) 291-306.

[95] T.N. Farris, S.Y. Chen, S. Chandrasekar, Contact mechanics of Hertzian cone cracking, International Journal of Solids and Structures, 32 (1995) 329-340.

[96] J.D. Kuntz, G.-D. Zhan, A.K. Mukherjee, Nanocrystalline-Matrix Ceramic Composites for Improved Fracture Toughness, MRS Bulletin, 29 (2011) 22-27.

[97] J.A. Yeomans, Ductile particle ceramic matrix composites—Scientific curiosities or engineering materials?, Journal of the European Ceramic Society, 28 (2008) 1543-1550.

[98] R.O. Ritchie, Mechanisms of fatigue-crack propagation in ductile and brittle solids, International Journal of Fracture, 100 (1999) 55-83.

[99] R. Narayan, Biomedical materials., Springer, (2009) 183-196.

[100] M. Maclean, Development and Characterization of Electroless Ni-P Composite Coatings with Superelastic Nano-NiTi Additions, Halifax: Dalhousie University, (2019).

[101] M.A. Islam, Erosion, corroion and erosion-corrosion of oil and gas pipeline steels, PhD Thesis, Halifax (2015) 1-254.

[102] W.D. Callister, J.D.G. Rethwisch, Materials Science and Engineering an Introduction, John Wiley & Sons, Inc., Eighth edition (2009) 212-214.

[103] M. Maaza, C. Sella, J.P. Ambroise, M. Kaabouchi, M. Miloche, F. Wehling, M. Groos, Determination of diffusion coefficient D and activation energy Q_a of nickel into Titanium in Ni-Ti multilayers by Grazing-Angle Neutron Reflectometry, Journal of Applied Crytallography, 26 (1993) 334-342.

[104] M.J. Sohrabi, H. Mirzadeh, Interdiffusion coefficients of alloying elements in a typical Ni-based superalloy, Vacuum, 169 (2019) 108875.

[105] ASTM, Standard Test Method for Vickers Indentation Hardness of Advanced Ceramics C1327-15, ASTM, W. Conshohocken PA, (2015).

[106] ASTM, Standard Test Method for Adhesion Strength and Mechannical Failure Modes of Ceramic Coatings by Quantitative Single Point Scratch Testing, ASTM int., C1624-05 (2015) 1-29.

[107] ASTM, Standard Test Method for Ranking Resistance of Materials to Sliding Wear Using Block-on-Ring Wear Test, ASTM int., G77-17 (2017) 1-11.

[108] Z. Li, Z.N. Farhat, G. Jarjoura, E. Fayyad, A. Abdullah, M. Hassan, Synthesis and characterization of scratch resistant Ni-P-Ti based composite coating, Tribology Transactions, 62 (2019) 880-896.

[109] A.T. Akono, F.J. Ulm, An improved technique for characterizing the fracture toughness via scratch test experiments, Wear, 313 (2014) 117-124.

[110] W.C. Oliver, G.M. Pharr, An improved technique for determining hardness and elastic modulus using load and displacement sensing indentation experiments, journal of materials research, 7 (1992) 1564-1583.

[111] A. Rauzaud, E. Barbier, J. Ernoult, E. Quesnel, A method for elastic modulus measurements of magnetron sputtered thin films dedicated to mechanical applications, Thin Solid Films, 270 (1995) 270-274.

[112] E. Harry, A. Rouzaud, M. Ignat, P. Juliet, Mechanical properties of W and W(C) thin films: Young's modulus, fracture toughness and adhesion, Thin Solid Films, 332 (1998) 195-201.

[113] D. Louapre, K. Breder, Hertzian Indentation Stress Field Equations, International Journal of Applied Ceramic Technology, 12 (2015) 1071-1079.

[114] K.L. Johnson, Contact mechanics, Cambridge University Press, Cambridge, U.K (1985).

[115] R. Neupane, Indentation and Wear Behavior of Superelastic TiNi Shape Memory Alloy, Dalhousie University, Halifax (2014).

[116] M.A. Islam, J. Jiang, Y. Xie, P. Fiala, Investigation of erosion-corrosion behavior of (WTi)C based weld overlays, Wear, 390-391 (2017) 155-165.

[117] ASTM, Standard test method for conducting potentiodynamic polarization resistance measurements, ASTM int. , G59-97 (2014) 1-4.

[118] ASTM, Standard Guide for Determining Synergism Between Wear and Corrosion, ASTM Int., G119-09 (2009) 1-7.

[119] M.D. Ger, B.J. Hwang, Effect of surfactants on codeposition of PTFE particles with electroless Ni-P coating, Materials Chemistry and Physics, 76 (2002) 38-45.

[120] S. Alirezaei, S.M. Monirvaghefi, M. Salehi, A. Saatchi, M. Kargosha, Effect of alumina content on wear behaviour of Ni−P−Al_2O_3(α) electroless composite coatings, Surface Engineering, 21 (2013) 60-66.

[121] F.E.T. Heakal, M.A. Maanoum, Role of Some Plating Parameters in the Properties of Ni-P/Al2O3 Nanocomposite Coatings on Mg alloy, International Journal of Electrochemical Science, 11 (2016) 7198-7215.

[122] S. Afroukhteh, C. Dehghanian, M. Emamy, Preparation of electroless Ni–P composite coatings containing nano-scattered alumina in presence of polymeric surfactant, Progress in Natural Science: Materials International, 22 (2012) 318-325.

[123] Y. Zhao, C. Jiang, Z. Xu, F. Cai, Z. Zhang, P. Fu, Microstructure and corrosion behavior of Ti nanoparticles reinforced Ni–Ti composite coatings by electrodeposition, Materials & Design, 85 (2015) 39-46.

[124] S. Wang, X. Huang, M. Gong, W. Huang, Microstructure and mechanical properties of Ni-P-Si_3N_4 nanowire electroless composite coatings, Applied Surface Science, 357 (2015) 328-332.

[125] H. Ashassi-Sorkhabi, S.H. Rafizadeh, Effect of coating time and heat treatment on structures and corrosion characteristics of electroless Ni–P alloy deposits, Surface and Coatings Technology, 176 (2004) 318-326.

[126] C.K. Chen, H.M. Feng, H.C. Lin, M.H. Hon, The effect of heat treatment on the microstructure of electroless Ni–P coatings containing SiC particles, Thin Solid Films, 416 (2002) 31-37.

[127] J.I.C.F.D. Data®, Powder Diffraction File(PDF) No. 00-004-0850, JCPDS: Netwon Square, PA, USA, (2019).

[128] A. Serek, A. Budniok, Electrodeposition and thermal treatment of nickel layers containing titanium, Journal of Alloys and Compounds, 352 (2003) 290-295.

[129] J.I.C.F.D. Data®, Powder Diffraction File (PDF) No. 00-008-5982, JCPDS: Netwon Square, PA, USA, (2019).

[130] G. Jiaqiang, L. Lei, W. Yating, S. Bin, H. Wenbin, Electroless Ni–P–SiC composite coatings with superfine particles, Surface and Coatings Technology, 200 (2006) 5836-5842.

[131] D. Dong, X.H. Chen, W.T. Xiao, G.B. Yang, P.Y. Zhang, Preparation and properties of electroless Ni–P–SiO2 composite coatings, Applied Surface Science, 255 (2009) 7051-7055.

[132] X. Wu, J. Mao, Z. Zhang, Y. Che, Improving the properties of 211Z Al alloy by enhanced electroless Ni–P–TiO2 nanocomposite coatings with TiO2 sol, Surface and Coatings Technology, 270 (2015) 170-174.

[133] J.I.C.F.D. Data®, Powder Diffraction File(PDF) No. 00-015-7502, JCPDS: Netwon Square, PA, USA, (2020).

[134] C. Lin, N. Dadvand, Z. Farhat, G. Kipouros, Electroless Nickel Phosphorous Plating on Carbon steel, Materials Science and Technology, 3 (2013) 2224-2237.

[135] C.R. Hubbard, R.L. Snyder, RIR-Measurement and use in quantitative XRD, Powder Diffraction, 3 (1988) 74-77.

[136] E.J. Mittemeijer, Fundamentals of Materils Science, Springer, (2010).

[137] Z.N. Farhat, Y. Ding, D. O. Northwood, A.T. Alpas, Effect of grain size on friction and wear of nanocrystalline aluminum, Materials Science and Engineering A, 206 (1996) 302-313.

[138] J.S.C. Jang, S.R. Jian, T.H. Li, J.C. Huang, C.Y.A. Tsao, C.T. Liu, Structural and mechanical characterizations of ductile Fe particles-reinforced Mg-based bulk metallic glass composites, Journal of Alloys and Compounds, 485 (2009) 290-294.

[139] J.S.C. Jang, J.B. Li, S.L. Lee, Y.S. Chang, S.R. Jian, J.C. Huang, T.G. Nieh, Prominent plasticity of Mg-based bulk metallic glass composites by ex-situ spherical Ti particles, Intermetallics, 30 (2012) 25-29.

[140] C.A. Klein, G.F. Cardinale, Young's modulus and Poisson's ratio of CVD diamond, Diamond and Related Materials, 2 (1993) 918-923.

[141] Y. Chen, O. Tyc, O. Molnárová, L. Heller, P. Šittner, Tensile Deformation of Superelastic NiTi Wires in Wide Temperature and Microstructure Ranges, Shape Memory and Superelasticity, 5 (2018) 42-62.

[142] Z. Farhat, G. Jarjoura, M. Shahirnia, Dent Resistance and Effect of Indentation Loading Rate on Superelastic TiNi Alloy, Metallurgical and Materials Transactions A, 44 (2013) 3544-3551.

[143] J.E. Garay, U. Anselmi-Tamburini, Z.A. Munir, Enhanced growth of intermetallic phases in the Ni–Ti system by current effects, Acta Materialia, 51 (2003) 4487-4495.

[144] R.O. Ritchie, Mechanisms of fatigue crack propagation in metals, ceramics and composites: Role of crack tip shielding, Materials Science and Engineering: A, 103 (1988) 15-28.

[145] H. Ruf, A.G. Evans, Toughening by Monoclinic Zirconia, Journal of the American Ceramic Society, 66 (1983) 328-332.

[146] J.F. Bartolome, M. Diaz, J.S. Moya, Influence of the Metal Particle Size on the Crack Growth Resistance in Mullite–Molybdenum Composites, Journal of American ceramic society, 85 (2002) 2778-2784.

[147] X. Sun, J.A. Yeomans, Microstructure and fracture toughness of nickel particle toughened alumina matrix composites, Journal of Materials and Science, 31 (1996) 875-880.

[148] P.A. Trusty, J.A. Yeomans, The Toughening of Alumina with Iron Effects of iron distribution on fracture toughness, Journal of the European Ceramic Society, 17 (1997) 495-504.

[149] D.R. Ni, Z.Y. Ma, Shape Memory Alloy-Reinforced Metal-Matrix Composites: A Review, Acta Metallurgica Sinica (English Letters), 27 (2014) 739-761.

[150] K. T. Faber, T. Iwagoshi, A. Ghosh, Toughening by stress-induced microcracking in two phase ceramics, Communications of the American Ceramic Society, 71 (1988) 399-401.

[151] J.F. Archard, Contact and Rubbing of Flat Surfaces, Journal of Applied Physics, 24 (1953) 981-988.

[152] H. Ogihara, H. Wang, T. Saji, Electrodeposition of Ni–B/SiC composite films with high hardness and wear resistance, Applied Surface Science, 296 (2014) 108-113.

[153] Y. Zhou, H. Zhang, B. Qian, Friction and wear properties of the co-deposited Ni–SiC nanocomposite coating, Applied Surface Science, 253 (2007) 8335-8339.

[154] D. Misra, S.M. Shariff, S. Mukhopadhyay, S. Chatterjee, Analysis of instrumented scratch hardness and fracture toughness properties of laser surface alloyed tribological coatings, Ceramics International, 44 (2018) 4248-4255.

[155] ASTM, Standard Test Method for Scratch Hardness of Materials Using a Diamond Stylus, ASTM int., G173-03 (2017) 1-7.

[156] Q.J. Zhou, J.Y. He, J.X. Li, W.Y. Chu, L.J. Qiao, Measurement of fracture toughness of nickel phosphorus coatings, Materials Letters, 60 (2006) 349-351.

[157] A.W. Thompson, H.J. Saxton, Structure, strength and fracture of electrodeposited nickel and Ni-Co alloys, Matallurgical Transactions, 4 (1973) 1599-1605.

[158] W. Dai, C. Oropeza, K. Lian, W. Wang, Experiment design and UV-LIGA microfabrication technology to study the fracture toughness of Ni microstructures, Microsystem Technologies, 12 (2005) 306-314.

[159] I. Ovidko, A. Sheinerman, Suppression of nanocrack generation in nanocrystalline materials under superplastic deformation, Acta Materialia, 53 (2005) 1347-1359.

[160] I.A. Ovid'ko, A.G. Sheinerman, Ductile vs. brittle behavior of pre-cracked nanocrystalline and ultrafine-grained materials, Acta Materialia, 58 (2010) 5286-5294.

[161] Y. Liu, J. Zhou, L. Wang, S. Zhang, Y. Wang, Grain size dependent fracture toughness of nanocrystalline materials, Materials Science and Engineering: A, 528 (2011) 4615-4619.

[162] C.R. Barrett, W.D. Nix, A.S. Tetelman, The Principles of Engineering Materials Prentice-Hall Inc., (1973).

[163] R. Liu, D.Y. Li, Y.S. Xie, R. Llewellyn, H.M. Hawthorne, Indentation behavior of pseudoelastic TiNi alloy, Scripta Materialia, 41 (1999) 691-696.

[164] V.V. Shastry, U. Ramamurty, Simultaneous measurement of mechanical and electrical contact resistances during nanoindentation of NiTi shape memory alloys, Acta Materialia, 61 (2013) 5119-5129.

[165] L. Wang, C. Wang, W. Lu, D. Zhang, Superelasticity of NiTi–Nb metallurgical bonding via nanoindentation observation, Materials Letters, 161 (2015) 255-258.

[166] X. Huang, J. Nohava, B. Zhang, A.G. Ramirez, Nanoindentation of NiTi shape memory thin films at elevated temperatures, International Journal of Smart & Nano Materials, 2 (2011) 39-49.

[167] N. Cameron, Z. Farhat, Investigation into the Wear and Dent Resistance of Ni/Ti Nanolaminates and Superelastic NiTi Coating, Journal of Materials Engineering and Performance, 28 (2019) 6033-6041.

[168] J. Chen, G. Zhao, Y. Zhang, S. Duan, K. Matsuda, Y. Zou, Metastable phase evolution and nanoindentation behavior of amorphous Ni–Cu–P coating during heat treatment process, Journal of Alloys and Compounds, 805 (2019) 597-608.

[169] M. Sribalaji, O.S. Asiq Rahman, T. Laha, A.K. Keshri, Nanoindentation and nanoscratch behavior of electroless deposited nickel-phosphorous coating, Materials Chemistry and Physics, 177 (2016) 220-228.

[170] A. Salicio-Paz, H. Grande, E. Pellicer, J. Sort, J. Fornell, R. Offoiach, M. Lekka, E. García-Lecina, Monolayered versus multilayered electroless NiP coatings: Impact of the plating approach on the microstructure, mechanical and corrosion properties of the coatings, Surface and Coatings Technology, 368 (2019) 138-146.

[171] S.K. Tien, J.G. Duh, Y.I. Chen, The influence of thermal treatment on the microstructure and hardness in electroless Ni-P-W deposit, Thin Solid Films, 469-470 (2004) 333-338.

[172] R. Valentini, P. Cavaliere, D. Valerini, Nanoindentation and scratch behaviour of Ni–P electroless coatings, Tribology - Materials, Surfaces and Interfaces, 14 (2020) 22-32.

[173] N. Kulo, S. He, W. Ecker, R. Pippan, T. Antretter, V.I. Razumovskiy, Thermodynamic and mechanical stability of Ni3X-type intermetallic compounds, Intermetallics, 114 (2019).

[174] Y. Cao, J.C. Zhu, Y. Liu, Z.H. Lai, Z.S. Nong, First-principles studies of the structural, elastic, electronic and thermal properties of gamma '-Ni3Ti, Physica B, 412 (2013) 45-49.

[175] H. Yang, Z. Wang, H. Zhang, Y. Ma, X. Liu, Z. He, Microstructure and nanoindentation behaviour of Ni surface modified Ti6Al4V, Surface Engineering, 31 (2015) 923-929.

[176] G. Laplanche, J. Pfetzing-Micklich, G. Eggeler, Orientation dependence of stress-induced martensite formation during nanoindentation in NiTi shape memory alloys, Acta Materialia, 68 (2014) 19-31.

[177] J. Pfetzing-Micklich, C. Somsen, A. Dlouhy, C. Begau, A. Hartmaier, M.F.X. Wagner, G. Eggeler, On the crystallographic anisotropy of nanoindentation in pseudoelastic NiTi, Acta Materialia, 61 (2013) 602-616.

[178] K. Raju, S. Bysakh, M.A. Sumesh, S. Kamat, S. Mohan, The effect of ageing on microstructure and nanoindentation behaviour of dc magnetron sputter deposited nickel rich NiTi films, Mater. Sci. Eng. A-Struct. Mater. Prop. Microstruct. Process., 476 (2008) 267-273.

[179] M.M. Sherif, O.E. Ozbulut, Tensile and superelastic fatigue characterization of NiTi shape memory cables, Smart Materials and Structures, 27 (2017) 015007.

[180] Z.N. Farhat, C. Zhang, The role of reversible martensitic transformation in the wear process of tini shape memory alloy, Tribology Transactions, 53 (2010) 917-926.

[181] C. Zhang, Z.N. Farhat, Sliding wear of superelastic TiNi alloy, wear, 267 (2009) 394-400.

[182] Y. Motemani, M. Nili-Ahmadabadi, M.J. Tan, M. Bornapour, S. Rayagan, Effect of cooling rate on the phase transformation behavior and mechanical properties of Ni-rich NiTi shape memory alloy, Journal of Alloys and Compounds, 469 (2009) 164-168.

[183] K.H. Krishnan, S. John, K.N. Srinivasan, J. Praveen, M. Ganesan, P.M. Kavimani, An overall aspect of electroless Ni-P depositions—A review article, Metallurgical and Materials Transactions A, 37 (2006) 1917-1926.

[184] Q.P. Cao, Y. Ma, Y. Xu, L.Y. Chen, C. Wang, Y.Y. Ruan, X.D. Wang, J.Z. Jiang, Bending behavior of electrodeposited glassy Pd–P and Pd–Ni–P thin films, Scripta Materialia, 68 (2013) 455-458.

[185] B.T. Lester, T. Baxevanis, Y. Chemisky, D.C. Lagoudas, Review and perspectives: shape memory alloy composite systems, Acta Mechanica, 226 (2015) 3907-3960.

[186] B. Bergman, On the variability of the fracture stress of brittle materials, Journal of Materials and Science Letters, 4 (1985) 1143-1146.

[187] B. Lawn, Fracture of Brittle Solids, Cambridge University Press, (1993).

[188] C. Greiner, S.M. Oppenheimer, D.C. Dunand, High strength, low stiffness, porous NiTi with superelastic properties, Acta Biomater, 1 (2005) 705-716.

[189] E. Bousser, L. Martinu, J.E. Klemberg-Sapieha, Solid particle erosion mechanisms of protective coatings for aerospace applications, Surface and Coatings Technology, 257 (2014) 165-181.

[190] H. Chai, B.R. Lawn, Fracture mode transitions in brittle coatings on compliant substrates as a function of thickness, Journal of Materials Research, 19 (2011) 1752-1761.

[191] W.Y. Li, J. Wang, H. Zhu, H. Li, C. Huang, On ultrahigh velocity micro-particle impact on steels—A single impact study, Wear, 305 (2013) 216-227.

[192] Z. Li, Z.N. Farhat, G. Jarjoura, E. Fayyad, A. Abdullah, M. Hassan, Investigation of the mechanical behavior of electroless Ni-P-Ti composite coatings, Journal of Engineering materials and technology 142 (2020) 1-12.

[193] S. S da Rocha, G.L.Adabo, G. E. Henriques, Vickers hardness of cast commercially pure titanium and Ti-6Al-4V alloy sumitted to heat treatments, Brazilian Dental Journal 17 (2006) 126-129.

[194] S. J. Hao, L.S. Cui, D. Q. Jiang, X. D. Han, Y. Ren, J. Jiang, Y. N. Liu, Z. Y. Liu, S. C. Mao, Y. D. Wang, Y. Li, X. B. Ren, X. D. Ding, S. Wang, C. Yu, X. B. Shi, M. S. Du, F. Yang, Y. J. Zheng, X. D. Li, D. E. Brown, J. Li A Transforming Metal Nanocomposite with Large Elastic Strain, Low Modulus, and High Strength, Science 339 (2013) 1191-1194.

[195] W. Zhang, J. Kim, N. Koratkar, Energy-absorbent composites featuring embedded shape memory alloys, Smart Mater. Struct, 12 (2003) 642-646.

[196] A.C. Ciubotariu, L. Benea, M. Lakatos–Varsanyi, V. Dragan, Electrochemical impedance spectroscopy and corrosion behaviour of Al2O3–Ni nano composite coatings, Electrochimica Acta, 53 (2008) 4557-4563.

[197] R.B. Diegle, N.R. Sorensen, C.R. Clayton, M.A. Helfand, Y.C. Yu, An XPS investigation into the passivity of an amorphous Ni-20P, Journal of Electrochemistry Society, 135 (1988) 1085-1092.

[198] M. Pourbaix, Altas of electrochemical equilibria in aqueous solutions, National association of corrosion engineers, Houston (1974).

[199] J.H. Xie, A.T. Alpas, D.O. Northwood, Mechano-electrochemical Effect Between Erosion and Corrosion, Journal of Materials and Science, 38 (2003) 4849-4856.

[200] J. Hu, L. Fang, X.L. Liao, L.T. Shi, Influences of different reinforcement particles on performances of electroless composites, Surface Engineering, 33 (2016) 362-368.

[201] J. Creus, H. Mazille, H. Idrissi, Porosity evaluation of protective coatings onto steel, through electrochemical techniques, Surface and Coatings Technology, 130 (2000) 224-232.

[202] M.A. Veloz, I. Gonzalez, Electrochemical study of carbon steel corrosion in buffered acetic acid solutions with chlorides and H_2S, Electrochemica Acta, 48 (2002) 135-144.

[203] E.M. Fayyad, M.K. Hassan, K. Rasool, K.A. Mahmoud, A.M.A. Mohamed, G. Jarjoura, Z. Farhat, A.M. Abdullah, Novel electroless deposited corrosion — resistant and anti-bacterial NiP–TiNi nanocomposite coatings, Surface and Coatings Technology, 369 (2019) 323-333.

[204] Z. Sharifalhoseini, M.H. Entezari, Enhancement of the corrosion protection of electroless Ni–P coating by deposition of sonosynthesized ZnO nanoparticles, Applied Surface Science, 351 (2015) 1060-1068.

[205] J.I.C.F.D. Data®, Powder Diffraction File (PDF) No. 04-011-2340, JCPDS: Netwon Square, PA, USA, (2020).

[206] A. Abdel Aal, Hard and corrosion resistant nanocomposite coating for Al alloy, Materials Science and Engineering: A, 474 (2008) 181-187.

[207] R.W. Revie, Uhlig's Corrosion Handbook, WILEY. inc., Ottawa, Canada(2011) 533-535.

[208] M. Es-Souni, M. Es-Souni, H. Fischer-Brandies, Assessing the biocompatibility of NiTi shape memory alloys used for medical applications, Anal Bioanal Chem, 381 (2005) 557-567.

[209] M. Gholizadeh-Gheshlaghi, D. Seifzadeh, P. Shoghi, A. Habibi-Yangjeh, Electroless Ni-P/nano-WO3 coating and its mechanical and corrosion protection properties, Journal of Alloys and Compounds, 769 (2018) 149-160.

[210] H.M. Wang, H.B. Tang, L.X. Cai, F. Cao, L.Y. Zhang, R.L. Yu, Microstructure and wear properties of laser clad Ti2Ni3Si/Ni3Ti multiphase intermetallic coatings, Applied Physics A, 80 (2004) 1677-1682.

[211] R. Liu, D.Y. Li, Experimental studies on tribological properties of pseudoelastic TiNi alloy wiht comparison to stainless steel 304, Metallugical and Materials Transactions A, 31A (2000) 2773-2783.

[212] Z.N. Farhat, C. Zhang, The Role of Reversible Martensitic Transformation in the Wear Process of TiNi Shape Memory Alloy, Tribology Transactions, 53 (2010) 917-926.

[213] C. Zhang, Z.N. Farhat, Sliding wear of superelastic TiNi alloy, Wear, 267 (2009) 394-400.

[214] R. Neupane, Z. Farhat, Wear and dent resistance of superelastic TiNi alloy, Wear, 301 (2013) 682-687.

[215] S.L. Angioni, M. Meo, A. Foreman, Impact damage resistance and damage suppression properties of shape memory alloys in hybrid composites—a review, Smart Materials and Structures, 20 (2011) 013001.

[216] Z. Li, Z. Farhat. Hertzian indentation behavior of Ni-P-Ti coatings Metallugical and Materials Transactions A, 51 (2020) 3674-3691.

[217] Z. Li, Z. Farhat, M.A. Islam, Investigation of Single-Particle Erosion Behavior of Electroless Ni-P-Ti Composite Coatings, Journal of Materials Engineering and Performance, 29 (2020) 1671-1683.

[218] W.Y. Ching, Electronic structures of amorphous Ni1-xPx glasses, Phys Rev B Condens Matter, 34 (1986) 2080-2087.

[219] K. Li, Y. Li, X. Huang, D. Gibson, Y. Zheng, J. Liu, L. Sun, Y.Q. Fu, Surface microstructures and corrosion resistance of Ni-Ti-Nb shape memory thin films, Applied Surface Science, 414 (2017) 63-67.

[220] M. Aminul Islam, Z.N. Farhat, Mechanical and Electrochemical Synergism of API X42 Pipeline Steel During Erosion–Corrosion, Journal of Bio- and Tribo-Corrosion, 1 (2015).

[221] M. Aminul Islam, Z.N. Farhat, E.M. Ahmed, A.M. Alfantazi, Erosion enhanced corrosion and corrosion enhanced erosion of API X-70 pipeline steel, Wear, 302 (2013) 1592-1601.

[222] J.S.C. Jang, Y.S. Chang, T.H. Li, P.J. Hsieh, J.C. Huang, C.Y.A. Tsao, Plasticity enhancement of Mg58Cu28.5Gd11Ag2.5 based bulk metallic glass composites dispersion strengthened by Ti particles, Journal of Alloys and Compounds, 504 (2010) S102-S105.

[223] M.A. Islam, Z. Farhat, Erosion-corrosion mechanism and comparison of erosion-corrosion performance of API steels, Wear, 376-377 (2017) 533-541.

[224] E. Kulik, N. Nishiyama, Y. Higo, N.A. Gaida, T. Katsura, Hardness of polycrystalline SiO_2 coesite, Journal of the American Ceramic Society, 102 (2019) 2251-2256.

[225] M.A. Islam, Z.N. Farhat, The synergistic effect between erosion and corrosion of API pipeline in CO_2 and saline medium, Tribology International, 68 (2013) 26-34.